UNIVERSITY OF SOUTHAMPTON

FACULTY OF ENGINEERING, SCIENCE AND MATHEMATICS

OPTOELECTRONICS RESEARCH CENTRE

Advanced waveguides for high power optical fibre sources

by

Daniel Beom Soo Soh

Thesis for the degree of Doctor of Philosophy

October 2005

UNIVERSITY OF SOUTHAMPTON

ABSTRACT

FACULTY OF ENGINEERING, SCIENCE & MATHEMATICS

OPTOELECTRONICS RESEARCH CENTRE

Doctor of Philosophy

Advanced waveguides for high power optical fibre sources

By Daniel Beom Soo Soh

This thesis reports on theoretical and experimental studies of wavelength-selective waveguide structures for high-power Nd^{3+}- and Yb^{3+}-doped fibre lasers. Cladding-pumped high-power fibre lasers based on these novel waveguide designs and operating at desired unconventional wavelengths were investigated through numerical simulations and fibre laser experiments.

Rare earth doped fibres have typically multiple emission bands of different effective strengths. Stimulate emission from strong bands dominates over, and *via* a reduced population inversion normally even suppresses, emission from weaker bands in conventional step-index waveguides. For efficient emission and laser operation on the weaker emission bands, it is necessary to suppress unwanted stimulated emission on the strong transitions by preventing power from building up at the unwanted wavelengths. Discrete "bulk" (non-waveguide) devices at a single or a few points are ineffective, if the gain at unwanted wavelength is sufficiently high to generate high-power amplified spontaneous emission even between filters. In such cases, waveguide structures which reduce the gain at unwanted wavelengths and prevent build-up of unwanted emission can be considered. The fibre itself acts as a distributed wavelength-selective filter, and a compact all-fibre laser can be made.

For short-wavelength operation when the gain at longer wavelengths needs to be suppressed, a helical core fibre is proposed. This induces a large bending loss at unwanted longer wavelengths while the bending loss at desired shorter wavelength remains relatively low. The required bending loss properties, for efficient operation at the desired shorter wavelength, can be achieved by designing the helix pitch and offset along with fibre core diameter and NA (numerical aperture). A Nd^{3+}-doped helical fibre laser operating at 0.92 μm was investigated through computer simulations.

Alternatively, there are fibres in which the fundamental mode can be cut off at a certain wavelength. I have studied fibres with a W-type refractive index profile and fibres with a hollow (air-filled) central region surrounded by a core and then a region with depressed refractive index, known as depressed-clad hollow fibre. With these fibre designs, the doped core guides the desired shorter wavelength but not the unwanted longer wavelengths. Nd^{3+}-doped W-type fibre lasers operating at 0.92 μm were simulated and experimentally demonstrated. Also Yb^{3+}-doped depressed-clad hollow fibre lasers operating at 0.98 μm were simulated and experimentally demonstrated.

For long wavelength operation, with a suppressed gain at shorter wavelengths, modified W-type designs are proposed. By designing the refractive index profile and using ring-shaped gain regions, the net gain on an intrinsically weak long-wavelength transition may become larger than that on an intrinsically stronger short-wavelength transition. Adopting this technique, Nd^{3+}-doped fibre amplifiers and lasers operating at 1.38 μm were simulated.

While fibre lasers that generate a nearly diffraction-limited single-mode beam are normally targeted, a multimode output is often obtained, e.g., in development stages with non-ideal fibres. Then it is important to characterise the modal properties of the beam. For this, two different modal power decomposition methods based on intensity measurements are proposed. The first method is based on a tomography technique that uses a Wigner function followed by an inverse Radon transform. The second method adopts a wavelength-sweeping optical source which induces beat patterns after propagation through a certain length of fibre. The feasibilities of the two proposed ideas were verified through numerical simulations.

Contents

PART I. BACKGROUND 1

CHAPTER 1. INTRODUCTION 2

1.1. Motivation of research 2
1.2. Problems to solve 5
1.3. Previously known results 6
1.3.1. Waveguide spectral filters 6
1.3.2. High power Nd^{3+}- and Yb^{3+}-doped fibre sources in different spectral bands 8
1.3.3. Modal decomposition of multimode beams 12
1.4. Major contributions of this research 13
1.5. Organisation of thesis 14

CHAPTER 2. A BRIEF REVIEW OF WAVEGUIDE THEORY 16

2.1. Maxwell equations and exact solutions 17
2.2. Modes in weakly guiding fibres 21

PART II. ADVANCED WAVEGUIDES 23

CHAPTER 3. HELICAL CORE FIBRES 24

3.1. Bending loss in helical core fibres 25
3.2. Fibre design for Nd^{3+}-doped fibre laser operating at 0.92 μm 34
3.3. Numerical simulation of Nd^{3+}-doped helical fibre laser operating at 0.92 μm. 39
3.4. Summary 45

CHAPTER 4. W-TYPE FIBRES 47

4.1. Properties and cut-off of the fundamental mode of W-type fibres 48
4.2. Numerical simulation of W-type Nd^{3+}-doped fibre lasers 55
4.3. Experimental investigations of W-type Nd^{3+}-doped fibre lasers 59
4.3.1. Practical issues 60
4.3.2. Germanosilicate Nd^{3+}-doped W-type fibre laser tuneable from 932 nm to 953 nm 62

4.3.3. Aluminosilicate Nd^{3+}-doped W-type fibre laser tuneable from 908 nm to 938 nm....68
4.4. Summary....76
CHAPTER 5. DEPRESSED-CLAD HOLLOW FIBRES 77
5.1. Design of depressed-clad hollow fibre....79
5.2. Numerical simulation of a Yb^{3+}-doped depressed-clad hollow optical fibre operating at 0.98 μm....88
5.3. Experimental results....93
5.4. Summary....97
CHAPTER 6. MODIFIED W-TYPE FIBRES FOR LONG-PASS FILTERS..... 98
6.1. Fibre design for long-pass filters....98
6.1.1. Long-pass filters involving active ions....100
6.1.2. Long-pass filter in passive fibres....107
6.2. Numerical simulation of 1.3 μm Nd^{3+}-doped fibre amplifier and laser....111
6.2.1. Fundamental limitations of Nd^{3+}-doped fibre amplifier operating at 1.3 μm....112
6.2.2. Numerical simulations for fibre amplifier....116
6.2.3. Numerical simulations for fibre laser....121
6.3. Summary....125
PART III. MODAL POWER DECOMPOSITION..... 127
CHAPTER 7. MODAL POWER DECOMPOSITION..... 128
7.1. Introduction to modal power decomposition....129
7.2. Modal power decomposition using tomography....130
7.2.1. Theory....130
7.2.2. Numerical simulations....143
7.3. Modal power decomposition using wavelength sweeping method....150
7.3.1. Theory....150
7.3.2. Numerical simulation....157
7.4. Summary....161

CHAPTER 8. CONCLUSIONS AND FUTURE PROSPECTS..... 162

8.1. Summary of the contribution 163

8.2. Future prospects 166

APPENDIX A. NUMERICAL SIMULATION OF FIBRE AMPLIFIERS AND LASERS 168

APPENDIX B. M^2 CALCULATION 173

BIBLIOGRAPHY 176

List of figures

1.1. Schematic of an optical fibre.

1.2. Partial energy level diagram of Nd^{3+} ions.

1.3. Energy level of Yb^{3+} ions.

1.1. Illustration of the core of a helical core fibre.

1.2. The coordinate systems for the helix.

3.3. The emission (red line) and the absorption (black line) cross-section spectra of an aluminosilicate Nd^{3+}-doped fibre (F432-LF197).

3.4. The effect of the core radius and the NA on the bending loss of a helical-core fibre.

3.5. Left: The offset and pitch pairs, for a fixed core radius of 3 μm and the NA of 0.1, in order to induce a large bending loss at 1.064 μm and a negligible bending loss at 0.92 μm. Right: The bending losses at 1.064 μm (solid line) and 0.92 μm (dashed line) for different pitch length (with corresponding solution offset position). Results from the approximate equation (3.28).

3.6. The bending loss *vs.* wavelengths of helical-core fibre. For this calculation, the design parameters used are $a_{co} = 3\mu m$, core NA = 0.1, P (pitch length) = 7.2 mm, and Q (offset) = 58 μm.

3.7. The Nd^{3+}-doped fibre laser setup assumed for the simulations.

3.8. A typical output spectrum of the helical Nd^{3+}-doped fibre laser operating at 927 nm. Result from simulations.

3.9. Tuning curve for the Nd^{3+}-doped helical fibre laser. The output signal power (triangle, dashed line) and the slope efficiency (circle, solid line) are shown. Results from simulations.

3.10. An optical spectrum of the output signal when the diffraction grating is tuned to 950 nm. Result from simulations.

3.11. The performance of 927 nm laser with varying pitch and offset.

3.12. The performance of 927 nm laser with varying core radius and NA.

4.1. Schematic diagram of a W-type refractive index profile.

4.2. Refractive indices n_{co} and n_{dp} that lead to a cut-off wavelength of 1 μm. Each curve is obtained through solving equation (4.2) with $a_{co} = 3.5\,\mu m$, $a_{dp} = 8.7\,\mu m$ (black), $a_{co} = 3\,\mu m$, $a_{dp} = 8.7\,\mu m$ (blue), and $a_{co} = 3.5\,\mu m$, $a_{dp} = 6\,\mu m$ (red).

4.3. Comparison of the effective refractive indices of two fibre designs. The curves represent the effective refractive indices of LP_{01} mode with $n_{co} = 1.4601$, $n_{dp} = 1.4258$ (solid curve) and $n_{co} = 1.4585$, $n_{dp} = 1.4561$ (dashed curve), respectively.

4.4. Comparison of the modal intensities of the LP_{01}-mode for two different fibre designs. The curves represent the modal intensity of LP_{01} mode at 0.927 μm with $n_{co} = 1.4601$, $n_{dp} = 1.4258$ (solid curve) and $n_{co} = 1.4585$, $n_{dp} = 1.4561$ (dashed curve), respectively.

4.5. Theoretical bending losses for two different fibre designs. Curves represent the bending losses of the LP_{01} mode at 0.927 μm with $n_{co} = 1.4601$, $n_{dp} = 1.4258$ (solid curve) and $n_{co} = 1.4585, n_{dp} = 1.4561$ (dashed curve).

4.6. Simulated optical spectrum of the output signal from a W-type Nd^{3+}-doped fibre laser operating at 932 nm. Simulation resolution 2 nm.

4.7. Cross-sectional view of the ORC made preform LF170 made at the ORC.

4.8. The transmission spectrum of the fibre F413-LF170 determined through cut-back measurements. Cut back fibre length 1.5 m, which included a 1 m long section that was bent to different radii. OSA resolution 0.5 nm.

4.9. Measured emission cross-section of fibre F413-LF170 (Nd^{3+}-doped germanosilicate).

4.10. Experimental setup for a germanosilicate Nd^{3+}-doped fibre laser at 0.94 μm.

4.11. Laser power characteristics of W-type Nd^{3+}-doped germanosilicate fibre laser, emitting at 0.944 μm.

4.12. Optical spectrum of the laser signal (OSA resolution 1 nm).

4.13. Measured (solid line) and simulated (dotted line) maximum output power and threshold pump power at different wavelengths.

4.14. Measured refractive index profile of F432-LF197 fibre.

4.15. Effective refractive indices of the idealised design (lines superscripted with 'I') and those of the measured refractive index profile (connected dots superscripted with 'M') for fibre F432-LF197.

4.16. Absorption (solid line) and emission (dashed line) cross-section spectra of Nd^{3+} in aluminosilicate (fibre F432-LF197).

4.17. Example of power spectrum of the tuneable Nd^{3+}-doped aluminosilicate fibre laser measured by an OSA with resolution 1 nm. Fibre length 14 m.

4.18. Laser power characteristics at different fibre lengths.

4.19. Tuning range and maximum output power for different fibre lengths.

4.20. Maximum output power and threshold pump power versus wavelength for Nd^{3+}-doped aluminosilicate fibre F432-LF197.

4.21. Optical output spectra at various tuning wavelengths.

5.1. Schematic refractive index profile of a depressed-clad hollow fibre.

5.2. The mode cut-off wavelength dependence on the core width and NA_{co}. The line in (a) represents the LP_{01} 1 μm cut-off and the line in (b) represents the LP_{11} 0.98 μm cut-off.

5.3. The LP_{01} mode of the designed fibre at 0.98 μm.

5.4. Bending loss of the LP_{01} mode at 0.98 μm of the designed fibre.

5.5. LP_{01} mode fields at a wavelength of 0.98 μm. The solid line and the dot-dashed curves represent the field from the modified and the original design, respectively.

5.6. Bending loss of the LP_{01} mode with the modified design.

5.7. The measured stimulated absorption (black) and emission (red) cross-section spectra from a Yb^{3+}-doped aluminosilicate fibre.

5.8. Fibre laser arrangement considered for numerical simulations.

5.9. A typical optical spectrum obtained from the numerical simulation of the fibre laser.

5.10. The power characteristics of the fibre laser at 0.98 μm, from numerical simulations.

5.11. The 0.98 μm laser output power dependence on the fibre length, according to simulations.

5.12. Cross-sectional view of the fabricated depressed-clad hollow fibre F645-LF239. Image of transmitted white light.

5.13. Transmission spectrum of the fabricated Yb^{3+}-doped depressed-clad hollow fibre when straight and when bent to 15 cm diameter. (OSA resolution 1 nm)

5.14. Experimental setup for 0.98 μm Yb^{3+}-doped depressed-clad hollow fibre laser.

5.15. The 0.98 μm laser power characteristics. Inset shows a typical spectrum of the laser (broadband graph resolution 1 nm, narrow band graph resolution 0.05 nm).

6.1. The mode fields of a step index fibre at 0.92 (dash-dotted), 1.05 (dashed), and 1.34 μm (solid line). The dotted line represents the doped region.

6.2. Refractive index profile for a W-type fibre with a raised ring.

6.3. Mode intensities of the W-type fibre with a raised–index outer ring. Dashed-dot line for LP_{01} mode at 0.92 μm, dashed line for LP_{01} mode at 1.05 μm, and solid line for LP_{01} mode at 1.34 μm. The dotted line represents the doped area.

6.4. The overlap factor $\Gamma_{1.34\,\mu m}$ (solid line) as a function of d_1. The dashed line represents $\Gamma_{1.34\,\mu m} / \Gamma_{1.05\,\mu m}$.

6.5. The bending loss of LP_{01} mode at 1.34 μm of the designed W-type fibre with a raised ring.

6.6. Refractive index profile for a passive long-pass filter.

6.7. The mode intensities of the designed fibre. The LP_{01} modes for 1.34 μm (solid line), 1.05 μm (dashed line), and 0.92 μm (dash-dotted line) are shown. Also shown is the region that would be doped in case of an amplifier (dotted line).

6.8. The doped region confinement factor $\Gamma_{1.34\,\mu m}$ along with the diameter of the doped region d_2 (solid line). The dashed line represents the ratio $\Gamma_{1.34\,\mu m} / \Gamma_{1.05\,\mu m}$.

6.9. The bending loss of LP_{01} mode at 1.34 μm from designed fibre.

6.10. Emission and absorption cross-section spectra of Nd^{3+}-doped aluminosilicate fibres. Emission cross-section from reference [83] (black solid), and emission (red dashed) and absorption cross-section (blue dotted) measured on fibre F432-LF197.

6.11. Cross-section spectra of Al-Nd doped fibre at 1.3 μm. Emission cross-section from reference [83] (black solid), emission cross-section of F432-LF197 fibre (red dashed), and absorption cross-section of F432-LF197 fibre (blue dotted).

6.12. OH^--ion absorption spectrum measured in the fibre F432-LF197.

6.13. Configuration assumed for the numerical simulation of an NDFA operating at 1.38 μm.

6.14. A typical spectrum of the output signal (blue solid) from the amplifier. For comparison, the spectrum of the input signal is also shown (red solid). Results of simulations.

6.15. The amplifier gain vs. wavelength for a 1.3 – 1.4 μm NDFA. Blue square-marked (red circle-marked) line represents the amplifier gain for 10 mW input signal without (with) OH^- ion absorption, respectively. Results of simulations.

6.16. Signal output power vs. pump power. The blue line with squares (red line with circles) represents the signal output power (the amplifier gain). The wavelength of the seed signal is 1385 nm with 100 mW input power. Results of simulations.

6.17. The effect of the inner radius of doped ring. The upper and the lower curves represent the gain of a NDFA for the input signal at 1385 nm and 1360 nm, respectively with OH^- ion absorption. Results of simulations.

6.18. Configuration used for simulations of a Nd^{3+}-doped fibre laser operating at 1.38 μm.

6.19. The optical output spectrum of a NDFL at 1385 nm. Results of simulations.

6.20. NDFL output power at 1385 nm vs. launched pump power. Results of simulations.

6.21. Signal output power and slope efficiency vs. operating wavelength. The red circle-marked and the blue triangle-marked curve represent the signal output power and the slope efficiency in the presence of OH^--ion absorption,

respectively. The dashed red circle-marked curve represents the signal output power without OH^--absorption. Results of simulations.

6.22. Signal output power (red, circles) and slope efficiency w.r.t. the absorbed pump power (blue, triangles) vs. fibre length for NDFL at 1385 nm. Results of simulations.

7.1. Measurement setup for determination of the mutual intensity profile.

7.2. The calculated intensity distribution of each mode: (a) the modal solutions inside fibre, (b) the modal solutions after the spherical lens

7.3. A test multimode beam with arbitrary assigned initial modal power: (a) the beam intensity inside fibre, (b) the free-space beam intensity at $z = f$.

7.4. Selected CCD images for different θ, ϕ , i.e., with different positions of the lenses and the CCD array.

7.5. The modal power distribution among modes. The test modal power distribution and the results with simulations A, B and C are shown.

7.6. Comparison between the test multimode beam and reconstructed beam from calculated results. The figure shows the intensity pattern of the test multimode beam inside the fibre (solid line), the reconstructed image from simulation A (dashed line), the reconstructed image from simulation B (dotted line), and the reconstructed image from simulation C (dash-dotted line). Figure 7.6(b) is a magnified portion of figure 7.6(a) to clarify the small differences between results.

7.7. A schematic of the experimental setup for the modal power decomposition using wavelength sweeping method

7.8. The intensity distribution of the test multimode beam inside the fibre. The beam is a combination of LP_{01} (4 W), LP_{11} (2 W), LP_{02} (3 W), and LP_{12} (1 W) modes.

7.9. An example of the RF spectrum of the experimental procedure. There appear six distinct frequency components.

7.10. The associated intensity patterns for each frequency.

7.11. The result of the modal power decomposition. Both the obtained normalised mode intensity patterns and the associated modal weights are presented.

A.1. An energy level illustration for Nd^{3+}-doped fibre amplifier numerical simulator

A.2. Numerical simulation results of a Nd^{3+}-doped fibre laser at 1.38 μm. (a) The pump power evolution, (b) the signal power evolution with dashed line (solid line) represents the backward (forward) signal power, respectively, (c) the optical spectrum of the output, and (d) the fraction of excited ions along the radial and longitudinal position in fibre core.

B.1. M^2 measurement diagram

List of tables

4.1. The change in laser output power at 932 nm, as the parameters of the W-type Nd^{3+}-doped fibre are changed by ± 5% from their design values, as calculated with the simulation model.

5.1. The fundamental mode cut-off wavelength change due to perturbed design parameters.

7.1. The table lists the modes of the step-index fibre considered in the simulations and their effective indices. For the numerical verification of our method, each mode was excited with a power represented by the test modal weight. This was then retrieved with three different simulation procedures, A (without retrieval of mutual intensity), B (with retrieval of mutual intensity, but without CCD noise), and C (with retrieval of mutual intensity including CCD noise), with the results shown in the table.

Declaration of authorship

I, Daniel Beom Soo Soh declare that the thesis entitled *Advanced waveguides for high power optical fibre sources* and the work presented in it are my own. I confirm that:

- this work was done wholly or mainly while in candidature for a research degree at this University;

- where any part of this thesis has previously been submitted for a degree or any other qualification at this University or any other institution, this has been clearly stated;

- where I have consulted the published work of others, this is always clearly attributed;

- where I have quoted from the work of others, the source is always given. With the exception of such quotations, this thesis is entirely my own work;

- I have acknowledged all main sources of help;

- where the thesis is based on work done by myself jointly with others, I have made clear exactly what was done by others and what I have contributed myself;

- Parts of this work have been published as detailed on the following page.

Daniel Beom Soo Soh

October 2005

List of publication

- The thesis is partly based on the following publications.

Journal papers

- D. B. S. Soh, J. Nilsson, J. K. Sahu, and L. J. Cooper, "Geometrical factor modification of helical-core fiber radiation loss formula," *Optics Communications*, vol. 222, pp. 235-242, 2003.
- D. B. S. Soh, S. Yoo, J. Nilsson, J. K. Sahu, K. Oh, S. Baek, Y. Jeong, C. Codemard, P. Dupriez, J. Kim, and V. Philippov, "Neodymium-doped cladding-pumped aluminosilicate fiber laser tunable in the 0.9 μm wavelength range," *IEEE Journal of Quantum Electronics*, vol. 40, pp. 1275-1282, 2004.
- S. Yoo, D. B. S. Soh, J. Kim, Y. Jung, J. Nilsson, J. K. Sahu, J. W. Lee, and K. Oh, "Analysis of W-type waveguide for Nd^{3+}-doped fiber laser operating near 940 nm," *Optics Communications*, vol. 247, pp. 153-162, 2005.
- D. B. S. Soh, J. Nilsson, S. Baek, C. Codemard, Y. C. Jeong, and V. Philippov, "Modal power decomposition of beam intensity profiles into linearly polarized modes of multimode optical fibers," *Journal of the Optical Society of America A*, vol. 21, pp. 1241-1250, 2004.

Conference papers

- D. B. S. Soh, S. W. Yoo, J. K. Sahu, L. J. Cooper, S. Baek, J. Nilsson, and K. Oh, "A cladding pumped neodymium-doped fiber laser tunable from 932 nm to 953 nm," in *Advanced Solid-State Photonics 2004 Technical Digest on CD-ROM* (The Optical Society of America, Washington DC, 2004), Paper MD-10.
- D. B. S. Soh, S. W. Yoo, J. Nilsson, J. K. Sahu, S. Baek, Y. Jeong, L. J. Cooper, C. Codemard, P. Dupriez, C. Alegria, V. Philippov, and K. Oh, "Cladding pumped Nd-doped fiber laser tunable from 908 to 938 nm," presented at Conference on Lasers and Electro-Optics, San Francisco, CA, 7-12 May 2004, Paper CMK4.
- J. Kim, P. Dupriez, D. B. S. Soh, J. K. Sahu, J. Nilsson, and D. N. Payne, "Nd:Al-doped depressed clad hollow fiber laser at 930 nm," in *Advanced Solid-*

State Photonics 2005 Technical Digest on CD-ROM (The Optical Society of America, Washington DC, 2005), Paper MC5.

- J. Kim, D. B. S. Soh, C. Codemard, S. Yoo, Y. Jeong, J. Nilsson, and J. K. Sahu, "Yb:Al-doped depressed clad hollow optical fiber laser operating at 980 nm," presented at Conference on Lasers and Electro-Optics Pacific Rim, Tokyo, 11-15 Jul 2005, Paper CTuI4-5.

- Other publications

Journal papers

- D. B. S. Soh, C. Codemard, S. Wang, J. Nilsson, J. K. Sahu, F. Laurell, V. Philippov, Y. Jeong, C. Alegria, and S. Baek, "A 980-nm Yb-doped fiber MOPA source and its frequency doubling," *IEEE Photonics Technology Letters*, vol. 16, pp. 1032-1034, 2004.
- S. Baek, D. B. S. Soh, Y. Jeong, J. K. Sahu, J. Nilsson, and B. Lee, "A cladding-pumped fiber laser with pump-reflecting inner-cladding Bragg grating," *IEEE Photonics Technology Letters*, vol. 16, pp. 407-409, 2004.
- Y. Jeong, J. K. Sahu, S. Baek, C. Alegria, D. B. S. Soh, C. Codemard, and J. Nilsson, "Cladding-pumped ytterbium-doped large-core fiber laser with 610 W of output power," *Optics Communications*, vol. 234, pp. 315-319, 2004.
- Y. Jeong, J. Nilsson, J. K. Sahu, D. B. S. Soh, G. Alegria, P. Dupriez, C. A. Codemard, D. N. Payne, R. Horley, L. M. B. Hickey, L. Wanzcyk, C. E. Chryssou, J. A. Alvarez-Chavez, and P. W. Turner, "Single-frequency, single-mode, plane-polarized ytterbium-doped fiber master oscillator power amplifier source with 264 W of output power," *Optics Letters*, vol. 30, pp. 459-461, 2005.
- Y. Jeong, J. Nilsson, J. K. Sahu, D. B. S. Soh, P. Dupriez, C. A. Codemard, S. Baek, D. N. Payne, R. Horley, J. A. Alvarez-Chavez, and P. W. Turner, "Single-mode plane-polarized ytterbium-doped large-core fiber laser with 633-W continuous-wave output power," *Optics Letters*, vol. 30, pp. 955-957, 2005.
- D. B. S. Soh, J. Nilsson, and A. B. Grudinin, "Efficient femtosecond pulse generation using a parabolic amplifier combined with a pulse compressor I. stimulated Raman scattering effect," *Journal of Optical Society of America B*, 2005, to appear.

- D. B. S. Soh, J. Nilsson, and A. B. Grudinin, "Efficient femtosecond pulse generation using a parabolic amplifier combined with a pulse compressor II. finite gain bandwidth effect," *Journal of Optical Society of America B*, 2005, to appear.
- Y. Jeong, J. K. Sahu, D. B. S. Soh, C. Codemard, and J. Nilsson, "High-power tunable single-frequency single-mode erbium:ytterbium co-doped large-core fiber master-oscillator power amplifier source," *Optics Letters*, to appear, 2005.

Conference papers

- K. H. Ylä-Jarkko, R. Selvas, D. B. S. Soh, J. K. Sahu, C. A. Codemard, J. Nilsson, S. A. Alam, and A. B. Grudinin, "A 3.5 W 977 nm cladding-pumped jacketed air-clad ytterbium-doped fiber laser," in *Advanced Solid-State Photonics 2003 Technical Digest*, vol. 83, *Trends in Optics and Photonics Series* (The Optical Society of America, Washington DC, 2003), pp. 103-107.
- C. Codemard, D. B. S. Soh, K. H. Ylä-Jarkko, J. K. Sahu, M. Laroche, and J. Nilsson, "Cladding-pumped L-band phosphosilicate erbium-ytterbium co-doped fiber amplifier," presented at Optical Amplifiers and their Applications, Otaru, Japan, 6-9 Jul. 2003, Paper TuC2.
- J. Nilsson, Y. Jeong, C. Alegria, V. Philippov, D. B. S. Soh, C. Codemard, S. Baek, J. K. Sahu, D. J. Richardson, W. A. Clarkson, and D. N. Payne, "Fiber lasers: flexible and functional solutions for today and the future," presented at 3rd International Symposium on Laser and Nonlinear Optical Materials, Colorado, 20-24 Jul. 2003, Paper VI-2.
- Y. Jeong, J. K. Sahu, S. Baek, C. Alegria, C. A. Codemard, D. B. S. Soh, V. Philippov, R. B. Williams, K. Furusawa, D. J. Richardson, D. N. Payne, and J. Nilsson, "The rising power of fibre lasers," in *2003 IEEE LEOS Annual Meeting Conference Proceedings, Vols 1 and 2* (IEEE, New York, 2003), pp. 792-793.
- D. N. Payne, J. Nilsson, Y. Jeong, C. Alegria, V. Philippov, D. B. S. Soh, C. Codemard, S. Baek, J. K. Sahu, D. J. Richardson, and W. A. Clarkson, "The revolution in high-power fiber lasers," presented at 2nd International Symposium on High-Power Fiber Lasers and their Applications, St. Petersburg, 1-3 Jul. 2003, Paper HPFL-1.2.

- V. Philippov, J. Nilsson, Y. Jeong, C. Alegria, D. B. S. Soh, C. Codemard, S. Baek, J. K. Sahu, W. A. Clarkson, and D. N. Payne, "Versatile and functional high power fiber sources," presented at 2nd International Symposium on High-Power Fiber Lasers and their Applications, St. Petersburg, 1-3 Jul. 2003, Paper HPFL-2.4.
- K. H. Ylä-Jarkko, S. U. Alam, P. W. Turner, J. Moore, J. Nilsson, R. Selvas, D. B. S. Soh, C. Codemard, and J. K. Sahu, "Cladding pumping technology for next generation of fiber amplifiers and lasers," presented at Optical Amplifiers and their Applications, Otaru, Japan, 6-9 Jul. 2003, Paper TuC1.
- D. B. S. Soh, C. Codemard, J. K. Sahu, J. Nilsson, S. Baek, S. Wang, and F. Laurell, "An 18 mW, 488.7 nm cw frequency doubled fiber MOPA source," in *Fiber Lasers: Technology, Systems, And Applications*, vol. 5335, *Proceedings Of The Society Of Photo-Optical Instrumentation Engineers* (SPIE International Society Optical Engineering, Bellingham, 2004), pp. 51-55.
- D. B. S. Soh, C. Codemard, J. K. Sahu, J. Nilsson, V. Philippov, C. Alegria, and Y. Jeong, "A 4.3W 977 nm ytterbium-doped jacketed-air-clad fiber amplifier," *Advanced Solid-State Photonics 2004 Technical Digest on CD-ROM* (The Optical Society of America, Washington DC, 2004), Paper MA3.
- Y. Jeong, J. K. Sahu, S. Baek, C. Alegria, D. B. S. Soh, C. Codemard, V. Philippov, D. J. Richardson, D. N. Payne, and J. Nilsson, "Ytterbium-doped double-clad large-core fiber lasers with kW-level continuous-wave output power," presented at Conference on Lasers and Electro-Optics, San Francisco, 16-21 May. 2004, Paper CMS
- J. K. Sahu, Y. Jeong, C. Alegria, C. Codemard, D. B. S. Soh, S. Baek, V. Philippov, L. J. Cooper, J. Nilsson, R. B. Williams, M. Ibsen, W. A. Clarkson, D. J. Richardson, and D. N. Payne, "Recent advances in high power fiber lasers," in *Advanced Solid-State Photonics 2004 Technical Digest on CD-ROM* (The Optical Society of America, Washington DC, 2004), Paper MA1.
- C. A. Codemard, L. M. B. Hickey, K. Yelen, D. B. S. Soh, R. Wixey, M. Coker, M. N. Zervas, and J. Nilsson, "400mW, 1060nm ytterbium doped fiber DFB laser," in *Fiber Lasers: Technology, Systems, and Applications*, vol. 5335, *Proceedings Of The Society Of Photo-Optical Instrumentation Engineers* (SPIE International Society Optical Engineering, Bellingham, 2004), pp. 56-63.

- C. Alegria, Y. Jeong, C. Codemard, J. K. Sahu, L. B. Fu, M. R. Mokhtar, M. Ibsen, S. Baek, D. B. S. Soh, V. Philippov, and J. Nilsson, "Wideband tunable high power narrow linewidth erbium-ytterbium doped fiber laser using compression-tunable fiber Bragg grating," in *Fiber Lasers: Technology, Systems, And Applications*, vol. 5335, *Proceedings Of The Society Of Photo-Optical Instrumentation Engineers* (SPIE International Society Optical Engineering, Bellingham, 2004), pp. 285-290.
- Y. Jeong, J. Nilsson, J. K. Sahu, D. B. S. Soh, C. Alegria, P. Dupriez, C. Codemard, D. N. Payne, R. Horley, L. M. B. Hickey, L. Wanzcyk, C. E. Chryssou, J. A. Alvarez-Chavez, and P. W. Turner, "Single-frequency polarized ytterbium-doped fiber MOPA source with 264 W output power," presented at Conference on Lasers and Electro-Optics, San Francisco, 16-21 May 2004, Paper CPDD1.
- D. B. S. Soh, J. Clowes, I. Godfrey, and A. B. Grudinin, "Compact 85 fs frequency doubled 810 nm fiber system with 60 mW of average power," in *Fiber Lasers II: Technology, Systems, And Applications*, vol. 5709, *Proceedings Of The Society Of Photo-Optical Instrumentation Engineers* (SPIE International Society Optical Engineering, Bellingham, 2005), pp. 23-26.
- J. Nilsson, J. K. Sahu, Y. Jeong, V. Philippov, D. B. S. Soh, C. Codemard, P. Dupriez, J. Kim, D. J. Richardson, A. Malinowski, A. Piper, J. H. V. Price, K. Furusawa, W. A. Clarkson, and D. N. Payne, "High power fiber lasers," presented at Optical Fiber Communications, Anaheim, 6-11 Mar. 2005, Paper OTuF1.
- Y. Jeong, D. B. S. Soh, C. Codemard, P. Dupriez, C. Farrell, V. Philippov, J. K. Sahu, D. J. Richardson, J. Nilsson, and D. N. Payne, "State of the art of cw fibre lasers," presented at Conference on Lasers and Electro-Optics Europe, Munich, 12-17 Jun. 2005, Paper TFII1-1.
- Y. Jeong, J. Nilsson, J. K. Sahu, D. B. S. Soh, P. Dupriez, C. Codemard, C. Farrell, J. Kim, D. J. Richardson, and D. N. Payne, "Beyond 1 kW the rising power of fibre lasers," presented at Opto-Electronics and Communications Conference, Seoul, 4-8 Jul. 2005, Paper 8D1-1.
- Y. Jeong, J. K. Sahu, D. B. S. Soh, C. Codemard, and J. Nilsson, "Tunable single-frequency ytterbium-sensitized erbium-doped fiber MOPA source with

150W (51.8 dBm) of output power at 1563 nm," presented at Optical Fiber Communications, Anaheim, 6-11 Mar. 2005, Paper PDP1.

- Y. Jeong, J. Nilsson, J. K. Sahu, P. Dupriez, C. Codemard, D. B. S. Soh, C. Farrell, J. Kim, D. J. Richardson, and D. N. Payne, "High power fiber lasers," presented at Conference on Lasers and Electro-Optics Pacific Rim, Tokyo, 11-15 Jul. 2005, Paper CwI4-1-INV.
- D. B. S. Soh, A. B. Grudinin, J. Nilsson, Y. Jeong, S. Yoo, J. Kim, C. Codemard, and P. Dupriez, "Stimulated Raman scattering effect on femtosecond pulse generation using a parabolic amplification and a pulse compressor," presented at ONERA Scientific Day, Paris, 27-28 Jun. 2005.
- P. Dupriez, J. Nilsson, Y. Jeong, J. K. Sahu, C. Codemard, D. B. S. Soh, C. Farrell, J. Kim, A. Piper, A. Malinowski, and D. J. Richardson, "Current progress in high-power fiber lasers and amplifiers," presented at Optical Amplifiers and their Applications, Budapest, 7-10 Aug. 2005, Paper TuD1.
- J. Nilsson, Y. Jeong, D. B. S. Soh, C. Codemard, P. Dupriez, C. Farrell, J. K. Sahu, J. Kim, S. Yoo, and D. N. Payne, "High-power fiber lasers: progress and opportunities," presented at 14th International Laser Physics Workshop, Kyoto, 4-8 Jul. 2005, Paper PS5 (plenary).

Acknowledgements

I would like to thank my supervisors; Johan Nilsson and Yoonchan Jeong. Johan taught me brilliant physical insights through endless creative discussions and encouragement. In time of darkness when I didn't know where to go, his excellent guidance always made a breakthrough. I would also like to thank his wife, Jae-Sun Koo, offering generous help and being a good friend to my family. Yoonchan became an example of what a fine scientist should be, especially on attitudes towards the most mysterious God's creation: light. I learned to be humble and curious all the time, facing the light.

My expression of gratitude goes also to my best friends; to Christophe Codemard; I confess that I couldn't achieve many good results without his ingenious ideas; to Jayanta Sahu, Seongwoo Yoo and Jaesun Kim, who fabricated excellent fibres; and to Pascal Dupriez, who always asked me the key question, contributing towards valuable improvements. My thanks go to Romeo Selvas-Aguilar, who taught me how to splice and cleave fibres. Valery Philippov became my best Russian friend. His jokes always made me laugh when I needed to. Thank you, Valery. I am also deeply grateful to Eleanor Tarbox and Carl Farrell for their proof reading of this thesis. I thank Anatoly Grudinin and John Clowes at Fianium Ltd. for helping me to understand the nonlinear optics, which now became the subject of my new life. Eve Smith, Dina Smith, and Jennifer Morley solved many tricky practical problems. I will never meet such fine secretaries in the world.

Eun-Hee, my wife, endured the boring life in England, waiting only for me to be a PhD. She was, is, and will be remaining by my side all the time. My precious daughter, Linn, gave me so much happiness and a vigorous will to live. I love two of you to death. I am indebted to my wife's and my own parents for their love and prayers. Without their prayers, I couldn't even exist. My gratitude and love go to my beloved Eun-Hae community church; Yoo-Il Park, Sang-Hee Cho, Hyon-Ju Byon, Shin-Hee Jeong, Jin-Woo Kim, Jae-Min Jeong, Yong-Ik Jin, and the rest of the family. They are the greatest Christians I should learn from and follow.

Finally, my greatest thanks go to my God, Jehova, who led me to Southampton to study, who forgives, and who loves all. I will always be your humble servant. I love you, my Lord.

Homo unius libri

Part I. Background

Chapter 1. Introduction

1.1. Motivation of research

Nd^{3+}- or Yb^{3+}-doped fibres have multiple emission bands of different effective strengths. Emission, and in particular stimulated emission, from strong bands dominates over, and *via* a reduced population inversion normally even suppresses, emission from weaker bands in conventional step-index waveguides. For efficient emission and laser operation on the weaker emission bands, it is necessary to suppress unwanted stimulated emission on the strong transitions by preventing power to build up at the unwanted wavelengths. It may be possible to use discrete "bulk" (non-waveguide) devices for this. However in many cases such filters at a single or a few points are ineffective, if the gain at unwanted wavelength is sufficiently high to generate high-power amplified spontaneous emission even between filters. In such cases, waveguide structures which reduce the gain at unwanted wavelengths and prevent build-up of unwanted emission can be considered. The fibre itself acts as a distributed wavelength-selective filter, and a compact all-fibre laser can be made.

Here, a Nd^{3+}-doped fibre laser operating at 0.92 μm can exemplify to stress the importance of waveguide filters. The pump saturation intensity at which 50% of the Nd^{3+}-ions are excited is approximately 25 kW/cm^2 = 0.25 $mW/\mu m^2$ with an 808 nm pump. This corresponds to a power of ~2 W in a fibre with a 100 μm inner cladding diameter. One would however typically operate on the long wavelength side of the emission peak, where the emission cross-section is larger than the absorption cross-section. Because of this quasi-four-level characteristic, it is sufficient to excite, say, 10 – 20% of the ions rather than 50% to reach gain and threshold inversion. On the other hand, efficient pumping of an extended fibre implies that the pump power must be high enough to produce gain even after a significant fraction of it has been absorbed. Thus, several watts of pump power is required for efficient cladding-

pumping of a 0.92 μm Nd^{3+}-doped fibre laser with a 100 μm inner cladding diameter. Currently available pump sources can fulfil this, but there is still another obstacle: The low overlap between the pump beam in the inner cladding and the Nd^{3+}-doped core means that long fibres are required to absorb the pump. This compounds the problem with ground-state absorption, in that the competing four-level gain at ~1.06 – 1.09 μm can reach unacceptably large values before the ground-state absorption at the three-level transition is overcome. Therefore, the emission at ~1.06 – 1.09 μm must be suppressed in an efficient cladding-pumped 0.9 μm neodymium-doped fibre laser. Several approaches have been used, often in combination.

One option is to reduce the ground-state absorption. The reduced thermal population of the Stark sub-levels that the transition terminates on enables a neodymium-doped fibre to act as a four-level system at 0.9 μm when cooled to liquid nitrogen temperatures. Thus a cladding-pumped, nitrogen-cooled, high power 938 nm amplifier was demonstrated [1]. However, liquid nitrogen is impractical for most applications. Another option is to use a fibre host composition, such as germanosilicate, with favourable spectroscopy even at room-temperature [2]. Using the W-type design and the favourable spectroscopy of the germanosilicate Nd^{3+}-doped fibres, I successfully demonstrated a fibre laser tuneable from 932 nm to 953 nm [3], which will be presented in chapter 4. In such fibres, the three-level emission cross-section can be higher than the four-level one (although the three-level ground-state absorption still needs to be overcome). However, quenching limits the allowable neodymium concentration to quite low values in germanosilicate (200 ppm mol Nd^{3+} ions without quenching) [2]. This can make the fibres impractically long and lead to significant background loss. The low permissible Nd^{3+}-concentration can, thus, lead to a low efficiency in a germanosilicate host. Instead, one can use an aluminosilicate host, which allows for higher neodymium concentrations. On the other hand, the spectroscopy is less favourable, but with a W-profile core with good enough rejection of four-level emission, 0.92 μm operation is still possible, and higher efficiencies have been obtained than with germanosilicate Nd^{3+}-doped fibres [4-6].

In order to address the need for novel waveguide filters, several approaches have been suggested and investigated in this thesis. By designing suitable waveguide structures for the core, various application oriented fibre lasers and amplifiers can be realised. One example is a helically wound core which has different bending losses

for different wavelengths. This method enables efficient suppression of longer wavelengths with a careful choice of the parameters of the helix.

As will be described in later chapters, wavelength filters that reject longer wavelengths can be implemented by using certain types of waveguides that simply cease to guide light beyond a certain cut-off wavelength. Such are W-type fibres (chapter 4) and depressed-clad hollow fibres (chapter 5).

Conversely, the core waveguide can be designed to amplify only the longer wavelengths. In the conventional single-step refractive index core, shorter wavelengths always tend to be guided better than longer wavelengths. However, other waveguide structures, notably micro-structured fibres, can act as a long-pass or band-pass spectral filter that reject short wavelengths [7]. Alternatively, a specially designed core waveguide structure can confine the shorter wavelengths into undoped regions while longer wavelengths can propagate through the doped region, hence, becoming amplified. The waveguides for longer wavelength pass filters are useful to realise, for instance, neodymium (Nd) doped fibre amplifiers operating at 1.3 μm, which are otherwise degraded by the strong transition ~1.06 μm [8]. They can also be used to realise high power erbium:ytterbium (Er:Yb) co-doped sources at ~1.55 μm while suppressing the competing Yb emission at ~1.06 μm.

The presence, excitation, and characteristics of modes are central to the analysis and understanding of advanced fibre designs such as those studied in this thesis. The possible presence of more than one mode makes experimental investigations of fibres much more challenging. Therefore, as an extension of my analysis of fibre waveguides, my research also aimed to devise methods for modal power decomposition of free-space beams into modes of multimode fibres. Modal decomposition of light beams in multimode optical fibres is a key problem in various areas such as optical fibre communications and optical fibre lasers. For instance, knowledge of the power distribution among modes is necessary in applications such as higher order mode dispersion compensation, mode beating devices, and free-space optical communication employing fibre lasers and amplifiers. Although the M^2 value is conventionally used to describe the beam quality, it is far from a comprehensive measure. For instance, the two beams with same M^2 value can couple into a single-mode fibre with different coupling efficiency. A decomposition of a beam into modes of a fibre is a much better description of the free-space beam as well as the light inside a multimode fibre.

The main subjects of this thesis are the design of the distributed waveguide filters for rejection of unwanted spectral regions while amplifying the desired spectral regions. Although the micro-structured holey fibres show excellent wavelength filtering abilities, they are out of the scope of this thesis since the solid type silica fibres are more suitable for cladding-pumping, which is vital for power scaling. As a supplemental analysis tool, this thesis also treats methods for modal power decomposition.

1.2. Problems to solve

This thesis describes how to design optical fibre waveguides to realise cladding-pumped high power fibre sources. Wavelength selection is a central theme. Therefore, it focuses on novel designs of the refractive index distribution that lead to intrinsically wavelength-selective waveguiding. These will eventually enable such high power fibre sources for the desired wavelength ranges. The subjects covered by this thesis are limited to rare-earth doped optical fibres, with certain geometries providing the desired waveguide properties. Furthermore, only cladding pumping is considered, as this provides a means to scale up the output power. More traditional core-pumping schemes are not considered. With these, it is considerably easier to design lasers for specific wavelengths, but the scope for power-scaling is quite limited. Filters can also be implemented as fibre Bragg gratings and through the incorporation of a dopant which absorbs unwanted radiation. However, such filters are not the objective of this thesis, since they do not rely on a waveguide effect for the filtering.

Optical waveguides are, by definition, structures that transport energy at wavelengths in the infrared, visible, or ultraviolet portions of the electromagnetic

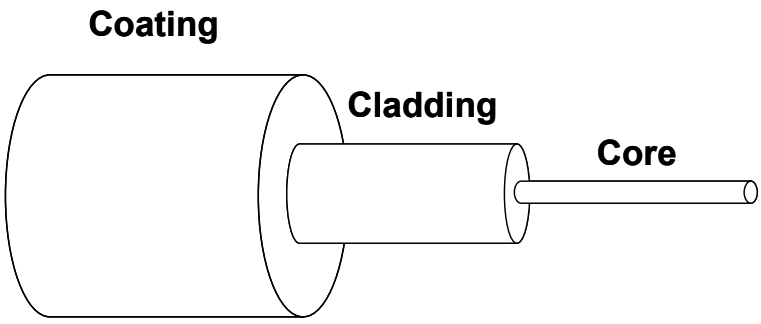

Figure 1.1. Schematic of an optical fibre

spectrum [9]. In conventional waveguides, the guidance of light results from total internal reflection due to the refractive index difference between the guiding medium and the surrounding medium. Optical fibres constitute one type of optical waveguides. They are highly flexible fibres composed of nearly transparent dielectric materials (typically glass) with waveguide structures for signal transmission in the core. In the case of cladding-pumped fibre lasers, the fibre is also configured to guide a pump beam in the cladding. Such a fibre is known as a double-clad fibre [10]. Figure 1.1 shows a typical schematic of an optical fibre. In case of a double-clad (optical) fibre, the cladding (or inner cladding) guides the pump light while the signal is confined in the core. In many double-clad fibres, the refractive index is highest in the core and lowest in the coating. In such a case the coating forms the outer cladding within which the pump beam is guided. Other types of double-clad fibres have separate outer cladding and coating. The core is doped with laser-active rare-earth dopants. It is also possible to dope the vicinity of the core, in addition or as an alternative.

Cladding pumped fibre sources are brightness converters. The pump light from low brightness sources such as highly multimode diode lasers is coupled into the cladding and becomes gradually absorbed by the doped core. Note that there is typically nothing to stop the pump light from entering the core, i.e., the core is in fact a part of the pump waveguide. As a consequence, the rare earth ions become excited and create gain. The signal, which is confined in the small core, becomes amplified by stimulated emission. Because of the small size of the core, the beam quality and brightness of the signal is high. Cladding-pumping has been widely used for high power fibre lasers and amplifiers due to the abundance of cheap multimode diode sources.

1.3. Previously known results

1.3.1. Waveguide spectral filters

Many devices exist which deserve the name ‘waveguide spectral filters’. Among them are the widespread wavelength-division multiplexing fibre couplers (WDM fibre couplers). There are also twin-core fibre spectral filters, which transmit only a selected spectral band [11], and antiresonant reflecting optical waveguide (ARROW) filters [12], which employ two parallelly positioned ARROW structures for spectrally selective coupling between the two waveguides. However, those devices employ a

periodical coupling between two adjacent waveguides so that a different length of devices leads to a different amount of coupling. Therefore, those devices are rather more suitable for pointwise spectral filtering than for distributed filtering over the whole length of the waveguide.

This thesis targets optical fibre waveguide spectral filters in which the core can be doped and which can utilise cladding pumping for power scaling. The optical fibre itself should filter out the unwanted spectral band in a distributed manner. An example of a previously known approach that meets these criteria is an idea of using dispersive materials [13]. In this result, the core and the cladding of the fibre were made of materials with different wavelength-dependence of the refractive indices. The refractive index difference between core and cladding became smaller at shorter wavelengths. At sufficiently short wavelengths, the index difference is so small (or even negative) that the fibre no longer guides. Furthermore, although the index step increases with wavelength, the V-value still decreases beyond some wavelength, so that the fibre also rejects sufficiently long wavelengths. The rejection is enhanced when the fibre is bent (e.g., coiled). When the fibre was bent with a suitable radius, it was calculated that the fibre acted as a band pass filter centred at 1.3 μm with a 3 dB transmission bandwidth of 0.2 μm. It was later found that the annealing condition plays an important role in the spectral characteristics of this kind of device [14]. Furthermore, the refractive index difference between the core and the cladding could be controlled by either heating or cooling the fibre, so that the mode-field diameter could be changed [15]. However, a practical difficulty in this kind of waveguide filter is that it is not easy to find matching dispersive materials for the specific wavelength pass filtering actions. For our purposes, these should also be compatible with efficient high-power laser operation, which significantly restricts the options. In practice, only silica-based fibres can be used.

The W-type refractive-index profile fibre has a core with a high refractive index surrounded by a region with a depressed refractive index (relative to the cladding). This is again surrounded by the cladding. It was first suggested by Kawakami in 1974, and was originally intended for fibres with shifted dispersion [16]. Later, it was found that such W-type refractive-index profile fibres could act as short wavelength pass filters [17]. The effective refractive index of the fundamental guided mode decreases with wavelength. In principle the effective refractive index of the fundamental mode can vary between the refractive index of the core and that of the depressed region. A

sufficiently long wavelength makes the effective refractive index equal to that of the cladding, which in turn means that light with longer wavelengths than this 'cut-off' wavelength cannot be guided in the core. Those are either radiated or guided in the cladding if the refractive index of the outer cladding (usually the coating) is lower than that of the cladding. Compared to the former dispersive material approach, the W-type refractive index profile fibres are easily modifiable for various applications of specific spectral bands of interest. Furthermore it is compatible with high-silica fibre fabrication methods, for example based on the modified chemical vapour deposition (MCVD) method and solution doping [18]. Lasers and amplifiers have also been demonstrated with this approach [19]. However, a limitation of W-type refractive index devices is that they can only act as short-pass filters. Furthermore, the core area that can be used is relatively small, while a large core area provides many advantages for high-power, cladding-pumped, fibre devices.

More recently, a long-wavelength pass filter was suggested employing photonic crystal structures. Mangan *et al.* developed a photonic crystal fibre with a depressed index core [7]. The core refractive index was made less than the silica cladding because it was doped with fluorine. Since the equivalent refractive index of the cladding decreases monotonically with the increasing wavelength, there exists a wavelength in which the core refractive index and the cladding refractive index become equal. Therefore, the core can guide light of the wavelengths above this critical wavelength, hence, the long-wavelength pass filter is achieved. In practice, such long-pass filters can be realised also without the use of a negative refractive index step, at least if the fibre is bent.

1.3.2. High power Nd^{3+}- and Yb^{3+}-doped fibre sources in different spectral bands

Nd^{3+}-ions were used for the first glass laser, which was demonstrated by Snitzer [20]. Figure 1.2 depicts the energy levels of Nd^{3+} ions, which are commonly used for generation of near-infrared fibre sources. For near-infrared operation, a typical pumping wavelength is 800 nm, which invokes the ${}^4I_{9/2} \rightarrow {}^2H_{9/2} + {}^4F_{5/2}$ transition. Ions excited to the energy level ${}^2H_{9/2} + {}^4F_{5/2}$ lose energy rapidly by multi-phonon relaxation and accumulate in the metastable level ${}^4F_{3/2}$. From there, the ions can relax through spontaneous emission in three different wavelength bands with representative

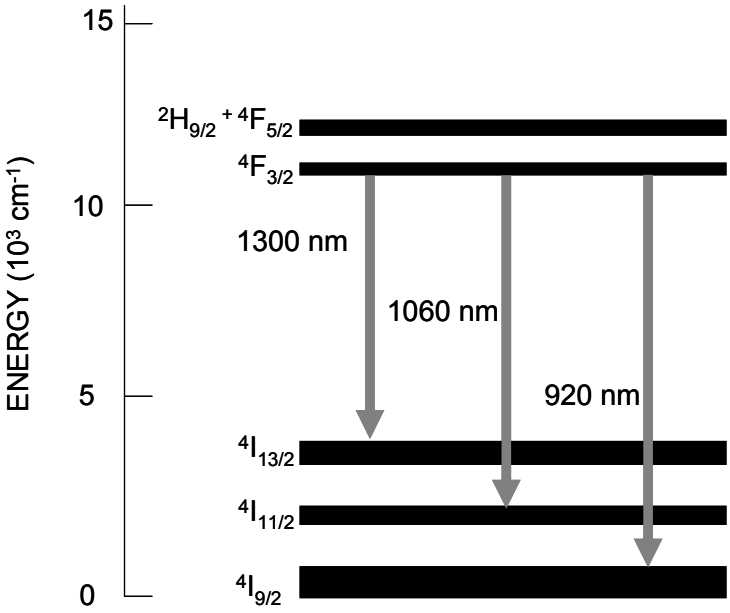

Figure 1.2. Partial energy level diagram of Nd^{3+} ions

wavelengths of 920 nm, 1060 nm, and 1300 nm. There have been serious research efforts towards the realisation of high power sources in each of these emission bands.

Apart from the 1550 nm transition in erbium, the 1060 nm transition of Nd^{3+} is probably the most thoroughly characterised transition in fibre laser history. It is a four-level transition with a high transition probability which therefore provides low laser thresholds and high gain efficiency. Nd^{3+}-doping is used in a wide range of important laser materials such as Nd:YAG. The first reported rare earth doped device based on a fibre fabricated with the modified chemical vapour deposition (MCVD) technology was a Nd^{3+}-doped fibre laser operating at 1088 nm [21]. Since the invention of the power-scaleable double-clad structure [22], the output power of the Nd^{3+}-doped fibre sources in the 1060 nm emission band has increased remarkably. Minelly *et al.* reached over 1 W of output power for the first time with a fibre source, by using this double-clad structure [23]. Soon after, Po *et al.* reached 5 W of output power with 51% slope efficiency [24]. Recent years have seen Nd^{3+}-doped fibre sources with 30 W output power in this spectral range [25]. Even at this level, the output power was limited by the available pump power at a wavelength of 800 nm. Tunability was demonstrated first at low powers with core pumping, and a tuning range of 1068 – 1145 nm (77 nm) was obtained with an external diffraction grating [26].

Nd^{3+}-doped fibres at ~1060 nm can undoubtedly be scaled to much higher powers than 30 W. However, this the most efficient of the Nd^{3+}-transitions overlaps with that of Yb^{3+}-doped fibre lasers. These are superior to Nd^{3+}-doped fibre lasers in all important respects, and there is therefore no interest in scaling Nd^{3+}-doped fibre lasers on this transition. Power-scaling the other transitions is both much more interesting and challenging.

The transition at 1.3 μm is useful primarily because it coincides with the second communication window. Initially, it was hoped that Nd^{3+}-doped glass fibre amplifiers would prove useful at this wavelength. However, the strong excited state absorption (ESA) from ${}^4F_{3/2} \rightarrow {}^4G_{7/2}$ at 1.3 μm seriously limited the performance [27]. It was found that the longer wavelength at ~1340 nm and beyond suffers much less ESA than the shorter wavelength at ~1320 nm. Po *et al*. demonstrated a silica Nd^{3+}-doped fibre laser at 1400 nm [28]. Later, it was found that ZBLAN glass shows much less ESA in the 1.3 μm band than silica [29]. However it was still too high at the telecom wavelengths (1300 – 1310 nm). Therefore, the research on the 1.3 μm Nd^{3+}-doped fibre amplifier was essentially discontinued thereafter. Nevertheless, for non-telecom applications, an efficient high-power fibre source on this transition at wavelengths longer than, e.g., 1340 nm, would still be highly interesting.

Lasers and amplifiers on the three-level transition at ~920 nm were thought to be

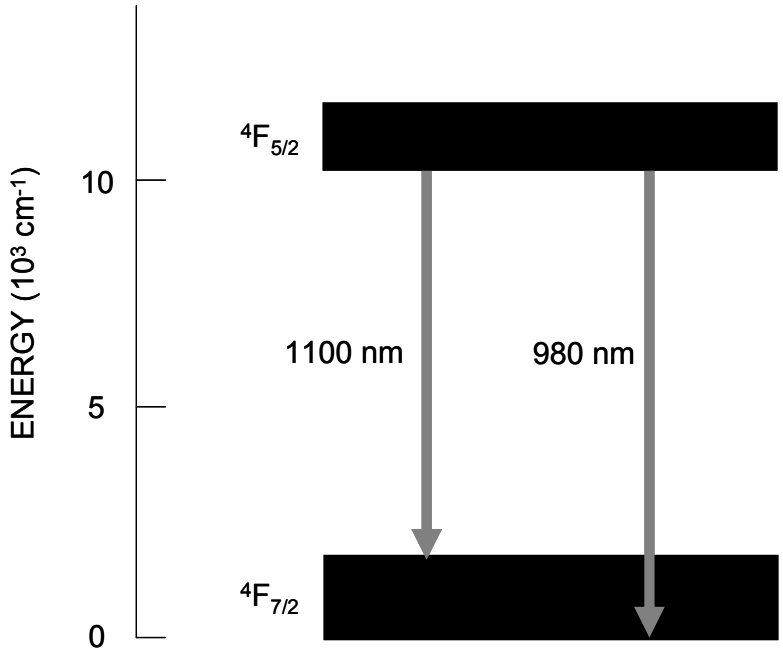

Figure 1.3. Energy level diagram of Yb^{3+} ions

difficult to realise with cladding pumping. The long lengths of fibres required to absorb the pump and the need to overcome the ground-state absorption at ~920 nm indirectly induced unacceptably high gain at 1060 nm. This degrades or even prevents amplification at 920 nm. Core-pumping is different, since it enables the use of relatively short fibres, thus reducing the reabsorption at 920 nm and therefore, indirectly, the gain at 1060 nm. Following the first demonstration of a Nd^{3+}-doped fibre laser operating at 938 nm [30], the most notable results were on a tuneable Nd^{3+}-doped fibre laser. It was tuneable from 892 nm to 936 nm with an output power level of 43 mW [31]. With cladding pumping, it was not until recently (after I commenced my PhD research) that the first fibre amplifier was demonstrated. The fibre was cooled with liquid nitrogen, which reduced the ground-state absorption [1].

Undoubtedly, Yb^{3+}-doped fibres have led the recent rapid development of high power fibre lasers. Figure 1.3 shows the energy levels of Yb^{3+} ions. There are only two levels (when the involved electrons are restricted to the 4f-shell, as is typical for trivalent RE-ions). The two energy levels, namely, $^4F_{7/2}$ and $^4F_{5/2}$, both comprise broad strongly coupled Stark-split sub-levels. Yb^{3+}-doped fibres benefit from an unusually broad absorption band, from below 850 nm to above 1070 nm, and are mainly pumped by 915 nm or 980 nm diodes due to the large absorption cross-sections at these wavelengths. The emission is also broad from 900 nm to 1200 nm. However, there are two main emissions; a 980 nm emission from an essentially two-level transition, and an emission at ~1080 nm that is essentially three-level in nature, in that it terminates on a high-lying Stark level that is nearly empty at room-temperature. Emission is also possible at intermediate wavelengths. For example, Yb^{3+}-ions, in the popular aluminosilicate host, have a secondary peak at 1030 nm, from a transition that terminates on a weakly populated Stark-level. The resulting reabsorption is still sufficient to preclude operation at this wavelength in conventional cladding-pumped fibres. However, core-pumped fibres often emit at 1030 nm.

Cladding-pumped 1080 nm Yb^{3+}-doped fibre sources work best when pumped by 980 nm diodes. The slope efficiency can reach up to 91% in theory and can come close to this in practice. This high conversion efficiency, together with other attractions such as the simplicity of the energy levels involved and the unusually high gain and absorption that is possible (several times higher than in Nd^{3+}-doped fibres because of the higher RE-concentrations that can be used), has made Yb^{3+}-doped fibre

sources operating at 1080 nm the preferred choice for high power fibre sources. There has been a remarkably fast progress in high power Yb^{3+}-doped fibre sources at this wavelength. For instance, Jeong *et al*. reached over 1 kW of output power with a nearly diffraction-limited beam quality [32], in an effort that I took a part in. There have been application-specific high power results, too, such as a singly-polarised single-frequency 264 W master-oscillator power-amplifier (MOPA) source [33].

In stark contrast to the situation at 1080 nm, the 980 nm transition is difficult to operate efficiently at high power. The required fraction of excited population is approximately 50%, since the emission and absorption cross-sections at this wavelength are comparable. If cladding pumping is used in a conventional step index double-clad fibre, the amplified spontaneous emission at 1030 - 1080 nm that result from the long fibre length and the high fractional excitation seriously degrades the 980 nm amplification. To overcome this and to realise cladding pumped 980 nm Yb^{3+}-doped fibre sources, Sahu *et al*. proposed to use a 'jacketed air-clad' ('JAC') structure that allowed high pumping intensity with high-power multimode diodes [34]. The fibre had a relatively small inner cladding (~30 μm diameter) that was surrounded by air holes. This structure allowed a relatively short fibre length of ~30 cm. An output power of 3.5 W was reached in a diffraction-limited beam from this fibre [35].

1.3.3. Modal decomposition of multimode beams

Interferometric measurement methods can be used to determine the shape of the wavefronts from a monochromatic laser source, including both the phase and the amplitude [36]. Once this information is found, one can calculate the modal power distribution by calculating the inner product between the wavefront (output field) and each modal field, with *a priori* knowledge of the modal fields. However, it is not so easy to retrieve the phase from such interferometric measurements, due to the noise in the measured data. By contrast, methods which use only intensity information are more robust in terms of measurement noise.

For intensity measurement methods, approximate methods for multimode fibres, which assumed that the modal space is continuous or the modal fields are azimuthally symmetric, were developed in the 1980's [37, 38]. More recently, a Hermite-Gaussian modal decomposition was demonstrated by Gori *et al*., who successfully decomposed a multimode Hermite-Gaussian beam into eigenmodes and determined the modal

power weights [39]. One advantageous feature of Hermite-Gaussian beams is the orthogonality properties of the Fourier-transformed modal intensity functionals, which unfortunately does not apply to the Bessel functions of the modes of step-index optical fibres. Optimising iterative methods with least square fitting were also used to determine the modal distribution, from measured intensity patterns of the laser beam and using the *a priori* knowledge of each modal field [40].

1.4. Major contributions of this research

In this thesis, high power cladding-pumped Nd^{3+}-doped fibre lasers operating at 0.92 μm and Yb^{3+}-doped fibre lasers operating at 0.98 μm were experimentally demonstrated using newly developed novel waveguides for short wavelength pass filters. Also a Nd^{3+}-doped fibre amplifier operating at 1.38 μm is numerically demonstrated using a waveguide for selection of long wavelengths. Regarding the modal power decomposition, two different methods using only beam intensity measurements are developed.

As presented in the previous section, cladding-pumped 0.92 μm and 0.98 μm amplifiers are known to be difficult to realise since they have competing emissions at longer wavelengths. Unwanted high-power emission can be generated at those longer wavelengths already at low excitation levels. It is demonstrated that the waveguide filters efficiently suppress those competing wavelengths in both cases. For these 0.92 μm lasers, I developed and analysed the helically wound core fibre, the W-type refractive index fibre, and the depressed cladding hollow core fibres (co-developed with J. Kim). As for the 0.98 μm Yb^{3+}-doped lasers, the essential fibre design, namely, 'JAC' fibre was developed by J. K. Sahu and others before I started the PhD research. I contributed to the further development of JAC fibre devices by scaling up the power, investigating new configurations, and applying them for frequency doubling. Thus, I demonstrated direct amplification of a 0.98 μm laser diode [41] and generation of blue light by way of frequency doubling [42, 43].

In addition, using a newly suggested waveguide for a long-wavelength pass filter, I demonstrated, through numerical simulation, the possibility of efficient 1.38 μm amplification in a Nd^{3+}-doped fibre. This waveguide effectively suppresses the competing wavelengths at 0.9 μm and 1.06 μm. Thus, apart from effects like

background loss, the efficiency is limited only by signal ESA, but not by stimulated emission at competing shorter wavelengths.

Two different methods for modal power decomposition, based on beam intensity data, are developed. The first utilises a tomography image reconstruction method. The other utilises heterodyne-type measurements, and was a collaboration with V. Philippov. In the latter method, the output multimode beam varies sinusoidally in intensity, when the frequency of launched light (or equivalently the wavelength of light) is linearly swept. By analysing the frequency of the sinusoidal variation, one can, under some conditions, determine the differences of effective refractive indices of each mode and reconstruct interferometric images corresponding to specific beat frequencies. By analysing this raw information, the power of a beam can be decomposed into power of the modes, and one can also obtain the modal shapes for each mode.

1.5. Organisation of thesis

Part I provides an introduction and a theoretical background in two chapters. In chapter 1 (this chapter), the main problem to be solved and previous known results are presented. Chapter 2 introduces relevant basic waveguide theory. Associated with chapter 2 is appendix A, where rate equations and propagation equations for fibre lasers and amplifiers are presented. The numerical solver for fibre lasers and amplifiers is also presented in appendix A.

Part II is dedicated to waveguide filters. Chapter 3 describes helical-core fibres which induce larger loss for longer wavelengths. The bending loss theory for helical-core fibres is presented. A design for efficient 0.92 μm Nd^{3+}-doped fibre lasers is discussed along with an analysis of the sensitivity and robustness of the design. A numerical simulation for a 0.92 μm Nd^{3+}-doped helical-core fibre lasers follows. Chapter 4 describes the W-type refractive index profile optical fibres, which have a long wavelength rejection filtering capability. Furthermore, a mode analysis is presented. The dependence of the spectral sharpness of the cut-off on bending radius and designs is analyzed, too. A design for an efficient 0.92 μm Nd^{3+}-doped fibre laser is presented with numerical laser simulation results. Then, experimental results for a cladding-pumped high power 0.9 μm tuneable Nd^{3+}-doped fibre laser are presented. Chapter 5 describes the depressed cladding hollow core optical fibres, which have

also a long wavelength rejection filtering capability with sharper spectral cut-off characteristics than the W-type fibres. This chapter is similar in structure to chapter 3 and 4. An experimental result on the 0.98 μm Yb^{3+}-doped fibre lasers is described. Chapter 6 describes fibres with a modified W-type refractive index profile that incorporate a raised ring. These can suppress shorter wavelengths. Its modes are analysed and a design for an efficient 1.3 μm Nd^{3+}-doped fibre amplifier is presented. Numerical amplifier simulations support the viability of this waveguide structure.

Part III treats modal decomposition techniques. Chapter 7 describes the methods for modal power decomposition of multimode free-space running beams based on intensity measurements only. Two different methods are presented, namely, a modal power decomposition by tomography and a modal power decomposition by a wavelength sweep. For each method, numerical simulation supports the feasibility.

Finally, a conclusion which includes possible future research directions is presented.

Chapter 2. A brief review of waveguide theory

The theory of waveguides and that of fibre lasers are used as basic tools that underpin my research. Both the waveguide theory [9, 44, 45] and the fibre laser theory including the rate equations and the propagation equations [46-53] are very well known and have been thoroughly described in the literature. My PhD research is focused more on the possibilities of new waveguide designs. For these, starting from the basic waveguide theory, new results and expressions are derived and heavily used throughout the thesis. Therefore, although well known in the literature, it is reasonable to here introduce the waveguide theory, while laser rate equations and equations for the evolution of the power of a mode are omitted. I refer to a list of references [46-53] for the laser theory. In addition, appendix A contains brief basics of the rate equations and the propagation equations.

It is necessary to understand the basic theory of waveguides, in order to apply the theory to complicated waveguide structures, including in particular optical fibres. Although the suggested waveguide structures in chapter 3, 4, 5, and 6 are considerably more complicated than the conventional step index optical fibres, the basic principle of all structures is the well-known electromagnetic theory.

In this chapter, a very brief review on the waveguide theory is presented. The presented theory will be used extensively throughout the thesis. I start with the Maxwell equations, which universally describe the behaviour of electromagnetic waves (including the optical signal) in a waveguide structure, however complicated it is. Then, Maxwell equations are applied for the specific case of the index guiding optical fibre waveguide structures in the weakly guiding condition.

2.1. Maxwell equations and exact solutions

This section briefly reviews the well known waveguide theory, for example, as in reference [9]. The general Maxwell equation is described as follows.

$$\begin{aligned} \vec{\nabla}\times\vec{\boldsymbol{\mathcal{E}}} &= -\frac{\partial\vec{\boldsymbol{\mathcal{B}}}}{\partial t}, \\ \vec{\nabla}\times\vec{\boldsymbol{\mathcal{H}}} &= \vec{J}+\frac{\partial\vec{\boldsymbol{\mathcal{D}}}}{\partial t}, \\ \vec{\nabla}\cdot\vec{\boldsymbol{\mathcal{B}}} &= 0, \\ \vec{\nabla}\cdot\vec{\boldsymbol{\mathcal{D}}} &= \rho, \end{aligned} \tag{2.1}$$

where $\vec{\boldsymbol{\mathcal{E}}}$ is the electric field (V/m), $\vec{\boldsymbol{\mathcal{B}}}$ magnetic flux density (Tesla), $\vec{\boldsymbol{\mathcal{D}}}$ electric displacement density (C/m^2), $\vec{\boldsymbol{\mathcal{H}}}$ magnetic field (A/m), $\vec{J}$ current density (A/m^2), and ρ electric charge density (C/m^3). In equation (2.1), $\vec{\nabla}\times$ and $\vec{\nabla}\cdot$ represent the curl and divergence operator, respectively and t is the time variable.

For a homogeneous (a medium for which the properties do not change from one point to another) and isotropic (for which its properties are the same for any direction at a given point) medium such as pure silica, the following hold:

$$\begin{aligned} \vec{\boldsymbol{\mathcal{B}}} &= \mu_0\vec{\boldsymbol{\mathcal{H}}}, \\ \vec{\boldsymbol{\mathcal{D}}} &= \varepsilon_0 n^2\vec{\boldsymbol{\mathcal{E}}}, \end{aligned} \tag{2.2}$$

where μ_0 and ε_0 are the free-space permittivity and permeability, respectively, and n is the refractive index. In addition, if the medium is source free, one can neglect $\vec{J}$ and ρ in equation (2.1). Then, using the vector identity $\vec{\nabla}\times\vec{\nabla}\times\vec{A} = -\nabla^2\vec{A}+\vec{\nabla}\left(\vec{\nabla}\cdot\vec{A}\right)$ where ∇^2 is the Laplacian and $\vec{\nabla}B$ represents the gradient of a scalar function B, one obtains a decoupled differential equation as follows.

$$\begin{aligned} \nabla^2\vec{\boldsymbol{\mathcal{E}}} - \mu_0\varepsilon_0 n^2\frac{\partial^2\vec{\boldsymbol{\mathcal{E}}}}{\partial t^2} &= -\vec{\nabla}\left(\vec{\boldsymbol{\mathcal{E}}}\cdot\frac{\vec{\nabla}n^2}{n^2}\right), \\ \nabla^2\vec{\boldsymbol{\mathcal{H}}} - \mu_0\varepsilon_0 n^2\frac{\partial^2\vec{\boldsymbol{\mathcal{H}}}}{\partial t^2} &= 0. \end{aligned} \tag{2.3}$$

Furthermore, if $\vec{\nabla}n^2=0$ in a certain layer of the structure, equation (2.3) in that layer reduces to

$$\nabla^2\vec{\mathcal{E}} - \mu_0\varepsilon_0 n^2 \frac{\partial^2\vec{\mathcal{E}}}{\partial t^2} = 0,$$
$$\nabla^2\vec{\mathcal{H}} - \mu_0\varepsilon_0 n^2 \frac{\partial^2\vec{\mathcal{H}}}{\partial t^2} = 0. \tag{2.4}$$

Hence, the calculation of the electromagnetic field of a waveguide comes down to solving the wave equation (2.4) under certain boundary conditions. For a step index fibre, equation (2.4) is solved for the core and the cladding separately, and boundary conditions are used to match the solutions. For a graded index fibre, in principle, equation (2.3) should be used. However, Marcuse has shown that, under certain conditions, it is possible to use the homogeneous wave equation in (2.4), and this holds even if the index is a function of the space coordinates [44]. This approximation is however only valid if the variation of the index is negligible over a distance of one wavelength.

The variables such as the electric field and the magnetic field consist of a time function and a space function as $\vec{\mathcal{C}} = \Re e\left(\vec{C}e^{i\omega t}\right)$ where $\vec{C}$ is the phase notation (a space function) of $\vec{\mathcal{C}}$ and ω is the optical angular frequency. Thus, adopting this representation, the equation (2.4) is converted to a phase notation as follows:

$$\nabla^2\vec{E} + n^2k_0^2\vec{E} = 0,$$
$$\nabla^2\vec{H} + n^2k_0^2\vec{H} = 0, \tag{2.5}$$

where k_0 is the free-space wavenumber ($k_0 = \omega/c = 2\pi/\lambda$, c is the speed of light in free-space, λ is the wavelength). An elementary, but important example of a solution to equation (2.5) is a plane wave, represented by $\vec{E} = \vec{E}_1 e^{-i\vec{k}\cdot\vec{r}}$, $\vec{H} = \vec{H}_1 e^{-i\vec{k}\cdot\vec{r}}$, where $\vec{k} = nk_0\vec{l}$, $\vec{l}$ is the unit vector in the direction of wave propagation, and $\vec{r}$ is the position vector. A direct application of this solution to the Maxwell equations in (2.1) results in the relationship between the electric and magnetic field as follows:

$$\vec{H} = \frac{1}{\eta}\vec{l}\times\vec{E},$$
$$\eta = \sqrt{\frac{\mu_0}{n^2\varepsilon_0}}, \tag{2.6}$$

where η represents the impedance of the medium. In other words, the wave propagates in the direction of $\vec{E}\times\vec{H}$. In addition, the Poynting vector $\vec{S}$, which describes the density of the power carried by the wave (W/m^2) is

$$\vec{S}=\frac{1}{2}\Re e\left(\vec{E}\times\vec{H}^{*}\right). \tag{2.7}$$

For a plane wave, the Poynting vector is given as $\vec{S}=\left(1/2\eta\right)\left|\vec{E}_1\right|^2\vec{l}$.

Consider now the core waveguide of optical fibres, where the refractive index profile depends only on the radial position (i.e., the profile is circularly symmetric and longitudinally invariant). For this, a cylindrical coordinate system is best suited. Then, the electric and magnetic fields are expressed as

$$\begin{aligned}\vec{\mathcal{E}}&=\Re e\left\{E_r\vec{r}+E_\phi\vec{\phi}+E_z\vec{z}\right\}e^{i(\omega t-\beta z)},\\ \vec{\mathcal{H}}&=\Re e\left\{H_r\vec{r}+H_\phi\vec{\phi}+H_z\vec{z}\right\}e^{i(\omega t-\beta z)},\end{aligned} \tag{2.8}$$

where $\vec{r},\vec{\phi},\vec{z}$ are the unit vectors in the direction of the orthogonal cylindrical coordinates and β is a propagation constant, which will be explained later. Then, by the Maxwell equation (2.1), one can obtain the relationship between the variables as follows:

$$\begin{aligned}E_r&=\frac{-i}{\gamma^2}\left(\beta\frac{\partial E_z}{\partial r}+k_0\eta_0\frac{1}{r}\frac{\partial H_z}{\partial\phi}\right),\\ E_\phi&=\frac{-i}{\gamma^2}\left(\beta\frac{1}{r}\frac{\partial E_z}{\partial\phi}-k_0\eta_0\frac{\partial H_z}{\partial r}\right),\\ \eta_0H_r&=\frac{-i}{\gamma^2}\left(\beta\eta_0\frac{\partial H_z}{\partial r}-n^2k_0\frac{1}{r}\frac{\partial E_z}{\partial\phi}\right),\\ \eta_0H_\phi&=\frac{-i}{\gamma^2}\left(\beta\eta_0\frac{1}{r}\frac{\partial H_z}{\partial r}+n^2k_0\frac{\partial E_z}{\partial r}\right),\end{aligned} \tag{2.9}$$

where $\eta_0\left(=n\eta\right)$ is the free-space impedance (377 Ω) and $\gamma=\sqrt{n^2k_0^2-\beta^2}$. Moreover, through equation (2.5) one obtains differential equations of the E_z and H_z components as follows:

$$\begin{aligned}\frac{\partial^2 E_z}{\partial r^2}+\frac{1}{r}\frac{\partial E_z}{\partial r}+\frac{1}{r^2}\frac{\partial^2 E_z}{\partial \phi^2}+\gamma^2 E_z=0,\\ \frac{\partial^2 H_z}{\partial r^2}+\frac{1}{r}\frac{\partial H_z}{\partial r}+\frac{1}{r^2}\frac{\partial^2 H_z}{\partial \phi^2}+\gamma^2 H_z=0.\end{aligned} \tag{2.10}$$

Once E_z and H_z components are solved using equation (2.10), one can find other components using equation (2.9). Equation (2.10) can be solved through a separation of variables and is obtained for a specific layer of constant refractive index n as

$$\begin{aligned}E_z&=\begin{cases}\left[AJ_m(ur)+BY_m(ur)\right]\cos(m\phi+\phi_0), & nk_0\geq\beta\\ \left[AI_m(wr)+BK_m(wr)\right]\cos(m\phi+\phi_0), & nk_0<\beta\end{cases}\\ H_z&=\begin{cases}\left[CJ_m(ur)+DY_m(ur)\right]\sin(m\phi+\phi_0), & nk_0\geq\beta\\ \left[CI_m(wr)+DK_m(wr)\right]\sin(m\phi+\phi_0), & nk_0<\beta\end{cases}\end{aligned} \tag{2.11}$$

where J_m, Y_m, I_m, K_m are Bessel functions of order m and A, B, C, D, and ϕ_0 are constants. Here, $u=\sqrt{n^2k_0^2-\beta^2}$ and $w=\sqrt{\beta^2-n^2k_0^2}$. Then, the constants A, B, C, D and the propagation constant β are determined by the boundary condition where the refractive index suddenly changes. The boundary conditions are (1) the field should be continuous and (2) the radial and angular derivative of the fields should also be continuous since the r and ϕ components of the fields are represented through the radial and angular derivative of the z component. The final equation that needs to be fulfilled to meet both the boundary conditions is called a characteristic equation. For a step index fibre, one obtains a very simple boundary condition but for a complicated multi-layer structured fibre, the characteristic equations are not easy to represent in a compact form.

For a step index fibre, one can find two simple solutions, namely, a TE (transverse electric) and a TM (transverse magnetic) mode. For the TE mode $E_z\equiv 0$ whereas for the TM mode $H_z\equiv 0$, hence their names. In addition, one can also find EH modes, where the normalised constant $V=a_{co}k_0NA_{co}$ (a_{co} is the core radius and $NA_{co}\left(=\sqrt{n_{co}^2-n_{cl}^2}\right)$ is the core NA) falls into the zeros of the Bessel function J_m. In addition there are HE modes where the normalised constant V satisfies a specific relationship between $J_m(V)$ and $J_{m-2}(V)$. From the normalised propagation constant

V , one can easily find the propagation constant β for each different mode. Additionally, V indicates the number of guided modes inside the fibre. For instance, if V is smaller than 2.405, there is only one mode (HE_{11}) guided in the fibre.

2.2. Modes in weakly guiding fibres

When the refractive indices of the multilayered refractive index profiled fibres are sufficiently close to each other (i.e., $n_1 \cong n_2 \cong \cdots \cong n_{cl}$ where n_i is the refractive index of each layer and n_{cl} is the cladding refractive index), the modes of the exact solutions degenerate. The conditions for the validity of the approximation of weakly guiding waveguides and limitations are well presented in references [9, 54, 55] and are not repeated here for compactness.

In the weakly guiding waveguides, one can assume $n_1 \cong n_2 \cong \cdots \cong n_{cl}$ in the final characteristic equations. Then, the characteristic equations simplify. For example, in the step index fibre, the characteristic equation for EH modes and HE modes reduces to

$$\begin{aligned} \frac{J_{m+1}(ua_{co})}{ua_{co}J_m(ua_{co})} &= \frac{-K_{m+1}(wa_{co})}{wa_{co}K_m(wa_{co})}, \quad (\text{EH modes}) \\ \frac{J_{m-1}(ua_{co})}{ua_{co}J_m(ua_{co})} &= \frac{K_{m-1}(wa_{co})}{wa_{co}K_m(wa_{co})}. \quad (\text{HE modes}) \end{aligned} \tag{2.12}$$

if $m > 1$. Then, by an identity of the Bessel functions, HE_{m+2} modes have the same propagation constant as the EH_m modes. They are therefore degenerate. One can easily show, by using the relationship in equation (2.9), that there are two polarised degenerate modes for each mode group, i.e., one mode with $E_x \left(= E_r \cos\phi - E_\phi \sin\phi\right) \cong 0$ and the other mode with $E_y \left(= E_r \sin\phi + E_\phi \cos\phi\right) \cong 0$. Furthermore, using equation (2.9), one obtains [45]

$$\left|\frac{E_z}{E_t}\right|^2 < \frac{\left|n_i^2 - n_{i+1}^2\right|}{n_i^2}, \tag{2.13}$$

where E_t is either E_x or E_y. Therefore, one obtains a full set of electric and magnetic field components as (for y-polarised mode)

$$\begin{array}{l|l} E_x = 0 & H_x = E_y / n_i\eta \\ E_y = \left[AJ_l(ur) + BY_l(ur) \right] \sin\left(l\phi + \phi_0\right) & H_y = 0 \\ E_z \approx 0 & H_z \approx 0 \end{array}, \qquad (2.14)$$

if $n_i k_0 \geq \beta$ and

$$\begin{array}{l|l} E_x = 0 & H_x = E_y / n_i\eta \\ E_y = \left[CI_l(wr) + DK_l(wr) \right] \sin\left(l\phi + \phi_0\right) & H_y = 0 \\ E_z \approx 0 & H_z \approx 0 \end{array}, \qquad (2.15)$$

if $n_i k_0 < \beta$. The x-polarised mode is similarly represented with exchanged x- and y-components in equations (2.14) and (2.15). l is the azimuthal dependence of the modes. Since the electric and magnetic fields have only one transverse component, the modes of weakly guiding waveguides are called LP (linearly polarised) modes. In a simple step index fibre, modes from the exact solutions (previous section) are degenerated into LP modes. The HE_{11} mode corresponds to the LP_{01} mode and the HE_{21}, TE_{01}, and TM_{01} modes correspond to the LP_{11} mode, for example.

The fundamental LP_{01} mode (or the HE_{11}-mode) is the most important mode. In a step-index fibre, it can be well approximated by a Gaussian shape. This is important since Gaussian beams are modes in free-space. We have, [56]

$$E_t = Ae^{-(r/w_0)^2}, \qquad (2.16)$$

where A is a constant and $w_0 = a_{co}\left(0.65 + 1.619/V^{3/2} + 2.879/V^6\right)$. This makes a good approximation when $V < 8$. Furthermore, since it is somewhat difficult to solve u and w from the characteristic equation even if the characteristic equation of the LP mode is much simpler than that of the hybrid (exact) modes, there exists a good analytical approximation of the solution [55]

$$ua_{co} \cong \frac{2.4V}{1 + \left(4 + V^4\right)^{1/4}}, \qquad (2.17)$$

which is valid up to $V < 8$. Then, w is obtained by $wa_{co} = \sqrt{V^2 - ua_{co}}$.

Part II. Advanced waveguides

Chapter 3. Helical core fibres

In this chapter, a fibre with a helically wound core (or a helical core fibre, or simply helical fibre) is presented as a waveguide filter that can provide a desired suppression of long-wavelength emission. Because the bending loss for long-wavelength radiation in a step index fibre is always larger than for shorter wavelengths (for the same mode), one can use bending loss to suppress the amplified spontaneous emission at the longer wavelength while maintaining the loss at shorter wavelength relatively low. The helix structure is a fibre design to control the bending loss towards that end. The bending loss in a helical fibre may be controlled by its geometric parameters, i.e., the pitch and offset of the helix. Chapter 3 consists of a brief introduction to the bending loss theory of helical fibres, a fibre design section on an efficient Nd^{3+}-doped fibre operating at 0.92 μm, and finally a section on numerical simulations of a helical core 0.92 μm Nd^{3+}-doped fibre laser.

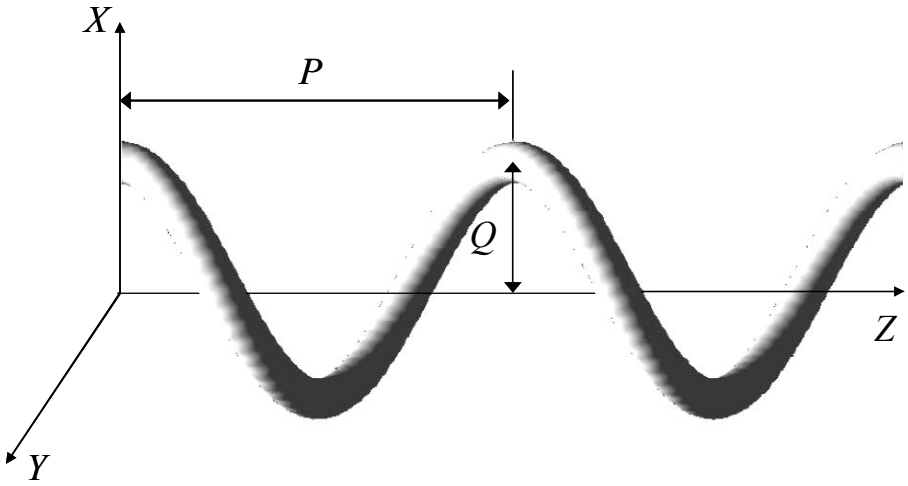

Figure 3.1. Illustration of the core of a helical core fibre.

3.1. Bending loss in helical core fibres

The geometry of a helical fibre is shown in figure 3.1. In the figure, the offset is exaggerated to obtain a clearer view. In practical helical fibres, the pitch is much larger than the offset. The helix has a pitch length P and an offset Q from the Z axis. The figure also shows the (conceptual) phase of the electrical field (the periodical pattern of black and white). The tangent vector of such a helix always has a nonzero angle against the Z axis. Insofar as the phase fronts are perpendicular to the local direction of the core, this also applies to them.

Helical fibres can be fabricated as follows [57]: A fibre preform with an offset core is made by drilling an off-centre hole in a large silica rod, parallel to its axis. A smaller rod, which contains a higher-index core, is then inserted into this hole. The fibre is drawn from a spinning preform. By changing the spinning speed and/or the pulling speed, one can adjust the helix pitch length. The offset position from the centre of the preform can be adjusted by changing the drilling position. The induced stress due to the torsion may be annealed out so that a low-loss circular core can be obtained.

The bending loss of helical fibres has been analysed in the literature [57-62]. However, the published results are based on the assumption that the electric field vector in helical core fibres is parallel to the X-Y plane. In fact, when the direction of light propagation in the helix is considered, the electric field polarisation changes during propagation. Therefore, I suggested a modification of the already known form of helical core bending loss, considering the changing electric field polarisation [63]. Below is a brief presentation of the modification.

In order to calculate the bending loss of such helical structure, I first review the theory of bending loss. The bending losses in fibres are mainly divided into two parts, namely the transition loss and the pure radiation loss. The transition loss is a one-off loss when the mode in a straight fibre travels into the bent section or vice versa. It happens when the bent and the unbent sections are clearly divided. Since the modes are deformed in a bent fibre, there is a mismatch between these modes and those in the straight fibre. The modal adjustment (mismatch) loss is calculated through an overlap integral between the deformed mode in the bent section and the unperturbed mode in the straight section [64]. However, the transition loss is often ignored because, in reality, the bending transition occurs slowly rather than abruptly. In this

case the mode adjusts adiabatically to the deformed mode if the bending radius changes sufficiently slowly.

The pure radiation loss is a continuous loss mechanism which originates from the antenna radiation from the equivalent volume-current (which will be described shortly) of the propagating mode in bent fibres [9]. Of course, the radiated light can also couple back into the fibre. Such back-coupled guided light may have a phase other than that of the original propagating mode. Therefore, the back coupled guided mode from the radiating mode may interfere with the original propagating mode constructively or destructively depending on the phase difference. Hence, the radiation loss may become oscillatory. However, for simplicity, such back-coupling contribution from the radiating mode to the guided mode is not considered in this chapter.

The bending loss in a helical-core fibre is dominated by radiation loss. The deformed mode in a helical core fibre has been calculated [60, 61]. However, with conventional helix dimensions, the pitch length will be so much larger than the offset length that the deformation will be negligible. On the other hand, because of the torsion in helix geometry, the polarisation rotates [65]. However, even with the rotation of the polarisation, it was shown that the radiated power does not change [59]. But, those analyses are based on an assumption that the fields have no component in the Z-axis (in figure 3.1). In fact, if a non-deformed modal shape is assumed, the wavefronts direct to the tangent of helix which is different from the Z-direction. In this case, the fields may have an oscillatory Z-axis component. The net radiation from the fields at each point of helix is then not simply a sum of each field contribution, but needs a more careful treatment due to the destructive interference of the radiated light, which becomes worse when the curvature of helix is smaller (e.g. with a large offset and a small pitch). This destructive interference phenomenon leads to a modification on the previously known helical-core fibre bending loss theory, resulting in a significant reduction (in some cases) from the theoretically known bending loss. For the analysis of the bending loss from a helical-core fibre, a single linear polarisation state is assumed with a non-deformed modal shape. In addition, only the pure radiation loss is considered (not the transition loss), and the fibre is assumed to be single-mode.

The bending loss calculation is based on the volume-current method. The electric field in the core region may be regarded as an equivalent volume-current distribution,

which acts as a travelling wave antenna, radiating power throughout the cladding space. The procedure to calculate the bending loss is to first obtain the equivalent volume-current and second, to calculate the vector potential which will eventually lead to the radiated power. The derivation is straightforward and simple to understand. The outline of the derivation in chapter 23 and related chapters in reference [9] is introduced in the following. Maxwell equations in a source-free medium are expressed as

$$\begin{aligned} \vec{\nabla} \times \vec{E} &= i\left(\mu_0 / \varepsilon_0\right)^{1/2} k\vec{H}, \\ \vec{\nabla} \times \vec{H} &= -i\left(\varepsilon_0 / \mu_0\right)^{1/2} kn^2 \vec{E}, \end{aligned} \tag{3.1}$$

where $\vec{\nabla}$ is the three-dimensional del operator, $\vec{E}$ and $\vec{H}$ are the electric and magnetic fields in a phasor form, as in Chapter 2. In addition, μ_0 and ε_0 are the permeability and the permittivity of free-space, k is the wavenumber in free-space, and n is the refractive index. In fibres, the second equation in equation (3.1) may be rearranged as follows.

$$\vec{\nabla} \times \vec{H} = i\left(\varepsilon_0 / \mu_0\right)^{1/2} k\left(n_{cl}^2 - n^2\right)\vec{E} - i\left(\varepsilon_0 / \mu_0\right)^{1/2} kn_{cl}^2 \vec{E}, \tag{3.2}$$

where n_{cl} is the refractive index of the cladding. Next, the equivalent volume-current density is defined as $\vec{J}_{eq} = i\left(\varepsilon_0 / \mu_0\right)^{1/2} k\left(n_{cl}^2 - n^2\right)\vec{E}$. Then, according to the antenna theory, the equivalent volume-current density acts as a miniature dipole antenna and radiates the power throughout the cladding space. The radiated power can be calculated through the vector potential $\vec{A}$ which is defined implicitly as $\left\{\vec{\nabla}^2 + k^2 n^2\right\}\vec{A} = -\mu_0 \vec{J}_{eq}$. By applying Green's function theorem and integrating, one obtains the vector potential $\vec{A}$ for any point in the space as

$$\vec{A}(s,\theta,\phi) = \frac{\mu_0}{4\pi s}\vec{M}\exp(iksn_{cl}), \tag{3.3}$$

where (s,θ,ϕ) denotes a point in the cladding space in spherical coordinates and

$$\vec{M}(s,\theta,\phi) = \int_{V_J} \vec{J}_{eq}(s',\theta',\phi')\exp(-iks' n_{cl}\cos\chi)dV\ . \tag{3.4}$$

In Equation (3.4), V_J denotes the entire volume which the equivalent volume-current density $\vec{J}_{eq}$ occupies. On the other hand, the electrical and magnetic field can be expressed through the vector potential $\vec{A}$, using the vector identity as follows

$$\begin{aligned} \vec{E} &= -\frac{ik}{(\mu_0\varepsilon_0)^{1/2}}\hat{r}\times(\hat{r}\times\vec{A}), \\ \vec{H} &= \frac{ikn_{cl}}{\mu_0}\hat{r}\times\vec{A}, \end{aligned} \tag{3.5}$$

$\hat{r}$ denotes the unit vector parallel to the vector from the origin to the point of interest. The Poynting vector $\vec{S}$ is calculated as

$$\vec{S} = \frac{1}{2}\vec{E}\times\vec{H}^* = \frac{c^2k^2n_{cl}}{2}\left(\frac{\varepsilon_0}{\mu_0}\right)^{1/2}\left|\hat{r}\times\vec{A}\right|^2\hat{r}, \tag{3.6}$$

where c denotes the speed of light in free-space. The radiated power is just a surface integral of the Poynting vector, i.e., $P_{rad} = \oint_{S_0}\vec{S}\cdot\hat{n}\,dA$ where S_0 is a closed surface containing the entire volume of the volume-current densities and $\hat{n}$ is the normal vector to the infinitesimal surface dA.

Now following the standard procedure described above, the bending loss from a helical-core fibre can be calculated. As is briefly explained above, although the bending loss of a helical-core fibre has been analysed in the past, that analysis

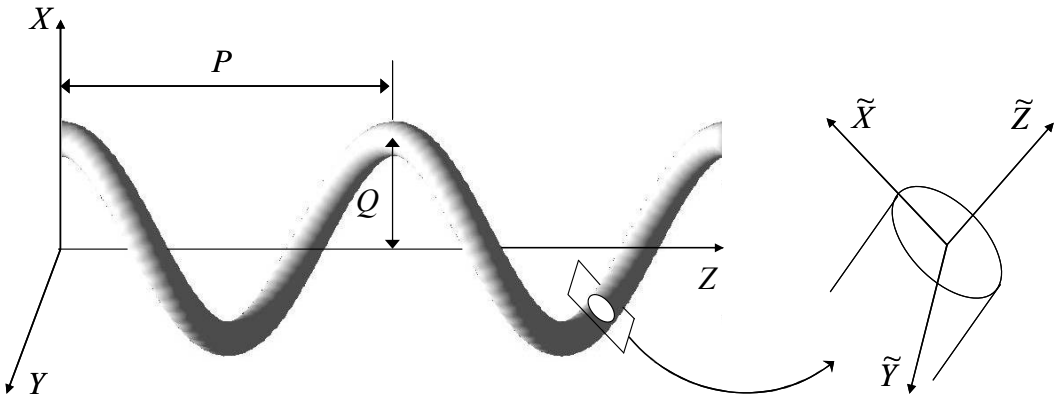

Figure 3.2. The coordinate systems for the helix.

assumed that the normal vector to the wavefronts is always parallel to the Z axis in figure 3.1 [62]. I proposed a modification to the existing theory that considers the actual orientation of the wavefronts, and does not assume that the wavefronts are perpendicular to the Z axis [63]. The modification becomes significant when the pitch length is short and the offset is large. It may lead to a 40% reduction of the bending-loss coefficient (in dB/m) in some cases.

The wavefronts are assumed to be perpendicular to the tangent of the helix. If the pitch is much larger than offset (i.e., the curvature is sufficiently large) so that non-deformed modal shape can be assumed, this assumption is valid. The local coordinate is shown in figure 3.2. The coordinate system XYZ represents the global coordinates whereas the coordinate system $\widetilde{X}\widetilde{Y}\widetilde{Z}$ represents the local coordinates with the $\widetilde{Z}$ axis parallel to the wave propagating axis, i.e. the normal vector to the wavefront plane and the $\widetilde{X}$ axis in the plane parallel to the $X-Z$ plane. The vector $\vec{C}$, from the origin of the global coordinate system to the point at the centre of the core, is represented as follows.

$$\vec{C} = \left[Q\sin\left(\frac{2\pi z}{P}\right),\ Q\cos\left(\frac{2\pi z}{P}\right),\ z \right]. \tag{3.7}$$

Then, the tangent unit vector to the curve representing the centre of the helix core is the normalised derivative of vector $\vec{C}$ with respect to z and is given by

$$\hat{t} = \frac{1}{\sqrt{1+\left(P/2\pi Q\right)^2}}\left[\cos\left(\frac{2\pi z}{P}\right), -\sin\left(\frac{2\pi z}{P}\right), \frac{P}{2\pi Q} \right]. \tag{3.8}$$

The direction of the $\widetilde{X}$ -axis becomes $\left[1,\ 0,\ -\left(2\pi Q/P\right)\cos\left(2\pi z/P\right)\right]$ in the XYZ coordinate system, which is easily verified by setting the Y -axis component to zero and $\hat{\tilde{x}}\cdot\hat{\tilde{z}} = 0$, where $\hat{\tilde{x}}$ and $\hat{\tilde{z}}$ represent the unit vector parallel to the $\widetilde{X}$ - and $\widetilde{Z}$ -axis, respectively. Now, a number of assumptions are made. A single-mode fibre with a single polarisation state is assumed and the rotation due to the torsion of the core is ignored since the rotation of the polarisation in the plane parallel to the wavefronts does not influence the bending loss. Therefore, the polarisation of the light wave will be assumed to be parallel with the $\widetilde{X}$ -axis. Furthermore, a local fundamental mode

approximation is made assuming that the curvature of the helix is sufficiently large, i.e. [9]

$$\frac{Q}{a_{co}\theta_p^2} >> \frac{4\pi V}{\sqrt{2\Delta}W^2}, \tag{3.9}$$

where $\theta_p = \hat{t}\cdot\hat{z}$, a_{co} is the core radius, $V = a_{co}k\sqrt{n_{co}^2 - n_{cl}^2}$, and $W = a_{co}k\sqrt{n_{eff}^2 - n_{cl}^2}$. n_{co}, n_{cl}, and n_{eff} represent the refractive indices of the core and the cladding, and the effective index of the mode, respectively. If equation (3.9) holds, the modal solution for the straight fibre well approximates the fundamental mode of the bent fibre [9]. Then, the electrical field in the core is approximated as

$$\vec{E} = E_{0\tilde{x}}\hat{\tilde{x}} = \frac{J_0\left(U\sqrt{\tilde{x}^2+\tilde{y}^2}/a_{co}\right)}{J_0(U)}\exp(i\beta\hat{s})\hat{\tilde{x}}, \tag{3.10}$$

where J_0 is the Bessel function and $\hat{s}$ represents the arc length along the helix. Although the rotation of the polarisation due to the torsion of the helix core, in the plane parallel to the wavefronts, is ignored, the polarisation of the lightwave still changes from position to position since the direction of the $\tilde{X}$-axis changes. It is the main modification factor I contributed to. It will lead to a significant modification of the final bending loss formula.

The electrical field can be decomposed into X- and Z-components. In this case, the radiation from the Z-components destructively interferes with itself and vanishes (averages to zero). Thus, only the X-component of the electrical fields contribute to the radiated power. The angle θ_x between the X- and $\tilde{X}$- axes is given by

$$\theta_x\left(=\arccos\left(\hat{x}\cdot\hat{\tilde{x}}\right)\right) = \frac{1}{\sqrt{1+\left(\frac{2\pi Q}{P}\right)^2\cos^2(2\pi z/P)}} \cong 1-\frac{1}{2}\left(\frac{2\pi Q}{P}\right)^2\cos^2(2\pi z/P). \tag{3.11}$$

In equation (3.11), a first-order Taylor approximation is taken, which is needed for the future derivation. The error of such an approximation is smaller than 4.4% when $2\pi Q/P$ <0.6. Then, using equation (3.2) – (3.6), the bending loss is obtained as follows: The equivalent volume-current which contributes to the radiation is

$$\vec{J}_{eq} = i\frac{2\pi a_{co}^2}{U}\frac{J_1(U)}{J_0(U)}\left(\frac{\varepsilon_0}{\mu_0}\right)^{1/2} k\left(n_{cl}^2 - n_{co}^2\right)\exp(i\beta s)\left\{1-\frac{1}{2}\left(\frac{2\pi Q}{P}\right)^2\cos^2\left(\frac{2\pi z}{P}\right)\right\}\hat{x}. \quad (3.12)$$

The radiated power P_{rad} is calculated as

$$P_{rad} = \frac{k^2 n_{cl}}{32\pi^2}\left(\frac{\mu_0}{\varepsilon_0}\right)^{1/2}\int_0^{2\pi}\int_0^{\pi}\left\{|M_\theta|^2 + |M_\phi|^2\right\}\sin\theta d\theta d\phi, \quad (3.13)$$

where M_θ and M_ϕ represents the θ- and ϕ-axis components of $\vec{M}$ in equation (3.4), in spherical coordinates. Here, θ is the angle between the Z-axis and the position vector and ϕ is the angle between the X-axis and the vector projected onto the $X-Y$ plane from the position vector. The vector $\vec{M}$ is calculated using equation (3.4) as

$$\vec{M} = \kappa\left\{J_0(kn_{cl}Q\sin\theta)F_0 + 2\sum_{m=1}^{\infty}(-i)^m J_m(kn_{cl}Q\sin(m\theta))F_m\right\}\hat{x}, \quad (3.14)$$

where

$$\kappa = i\frac{2\pi a_{co}^2}{U}\frac{J_1(U)}{J_0(U)}\left(\frac{\varepsilon_0}{\mu_0}\right)^{1/2} k\left(n_{cl}^2 - n_{co}^2\right), \quad (3.15)$$

$$F_m = \int_{-L}^{L}\cos\left\{m\left(\phi - \frac{2\pi z}{P}\right)\right\}\exp\left\{i\left(\frac{\beta}{\cos\theta_p} - k\cos\theta\right)z\right\}\left\{1-\frac{1}{2}\left(\frac{2\pi Q}{P}\right)^2\cos^2\frac{2\pi z}{P}\right\}dz, \quad (3.16)$$

and $2L$ is the length of the fibre of interest. In equation (3.14), the following identity is used:

$$\exp(-iz\cos\theta) = J_0(z) + 2\sum_{m=1}^{\infty}(-i)^m J_m(z)\cos(m\theta). \quad (3.17)$$

On the other hand, taking advantage of the following identity

$$\lim_{L\to\infty}\int_{-L}^{L}\cos\left\{m\left(\phi-\frac{2\pi z}{P}\right)\right\}\exp\left\{i\left(\frac{\beta}{\cos\theta_p}-kn_{cl}\cos\theta\right)z\right\}=Si\left(\frac{2m\pi L}{P}\right), \quad (3.18)$$

where

$$Si(\xi)=\frac{\sin\{L(\beta/\cos\theta_p-kn_{cl}\cos\theta+\xi)\}}{L(\beta/\cos\theta_p-kn_{cl}\cos\theta+\xi)}\exp(im\phi)+\frac{\sin\{L(\beta/\cos\theta_p-kn_{cl}\cos\theta-\xi)\}}{L(\beta/\cos\theta_p-kn_{cl}\cos\theta-\xi)}\exp(-im\phi), \quad (3.19)$$

the equation (3.16) changes to

$$F_m=L\left\{1-\frac{1}{4}\left(\frac{2\pi Q}{P}\right)^2\right\}Si\left(\frac{2m\pi}{P}\right)-\frac{L}{8}\left(\frac{2\pi Q}{P}\right)^2\left\{Si\left(\frac{2\pi(m-2)}{P}\right)+Si\left(\frac{2\pi(m+2)}{P}\right)\right\}. \quad (3.20)$$

The function Si has peaks when $\beta/\cos\theta_p-kn_{cl}\cos\theta-\xi=0$. Then, the vector $\vec{M}$ is well approximated as

$$\vec{M}=M_x\hat{x}=2\kappa L\left[\begin{array}{l}\sum_{m'}J_{m'}^2(kn_{cl}Q\sin\theta_{m'})Si^2\left(\frac{2m\pi}{P}\right)\left\{1-\frac{1}{4}\left(\frac{2\pi Q}{P}\right)^2\right\}^2\\+\sum_{m^-}J_{m^-}^2(kn_{cl}Q\sin\theta_{m^-})Si^2\left(\frac{2\pi(m^--2)}{P}\right)\frac{1}{64}\left(\frac{2\pi Q}{P}\right)^4\\+\sum_{m^+}J_{m^+}^2(kn_{cl}Q\sin\theta_{m^+})Si^2\left(\frac{2\pi(m^++2)}{P}\right)\frac{1}{64}\left(\frac{2\pi Q}{P}\right)^4\end{array}\right]^{1/2}\hat{x}, \quad (3.21)$$

where $\theta_{m'},\theta_{m^\pm},m',m^\pm$ ($m',m^\pm$ are integers) are the solutions of

$$\cos\theta_{m'}=\frac{1}{kn_{cl}}\left\{\frac{\beta}{\cos\theta_p}-\frac{2\pi m'}{P}\right\},\quad \cos\theta_{m^\pm}=\frac{1}{kn_{cl}}\left\{\frac{\beta}{\cos\theta_p}-\frac{2\pi(m\pm2)}{P}\right\}. \quad (3.22)$$

From reference [9], the radiated power is expressed as

$$P_{rad}=\frac{k^2n_{cl}}{32\pi^2}\left(\frac{\mu_0}{\varepsilon_0}\right)^{1/2}\int_0^{2\pi}\int_0^{\pi}\sin\theta(1-\sin^2\theta\sin^2\phi)|M_x|^2\,d\theta d\phi. \quad (3.23)$$

Using equations (3.21) – (3.23) and the technique in [58], one obtains the loss coefficient γ (Np/m) as

$$\gamma = C_f \left(\frac{2}{a_{co}} \right)^{1/2} \frac{\pi^2}{\Delta^{1/4}} \frac{Q}{P^{3/2}} \frac{V^{5/2}}{U^2} \frac{1}{(1+\varepsilon)^{1/4}} \exp\left(-\frac{2}{3} \frac{\Delta^{1/2}}{\pi} \frac{S}{a_{co}} \frac{W^2}{V} \frac{1}{(1+\varepsilon)^{1/2}} \right), \quad (3.24)$$

where $\varepsilon = 2\left(\theta_p V / \sqrt{2\Delta} W\right)^2$ and S is the arc length for one pitch ($S = P/\cos\theta_p$). C_f in equation (3.24) is the modification factor and is given as

$$C_f = 1 - \frac{1}{2}\left(\frac{2\pi Q}{P}\right)^2 + \frac{3}{32}\left(\frac{2\pi Q}{P}\right)^4. \quad (3.25)$$

The factor C_f represents the difference between the current derivation and the previous result. Thus, if $C_f = 1$ equation (3.24) reduces to the result in [58].

When the fibre supports multiple modes, the differential in bending loss between different modes can be used for mode-selection so that only the fundamental mode is guided effectively. With a multimode helical core one can achieve single-mode operation by changing the pitch and off-set parameter. The higher order modes have larger bending loss because their guidance is weaker. In addition, higher-order modes are more vulnerable to modal deformation by the bending. Therefore, there may exist an effective cut-off wavelength above which only the fundamental mode can propagate. Marcuse [66] successfully derived the effective modal cut-off condition, using the modal field deformation theory, as

$$n_{eff}^{cut-off} = n_{cl} \frac{R_b + a_{co}}{R_b}, \quad (3.26)$$

where R_b is the radius of curvature of the bent fibre. Marcuse concluded that if the effective index of a particular mode is less than $n_{eff}^{cut-off}$ in equation (3.26), the mode will completely radiate its energy. The result in reference [66] is based on the modal field deformation due to the bending. This deformation is assumed to be negligible in the above derivation when the condition of equation (3.9) applies. However, when a mode is cut off according to equation (3.26), the condition in equation (3.9) is

violated and the result in equation (3.24) is no longer valid. In the helix geometry, the radius of curvature is calculated through the Euler angle as

$$R_b = \frac{Q}{\sin^2 \theta_p} = \frac{S^2}{4\pi^2 Q}. \tag{3.27}$$

Therefore, equations (3.26) and (3.27) give the mode cut-off criterion, while the assumption of equation (3.9) no longer holds near cut-off.

3.2. Fibre design for Nd^{3+}-doped fibre laser operating at 0.92 μm

In this section I present a helical fibre design procedure for a Nd^{3+}-doped fibre laser operating on the $^4F_{3/2} \rightarrow {}^4I_{9/2}$ transition at ~0.92 μm. Nd^{3+}-doped fibres have three wavelength bands of emission, namely at 0.9 μm, 1.06 μm, and 1.38 μm (in aluminosilicate). The emission at 1.38 μm suffers from OH^- ion absorption, which peaks at 1.38 μm, and a strong ESA. Therefore, the gain at this wavelength is

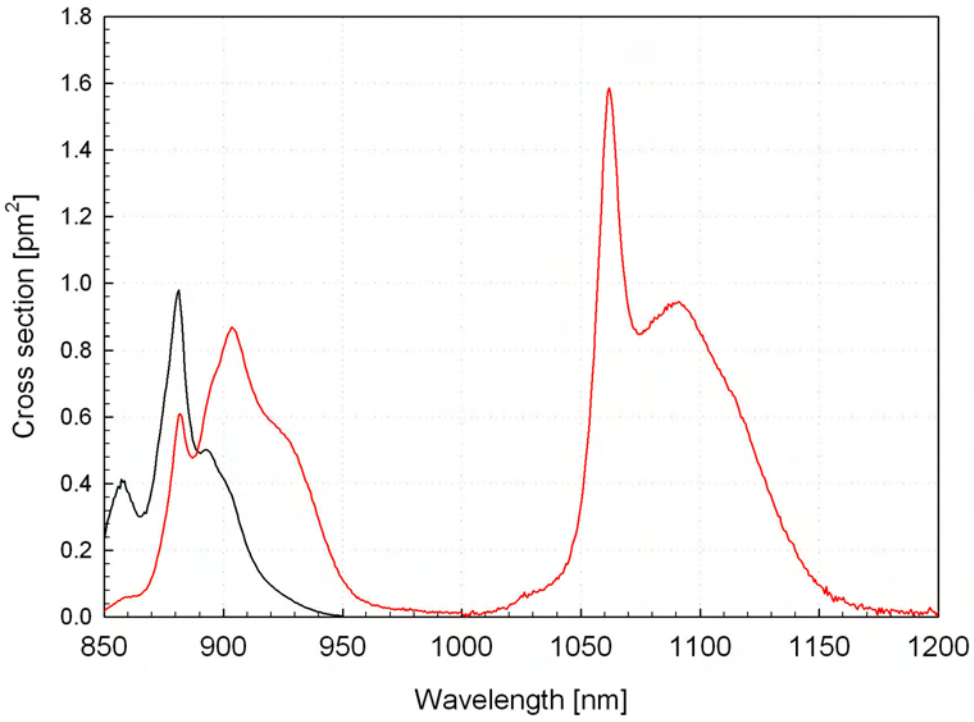

Figure 3.3. The emission (red line) and the absorption (black line) cross-section spectra of an aluminosilicate Nd-doped fibre (F432-LF197).

relatively low compared to that in the 0.9 μm and the 1.06 μm emission bands. In addition, amplified spontaneous emission can build up to high power in the stronger short-wavelength emission bands, which makes operation at 1.38 μm even more difficult. Nd^{3+}-doped fibres for the 1.38 μm band will be discussed in Chapter 6. In this chapter, however, the emission at 1.38 μm is neglected because of its weakness.

The main obstacle to overcome to achieve an efficient Nd^{3+}-doped fibre laser operating at ~0.92 μm is the strong amplified spontaneous emission at ~1.06 μm. While the oscillator strengths and peak cross-sections of these two emission bands are comparable, the ${}^4F_{3/2} \rightarrow {}^4I_{9/2}$ transition occurs to the ground-state and suffers therefore from ground-state absorption. Thus, gain occurs more readily at longer wavelengths (~0.92 μm), where the ground-state absorption is much reduced, than the emission peak at 0.90 μm. However as the emission cross-sections are lower here and the ground-state absorption is still a significant factor, the 0.92 μm gain is much lower than that at 1.06 μm. The 0.92 μm ground-state absorption also leads to a relatively high threshold, but the laser threshold would still be reached provided that a sufficient pump is present. However, if the amplified spontaneous emission at 1.06 μm is not suppressed, it clamps the fraction of excited ions so that the gain at 0.92 μm reduces significantly, hindering efficient operation at 0.92 μm. In some cases when the gain at 1.06 μm becomes too large, the fibre starts lasing at 1.06 μm and the required population inversion for a positive gain at 0.92 μm is never achieved. Figure 3.3 shows the emission and absorption cross-section spectra of an aluminosilicate Nd^{3+}-doped fibre (F432-LF197), which was made in ORC. This data is obtained through the cross-section calculation technique described in reference [53].

One can calculate the small signal gain using the cross-sections in figure 3.3. For this, we assume a single-mode fibre with a core of 3 μm radius and 0.11 NA so that the single-mode cut-off wavelength becomes 0.86 μm. The overlap factors Γ are 78% and 70% at 0.92 μm and 1.064 μm, respectively. The threshold of fraction of excited ions for positive gain at 0.92 μm is calculated as 12.8% by taking $\sigma_e^{0.92\,\mu m} = 0.6095\,pm^2$, $\sigma_a^{0.92\,\mu m} = 0.0896\,pm^2$, and $\sigma_a^{0.808\,\mu m} = 2.405\,pm^2$. The concentration of Nd^{3+} ions is 1.6×10^{25} ions$/m^3$. One can assume that the laser cavity consists of a 4% Fresnel reflection from a flat cleave at one end (14 dB loss) and a bulk grating with a total loss of, say, 2 dB. The cavity loss becomes 16 dB in total, if we neglect fibre propagation losses. If the fibre length is 5 m, the average fraction of

excited ions should be 17%, in order to achieve the round-trip gain of 16 dB at 0.92 μm, matching the cavity loss. Therefore, a 17% average fraction of excited ions corresponds to the threshold for a 0.92 μm laser. However, in this case, the small signal round-trip gain at 1.064 μm becomes 131 dB ($\sigma_e^{1.064\mu m} = 1.5868\, pm^2$). Long before exciting 17% of the ions, the 1.06 μm emission would build up to strong power, either from amplified spontaneous emission or from lasing from spurious feedback. The excited-state fraction clamps at a level below 17%, so 0.92 μm lasing cannot be achieved. For operation at 0.92 μm, the net fibre gain at 1.064 μm should not exceed 40 dB. This can be achieved by introducing a waveguide loss at 1.064 μm of ~100 dB. At the same time, the loss induced at 0.92 μm must be low for efficient operation.

Bending loss, e.g., in a helical-core fibre, can induce a high loss at longer wavelengths (1.06 μm) while the loss at shorter wavelengths (0.92 μm) can remain low. This opens up the possibility for an efficient Nd^{3+}-doped fibre laser operating at 0.92 μm using the helical fibre. Important issues are, firstly, that the bending loss at 1.064 μm should be sufficiently large (hundred dB or more) while that at 0.92 μm stays at a tolerable level (at most ~ 1 dB). Secondly, the fibre preferably should support only the fundamental mode at 0.92 μm. It could be achieved either by designing a strictly single mode fibre at 0.92 μm or otherwise rejecting (effectively

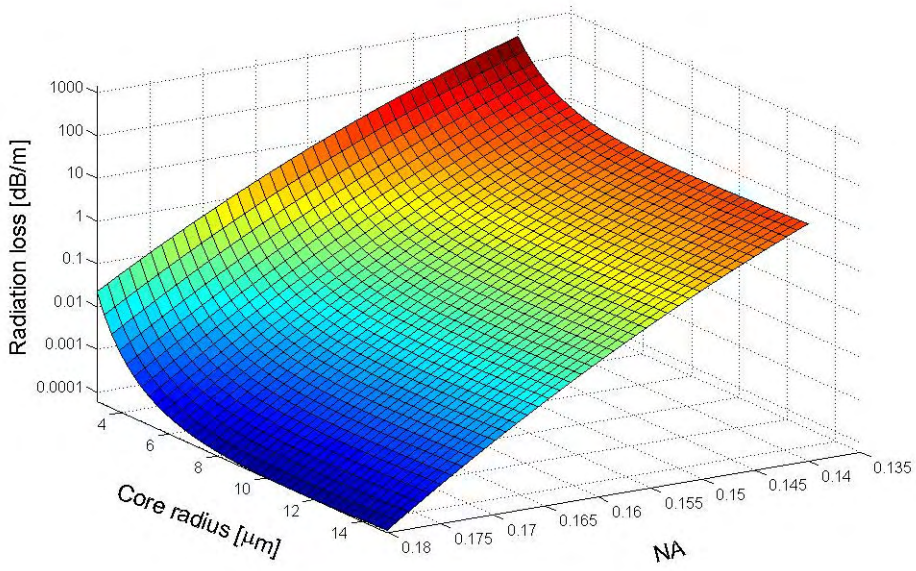

Figure 3.4. The effect of the core radius and the NA on the bending loss of a helical-core fibre.

cutting off) higher modes according to equation (3.26). Helical-core fibres can be manufactured with helical pitches of a few millimetres or more and offsets, say, up to 200 μm (and down to arbitrarily small values). The core diameter can vary over a wide range. It seldom exceeds 40 μm and is normally considerably smaller, e.g., 10 μm. The NA of the fibre core may vary in the range 0.1~0.3 for helical-core fibres.

The dependence of bending loss on core size and NA is shown in figure 3.4. For this calculation, the pitch length P and the offset Q were fixed to 3.5 mm and 150 μm, respectively. The wavelength was assumed to be 1.064 μm and the LP_{01} mode only is considered. The figure shows that the bending loss increases as the NA of the core and the core radius become smaller. Within the range of the parameters used for this calculation, the bending loss is very sensitive to a change of NA. An increase of the NA of 0.067 induced an order of magnitude decrease in the bending loss.

In order to design a helical fibre for an Nd^{3+}-doped fibre laser operating at 0.92 μm, one must design the fibre with a negligible bending loss at 0.92 μm. Preferably it should be negligible compared to other losses and no more than around 0.1 dB/m for a typical fibre length of 10 m. For shorter fibres the loss can be higher. At the same time, we need a significant bending loss at 1.06 μm (say, a few tens of dB/m). Thus, the dependence of the bending loss on wavelength must be quite strong. In order to see clearly how to fulfil this condition, it helps to describe the differential bending loss in an approximate quantitative. One can obtain $\partial\gamma/\partial\lambda$ approximately as follows:

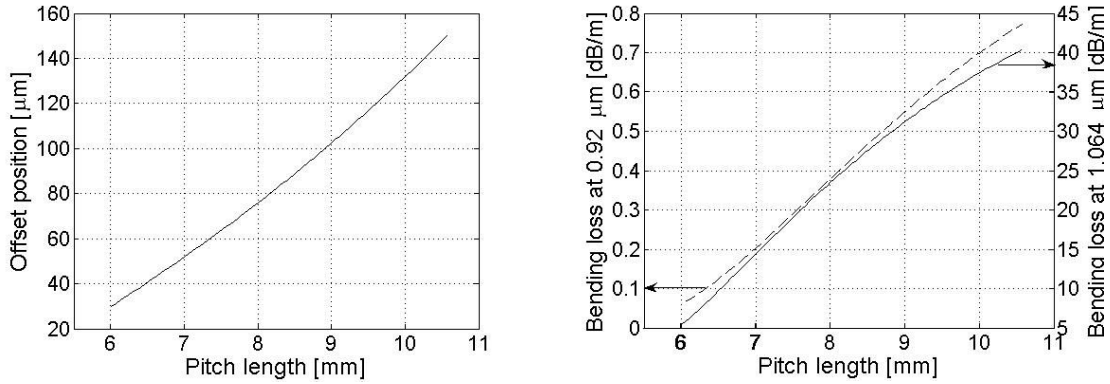

Figure 3.5. Left: The offset and pitch pairs, for a fixed core radius of 3 μm and the NA of 0.1, in order to induce a large bending loss at 1.064 μm and a negligible bending loss at 0.92 μm. Right: The bending losses at 1.064 μm (solid line) and 0.92 μm (dashed line) for different pitch length (with corresponding solution offset position). Results from the approximate equation (3.28).

$$\frac{\partial \gamma}{\partial \lambda} \cong \left(\frac{\partial V}{\partial \lambda}\right)\left(\frac{\partial \gamma}{\partial V}\right) \cong \frac{2\pi a_{co} NA}{\lambda^2}\left\{\frac{2\Delta^{1/2} S}{3\pi a_{co}(1+\varepsilon)^{1/2}} - \frac{5}{2}\frac{\gamma}{V}\right\}. \tag{3.28}$$

In equation (3.28), $\varepsilon \cong 4\pi^2 Q^2 / \Delta S^2$ is used. Therefore, by using equations (3.24) and (3.28), one can decide the design parameters a_{co}, NA, P, and Q to match simultaneously the desired bending losses at 0.92 μm and 1.064 μm. Among the design parameters, the NA of the core is relatively difficult (but still quite possible) to vary. In particular, the NA and the refractive-index profile as a whole are difficult to control with high precision. The offset, the pitch length, and the core size are easier to change and control in the fabrication process (more exactly, in the pulling stage). However, if one wants to change the core size in the pulling process and, thus, vary the entire cross-sectional fibre diameter, the offset position changes, too, and vice versa. Furthermore considerations such as power handling and energy storage may make it difficult to change the core size. Therefore, once a preform is made, it is most

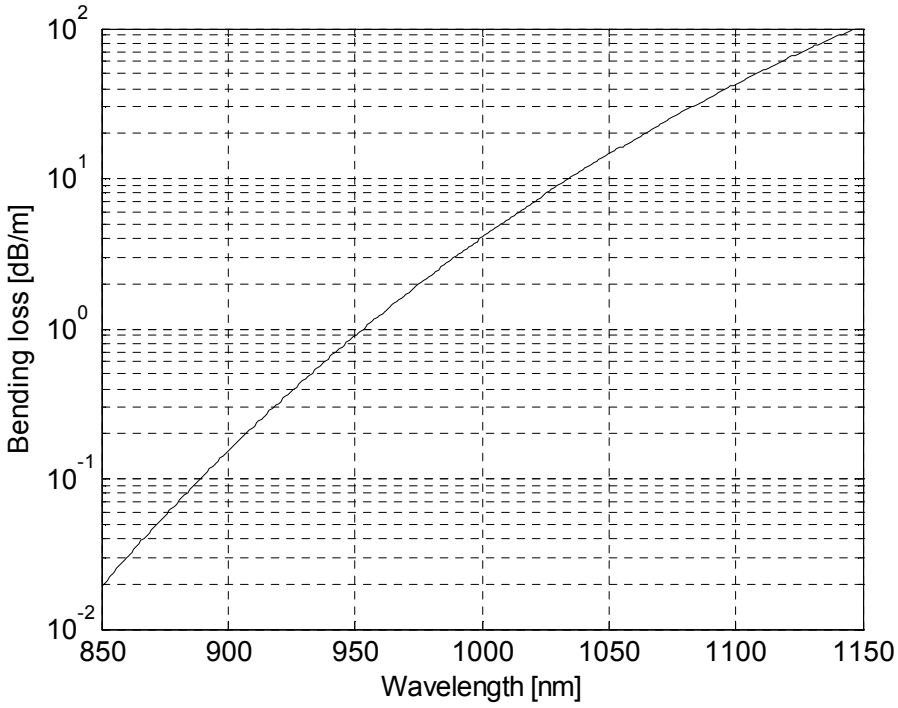

Figure 3.6. The bending loss *vs.* wavelengths of helical-core fibre. For this calculation, the design parameters used are $a_{co} = 3\mu m$, core NA = 0.1, P (pitch length) = 7.2 mm, and Q (offset) = 58 μm.

practical to vary only the pitch length during the pulling process in order to meet the bending loss specification, while the core size, NA, and offset are fixed.

For demonstration of helical fibre design, the core radius and the NA of the fibre are fixed to 3 μm and 0.10, respectively, so that only a single mode is supported at the 0.92 μm signal wavelength. Now, the offset and the pitch length can be determined through equations (3.24) and (3.28). For example, if one wants to induce 20 dB/m at 1.064 μm while the bending loss at 0.92 μm is kept negligible, the value of $\partial\gamma/\partial\lambda$ should be roughly $3.2\times10^{7}\,[Np/m^{2}]$ at λ = 1 μm. Figure 3.5 (left) shows the solution set of equation (3.27), which satisfy $\partial\gamma/\partial\lambda = 3.2\times10^{7}\ Np/m^{2}$ for the fixed core radius and the NA of the fibre. The right figure in figure 3.5 shows the corresponding bending losses at 1.064 μm and 0.92 μm for the solution pairs (each pitch represents the pair of pitch and offset shown in the left figure). For instance, the figure shows that with a pitch of 7.5 mm (and the corresponding offset of 61 μm), the fibre induces bending loss of 20 dB/m at 1.064 μm and only 0.3 dB/m at 0.92 μm. Thus, if the preform geometry corresponds to an offset of 61 μm in the fibre, the fibre should be fabricated with a pitch of 7.5 mm to get the targeted bending losses at 1.064 μm and 0.92 μm.

3.3. Numerical simulation of Nd^{3+}-doped helical fibre laser operating at 0.92 μm

In this section, a Nd^{3+}-doped fibre laser of this fibre design is numerically simulated. The purpose is, firstly, to estimate the performance of the designed fibre and, secondly, to determine the tolerances. It is important to consider the tolerance of the design against small deviations of the design parameters, e.g. the core size and the NA, since the fibre fabrication, and characterisation, always imposes some uncertainty in the fibre parameters.

The stimulated emission and absorption cross-sections in the figure 3.3 were used for the simulations. The core radius is 3 μm and the NA is 0.1. The pitch and offset are determined through the process described in the previous section. For this, the bending loss at 1.064 μm is targeted to 20 dB/m while the bending loss at 0.92 μm is minimised. The resulting pitch and the offset are 7.2 mm and 58 μm, respectively. Figure 3.6 shows the bending loss against the wavelength for the designed fibre. The designed fibre induces 20 dB/m bending loss at 1.064 μm and 0.35 dB/m at 0.92 μm.

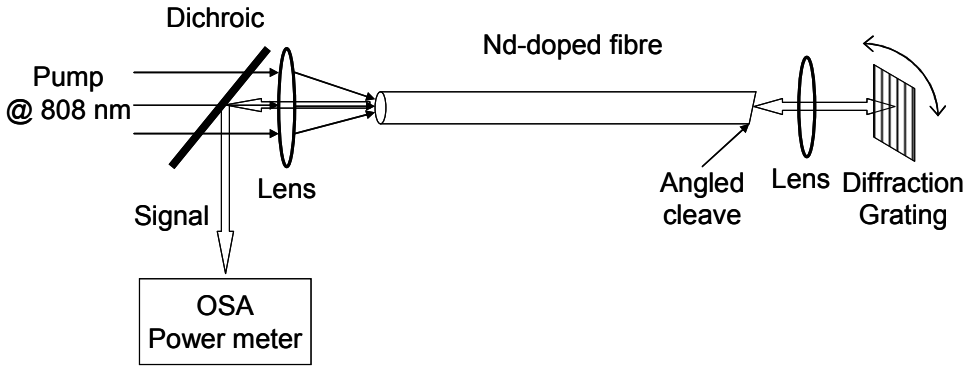

Figure 3.7. The Nd^{3+}-doped fibre laser setup assumed for the simulations.

The cladding radius must be larger than the offset and is assumed to be 65 μm. The Nd^{3+} ion concentration was taken to be $3.29\times10^{25}\ ion/m^3$. The fibre length is fixed to 12 m, which provides sufficient pump absorption. Note that the loss at 0.92 μm is relatively high and can be expected to impair the efficiency. The maximum launched pump power that is considered is 20 W at 808 nm.

Figure 3.7 shows the setup assumed for the simulation. A multimode pump at 808 nm is launched into the cladding through one end of the Nd^{3+}-doped fibre, through a dichroic mirror (which separates the signal from the pump) and a focusing lens. At the other end of the fibre, the signal is fed back through a collimating lens and an external diffraction grating. The loss of the signal feedback is assumed to be 20%, including the diffraction grating reflection and loss at the lens and coupling. In fact, a 20% feedback loss is rather optimistic and in reality, such feedback loss may well exceed 60%. However, alternatively one may consider a fibre Bragg grating, which has loss of only a few percent. (On the other hand, it is difficult to splice the fibre Bragg grating to a helical fibre.) For simulation purpose, I took a value of 20%. Though this is rather arbitrary it is not very critical. The fibre end at the diffraction grating is assumed to be angle-cleaved with wavelength-independent feedback from the Fresnel reflection of 0.1% (–30 dB). A 4% Fresnel reflection from the cleaved pump launching end of the fibre and the 80% reflection from the grating end of the fibre provide the feedback for the laser cavity. The diffraction grating can be rotated to tune the signal wavelength. No wavelength dependence is assumed for the peak reflection from the diffraction grating as it is tuned. The output signal is coupled out from the cavity in the pump launch end of the fibre into free-space through the perpendicular cleave, and is subsequently reflected by the dichroic mirror. Note that the 4% Fresnel

reflection implies that the fibre cleave is perpendicular to the core rather than to the fibre. As a consequence, the signal beam will emerge at an angle, which is different from the direction of the centre of the pump beam. This leads to practical problems, but do not affect the simulations. A more fundamental problem is that the helical core creates a scattering loss for the pump beam as it propagates in the inner cladding. This effect can be significant, but is ignored in the simulations.

The helical fibre induces the total round-trip bending loss of 480 dB at 1.064 µm and 8.4 dB at 0.92 µm. Although the loss at 0.92 µm is not negligibly small, the simulation result will show that, due to high gain at 0.92 µm, the performance of the 0.92 µm laser signal may be still considered to be reasonable. In fact, it is possible to reduce the bending loss at 0.92 µm. However, reducing the bending loss at 0.92 µm also reduces the bending loss at 1.064 µm and, consequently, it may become an obstacle to 0.92 µm emission. Although the previous theoretical calculation predicted that a 100 dB loss at 1.064 µm is required, it was based on the small signal gain where the strong amplified stimulated emission build-up at 1.064 µm was ignored. But, the numerical simulation results show much larger bending loss at 1.064 µm is needed when the amplified stimulation emission at 1.064 µm is considered. The performance

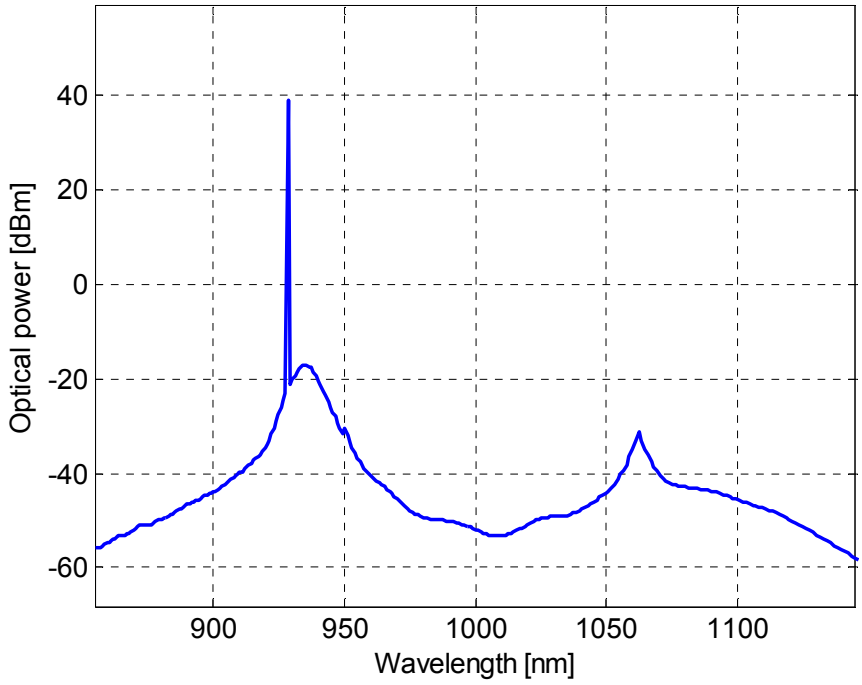

Figure 3.8. A typical output spectrum of the helical Nd-doped fibre laser operating at 927 nm. Result from simulations.

degradation, with respect to the design parameter deviation (which changes the bending loss at 1.064 µm), will be shown later in details. In those analysis, slight change of the designed parameters (i.e., a small reduction of the bending loss at 1.064 µm) leads to a significant performance degradation. The simulations were performed for the wavelength range between 850 nm to 1150 nm with 300 wavelength slots, hence, spectral resolution 1 nm.

Figure 3.8 shows a typical output spectrum of the Nd^{3+}-doped fibre laser operating at 0.927 µm. For this simulation, the launched pump power was 20 W. The external diffraction grating was tuned to 927 nm. From the output spectrum in figure 3.8, the competing (normally) stronger emission at 1.064 µm wavelength is efficiently suppressed due to the helical bending loss. The absorbed pump power was 14.7 W, i.e., 73.5% of the 20 W of launched pump power. The signal output power was 7.5 W. The slope efficiency is 38% and the threshold pump power is 0.12 W, both with respect to the launched pump power.

Figure 3.9 shows the tunability of the fibre laser. The fibre laser is tuneable from 925 nm to 945 nm. The slope efficiency decreases as the signal wavelength becomes

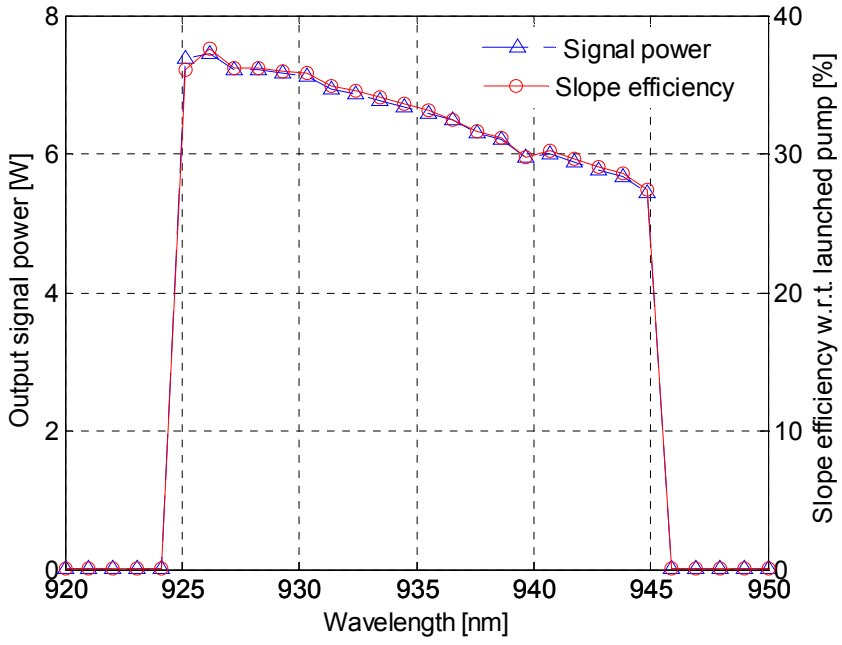

Figure 3.9. Tuning curve for the Nd-doped helical fibre laser. The output signal power (triangle, dashed line) and the slope efficiency (circle, solid line) are shown. Results from simulations.

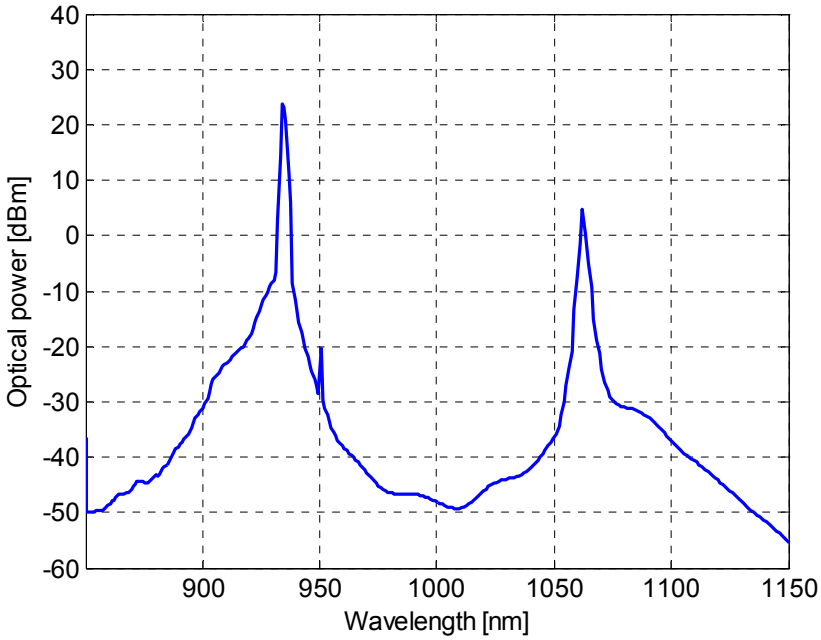

Figure 3.10. An optical spectrum of the output signal when the diffraction grating is tuned to 950 nm. Result from simulations.

longer due to the higher bending loss. Furthermore, in general, the slope efficiency is much smaller than the quantum limit of ~ 87%, which can be explained by the bending losses at the signal wavelengths. The factor that limits the tuning range is lasing at 934 nm. This corresponds to the gain peak. When the grating is tuned to wavelengths with lower gain, the 934 nm gain eventually becomes high enough for lasing, even with the 0.1% broadband feedback from the angle-cleaved facet. Figure 3.10 shows the optical spectrum of the output signal when the diffraction grating is tuned to 950 nm. It shows that laser emits at 934 nm rather than the desired 950 nm. Therefore, as far as the tunability is concerned, suppressing the spurious feedback from the angle-cleaved fibre end facet is important.

The signal power varied between 7.5 W at 927 nm and 5.5 W at 945 nm. The threshold pump power was between 0.12 W (at 927 nm) and 0.17 W (at 945 nm), with respect to the launched pump power. The absorbed pump power was 14.5 W with small dependence on the tuning wavelength when 20 W pump power is launched.

A big issue for helical fibre lasers in general is the robustness of the laser performance against deviations of the design parameters such as core size, NA, pitch, and offset position. In order to investigate the tolerances, one can see what happens to the output signal power for a laser tuned to 927 nm as the fibre parameters vary. For

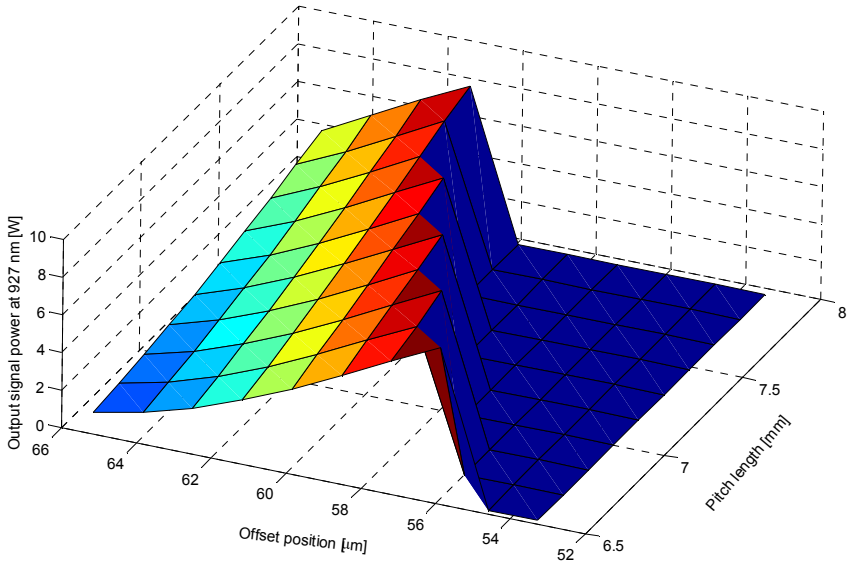

Figure 3.11. The performance of 927 nm laser with varying pitch and offset.

all comparisons, the fibre length and the launched pump power are fixed to 12 m and 20 W, respectively.

First, the output signal power variations for changing pitch and offset by ± 10% is shown in figure 3.11. When the pitch becomes longer and the offset position becomes smaller, the bending loss at 1.064 μm reduces. Then, the strong gain at 1.064 μm may lead to 1.064 μm lasing, which would frustrate the lasing at 0.92 μm. The figure shows that for large values of the pitch and small values of the offset, the 927 nm does not start lasing at all. On the other hand, when the pitch becomes smaller and the offset becomes larger, the increased bending loss at the desired signal at 927 nm may degrade the output power. Even a small change of the pitch length and the offset dramatically changes the laser performance at 927 nm. The highest power occurs with the design parameters of the pitches and the offsets, which coincide with the solution pairs of the pitch and the offset in figure 3.5 (left). The pitch length and offset position should be very carefully controlled, to within 1%, in order to make an efficient fibre.

The output signal power variations for a change of core size and NA by ± 5% is shown in figure 3.12. For this simulation, the pitch and the offset are fixed to 7.2 mm and 59 μm, respectively. When the core size and the NA become smaller, the bending loss increases as is discussed earlier. As before, both an increase and a decrease in

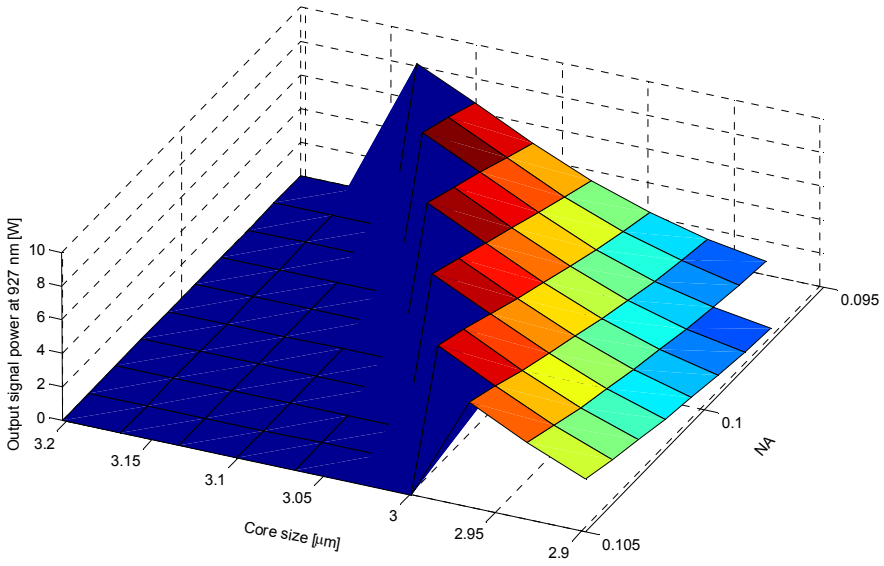

Figure 3.12. The performance of 927 nm laser with varying core radius and NA.

parameter values are detrimental. In the figure, even a small change of the core and/or the NA of 1% degrades the performance of 927 nm dramatically.

An important factor affecting the performance of the laser is the fibre length variation, which is omitted in this context. In general, the performance of fibre lasers based on three-level transition tends to be more sensitive to the fibre length than four-level lasers due to the ground state absorption. It is possible that variations in the core parameters that affect the performance may be compensated by using a longer fibre length, resulting in stronger suppression of the longer wavelength emission. However, a longer fibre also increases the bending loss at the signal wavelength, which eventually degrades the laser performance. The situation is improved somewhat if "external" bending of the fibre is used to fine-tune the bending loss.

3.4. Summary

In this chapter, a helical fibre was investigated for suppression of long wavelength emission by inducing bending loss. A helical fibre was designed for a Nd^{3+}-doped fibre laser operating at 0.92 μm and a numerical simulation predicted that such a helical fibre laser could be efficient. However, the low tolerance of the helical fibre to deviations in the fibre parameters indicates that the fabrication process should be very carefully controlled. For example, a deviation in the offset of 1% leads to a dramatic

change in the output power. Without sufficient control, the desired bending losses for the longer and the shorter wavelengths may never be achieved. It is the most difficult practical issue for realising a Nd^{3+}-doped helical fibre laser operating at 0.92 μm. Although the theory predicts that such a helical fibre laser is possible, it is still difficult to meet the design requirements. Therefore, in order to realise high power fibre lasers at 0.92 μm, I moved to an alternative waveguide design to suppress the longer wavelength, a so-called W-type fibre, which will be discussed in the next chapter.

Chapter 4. W-type fibres

Chapter 3 described the helical fibre for suppression of the longer wavelength emission. Although the theory predicts that a Nd^{3+}-doped fibre laser operating at 0.92 μm can be realised through careful fibre design, the tolerances for high efficiency would be very tight. While we (the ORC) did not try to realise a helical-core 0.92 μm Nd^{3+}-doped fibre laser, it seems clear that this would be very difficult in practice. Therefore, I needed an alternative waveguide design for suppression of long wavelength emission, more suitable for realisation and experimental demonstration.

A fibre with a W-type core refractive index profile can provide the required filtering, and is the method used in this chapter. Such W-profile cores were studied thoroughly in the 1970s [16] as well as more recently, mostly for dispersion compensation purposes. However, it is also well known that a W-type refractive index profile core can act as a low-pass filter since even the fundamental LP_{01} mode can have a nonzero cut-off beyond which no mode is guided [17]. This is in contrast to conventional step-index cores, which theoretically do not have a fundamental-mode cut-off. In practice a conventional fibre does have a fundamental-mode cut-off, because of bending-loss effects. However, this effective cut-off is not sufficiently sharp for the required filtering. A double-clad fibre further complicates the picture, since a mode that would otherwise be cut off becomes guided in the inner cladding. However, with typical diameters of the inner cladding (e.g., 100 μm or more), the overlap with the amplifying core of such cladding-modes can be expected to be sufficiently small, and therefore the resulting gain to be sufficiently low, to still ensure adequate suppression of emission into unwanted cladding-modes at unwanted wavelengths. Although the cut-off wavelength of a W-type (and a step-index) fibre is not entirely clear in practice, it is easily determined in theory and this theoretical cut-

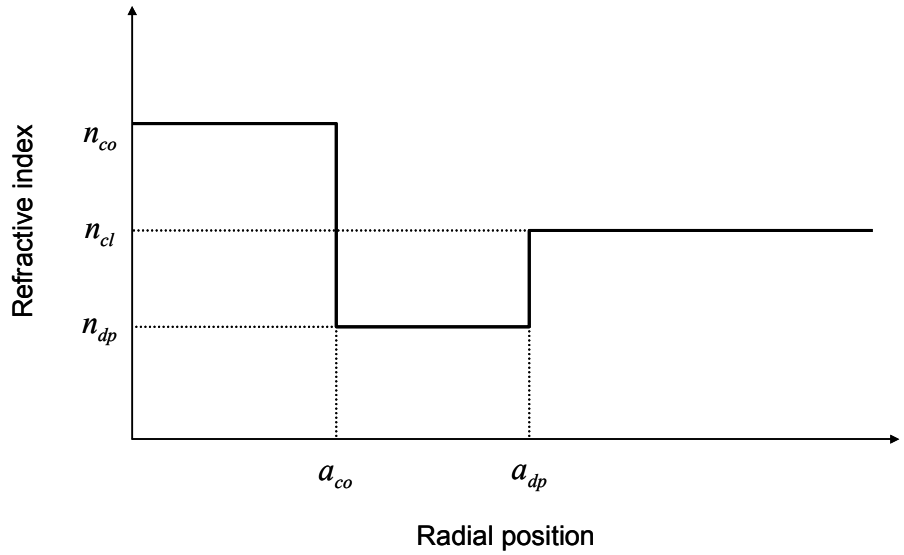

Figure 4.1. Schematic diagram of a W-type refractive index profile

off wavelength is still quite useful for the design of fibres with desired filter characteristics.

In this chapter, a design of a W-type fibre for efficient suppression of the 1.06 μm Nd^{3+}-emission is presented. The suitability of the fibre design is considered in terms of the wavelength-dependence of the effective index. Another section presents numerical simulations of the fibre laser with an analysis of the tolerances of the design. It will be shown that the W-type fibre design is much more robust than the helical fibre in chapter 3. Then, I present experimental results on a high power cladding pumped Nd^{3+}-doped fibre laser operating at 0.92 μm and discuss practical issues.

4.1. Properties and cut-off of the fundamental mode of W-type fibres

Figure 4.1 shows the schematic refractive index profile of the W-type fibre of concern. The fibre has a high-index (doped) core. A depressed-index region surrounds the core. This is often called the inner cladding, but that term has another meaning with double-clad fibres. I will denote it depressed-index region or depressed-index cladding or first cladding. This is surrounded by the remainder of the cladding, or the second cladding. The fundamental mode (LP_{01}) cut-off of W-type fibres is a result of an average refractive index in the core and depressed-cladding region that is lower than the refractive index of the cladding. Light at short wavelengths can be well confined in

the core region, in guided modes with effective indices higher than the cladding index. However, longer wavelengths penetrate further into the depressed region, which leads to a lower effective index. Eventually, at the fundamental-mode cut-off, the effective index becomes equal to the cladding index. The mode is no longer guided by the core. Instead, a part of the light may be confined in the cladding if the cladding is surrounded by a low index coating. Whether or not there is a fundamental-mode cut-off in a W-type fibre is determined by the average refractive index of the core and depressed region.

Figure 4.1 shows a raised core with refractive index n_{co}, a first cladding with depressed refractive index n_{dp}, and a second cladding with refractive index n_{cl}. In cladding-pumping terminology, the first and the second cladding would constitute the inner cladding. The core radius is a_{co}, and the outer radius of the depressed region is a_{dp}. Then, assuming weak guidance and linearly polarised (LP) modes, the radial dependence of the (core-guided mode) transversal field component becomes [9]

$$\psi(r)=\begin{cases} A_0 J_m(ur/a_{co}), & r \le a_{co} \\ A_1 I_m(w'r/a_{dp}) + A_2 K_m(w'r/a_{dp}), & a_{co} < r < a_{dp} \\ A_3 K_m(wr/a_{dp}), & r \ge a_{dp} \end{cases}. \tag{4.1}$$

Here r is the radial position, $A_i (i=0,1,2,3)$ is a constant and J_m, K_m, I_m are Bessel function, modified Bessel function of the first kind, and modified Bessel function of the second kind, respectively. The modal parameters are defined, as is conventional as $u = a_{co}k_0\sqrt{n_{co}^2 - n_{eff}^2}$, $w' = a_{dp}k_0\sqrt{n_{eff}^2 - n_{dp}^2}$, and $w = a_{dp}k_0\sqrt{n_{eff}^2 - n_{cl}^2}$, where n_{eff} is the effective refractive index of the mode and k_0 is the vacuum wavenumber. The boundary conditions are that the field and its radial derivative are continuous on the two boundaries, $r = a_{co}$ and $r = a_{dp}$. This condition leads to the characteristic equation as follows [17]:

$$\frac{\left[\hat{J}_m(u) - \hat{K}_m(w'q)\right]\left[\hat{K}_m(w) - \hat{I}_m(w')\right]}{\left[\hat{J}_m(u) + \hat{I}_m(w'q)\right]\left[\hat{K}_m(w) - \hat{K}_m(w')\right]} = \frac{I_{m+1}(w'q)K_{m+1}(w')}{I_{m+1}(w')K_{m+1}(w'q)}, \tag{4.2}$$

where $\hat{Z}_m(x) = Z_m(x)/\{xZ_{m+1}(x)\}$ (Z represents Bessel functions) and $q = a_{co}/a_{dp}$.

All the modal parameters are functions of the effective refractive index n_{eff}, and equation (4.2) can be solved numerically for the quantised effective refractive index n_{eff}. Then, the modal parameters u, w, w' as well as the mode profiles can be readily computed. Here, however, we are primarily interested in whether the LP_{01} mode has a (positive) cut-off wavelength. By calculation of equation (4.2) for many different fibre designs, it was empirically shown [17] that this is the case when the relative volume refractive index defined by

$$\hat{n}_{vol} = \int_0^{a_{dp}} \left[n(r) - n_{cl} \right] r dr \tag{4.3}$$

becomes negative.

An important practical issue of any fibre design is the bending loss. If the effective refractive index of the guided mode at 0.92 μm is too close to n_{cl}, the mode is not well confined in the core. This makes the fibre prone to bending loss (see Chapter 3 and 6). Therefore, it is important to make sure that the refractive index of the fundamental mode at 0.92 μm is sufficiently large (in practice this means as large as possible) while that at 1.06 μm should be sufficiently lower than the cladding index.

A cut-off wavelength of 1 μm is a sensible choice in our case, so that a 0.92 μm signal from the Nd^{3+}-doped fibre is well guided and amplified by the core whereas a mode at 1.06 μm is cut off and essentially propagates outside the doped core. From equation (4.2), in principle one can obtain a solution surface of the design parameters $n_{co}, n_{dp}, a_{co}, a_{dp}$ which make the effective index of the fundamental mode at 1 μm equal to n_{cl}. This is the condition for a fundamental-mode cut-off at 1 μm. One may in principle obtain an explicit analytical solution of the effective index by solving equation (4.2). With such a solution it would be possible to determine the set of parameters which is best in terms of effective index dispersion. However there is no known analytical solution. Because of the large parameter space it is also difficult to study the problem numerically. Still, this is feasible, but may not bring much insight. By contrast, an intuitive and well-known way to make the dispersion large is to increase n_{co} and decrease n_{dp}. (Note that the range of solutions to equation (4.2) (i.e., the effective index) is between n_{co} and n_{dp}.)

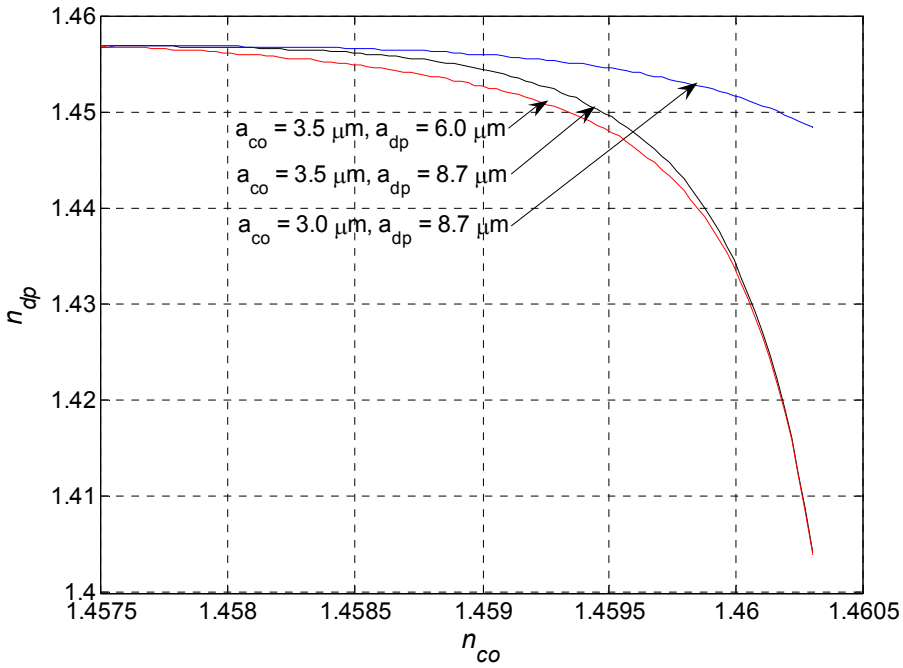

Figure 4.2. Refractive indices n_{co} and n_{dp} that lead to a cut-off wavelength of 1 μm. Each curve is obtained through solving equation (4.2) with $a_{co} = 3.5\,\mu m$, $a_{dp} = 8.7\,\mu m$ (black), $a_{co} = 3\,\mu m$, $a_{dp} = 8.7\,\mu m$ (blue), and $a_{co} = 3.5\,\mu m$, $a_{dp} = 6\,\mu m$ (red).

In order to find fibre parameters for a cut-off wavelength of 1 μm, one can replace n_{eff} of the fundamental mode at 1 μm with n_{cl} in equation (4.2). Then, the solution set of the desired parameters can be obtained as is shown in figure 4.2. For this, a_{co} and a_{dp} are fixed first and the desired n_{dp} are obtained as a function of n_{co} , assuming $n_{cl} = 1.457$ at 1 μm. Please note that the material dispersion is not considered in this chapter since the wavelengths of interest are sufficiently close. The resulting solution curves are presented in the figure for different pairs of a_{co} and a_{dp} . The design parameters of $a_{co} = 3.5\,\mu m$ and $a_{dp} = 8.7\,\mu m$ are the actual ones which were used for the aluminosilicate Nd^{3+}-doped W-type fibre F432-LF197, made at the ORC. For this fibre, $n_{co} = 1.459$ and $n_{dp} = 1.4546$ were chosen (with $n_{cl} = 1.457$), which in fact belongs to the black curve in the figure. In the figure, the higher n_{co} needs the lower n_{dp} in order to make the fundamental cut-off wavelength to be 1 μm. In the case for

$a_{co} = 3.5\,\mu m$ and $a_{dp} = 8.7\,\mu m$, the required n_{dp} changes dramatically if n_{co} is larger than 1.4595 (equivalent $NA_{co}\left(=\sqrt{n_{co}^2 - n_{cl}^2}\right)$ of 0.085). In practice, the depressed refractive index can be realise by doping with boron (B), which allows typically down to a negative $NA_{dp}\left(=-\sqrt{n_{cl}^2 - n_{dp}^2}\right)$ of -0.3 (equivalent n_{dp} of 1.4258). Therefore, in this case, n_{co} should not exceed 1.4601. Fluorine can also be used as an index-depressant, but the index-dip that can be reached is not as large.

Figure 4.2 also shows the effect of a_{co}. When a_{co} becomes smaller, the solution curve shifts to the upper region (with larger n_{dp}) compared to the case with a bigger a_{co}. This is reasonable as seen from equation (4.3). Then, one does not need as low a value for n_{dp} to realise a cut-off wavelength of 1 μm. However, too small a_{co} leads to an inefficient pump absorption with cladding-pumping, because of the poor area ratio. This necessitates the use of long fibre, but this can be an issue for the bending loss,

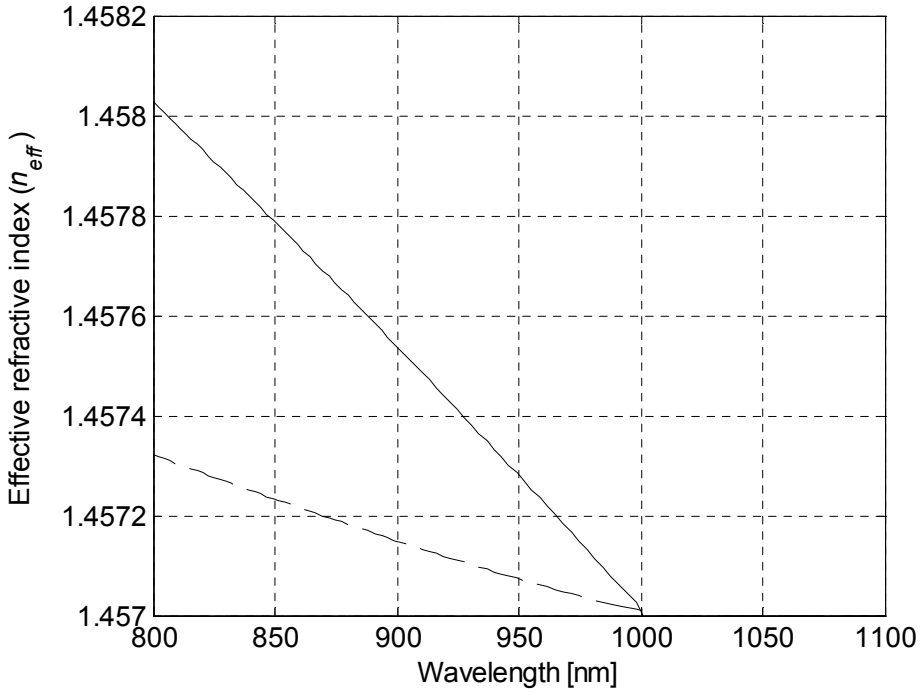

Figure 4.3. Comparison of the effective refractive indices of two fibre designs. The curves represent the effective refractive indices of LP_{01} mode with $n_{co} = 1.4601$, $n_{dp} = 1.4258$ (solid curve) and $n_{co} = 1.4585$, $n_{dp} = 1.4561$ (dashed curve), respectively.

and more importantly, it increases the ground-state absorption at 0.92 μm. As a result, 1.06 μm lasing becomes more difficult to suppress. On the other hand, the effect of a_{dp} is also shown in figure 4.2. Although not necessarily clear from the figure, the value of a_{dp} is not so important, as long as it is larger than 5 μm. However, if a_{dp} becomes smaller than 5 μm, the characteristics in terms of required n_{dp} and n_{co} changes dramatically.

Figure 4.3 shows the modal dispersion, i.e., how the effective index depends on the wavelength for two different fibre designs, both of which belong to the curve for $a_{co} = 3.5\,\mu m$ and $a_{dp} = 8.7\,\mu m$ in figure 4.2. The solid line represents the effective index of the LP_{01} mode with $n_{co} = 1.4601$ ($NA_{co} = 0.095$) and $n_{dp} = 1.4258$ ($NA_{dp} = -0.3$) whereas the dashed line represents that with $n_{co} = 1.4585$ ($NA_{co} = 0.066$) and $n_{dp} = 1.4561$ ($NA_{dp} = -0.051$). Both designs have a cut-off wavelength of 1 μm. However, the modal dispersion is different. The case with the larger refractive index step (solid line) has a higher dispersion than the case with a

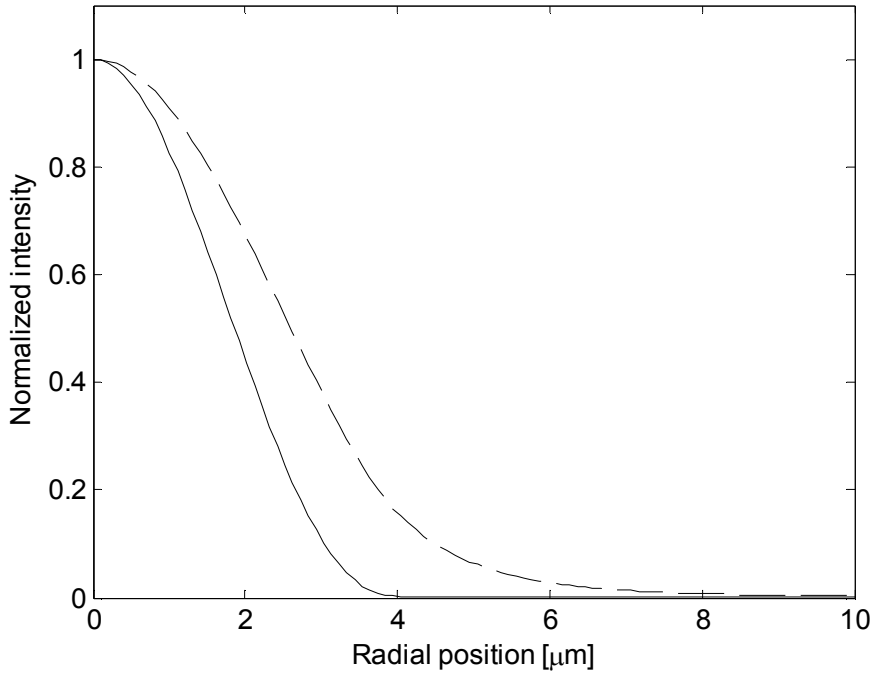

Figure 4.4. Comparison of the modal intensities of the LP_{01}-mode for two different fibre designs. The curves represent the modal intensity of LP_{01} mode at 0.927 μm with $n_{co} = 1.4601$, $n_{dp} = 1.4258$ (solid curve) and $n_{co} = 1.4585$, $n_{dp} = 1.4561$ (dashed curve), respectively.

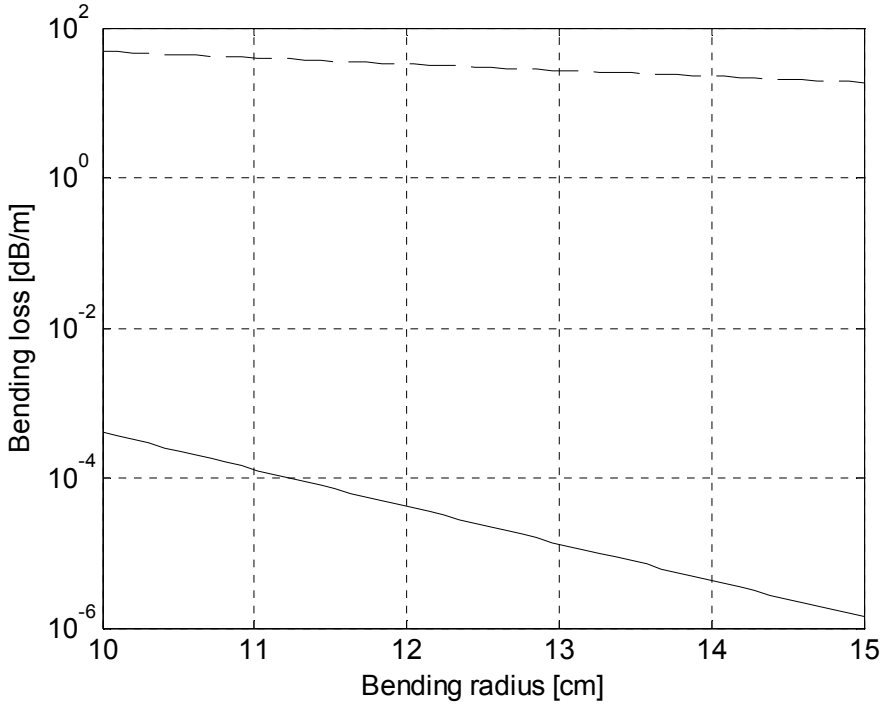

Figure 4.5. Theoretical bending losses for two different fibre designs. Curves represent the bending losses of the LP_{01} mode at 0.927 μm with $n_{co} = 1.4601$, $n_{dp} = 1.4258$ (solid curve) and $n_{co} = 1.4585$, $n_{dp} = 1.4561$ (dashed curve).

smaller step (dashed line) with the same cut-off wavelength at 1 μm. Thus, the effective refractive index of the signal wavelength for the case with a larger difference in refractive indices is much larger. As discussed in earlier sections, this leads to different confinement factors, and thus, a difference in bending loss characteristics.

The effective refractive indices are 1.4574 for the solid curve and 1.4571 for the dashed curve at 0.927 μm. Figure 4.4 shows the modal field intensities for those two cases. The fibre with the larger index step (solid curve) is much more confined in the doped core than the dashed curve. As seen from equation (4.1), the larger the difference between n_{dp} and n_{eff} becomes, the greater w' becomes, which again implies a fast drop of the modal intensity in the depressed region (due to the nature of the Bessel functions I_m and K_m). This implies better confinement of the mode in the high indexed core.

The core confinement factor is 99% for the fibre with the larger index step (solid curve in Fig. 4.4) and 71% for the smaller index step. This relatively large difference of the confinement factors leads to a great difference in the bending loss. Figure 4.5

shows the bending loss for the two cases against the bending radius. The fibre with the small refractive index step has a huge bending loss even with relatively large bending radii. The calculated bending loss for this case reaches 48 dB/m with 10 cm bending radius whereas that for the other case is only 0.0004 dB/m with the same bending radius. In realising such a W-type fibre, it is important to avoid unacceptable bending loss by using sufficiently large refractive index steps.

4.2. Numerical simulation of W-type Nd^{3+}-doped fibre lasers

It is not easy to simulate amplification in a W-type fibre since the modes at wavelengths above the cut-off wavelength are not well defined. Though these are cut off, they can still influence the amplification, in particular in a double-clad fibre in which such modes are still guided in the inner cladding. One option is to assume that the modes at the longer wavelength above the cut-off wavelength are evenly distributed through the (inner) cladding cross-section, which is not true in general. However, with a D-shaped inner cladding and with significant mixing of cladding-modes, this assumption may be regarded as valid [67]. The gain per unit length is also important, i.e., the gain in the core at the wavelength in question (e.g., 1.06 μm) should be small compared to mode dephasing and mixing rates. The pump absorption is another difficulty. It is not clear to what degree the depressed region will prevent the pump from reaching the core and exciting the Nd^{3+}-ions in it. However, most energy in the pump propagates at quite high NAs (up to 0.4, typically), and can then readily penetrate the depressed region. Furthermore, in a modal description, a D-shaped cladding may still lead to relatively uniform cladding-modes that are evenly distributed across the fibre cross-section, and that are scrambled at a relatively high rate [67]. Thus, the reflection of pump rays off the depressed cladding may be neglected for simplicity.

One of the advantages of the W-type fibre is that one can use a fibre that is sufficiently long to absorb the pump. Two- and three-level laser systems have to compete against any emission from the four-level transition at longer wavelengths, in conventional step indexed core fibres. In conventional step-index fibres without fundamental-mode cut-off and with negligible background losses, four-level transitions will amplify even with the smallest fraction of excited Nd^{3+}-ions. At the

point where a sufficient fraction of ions are excited to create gain on the three-level transition, the four-level gain will have a certain value that can be high. In order to keep this gain at reasonable values, the fibre must be short, often even too short for adequate pump absorption. For example, it is well known that step-index Yb^{3+}-doped fibre lasers for 0.98 μm emission (to the ground-state) use short fibres in which the pump absorption is a problem. With longer fibres, the competing four-level emission dominates. The W-type structure efficiently suppresses emission at the long wavelength by filtering out the long-wavelength emission from the core. Even though the long-wavelength radiation remains guided in the inner cladding in case of a double-clad fibre, its intensity in the core is sufficiently low to make stimulated emission negligible. Therefore, provided that sufficient pump intensity is present along the fibre, the desired short wavelength may be amplified efficiently even in long fibres. However, this is not true for the helical fibre in chapter 3. The helical fibre always suffers from a nonzero bending loss even at the signal wavelengths. This is typically much larger than the background loss, and can be significant. Therefore, if the fibre length becomes long, the performance of the helical fibre laser degrades.

For numerical simulations, the configuration described in chapter 3 (figure 3.7) is used again. The fibre length and the Nd^{3+} ion dopant concentration are 25 m and 1000 ppm mol. The cladding is assumed to be D-shaped so that the pump absorption rate along the fibre does not change due to differences in the absorption of different pump-modes [67]. The cladding diameter is 80 μm. The W-type fibre parameters chosen for the numerical simulation are $a_{co} = 3.5\,\mu m$, $a_{dp} = 8.7\,\mu m$, $n_{co} = 1.4601$, and $n_{dp} = 1.4258$ ($n_{cl} = 1.457$). The cross-sections for stimulated emission and absorption of the Nd^{3+} ions are the same as those used in chapter 3 (figure 3.3). The maximum launched pump power I consider is 20 W. The bending loss at the signal wavelength is neglected as motivated by figure 4.5. The background propagation loss is assumed to be 0.03 dB/m for all wavelengths and modes.

Since the fibre is relatively long, the centre signal wavelength tends to move towards the longer wavelengths within the quasi-three level $F_4^{3/2} \rightarrow I_4^{9/2}$ transition. Longer wavelengths have a larger stimulated emission-to-absorption cross-section ratio and so are less affected by ground-state absorption. Therefore, the diffraction grating is tuned to 932 nm, whereas experience-wise, most 0.9 μm aluminosilicate Nd^{3+}-doped fibre lasers have worked best at 927 nm.

Figure 4.6 shows the simulated output optical spectrum when the external diffraction grating is tuned to 932 nm. The output signal power in this case is 10.32 W when 20 W of 808 nm pump was launched. The absorbed pump power is 15.2 W. The slope efficiency with respect to the absorbed pump power is 69%. This is less than the quantum limit of 85%, primarily due to the background propagation loss combined with the long fibre length. The threshold absorbed pump power is 0.11 W. The numerically simulated optical spectrum shows an abrupt change at 1 µm. It is due to the abrupt change of the beam profile of emitted radiation at this wavelength. Below 1 µm, the signal beam corresponds to the guided fundamental mode and is relatively well confined. In contrast, above 1 µm, the emitted radiation is assumed to propagate in a beam that is evenly distributed across the cladding cross-section. Therefore, there is an abrupt change in the overlap factor and consequently the gain around the cut-off. This may not be the case in reality. The beam profile does not change abruptly as is assumed. For instance, the fundamental cladding mode at 1060 nm may well be similar to a weakly guided core-mode near cut-off. In this case, the optical spectrum would not change abruptly.

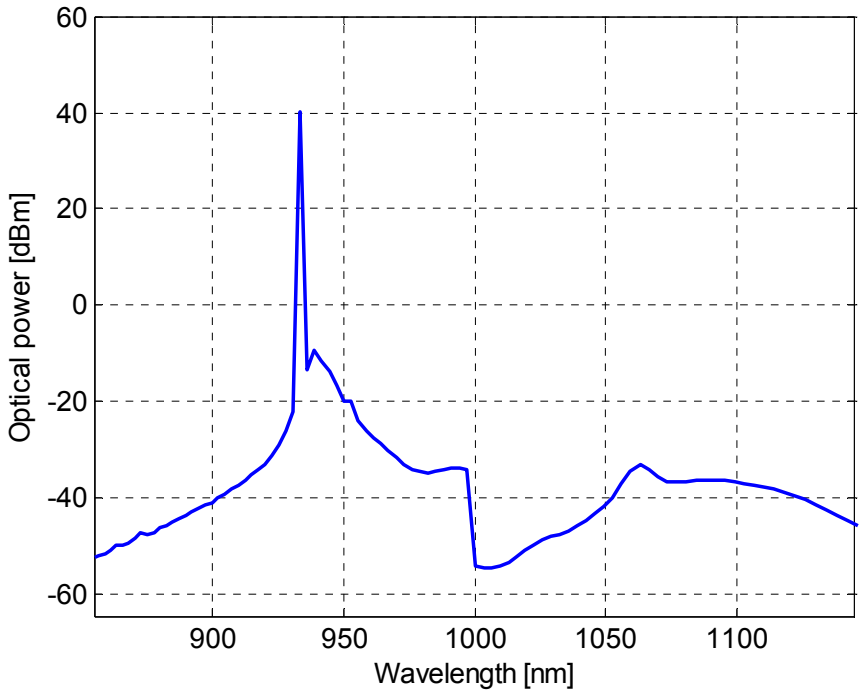

Figure 4.6. Simulated optical spectrum of the output signal from a W-type Nd-doped fibre laser operating at 932 nm. Simulation resolution 2 nm.

Design parameters	Deviation	Cut-off wavelength (nm)	Output power deviation
a_{co}	+5%	1030	-0.220%
	-5%	965	-0.319%
a_{dp}	+5%	998	0.000%
	-5%	1002	0.000%
NA_{co}	+5%	1033	-0.120%
	-5%	962	-0.302%
NA_{dp}	+5%	991	-0.020%
	-5%	1010	-0.012%
Original design	0%	1000	0% (10.32 W)

Table 4.1. The change in laser output power at 932 nm, as the parameters of the W-type Nd^{3+}-doped fibre are changed by ± 5% from their design values, as calculated with the simulation model.

Next I consider the tolerance of the fibre design against deviations of the parameter values. Table 4.1 shows how such deviations affect the laser output power, as calculated with the simulation model. For this, the parameters a_{co}, a_{dp}, NA_{co}, and NA_{dp} are varied by ± 5% from their design values of $a_{co} = 3.5\,\mu m$, $a_{dp} = 8.7\,\mu m$, $NA_{co} = 0.0951$, and $NA_{dp} = -0.3$, respectively (i.e., same as before). When the parameters deviate, two important changes are possible. Firstly, the cut-off wavelength changes. If the cut-off wavelength is above ~ 1.06 µm, 4-level operation on the ${}^4F_{3/2} \rightarrow {}^4I_{11/2}$ transition will commence, and then prevent lasing at 932 nm. Secondly, if the cut-off wavelength reduces and becomes too close to the signal wavelength, the bending loss may become serious. When a_{co} and NA_{co} reduce by 5%, the bending loss changes to a great degree. The bending loss of the original design

was only 0.0004 dB/m with 10 cm bending radius whereas that of the modified design reaches up to 0.07 dB/m with 10 cm bending radius and 0.003 dB/m with 15 cm bending radius. But, when the fibre is bent with a sufficiently large bending radius, the effect of the bending loss change may still be negligible. The comparative simulations in table 4.1 assumed the bending radius is sufficiently large so that the bending loss of the modified design is negligible. In practice, if the bending radius can be controlled, it is possible to adjust this to compensate for small variations of the fibre parameters.

As is seen from the table, the W-type fibre is quite robust against deviation of the fibre parameters. The performance degradation from a 5% deviation in a_{dp} or NA_{dp} is negligible. A change of a_{co} or NA_{co} leads to a larger change in the efficiency as well as in the cut-off wavelength. Once the cut-off wavelength becomes 1.05 μm (7% increase of a_{co} or NA_{co}), 1.05 μm started lasing, which prevented lasing at the signal wavelength of 932 nm. However, in general, the performance degradation is well within 0.5% with 5% parameter deviation. Compared to the very tight design tolerances of the helical-core fibre, the W-type fibre shows an excellent robustness to parameter variations. This is of great practical importance in realising high power fibre lasers since the fabrication process always entails some deviations of the fibre geometry. Therefore, the W-type fibre makes a good candidate for fabrication and experimental demonstration of a high power Nd^{3+}-doped fibre laser operating at 0.9 μm.

4.3. Experimental investigations of W-type Nd^{3+}-doped fibre lasers

This section describes experimental details and results for cladding pumped germanosilicate and aluminosilicate Nd^{3+}-doped fibre lasers. It expands on already published results [3, 68, 69]. There are many important issues other than the waveguide design for the realisation of a high-power cladding-pumped Nd^{3+}-doped fibre laser operating around 0.92 μm, such as the host material, pump absorption, and Nd^{3+} ion quenching. Moreover, it is not easy to make a preform that exactly matches the design.

4.3.1. Practical issues

With traditional core-pumping, it is relatively easy to excite a sufficient fraction of the Nd^{3+} ions to achieve gain at around 0.92 μm. Published results include a 42 mW core-pumped fibre laser tuneable from 892 to 936 nm [31]. While the 1.064 μm gain will still exceed the 0.92 μm gain in most or even all cases, because of the high Nd^{3+}-excitation and high pump absorption, the difference can be small enough to be reversed with wavelength-selective end-reflectors in the case of core pumping. However, because of the low power of suitable pump sources, the powers that can be reached with core pumping are rather low. By contrast, the power from multimode pump sources appropriate for cladding-pumping is high. However, the intensity is relatively low, which makes it difficult to excite a sufficient fraction of Nd ions and to achieve efficient operation of the three-level system at 0.92 μm. The challenge is to overcome these difficulties, and thus enable efficient high-power emission at ~ 0.92 μm.

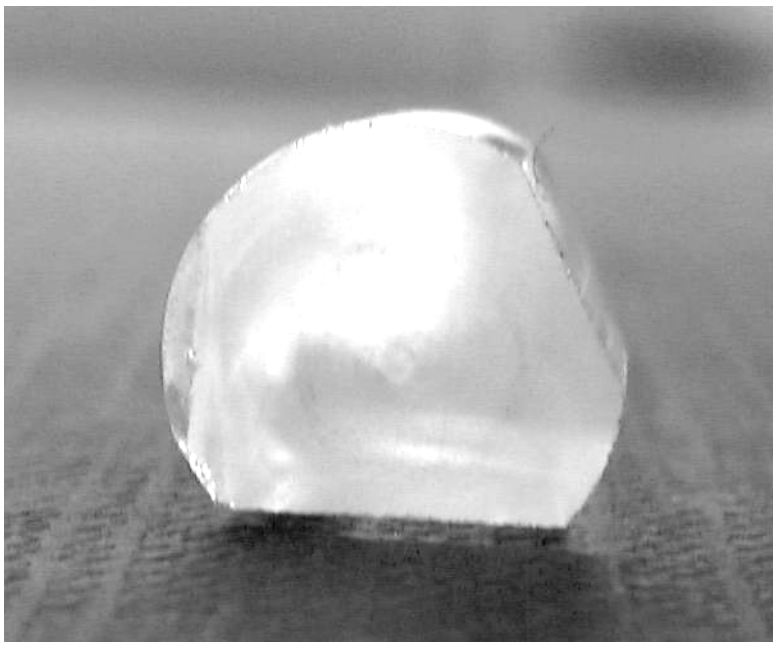

Figure 4.7. Cross-sectional view of the preform LF170 made at the ORC.

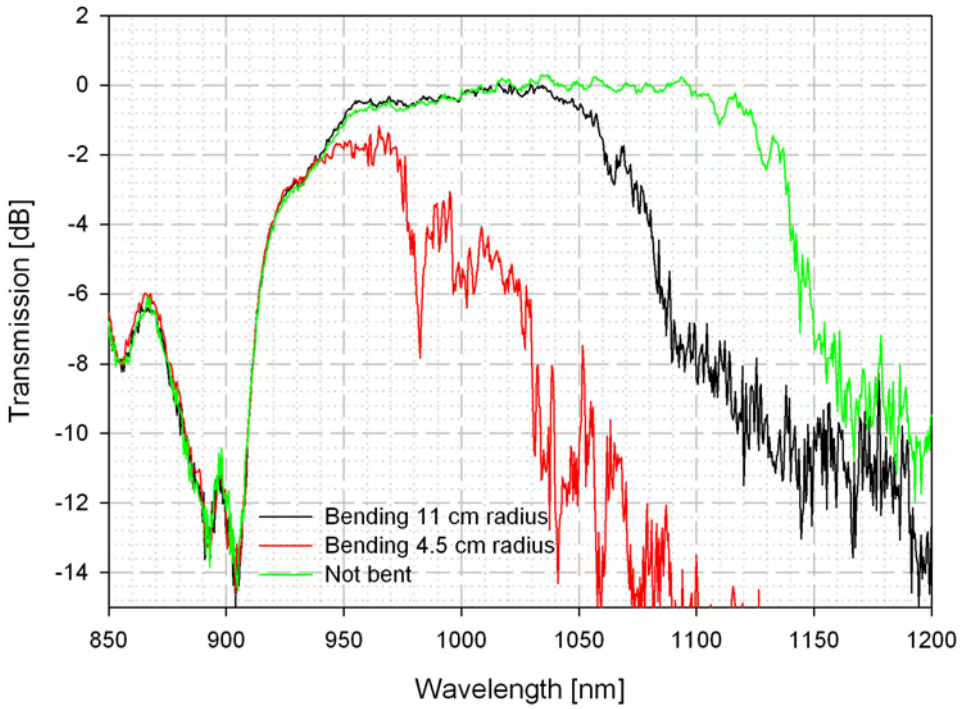

Figure 4.8. The transmission spectrum of the fibre F413-LF170 determined through cut-back measurements. Cut back fibre length 1.5 m, which included a 1 m long section that was bent to different radii. OSA resolution 0.5 nm.

Reference [6] is my own work (in collaboration with colleagues at the ORC), performed at a similar time as the work of references [4, 5]. Indeed, there have been a number of previous research activities on high power cladding pumped Nd^{3+}-doped fibre laser operating at 0.92 µm, such as the theoretical feasibility analysis of Selvas [70]. Very recently, Yoo *et al.* analyzed, more in-depth, the W-type fibres for Nd^{3+}-doped fibre laser operating at 0.94 µm, focusing on the bending loss characteristics [71], where I took a part. In addition, Kim and I (and other ORC colleagues) collaborated to develop a depressed-clad hollow Nd^{3+}-doped optical fibre laser operating at 0.93 µm [72], the waveguide structure of which will be described in Chapter 5. The next sections will present the experimental results of my work.

4.3.2. Germanosilicate Nd^{3+}-doped W-type fibre laser tuneable from 932 nm to 953 nm

I designed a W-type fibre and Dr. S. W. Yoo fabricated a germanosilicate Nd^{3+}-doped fibre (F413-LF170) according to the design. The designed waveguide parameters are $a_{co} = 5.3\,\mu m$, $a_{dp} = 9.3\,\mu m$, $NA_{co} = 0.11$, and $NA_{dp} = -0.10$, so that the cut-off wavelength was designed to 1.10 μm. The LP_{11} mode cut-off wavelength was estimated as 0.6 μm. The cladding diameter was 80 μm, with a doubly truncated D-shape as is seen from figure 4.7.

The transmission characteristic of the core was measured using a cut-back method. A white light source was coupled to a single mode fibre with a conventional high-index coating and a second-mode cut-off of 0.86 μm. This is spliced to the doped fibre. The output end of the doped fibre was also spliced to a piece of the same single mode fibre with high-index coating. The white-light spectrum transmitted through these fibres was measured. Then, after cutting back the doped fibre, resplicing to the single mode fibre, and measuring the transmitted spectrum again, the transmission

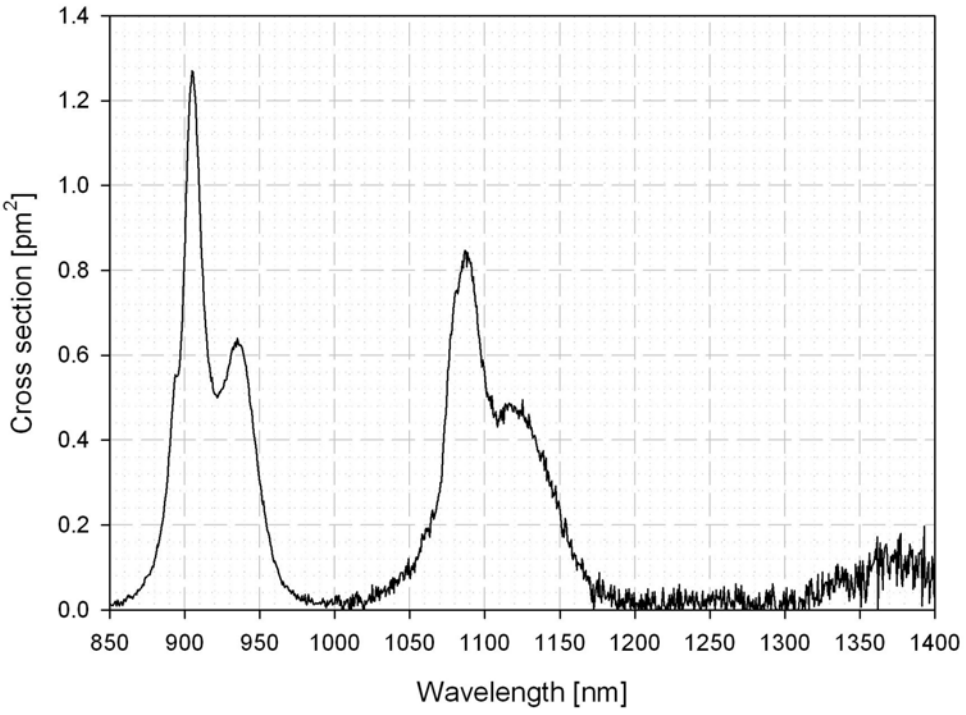

Figure 4.9. Measured emission cross-section of fibre F413-LF170 (Nd-doped germanosilicate).

spectrum of the Nd^{3+}-doped fibre could be determined. Figure 4.8 shows the transmission characteristics of a 1.5 m long piece of the Nd^{3+}-doped fibre with different bending radii (the length of the bent section was 1 m). The Nd^{3+} absorption band in the 0.9 μm wavelength region influences the transmission, but it is still possible to discern the (effective) cut-off wavelength from the figure. When the fibre was not bent, the cut-off wavelength was 1.1 μm. When the fibre is bent with 4 cm and 11 cm, the effective cut-off wavelength moved to 0.97 μm and 1.05 μm, respectively. It suggests that with an appropriate bending radius the competing longer wavelength emission can be efficiently suppressed.

The emission cross-section spectrum of Nd^{3+}-doped germanosilicate fibres is well known to be red shifted relative to that of aluminosilicate ones. Figure 4.9 shows the measured emission cross-section spectrum of F413-LF170, using the technique in reference [53]. There are three main emission peaks, at 0.90 μm, 1.09 μm, and 1.38 μm. In aluminosilicate fibre, the emission peaks are at 0.88 μm, 1.064 μm, and 1.36 μm, as will be shown in the next section. Furthermore, the branching ratio favours emission at 0.9 μm over that at 1.1 μm (and 1.3 - 1.4 μm) in germanosilicate Nd^{3+}-doped fibres as seen from figure 4.9. By contrast, the branching ratio favours 1.06 μm emission in Nd^{3+}-doped aluminosilicate. While ground-state absorption still has to be overcome, the competing emission from the 1.09 μm transition could be suppressed for efficient 0.9 μm emission even by slightly bending the fibre.

The Nd^{3+} ion quenching in the germanosilicate host is notorious [2]. Concentration-quenching, or self-quenching, of Nd^{3+}-ions occurs through a cross-relaxation process (or possibly an upconversion process) followed by rapid multi-phonon relaxation. Another quenching route is *via* energy transfer to OH^--ions, so the OH^- content should be as low as possible. As the limitations of the Nd^{3+} ion concentration in germanosilicate (or pure silica) host without quenching is known to be 200 ppm mol, we had to fabricate several preforms with different Nd^{3+} ion concentration in order to be close to the concentration limit but not exceed it. It was important to increase the rare-earth ion concentration lest the operational fibre length should become long enough to significantly attenuate the signal. The fabricated preforms are LF170 (240 ppm mol Nd^{3+}), LF175 (540 ppm mol Nd^{3+}), and LF180 (320 ppm mol Nd^{3+}) and pulled fibres from each of the preforms are F413-LF170, F380-LF175, and F416-LF180. The measured fluorescence lifetime from the fibres

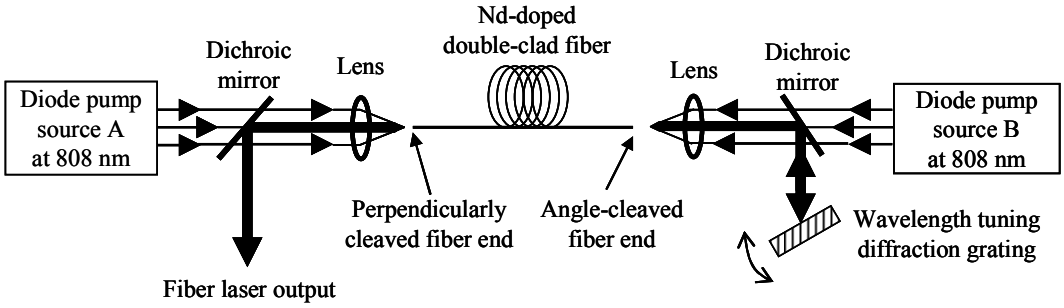

Figure 4.10. Experimental setup for a germanosilicate Nd-doped fibre laser at 0.94 μm.

are 420 μs, 250 μs, and 320 μs respectively whereas the unquenched pure radiative metastable lifetime of Nd^{3+} ions in germanosilicate is known to be over 500 μs [2]. I have reached high output powers from fibre lasers operating in the 0.9 μm wavelength region with fibres F413-LF170 and F416-LF180, but not with F380-LF175. Furthermore, the fibre F380-LF175 showed a surprisingly high pump threshold (~3 W absorbed) even at 1088 nm, which implies that the Nd^{3+}-ions are severely quenched in that fibre. Although the fibre F416-LF180 performed slightly worse than, but still comparable to, F368-LF170, the threshold pump power was higher than with the fibre F413-LF170. Hence, the output power was low. Therefore, the fibre F413-LF170 was chosen for optimisation of the output power at 0.93 – 0.95 μm. The pump absorption in the cladding was measured to be 0.25 dB/m at 808 nm. The background loss in the cladding was measured to be 0.01 dB/m at 1.3 μm.

Using this fibre, I made an experimental laser setup, the schematic of which is shown in figure 4.10. The Nd^{3+}-doped fibre was pumped through both ends by two 808 nm diode sources with maximum launched power of 4.5 W for the output coupling (left) end (PUMA, New Optics, 808 nm) and 3.5 W for the right end (Unique Mode, 808 nm). The pump beams were focused onto the fibre ends by lenses with 8 mm focal length and 0.5 NA. The used NA was estimated to be 0.4, as determined by the diameter of the pump beams incident on the lenses. The relative values of the pump powers were kept constant when the total pump power was varied. A 4% Fresnel reflection from a perpendicularly cleaved fibre facet and the feedback from a diffraction grating with 63% reflection efficiency (measured at 0.94 μm) created a laser cavity. The fibre was 57 m long with 12 dB single-pass pump absorption. The pump absorption was large enough to allow for double-ended

pumping without risk for pump diode damage. A dichroic mirror was used in each end of the fibre to separate the pump and the signal beam paths.

The diffraction grating at the feedback end could be replaced with a broadband dichroic mirror which has a better reflection at the signal wavelengths. A dichroic mirror with 99% reflectivity at 0.9 μm was used to maximise the output signal power. The laser produced 705 mW at 944 nm with 2 nm linewidth. Figure 4.11 shows the laser power characteristics. The threshold pump power was 2 W and the slope efficiency was 12%, both with respect to the launched pump power. The low efficiency can be explained by the long fibre, in which the propagation losses were significant. The fibre was arbitrarily bent in order to, firstly, enhance the pump absorption and, secondly, reduce the propagation of the undesired 1.09 μm emission. There may have been some bending loss at 944 nm as well, which would also explain the low slope efficiency. The beam quality of the free-space running output signal was measured with an M^2 value of 1.14, which may be considered to be diffraction-limited. Figure 4.12 shows a typical spectrum of the fibre laser, measured with an optical spectrum analyzer with 1 nm resolution. It shows that the normally dominating 1.09 μm emission is suppressed, thanks to the W-type profile and the favourable spectroscopic properties in germanosilicate.

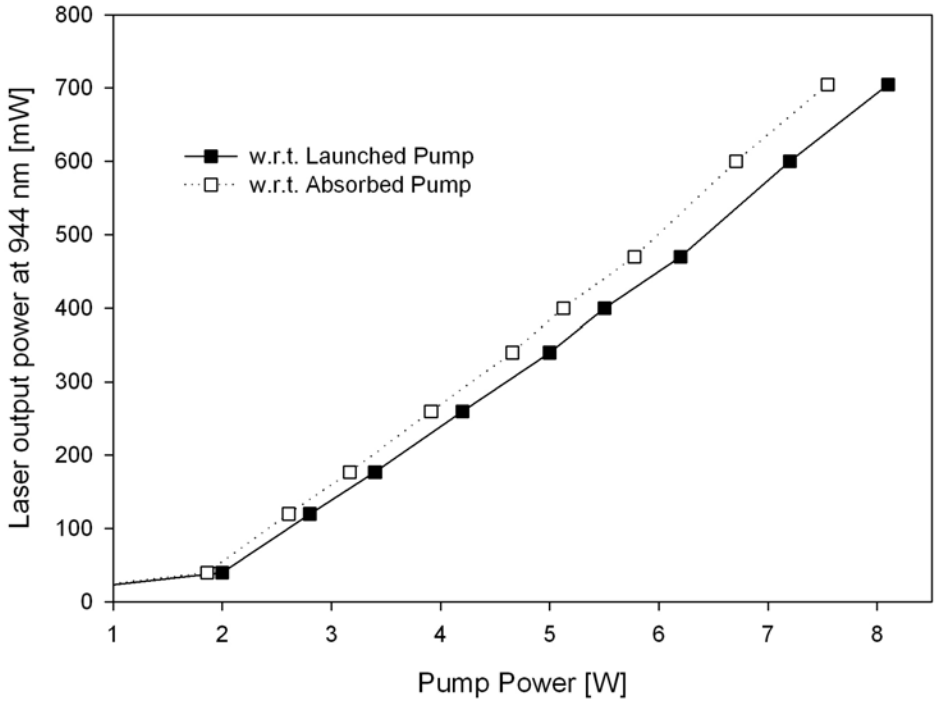

Figure 4.11. Laser power characteristics of W-type Nd-doped germanosilicate fibre laser, emitting at 0.944 μm.

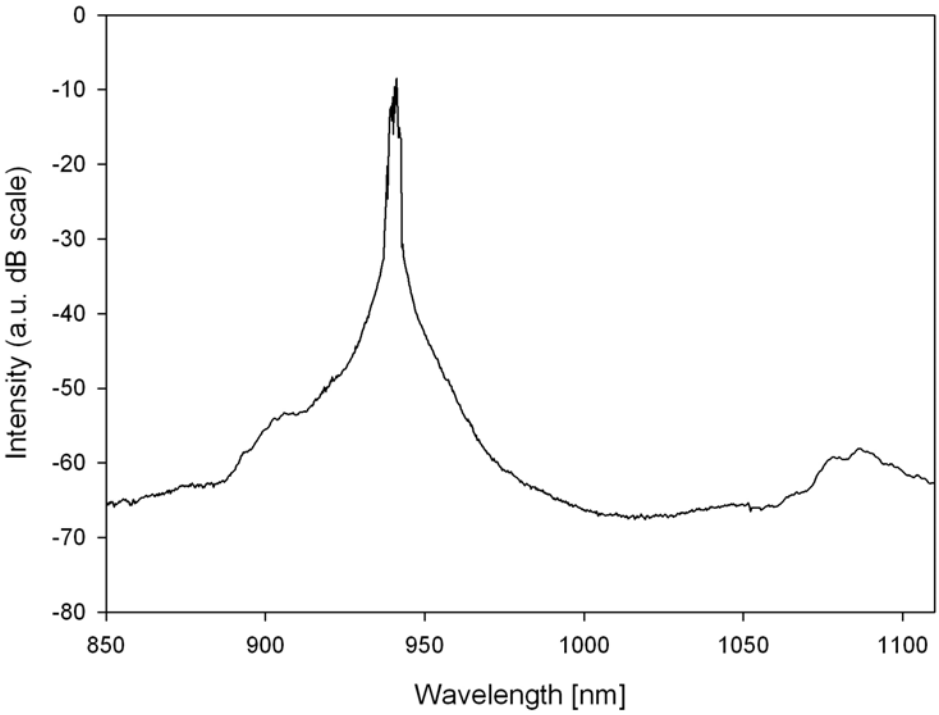

Figure 4.12. Optical spectrum of the laser signal (OSA resolution 1 nm).

In order to investigate wavelength-tuning, the diffraction grating was used instead of the broadband mirror for the signal feedback. Figure 4.13 shows the measured laser tuning characteristics with signal power and the threshold pump power for each wavelength. The maximum power was 560 mW. This is lower than with mirror feedback due to the low reflectivity from the diffraction grating. It was possible to tune the laser from 932 nm to 953 nm, although the power dropped significantly towards the ends of the tuning range. When the diffraction grating was tuned for the wavelength outside the tuning range, the fibre lased at 944 nm when pumped with high power.

Figure 4.13 also shows the result of the simulation results. In the laser simulations, the signal background loss (including the bending loss) played an important role, which is expected for long fibres. The simulation results shown in figure 4.13 correspond to a best fit with a signal background loss of 0.21 dB/m. However, small differences in signal background loss caused large differences both in power and tuning range. For instance, if the background loss was taken as 0.19 dB/m, the tuning range reached down to 926 nm with a maximum signal power of 556 mW while the maximum power occurred at 944 nm with 770 mW. There was relatively little

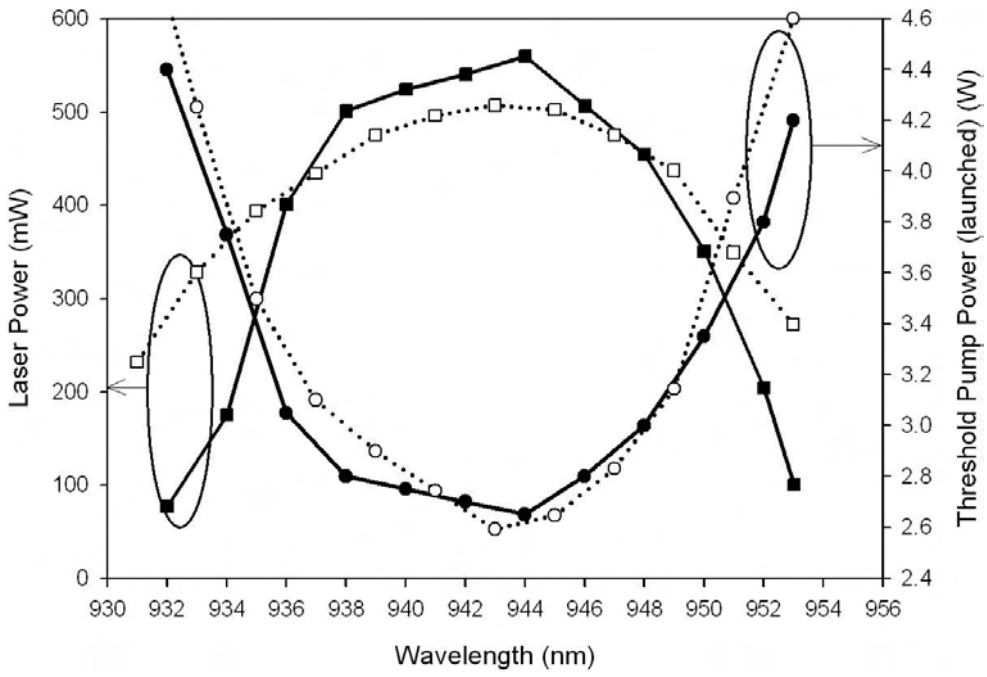

Figure 4.13. Measured (solid line) and simulated (dotted line) maximum output power and threshold pump power at different wavelengths.

variation in the upper limit of the tuning range. The simulations indicated also that with more pump power one can tune to shorter wavelengths, which can be explained by the higher fraction of the inverted population that can be reached. For instance, with a background loss of 0.21 dB/m and 16 W of total pump power, the simulations suggested that an output power of 840 mW would be achievable at 926 nm. However this assumes that lasing at 944 nm can be suppressed. Unfortunately, it was difficult to measure the core background loss precisely, due to the ground-state absorption at the signal wavelength. In addition to the background loss, the quenching might have led to unsaturable absorption, similar to background loss, at wavelengths with ground-state absorption.

4.3.3. Aluminosilicate Nd^{3+}-doped W-type fibre laser tuneable from 908 nm to 938 nm

Due to the low efficiency of the germanosilicate Nd^{3+}-doped fibre laser, I turned to the aluminosilicate host which allows a much larger Nd^{3+}-concentration to be incorporated before concentration quenching, *via* Nd^{3+} ion cross-relaxation, sets in.

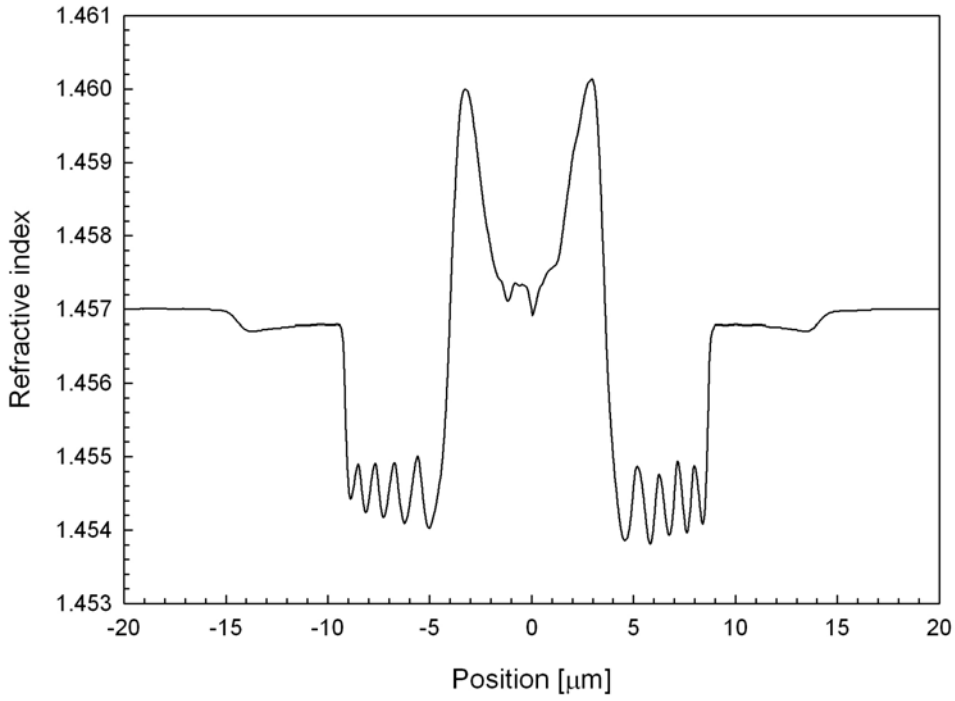

Figure 4.14. Measured refractive index profile of F432-LF197 fibre.

I designed an aluminosilicate W-type fibre with $a_{co} = 3.5\,\mu m$, $a_{dp} = 8.6\,\mu m$, $n_{co} = 1.4590$ (equivalent $NA_{co} = 0.076$), and $n_{dp} = 1.4546$ (equivalent $NA_{dp} = -0.0835$). This design was discussed in section 4.2. S. Yoo fabricated a preform (F432-LF197) according to my design. However, the MCVD process left a central dip of the refractive index as shown in figure 4.14. In order to see the effect of these deviations from the ideal W-type profile, I calculated the effective indices of guided modes based on the measured refractive index profile. For this, a mode solver for circularly symmetric structures with an arbitrary index profile is used. This is explained in detail in appendix B [73]. For comparison, figure 4.15 shows the modal effective indices for the measured refractive index profile (lines with symbols, labelled with superscript 'M'), in addition to those of the idealised index profile.

Beside the similar fundamental-mode cut-offs (at ~ 1 μm), two things are noticed. Firstly, the LP_{02} mode cut-off of the measured refractive index profile occurs at much shorter wavelength than that of the idealised refractive index profile, due to the dip in the middle. Secondly, the effective index of the fundamental LP_{01} mode is larger than with the idealised index profile for laser wavelengths in the 0.9 μm range. This

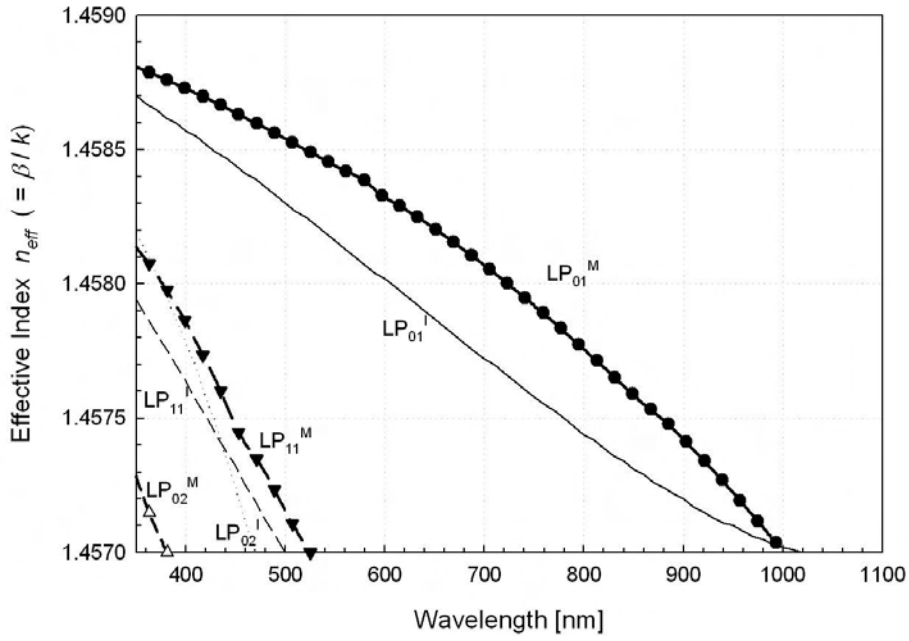

Figure 4.15. Effective refractive indices of the idealized design (lines superscripted with 'I') and those of the measured refractive index profile (connected dots superscripted with 'M') for fibre F432-LF197.

suggests that the measured profile reduces the sensitivity to the bending losses relative to the ideal (i.e., targeted) profile. The bending loss of the idealised profile is calculated as 0.19 dB/m with a bending diameter of 33 cm, at 942 nm whereas the measured profile has a bending loss calculated to only 0.03 dB/m.

The pump absorption can be undesirably low in a fibre with a core diameter as small as 7 μm, in particular in the case of Nd which is relatively susceptible to concentration quenching. The cladding is doubly truncated, as is illustrated in figure 4.7. The same cladding design as with F368-LF170 was used. The use of a doubly truncated inner cladding increased the cladding absorption to 11.2 dB, with a fibre length of 14 m, which is the shortest fibre length used in the experiment. The absorption is up from 7 dB with a circularly shaped inner cladding, The truncation to increase the pump absorption does however come at a price. The inner cladding size becomes 19% smaller. This by itself increases the pump absorption by reducing the inner cladding-to-core area ratio. The disadvantage is that the 19% reduction in the inner cladding area reduces the amount of pump power that could be launched. In this case, the reduction of the launched pump power was 11%, but this value will of course depend on the characteristics of the pump source and can be as high as 19%.

Although the increase of the absorption may appear relatively modest, even small improvements can be important for a three-level laser. The increased pump absorption reflects a stronger interaction between the pump and the gain medium, which implies that the pumping will be stronger with the same pump power. As a consequence, it will be easier to reach threshold, even if the fibre length stays the same. While the non-truncated circular fibre requires 30 m fibre length for 12 dB absorption, the truncated fibre only needed 15 m. This is beneficial when a large background loss (including the bending loss) and ground-state absorption is involved.

Figure 4.16 shows the emission and absorption cross-section spectra of Nd^{3+} for the signal transition, as measured with the techniques described in reference [53]. They were measured on the aluminosilicate fibre F432-LF197. The emission cross-section spectrum peaks at 906 nm while the absorption spectrum peaks at 880 nm, within the ${}^4F_{3/2} \leftrightarrow {}^4I_{9/2}$ transition. The spectroscopy indicates that the fibre laser may be tuned between 0.87 μm and 0.94 μm, provided that sufficient pump intensity is present along the fibre and the competing emission at the longer wavelength is efficiently suppressed. The fraction of excited ions will be high at threshold for short

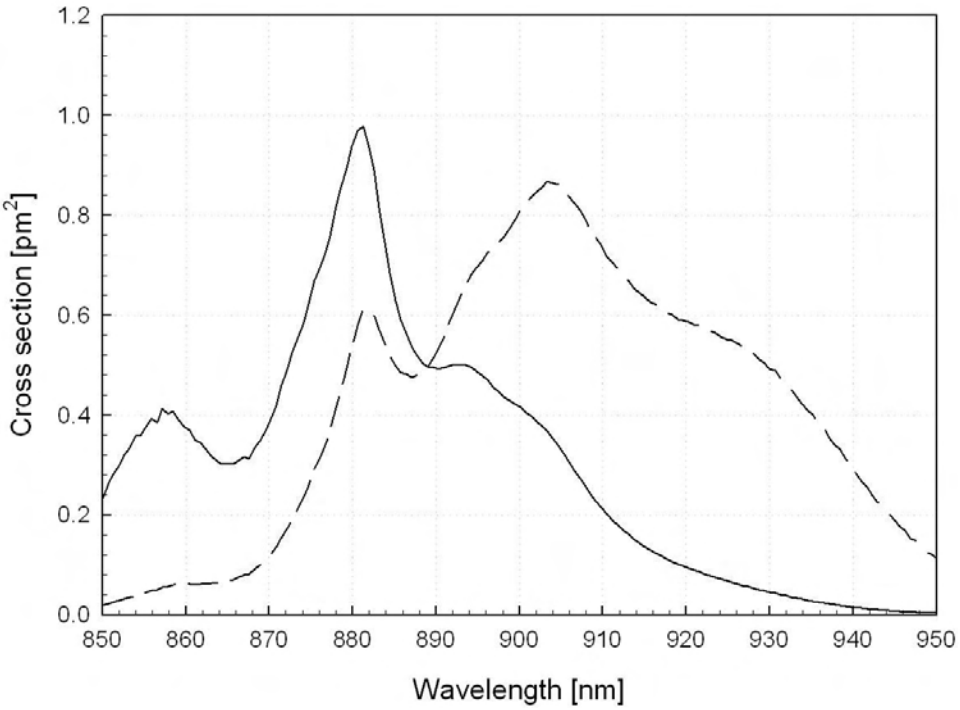

Figure 4.16. Absorption (solid line) and emission (dashed line) cross-section spectra of Nd^{3+} in aluminosilicate (fibre F432-LF197).

wavelengths because of the large ground-state absorption, as well as for long wavelengths because of the low emission cross-sections.

The configuration shown in figure 4.10 was used for the laser experiments. The fibre length varied between 14 m and 25 m, which allowed a pump absorption sufficiently large (at least 12 dB operating pump absorption) to avoiding pump cross-talk and damage. The fibre length is an important parameter of any fibre laser. For example, because of the wavelength dependence of the ground-state absorption, it will influence the tuning range [74]. Therefore, the laser characteristics at different fibre lengths are measured. I started with 25 m long fibre and cut it back several times to finally stop at 14 m. For every fibre length, I determined the slope efficiency and the threshold pump power as well as the wavelength tuning range. With the 14 m fibre, the operating, hot cavity, pump absorption was 12.1 dB. The maximum laser power occurred when the wavelength was tuned to 926 nm. The slope efficiency was 41% and the threshold pump power was 1.62 W, both with respect to launched pump power. The maximum output power was 2.4 W. This was the highest power achieved at any tuning wavelength.

Figure 4.17 shows a typical laser output spectrum, measured with an optical spectrum analyzer with a resolution bandwidth of 1 nm. The suppression of the competing 1.06 μm transition was excellent. The laser linewidth was 0.26 nm (FWHM) as measured with a resolution of 0.05 nm. The beam propagation parameter M^2 was 1.05 when the output power was 2 W, i.e., the output was diffraction-limited.

Figure 4.18 shows how the laser output power depends on pump power for different fibre lengths. For each length, the grating was tuned to provide maximum output power. This happened for wavelengths in the range 926 nm – 931 nm, depending on the fibre length. As I cut back the fibre, the slope efficiency increased and the threshold pump power decreased, which is mainly due to the signal propagation loss. Although the bending loss of the signal wavelength from the measured refractive index profile was practically negligible (0.03 dB/m with 33 cm bending diameter), the fibre in the experiment was locally bent to enhance the pump absorption by mixing the pump modes. Therefore, it is difficult to predict the bending loss at the signal wavelength precisely. From the figure, it appears as if higher output

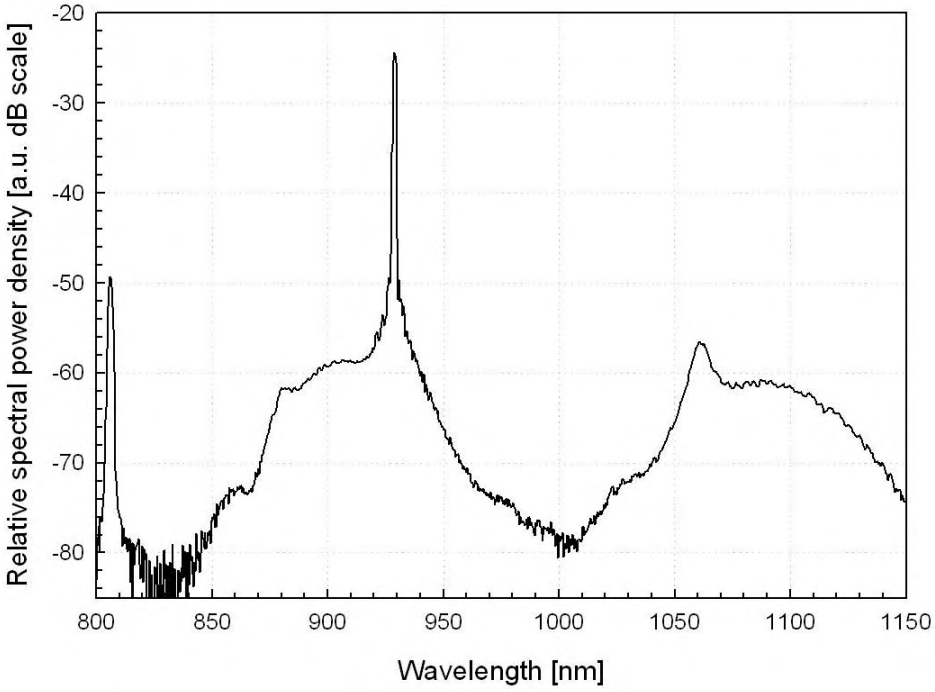

Figure 4.17. Example of power spectrum of the tuneable Nd-doped aluminosilicate fibre laser measured by an OSA with resolution 1 nm. Fibre length 14 m.

power would have been achieved if I had shortened the fibre further. But, this would have jeopardised the pump sources so I refrained from doing this. However, with a smaller inner cladding and better pump beam quality, the pump absorption per unit length would increase. I could then use shorter fibres, with which the slope efficiency probably would be higher.

As expected, the tuning range also changed with fibre length. This is shown in figure 4.19. The tuning range shifted to shorter wavelengths for shorter fibres. Thus, the tuning range was 908 nm - 938 nm for a 14 m long fibre, and 922 nm – 942 nm for a 25 m long fibre. Figure 4.20 shows the tuning curve at full pump power for a 14 m long fibre. The maximum power occurred at 926 nm. The power at the edge of the tuning range dropped significantly because of the increasing threshold, also shown in the figure. The limiting factor for the tunability was, in practice, a strong gain at 926 nm. This appeared when the diffraction grating was tuned to the edge of the tuning range, because of the large fraction of excited Nd^{3+} ions needed for lasing at the edge. As a consequence, 926 nm could start lasing from spurious reflections, e.g., from the angle-cleaved fibre end or the diffraction grating. I found that for better tunability, minimisation of reflection from the angle-cleaved fibre end was critical. Such behaviour is typical at high gains of 30 dB or more, which then suggests that our fibre would be capable of high gain amplification at 926 nm. Finally, figure 4.21 shows laser output spectra for different tuning wavelengths between 908 nm and 938 nm, measured with 0.05 nm resolution. The measured linewidth was in each case 0.26 nm.

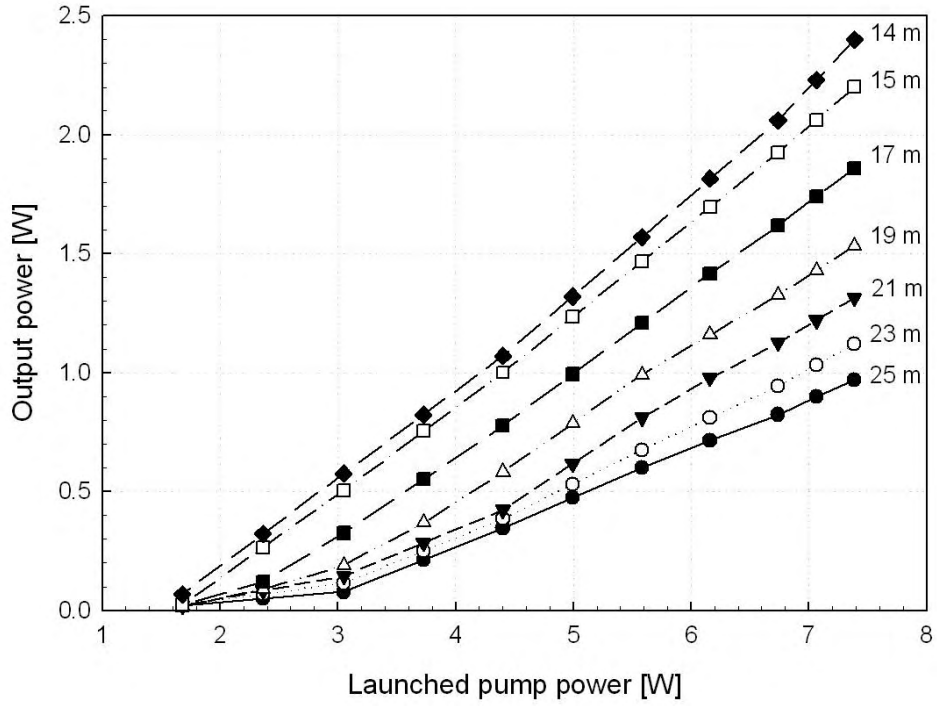

Figure 4.18. Laser power characteristics at different fibre lengths.

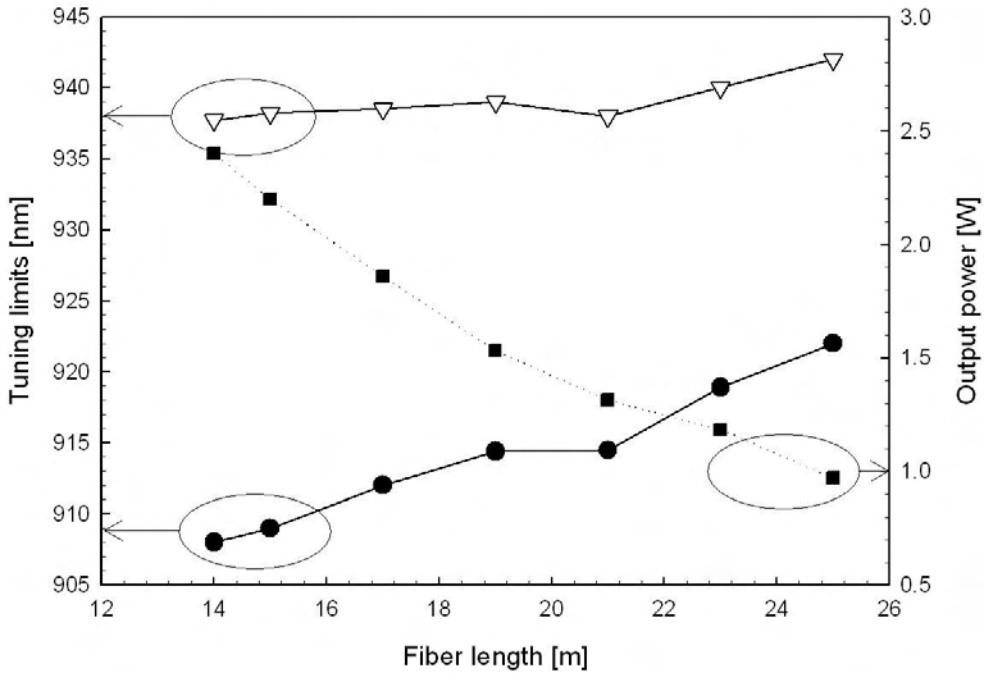

Figure 4.19. Tuning range and maximum output power for different fibre lengths.

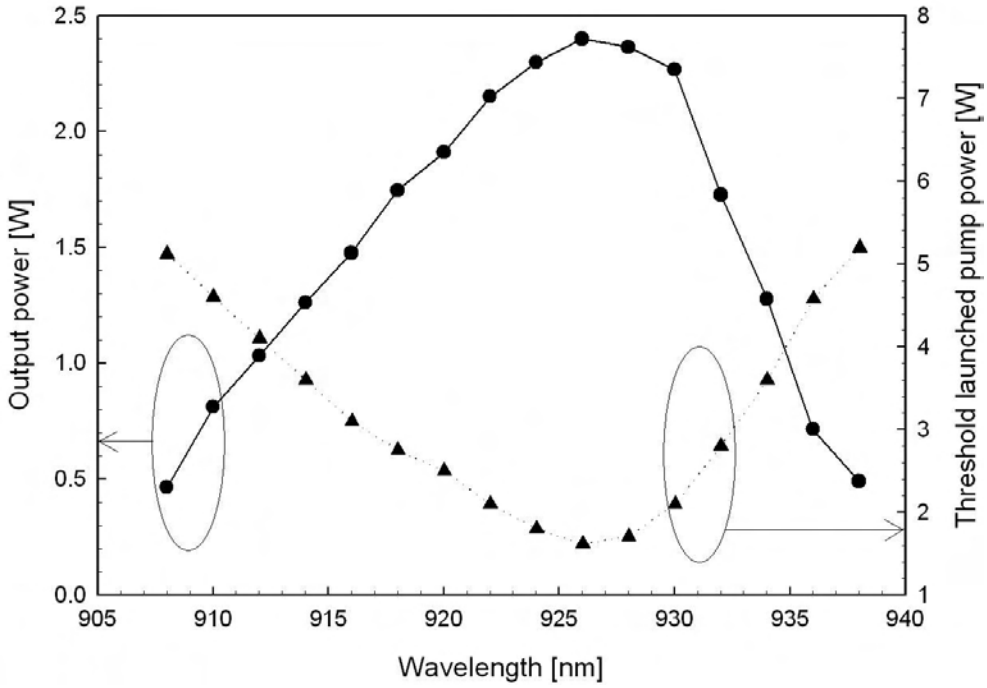

Figure 4.20. Maximum output power and threshold pump power versus wavelength for Nd-doped aluminosilicate fibre F432-LF197.

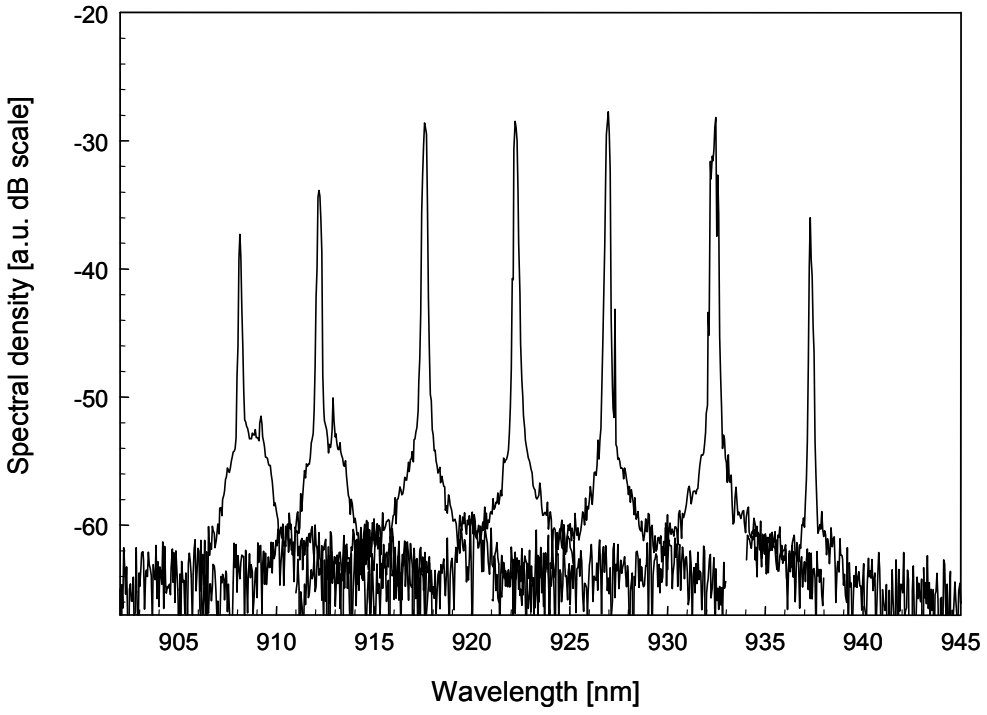

Figure 4.21. Optical output spectra at various tuning wavelengths.

4.4. Summary

In this chapter, I have investigated the use of W-type fibres for Nd^{3+}-doped fibre lasers operating at 0.9 μm. The spectral filtering provided by the W-type fibre is sufficiently strong to allow for an efficient high power cladding-pumped fibre laser at 0.9 μm. In addition, the W-type fibre is much more robust against errors in the fibre parameters compared to the helical fibre in chapter 3. Therefore, it was suitable for the realisation of high power cladding-pumped fibre lasers.

Experimental results using the W-type design in germanosilicate and aluminosilicate host Nd^{3+}-doped fibre lasers were presented. Despite a better spectroscopy, the low permissible concentrations and the tendency to quench, as well as the long fibre lengths make those germanosilicate host fibres less efficient. The result of the germanosilicate W-type Nd^{3+}-doped fibre laser at 0.94 μm contrasts also with Dawson's work [1], which reaches high efficiency but with a large core. On the other hand, the aluminosilicate host showed better performance (slope efficiency) than the germanosilicate host, mainly because it can avoid the Nd^{3+} ion quenching. However, the slope efficiency of 41%, which is far less than the quantum limit of 87%, suggests that the fibre laser suffers from bending loss at the signal wavelength. Large cores are not possible with W-fibres. In fact this is a serious drawback with W-fibres. An alternative to the W-type is the depressed-clad hollow core fibre, which will be described in chapter 5. The advantage of such DCHF is that the depression of the refractive index does not have to be so large. It can still maintain an excellent signal mode confinement in the doped core, because of the hole in the middle. In addition, a large core is possible with such depressed-clad hollow core fibre.

Chapter 5. Depressed-clad hollow fibres

The previous chapter described a W-type refractive index fibre. Using such W-type fibres one can realise high power Nd^{3+}-doped fibre lasers operating at 0.9 μm. However, one of the disadvantages of such W-type fibres is that it is difficult to realise a large core area. This limits the energy storage of the fibre as far as pulsed lasers are concerned. In addition, the small core area with a large cladding size may lead to insufficient pump absorption (per unit length) with cladding-pumping. Small pump absorption leads to a longer fibre length for sufficient total pump absorption, which is not desirable because of propagation losses and nonlinear effects.

A depressed-clad hollow fibre addresses these issues. The position of the doped ring-shaped core with high index is located further out to the cladding than with the W-type fibre and can have a larger area. Hence, the pump absorption rate may be significantly increased so that shorter fibres can be used. At the same time, like a W-type core structure, the waveguide can have a fundamental modal cut-off. The air hole in the middle acts as a large volume refractive index depression. Because of the significant depression, one may use a comparatively large core with high refractive index whilst still maintaining the condition for a fundamental mode cut-off [17]. This means the effective index of the guided mode can be larger than that of W-type fibres. Therefore one can have a sharper fundamental cut-off against the wavelength. Therefore, one may consider a more critical cut-off using the depressed-clad hollow fibre. This is required for Yb^{3+}-doped fibre laser operating at 0.98 μm as the competing stronger emission at 1.03 – 1.1 μm (only as little as 50 nm apart) needs to be suppressed. This may be compared to the less critical requirement on the cut-off characteristics for the W-type fibre of Chapter 4, discriminating 0.92 μm from 1.06 μm (140 nm apart).

The hollow optical fibre has been developed for atomic guiding and funnelling [75]. Other research groups have also focused on mode conversion applications [76]. However, no one had investigated the wavelength filtering characteristics of such hollow fibres, until our group in the ORC developed rare-earth doped depressed-clad hollow optical fibres. The depressed-clad hollow fibre was initially designed for the efficient operation of a cladding-pumped Nd^{3+}-doped fibre laser operating at 0.9 μm [72]. The additional depressed refractive index region surrounding the doped core is implemented to increase the mode confinement at the signal wavelength. Later, it was discovered that an additional depressed refractive index region also contributes towards better fundamental cut-off characteristics. Initially, it was postulated that the main advantage of such depressed-clad hollow fibres over the already developed W-type fibres [3, 6, 68, 69] was a larger core (with low NA) and the increased pump absorption rate that follows. The W-type fibre with low NA may suffer from unwanted large bending loss at the signal wavelength, due to slow cut-off characteristics. Later, it was found that such depressed-clad hollow fibres are superior to W-type fibres in terms of the fundamental mode cut-off characteristics as well, i.e., it can offer at the same time sharper cut-off characteristics, lower bending loss for the desired wavelength, and larger core size. Therefore one can utilise the depressed-clad hollow fibre for Yb^{3+}-doped fibre lasers operating at 0.98 μm, which is challenging for the W-type fibre.

It is worth here to clarify that the concept of the depressed-clad hollow fibre was originally jointly suggested by J. Kim and myself. J. Kim directed the fibre design to meet the 1 micrometer cut-off wavelength requirement and I reviewed his fibre design. Then, I carried out the theoretical analysis prior to the preform fabrication. This included the bending loss analysis and the numerical simulation of the fibre laser, presented in this chapter. J. Kim fabricated the Yb-doped depressed-clad hollow fibre (F645-LF239) and led the fibre laser experiment with my help.

This chapter presents the design of a depressed-clad hollow fibre for an Yb^{3+}-doped fibre laser operating at 0.98 μm. Numerical simulation results will support the advantages of the depressed-clad hollow fibre against other types of wavelength filtering waveguides. Finally experimental results will be shown.

5.1. Design of depressed-clad hollow fibre

A schematic of the refractive index profile of a depressed-clad hollow fibre is shown in figure 5.1. It has an air hole in the middle with a radius of a_{air}. The refractive index of air is $n_{air} = 1$. The air hole is surrounded by a doped high index, ring-shaped, core with outer diameter of a_{co} and refractive index n_{co}. A depressed refractive index region with outer diameter of a_{dp} and refractive index n_{dp} surrounds the doped ring core. Finally, the inner cladding with refractive index n_{cl} surrounds the other structures.

It is problematic to assume that the modes are weakly guided and linearly polarised due to the large refractive index difference between the air hole and the doped core. However, as far as the fundamental mode cut-off is concerned, the difference between the full vectorial calculation and the LP mode approximation is found to be negligibly small. To arrive at this, results using an arbitrary mode solver based on reference [73] and a commercial software (Femlab, Comsol) are compared. The errors in the normalised effective refractive indices of the guided modes were within 1% in most cases. Therefore, the linearly polarised mode approximation was used for simplicity. In this case, the electrical field of the guided mode is represented

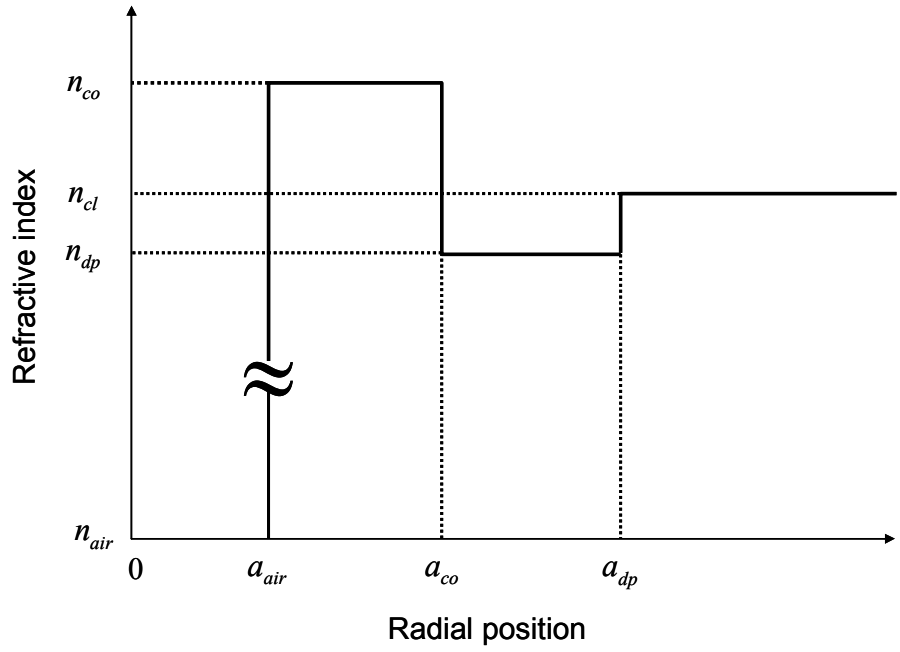

Figure 5.1. Schematic refractive index profile of a depressed-clad hollow fibre.

by $E_{lp}(r,\phi;t) = e_{lp}(r)\cos(l\phi)\exp(i\omega t)$ where l, p are modal numbers, $\omega(=2\pi c/\lambda)$ is the optical angular frequency and r,ϕ are the coordinate variables of the plane perpendicular to the fibre axis. Furthermore $e_{lp}(r)$ is an eigensolution of the Helmholtz equation and is represented by [9]

$$e_{lp}(r) = \begin{cases} A_0 I_l(vr), & r < a_{air} \\ A_1 J_l(ur) + A_2 Y_l(ur), & a_{air} \le r < a_{co} \\ A_3 I_l(wr) + A_4 K_l(wr), & a_{co} \le r < a_{dp} \\ A_5 K_l(sr), & a_{dp} \le r \end{cases} \tag{5.1}$$

where J_m , Y_m , I_m , and K_m are Bessel functions and $v = k\sqrt{n_{eff}^2 - n_{air}^2}$, $u = k\sqrt{n_{co}^2 - n_{eff}^2}$, $w = k\sqrt{n_{eff}^2 - n_{dp}^2}$ and $s = k\sqrt{n_{eff}^2 - n_{cl}^2}$. Here n_{eff} is the effective index of the guided mode with modal number l, p , and is again an eigenvalue of the Helmholtz equation. In order to find the eigenvalue n_{eff} , one has to solve the following equation with boundary conditions at $r = a_{air}$, $r = a_{co}$, and $r = a_{dp}$.

$$\begin{vmatrix} I_l(va_{air}) & -J_l(ua_{air}) & -Y_l(ua_{air}) & 0 & 0 & 0 \\ vI_l^d(va_{air}) & -uJ_l^d(ua_{air}) & -uY_l^d(ua_{air}) & 0 & 0 & 0 \\ 0 & J_l(ua_{co}) & Y_l(ua_{co}) & -I_l(wa_{co}) & -K_k(wa_{co}) & 0 \\ 0 & -uJ_l^d(ua_{co}) & -uY_l^d(ua_{co}) & -wI_l^d(wa_{co}) & -wK_l^d(wa_{co}) & 0 \\ 0 & 0 & 0 & I_l(wa_{dp}) & K_l(wa_{dp}) & -K_l(sa_{dp}) \\ 0 & 0 & 0 & wI_l^d(wa_{dp}) & wK_l^d(wa_{dp}) & -sK_l^d(sa_{dp}) \end{vmatrix} = 0, \tag{5.2}$$

where $Z_l^d(ur) = \partial Z_l(ur)/\partial r$ and Z_l is any Bessel function. Here, $|\cdot|$ represents the determinant of a matrix. Equation (5.2) is difficult to represent in a compact form and it is therefore difficult to obtain an analytical solution for n_{eff} . Instead, one can resort to the arbitrary mode solver in reference [73] or another numerical solution technique. Even without the analytical form of the solution n_{eff} , one can predict the fundamental mode cut-off behaviour qualitatively as follows. The condition for shorter cut-off wavelength is a combination of (1) a large air hole, (2) a smaller core thickness

Parameters	Nominal value	Perturbed value (amount of change)	Cut-off wavelength of the perturbed parameter	Change in cut-off wavelength
a_{air}	15 μm	14.25 μm (-5%)	1000 nm	0 nm
$a_{co} - a_{air}$	2 μm	1.9 μm (- 5%)	1052 nm	52 nm
$a_{dp} - a_{co}$	5 μm	4.75 μm (- 5%)	1000 nm	0 nm
NA_{co}	0.1585	0.1506 (- 5%)	1065 nm	65 nm
NA_{dp}	-0.1000	-0.0950 (5%)	1008 nm	8 nm

Table 5.1. Change in fundamental mode cut-off wavelength due to perturbed design parameters.

($a_{co} - a_{air}$), (3) a deeper depression (i.e., lower n_{dp}), and (4) a larger depressed region (i.e., larger a_{dp}). However, since the centre air hole acts as a huge negative volume index, it is expected that a small change of the air hole size or the surrounding depressed region will not have a major effect on the cut-off wavelength. The depressed region size ($a_{dp} - a_{co}$) and n_{dp} are in fact fine tuning factors of the modal field shape rather than a critical parameter for the cut-off wavelength. Therefore, the most critical parameters for the cut-off wavelength are expected to be the core thickness ($a_{co} - a_{air}$) and n_{co}. In order to show this quantitatively, one can consider examples which perturb other parameters by a small amount to see the effect on the cut-off wavelength. One example is shown in table 5.1.

For this, $NA_{co} = \sqrt{n_{co}^2 - n_{cl}^2}$ and $NA_{dp} = -\sqrt{n_{cl}^2 - n_{dp}^2}$ are considered as design parameters. The nominal (unperturbed) parameters are chosen so that the cut-off wavelength becomes 1000 nm. Each parameter is perturbed by 5% and the resulting changes in cut-off wavelength are shown. From table 5.1, it is evident that the most critical parameters for the fundamental cut-off wavelength are the core thickness $a_{co} - a_{air}$ and NA_{co}. Already a 5% change of these parameters leads to more than 50 nm change in the cut-off wavelength. On the other hand, the effect of perturbing the air hole radius a_{air}, the depressed index region thickness $a_{dp} - a_{co}$ and NA_{dp} are minimal as expected.

The outer depressed region is added for a better mode confinement of the guided mode in the core. It is also possible to implement the fundamental mode cut-off

without the outer depressed region. However, in this case the modal field is not well confined in the core, which is easily deduced from the modal field in equation (5.1). Note that the field in the depressed region rapidly reduces with the increasing radial position according to the characteristics of the modified Bessel functions I_l, K_l. Consequently, the field is more confined in the doped high index core than the hollow fibre structure without the depressed region.

Thus, it is possible to design a Yb^{3+}-doped fibre with a fundamental-mode cut-off wavelength of 1.00 μm for operation at 0.98 μm. However, even if the fundamental mode is cut off at 1 μm, the emission at 1.03 – 1.1 μm is still confined in the cladding. Then this emission may experience gain, even though it may be small. This gain is nearly proportional to the fibre length and once the gain at longer wavelengths becomes comparable to the gain at 0.98 μm in the core, it may cause unwanted performance degradation. Therefore, even if the fundamental mode is not guided in the core at the unwanted wavelengths, one may still have to make the fibre short with sufficient pump absorption. In order to increase the pump absorption rate, one can consider a larger core thickness and lower NA_{co} compared to the example in table 5.1. This can be achieved while still maintaining the same fundamental mode cut-off wavelength. However, the low NA_{co} is not desirable in the sense that it implies a low effective refractive index of the guided mode and consequently small mode confinement in the doped core (see equation (5.1)). If the mode is not well confined in the core it may suffer from a large bending loss. Therefore, a high NA_{co} is desired, which is also good for a sharper cut-off property. Therefore, one has to make a compromise for NA_{co} to achieve both a good pump absorption rate and less bending loss.

For a Yb^{3+}-doped fibre laser operating at 0.98 μm, the effective index at 0.98 μm will be low since the cut-off wavelength should be located at ~1.00 μm, which is quite near to 0.98 μm. Therefore it is to be expected that the performance of a fibre laser at 0.98 μm, which employs a fibre design with the fundamental cut-off wavelength at 1 μm, may be degraded due to bending loss at the signal wavelength. A fibre design with 1 μm cut-off wavelength that minimises the bending loss at 0.98 μm while maximising the pump absorption can be difficult to optimise. However, once the fibre core waveguide is designed to have the fundamental mode cut-off wavelength at 1 μm,

one can still use a numerical laser simulator to modify, for instance, the rare-earth ion concentration, fibre length, etc. Although the optimisation process using the numerical laser simulator is not presented in this chapter, the effects of design parameters on the laser performance are explained in section 5.2 (numerical simulations).

Since the air hole radius a_{air} is not critical in determining the fundamental-mode cut-off wavelength, it is convenient to fix a_{air} to say, a_{air} = 8 µm. The depressed region width $a_{dp} - a_{co}$ and NA_{dp} are not critical either. Therefore they are fixed to values of $a_{dp} - a_{co}$ = 11 µm and NA_{dp} = -0.07. The effect of these two parameters will be discussed later. In this case, the design parameters to be determined reduce to just the core width $a_{co} - a_{air}$ and NA_{co}. Figure 5.2 shows the LP_{01} and LP_{11} mode cut-off wavelength depending on $a_{co} - a_{air}$ and NA_{co} with all other parameters fixed. As is expected, the fundamental mode cut-off wavelength becomes shorter with smaller $a_{co} - a_{air}$ and lower NA_{co}. Also shown in figure 5.2(a) (the black line) are the solution $(a_{co} - a_{air}, NA_{co})$ pairs, which make the fundamental mode cut-off wavelength to be 1 µm. Figure 5.2 (b) shows the second mode, namely, LP_{11} cut-off. In figure 5.2 (b), the line represents the 0.98 µm cut-off wavelength. Therefore, the fibre design using the solutions in figure 5.2 (a) (the parameter pairs on the line) supports only the LP_{01} mode at 0.98 µm. The LP_{11} mode cut-off wavelength for the fibres using the solution in figure 5.2 (a) is 0.92 µm.

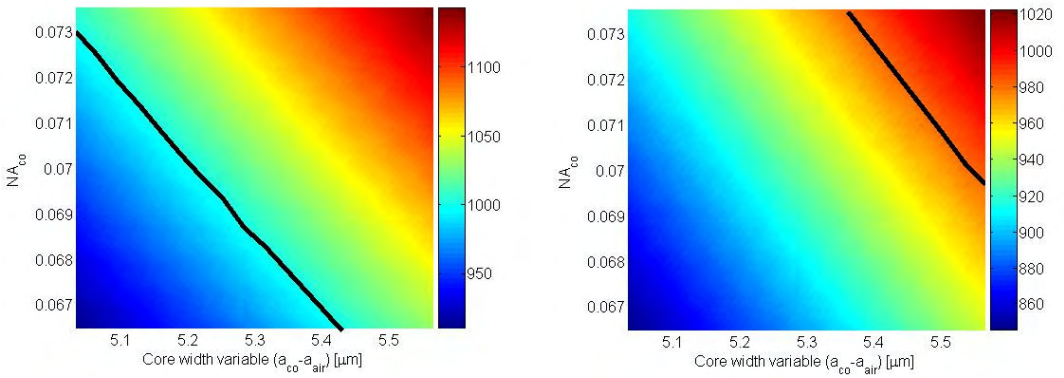

(a) LP_{01} mode cut-off wavelength (b) LP_{11} mode cut-off wavelength

Figure 5.2. The mode cut-off wavelength dependence on the core width and NA_{co}. The line in (a) represents the LP_{01} 1 µm cut-off and the line in (b) represents the LP_{11} 0.98 µm cut-off.

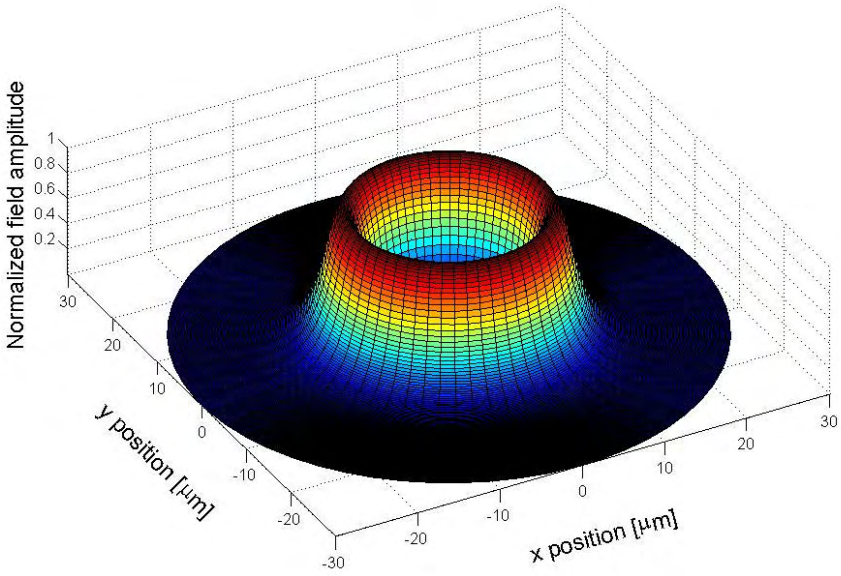

Figure 5.3. The LP_{01} mode of the designed fibre at 0.98 μm.

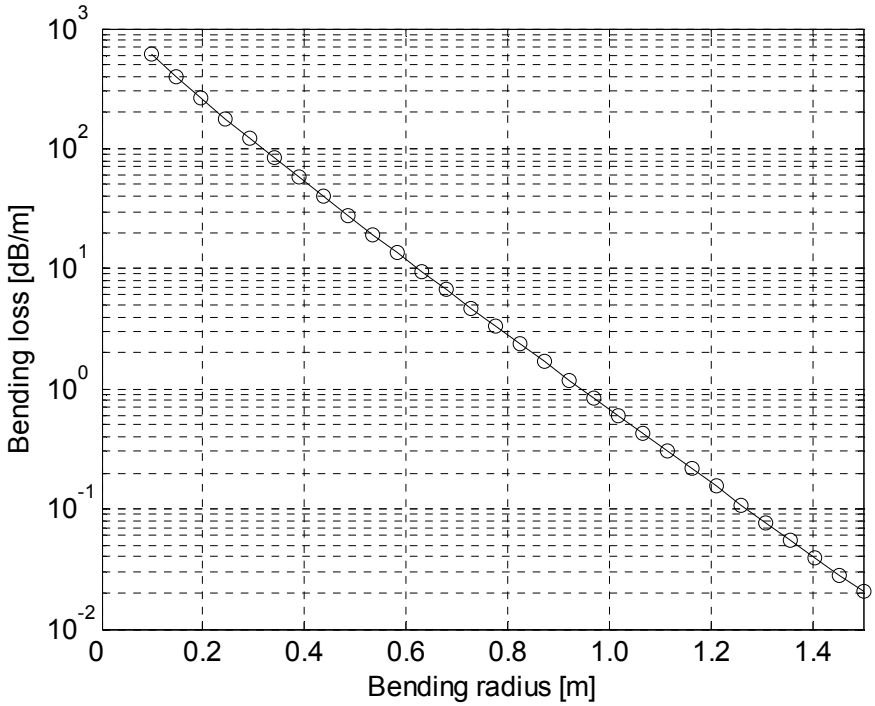

Figure 5.4. Bending loss of the LP_{01} mode at 0.98 μm of the designed fibre.

Using this result, one may choose the appropriate pair of values for $a_{co} - a_{air}$ and NA_{co}, by which the fibre has a fundamental mode cut-off wavelength of 1 μm and at the same time, supports only the fundamental LP_{01} mode. For instance, one may choose $a_{co} - a_{air}$ = 5.2 μm and NA_{co} = 0.07.

With the design parameters fixed as above, the interesting properties are the mode field profiles indicating the core confinement factor affecting the bending loss. Figure 5.3 shows the three-dimensional modal field at 0.98 μm of the designed fibre. The fundamental LP_{01} mode profile is ring-shaped with a hole inside. The calculated mode intensity confinement factor is 61%.

From the calculated modal intensity, one can calculate the bending loss by using the theory in reference [77]. Figure 5.4 shows a graph of the calculated bending loss versus bending radius for the LP_{01} mode at 0.98 μm. From the calculated result, it is apparent that the designed fibre is inefficient due to the huge bending loss and, thus, cannot be used. This is the moment when one should consider the remaining design parameters, namely, the depressed region width $a_{dp} - a_{co}$ and the NA_{dp}. Of course, raising NA_{co} reduces the bending loss. But, the change in NA_{co} alters the fundamental cut-off wavelength significantly. Remember, by contrast, that the fundamental mode cut-off wavelength is relatively insensitive to a small change (say, ± 5%) in $a_{dp} - a_{co}$ and NA_{dp}. So by modifying these two parameters, one can fine tune and hopefully improve the bending loss characteristics.

It is true for most cases to say that the bending loss reduces with a better mode confinement in the core. Therefore, one may postulate that the bending loss may become smaller with a large depressed region width $a_{dp} - a_{co}$ or $\left|NA_{dp}\right|$ (implying rapid decay of the modal field in this region, see equation (5.1)). However, the bending loss is not a simple process. In other words, the bending loss is not entirely dependent on only the mode confinement, but on the effective index of the guided mode, too. With a larger depressed region width $a_{dp} - a_{co}$ or $\left|NA_{dp}\right|$, the effective index of the guided mode becomes smaller, which counteracts the bending loss reduction from the better mode confinement. Therefore, one should be careful to consider both the modal confinement and effective index of the guided mode. In general, due to the complex mathematical form of the bending loss, it is difficult to

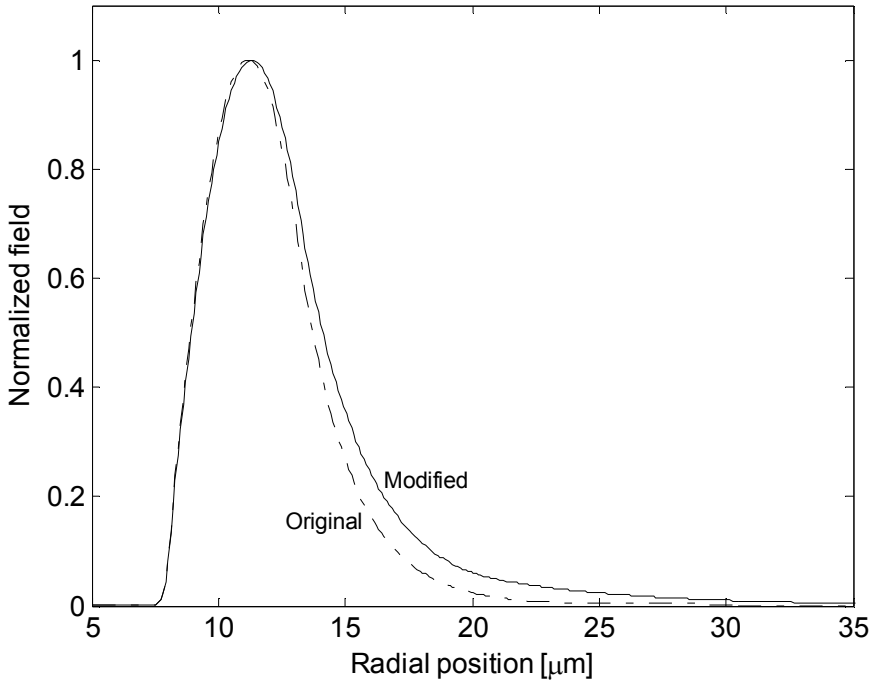

Figure 5.5. LP_{01} mode fields at a wavelength of 0.98 μm. The solid line and the dot-dashed curves represent the field from the modified and the original design, respectively.

say which dominates between the two (i.e., the mode confinement or the effective refractive index). It becomes more difficult to predict with such a complicated refractive index profile as the depressed-clad hollow fibre.

In order to see this point more clearly, two cases are compared. The first case is for $a_{dp} - a_{co}$ = 11 μm and NA_{dp} = -0.07 (the original design) and the second case is $a_{dp} - a_{co}$ = 8 μm and NA_{dp} = -0.05 (the modified design). The original design makes the fundamental mode cut-off wavelength to be 1.00 μm whereas the modified design makes it to be 1.05 μm. Figure 5.5 compares the LP_{01} mode fields of the original and the modified designs, which are scaled to a unity peak value. It is shown that due to the smaller depressed region, the mode field of the modified design spreads further to the cladding. On the other hand, the effective indices of the LP_{01} modes from the original and the modified designs are 1.45706 and 1.45720, respectively. Note that the effective refractive index of the LP_{01} mode of the original design is very close to the cladding refractive index (1.457). This caused the unacceptably large bending loss shown in figure 5.4.

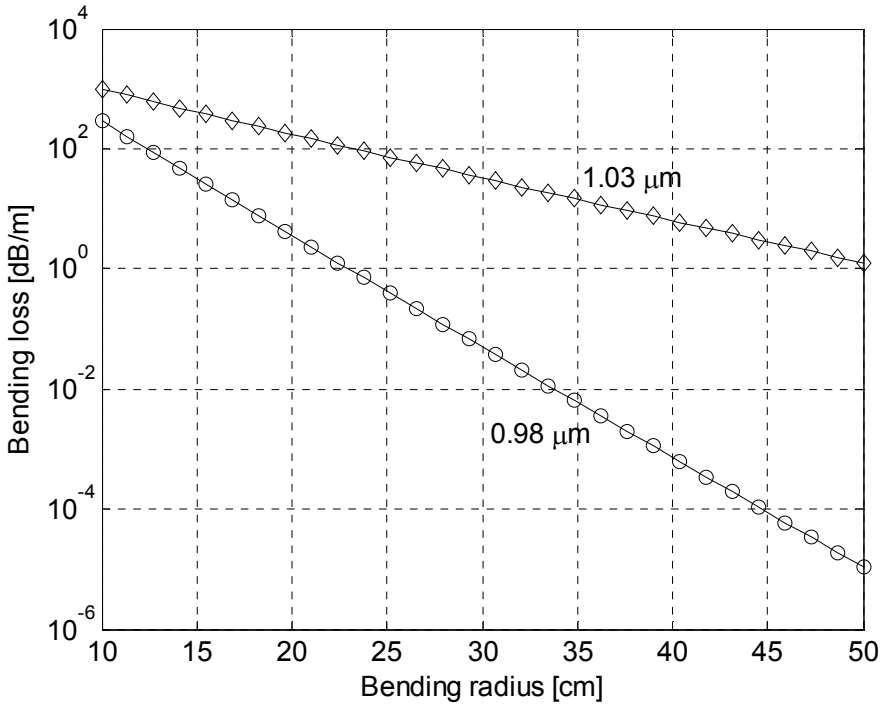

Figure 5.6. Bending loss of the LP_{01} mode with the modified design.

Figure 5.6 shows the calculated bending loss of the LP_{01} mode using the modified design. Compared to figure 5.4 (i.e., the bending loss from the original design), the bending loss from the modified design is significantly reduced at 0.98 μm. Figure 5.6 also shows the bending loss of the LP_{01} mode at 1.03 μm, which is significantly higher. Even though 1.03 μm radiation is guided (i.e., not cut off), the large bending loss at this wavelength indicates the mode even enters the field deformation regime described in reference [64]. Therefore, in the final laser set-up, one can adjust the bending radius so that 0.98 μm suffers a negligible bending loss while 1.03 μm suffers a large bending loss. For instance, using a 35 cm bending radius, the bending loss at 0.98 μm is only 0.05 dB/m whereas that at 1.03 μm reaches 30 dB/m.

In summary, a depressed-clad hollow fibre was designed for a fibre laser operating at 0.98 μm. Although the signal wavelength (0.98 μm) is very close to the competing 1.03 – 1.1 μm, it is still possible to design such fibres thanks to the additional design freedom relative to the W-type fibre. In fact, from figure 4.4 in chapter 4, one can estimate the effective refractive index of the guided mode at 0.98 μm from a W-type design should be 1.45708 (in the best case), which is somewhat similar to the

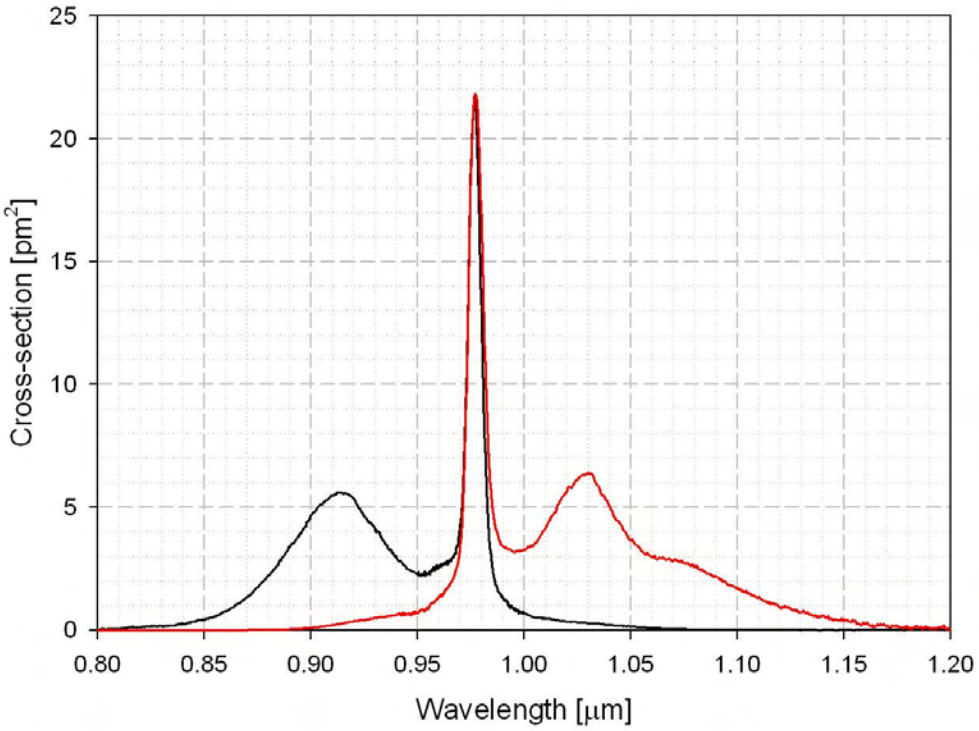

Figure 5.7. The measured stimulated absorption (black) and emission (red) cross-section spectra from a Yb-doped aluminosilicate fibre.

unmodified design. This of course induces an unacceptably large bending loss at 0.98 μm.

5.2. Numerical simulation of a Yb^{3+}-doped depressed-clad hollow optical fibre operating at 0.98 μm

In order to further study the characteristics of a Yb^{3+}-doped fibre laser at 0.98 μm, the Yb absorption and emission cross-sections in an aluminosilicate fibre were measured using the method in [53], i.e., the absorption cross-section was measured and calculated from the cut-back method and the stimulated emission cross-section was measured and calculated from the spontaneous emission spectrum. Figure 5.7 shows the resulting emission and absorption cross-section spectra. These were then used for simulations of a fibre laser according to the model described in appendix A. For the fibre, the modified design in the previous section is used, that is a_{air} = 8 μm, a_{co} = 13.2 μm, a_{dp} = 21.2 μm and cladding radius 50 μm. In addition, NA_{co} = 0.07 and NA_{co} = -0.05. In fact, the cladding radius of 50 μm is quite large for a 0.98 μm Yb^{3+}-doped fibre laser, which is compared to the 14 μm cladding radius of the JAC Yb^{3+}-

doped fibre in reference [35]. (Although JAC structures allow a large pump coupling into the cladding due to the high index contrast between the silica inner cladding and the air outer cladding, any core design can be implemented in a JAC structure.) The large cladding size is a huge advantage of the depressed-clad fibre since it enables us to use higher-power diode pump sources. The fundamental mode cut-off wavelength of this fibre is calculated to be 1.05 μm. The bending loss is calculated for the wavelength region of interest. Assuming the bending radius is 35 cm, this induces a loss of 0.05 dB/m at 0.98 μm and 30 dB/m at 1.03 μm. The Yb^{3+}-ion concentration is assumed to be 1.645×10^{25} ions/m^3.

The fibre laser set-up considered for the numerical simulation is shown in figure 5.8. It is the same as in previous chapters. The maximum launched pump power is assumed to be 20 W at 915 nm. The laser cavity feedback comes from a 4% Fresnel reflecting perpendicularly cleaved fibre facet, in the combined pump launching and out-coupling end, and an external diffraction grating with 60% feedback (inclusive of all losses) in the other end of the fibre. The fibre length is initially 4 m, which absorbs 75% of the launched pump power in a 'hot' cavity, i.e., when the laser is operating with at least 50% of the ions excited (averaged along transverse and longitudinal core position). The pump absorption is different at different ion excitation, but at least ~50% excitation is required to obtain lasing.

The numerical simulation of the depressed-clad hollow fibre is difficult since there is no guided mode above the fundamental mode cut-off wavelength. In the previous chapter, it was assumed that the wavelength components which are not guided in the

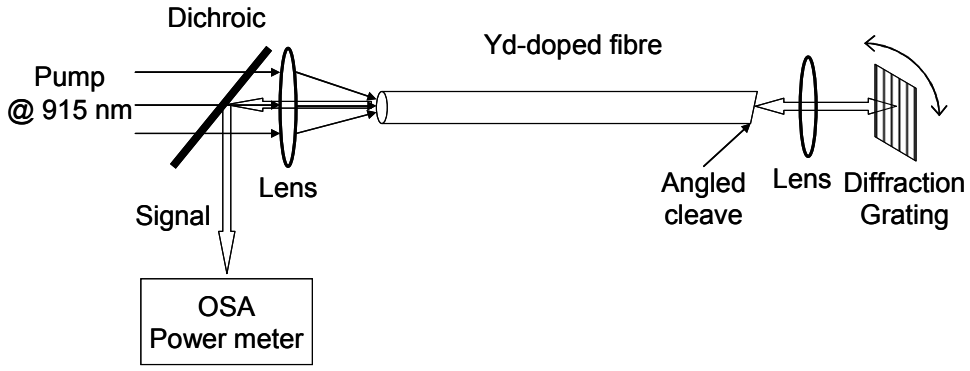

Figure 5.8. Fibre laser arrangement considered for numerical simulations.

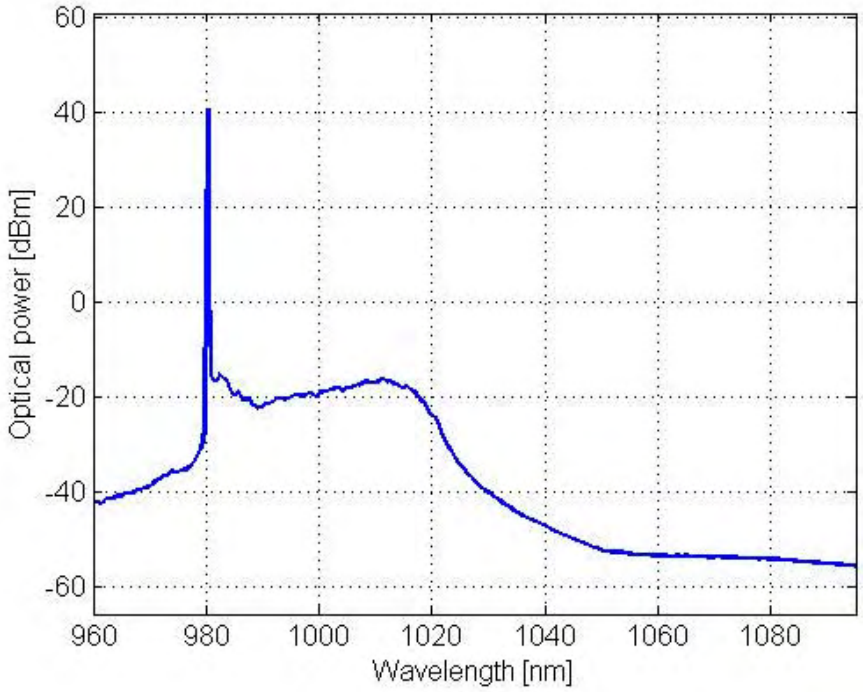

Figure 5.9. A typical optical spectrum obtained from the numerical simulation of the fibre laser.

core are confined in the cladding, with a uniformly distributed intensity profile. In this case, an abrupt discontinuity in the signal optical spectrum occurs. Figure 5.9 shows the output signal spectrum when 20 W pump is launched. The discontinuity should be located at 1.05 μm, which is the fundamental mode cut-off wavelength. The discontinuity is not clearly shown because of the well suppressed signal of the guided mode at 1.05 μm due to the huge bending loss. Thanks to the fibre design and the appropriate bending radius, the normally stronger emission at 1.03 μm is significantly reduced. (The bending loss is 30 dB/m at 1.03 μm and 100 dB/m at 1.05 μm.) Note the gradual decrease from 1.01 μm and above due to the fast increase of the bending loss. Figure 5.10 shows the output power characteristics of the 0.98 μm laser, as obtained from the numerical simulations. The slope efficiency is 64% and the threshold pump power is 0.5 W, both with respect to the launched pump power. The laser efficiency is as high as 85% with respect to absorbed pump power, which is quite near the quantum limit of 93%. The small difference can be ascribed to the cavity losses including the small bending loss at the signal wavelength. This result is comparable to the experimental result obtained with the so-called jacketed air clad (JAC) Yb^{3+}-doped fibre in reference [35]. There, the slope efficiency was 65% and the threshold pump power was 0.3 W, with respect to the absorbed pump power.

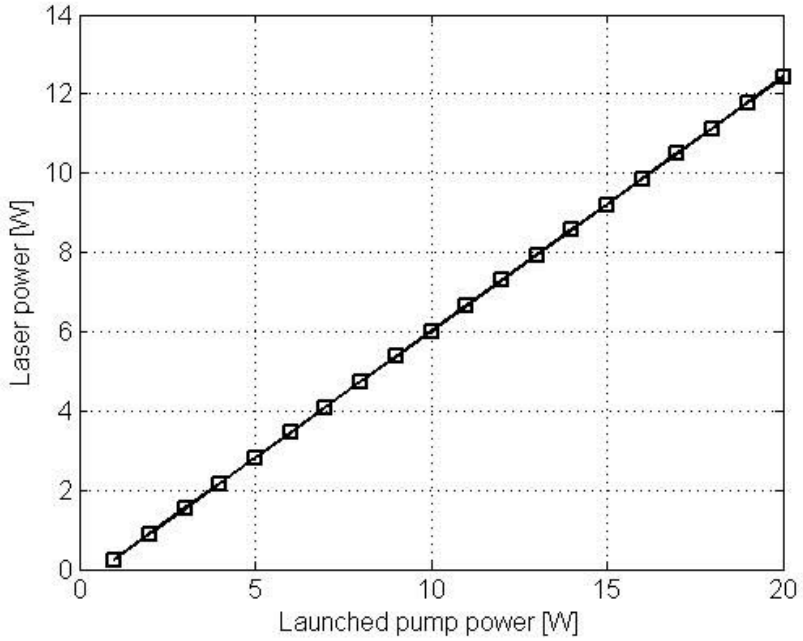

Figure 5.10. The power characteristics of the fibre laser at 0.98 μm, from numerical simulations.

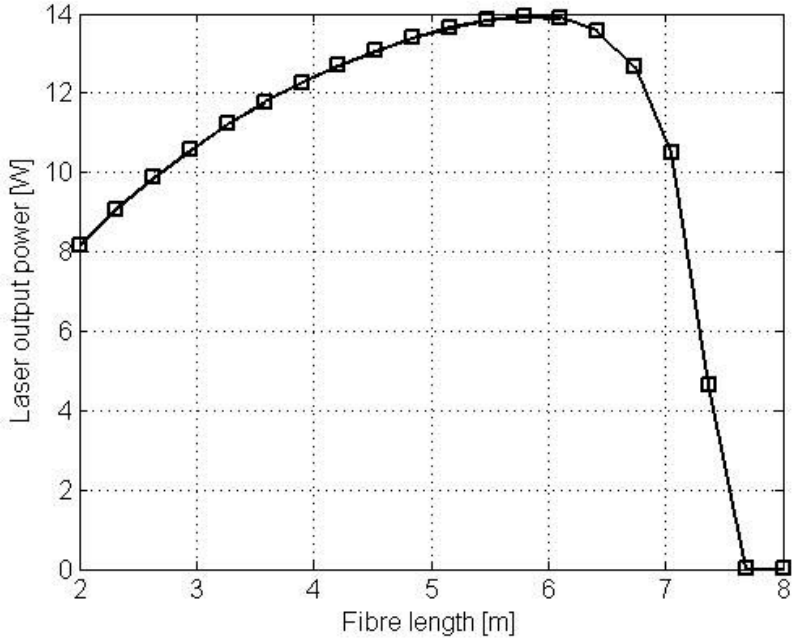

Figure 5.11. The 0.98 μm laser output power dependence on the fibre length, according to simulations.

Next, the effect of the fibre length is demonstrated with a fixed launched pump power of 20 W. With a fibre that is too long, the signal will suffer signal reabsorption due to an insufficient pump intensity at the feedback end. On the other hand, if the fibre length is too short, the pump is not sufficiently absorbed. Therefore, in a two-level fibre laser system with ground-state absorption, the fibre length plays an important role in terms of the laser performance. Figure 5.11 shows the result. The fibre length is varied from 2 m to 8 m. The dependence of the signal output power against fibre length is very strong. Note the fast drop of the signal power with fibre lengths longer than 6.5 m. At 7.6 m fibre length, the signal is almost entirely reabsorbed. The maximum signal output is 14 W at fibre length of 5.8 m. Then, the slope efficiency is 74% and the threshold is 1 W, both with respect to the launched pump power. Note that in this case the 'hot cavity' absorbed pump power is 17.4 W out of 20 W launched pump power.

In summary, the numerical simulation results show that one can achieve a very efficient Yb^{3+}-doped hollow fibre laser operating at 0.98 μm with proper optimisation of all parameters. The beam quality of the output 0.98 μm signal is expected to be poor with a ring shape. However, by collapsing the air hole, one can achieve a relatively good beam quality, which will be addressed in the experimental result.

Figure 5.12. Cross-sectional view of the fabricated depressed-clad hollow fibre F645-LF239. Image of transmitted white light.

5.3. Experimental results

In this section, experimental results on a Yb^{3+}-doped depressed-clad hollow fibre laser operating at 0.98 µm are presented. The results were published in reference [78]. They may be compared with the results of the JAC Yb^{3+}-doped fibre laser at 0.98 µm which our team at the ORC demonstrated earlier [35, 41, 43]. Especially in reference [41], an amplified single-mode 0.98 µm laser source with 4.3 W of output power was presented with 11 W launched power. The JAC Yb^{3+}-doped fibre laser is limited by the available power of pump sources with high beam quality [35]. The newly fabricated Yb^{3+}-doped depressed-clad hollow fibre overcomes this limitation by adopting a large cladding diameter of 120 µm. The inner cladding area is more than an order of magnitude larger than that of the JAC fibre of reference [35]. This is a huge advantage in terms of power scaling and cost since one can now utilise pump sources with higher power and lower brightness.

A Yb^{3+}-doped depressed-clad hollow fibre (F645-LF239) was fabricated using the MCVD and solution doping technique. At the final collapsing stage, a hole of 0.5 mm

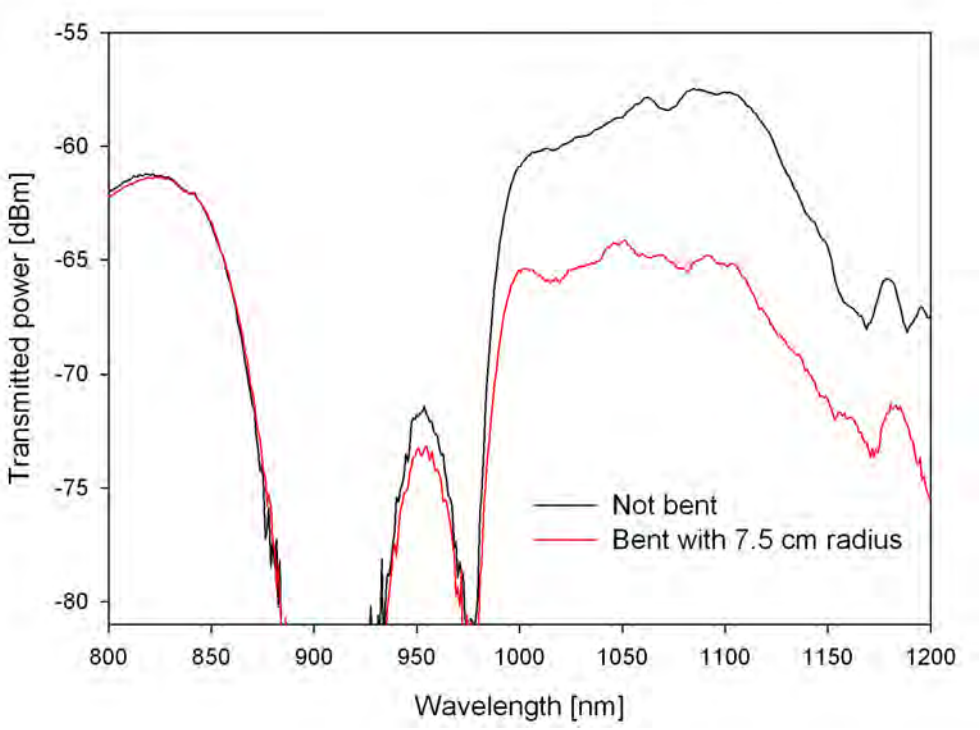

Figure 5.13. Transmission spectrum of the fabricated Yb-doped depressed-clad hollow fibre when straight and when bent to 15 cm diameter. (OSA resolution 1 nm)

diameter was left in the preform which was then milled to a double D-shape to improve the pump absorption by breaking the circular symmetry. The preform was drawn to a fibre with a 120 μm diameter pure-silica inner cladding and coated with a low-index polymer outer cladding. This provided a nominal inner cladding NA of 0.48. Figure 5.12 shows the cross-section of the fabricated fibre. In this picture, of transmitted light, bright parts indicate high-index regions. The parameters of the fabricated depressed-clad hollow fibre were a_{air} = 8 μm, a_{co} = 13.7 μm (core width of 5.7 μm), a_{dp} = 24.7 μm (depressed index region width of 11 μm) and NA_{co} = 0.07, NA_{dp} = - 0.06. This gives the fundamental mode cut-off wavelength at 1050 nm. Unfortunately, the fabricated fibre had a longer cut-off wavelength than designed due to limited control in the fabrication process.

The core transmission loss of the fabricated fibre is measured using a 30 cm sample. The result is shown in figure 5.13. Both ends of the doped fibre were spliced to single mode fibres in order to remove the guided cladding modes. A white light source is used for the measurement. In figure 5.13, the bending loss at 1030 nm is 16 dB/m using a moderate bending radius of 7.5 cm. Hence, although the fundamental mode at 1030 nm is guided in the fibre core, an appropriate bending may be induced to suppress the amplified spontaneous emission at 1030 nm. In the figure, huge absorption around 915 nm and 980 nm are shown. The effect of bending on 980 nm signal was not shown clearly in the figure, due to the limited spectral power density of the available white light source (tungsten filament lamp) and the dynamic range of the optical spectrum analyzer. However, 950 nm light suffered from bending loss. This suggests that the bending loss at 980 nm may be undesirably large.

The laser configuration is shown in figure 5.14. The fibre was pumped by two equivalent 915 nm multimode laser diodes, each of which deliver the pump power through a 200 μm diameter, 0.2 NA multimode fibre. A maximum power of 19 W could be launched into the fibre. A laser cavity was formed between a perpendicularly cleaved end facet (4% Fresnel reflection) and a 100% reflective dichroic mirror. The dichroic mirror is highly reflective at 980 nm and highly transmissive at 1030 nm and above, up to 1200 nm. However, since the dichroic mirror is not perfect, it was expected that some fraction of light at longer wavelengths (~1030 nm) may have been reflected and coupled back to the fibre. The fibre length used was 6 m long and the operating 'hot-cavity' single-pass pump absorption was measured to 10 dB.

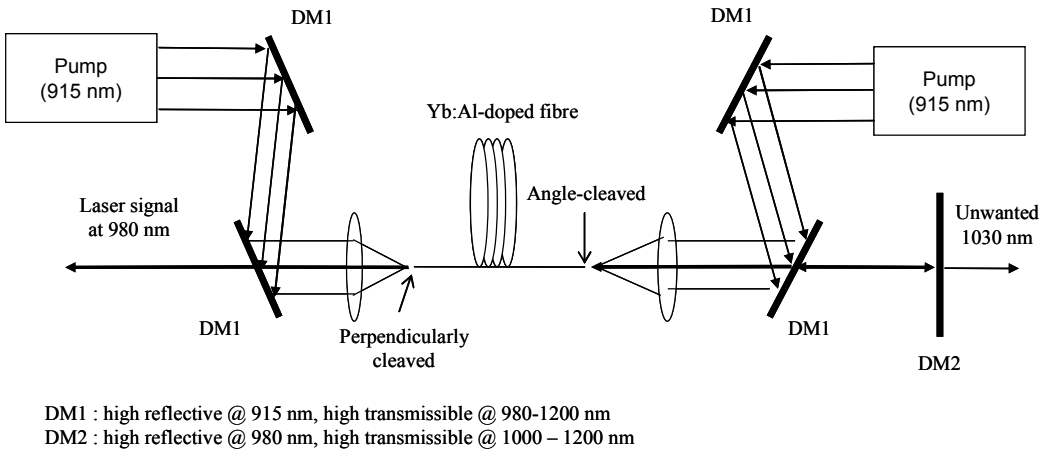

Figure 5.14. Experimental setup for 0.98 μm Yb-doped depressed-clad hollow fibre laser

When the fibre was less bent with a relatively large bending radius, lasing at 1030 nm was observed, even with wavelength-selective feedback (dichroic mirror reflection and angled cleave). The fibre had to be bent more sharply to suppress such 1030 nm lasing through the bending loss, which however caused a significant amount of bending loss at 980 nm as well. Figure 5.15 shows a typical optical spectrum of the 980 nm laser signal. It shows an efficient suppression of the competing 1030 nm emission thanks to the waveguide design and the bending loss suppression technique. Since the feedback dichroic mirror (DM2) is broadband at 980 nm, the laser wavelength is not well defined. The small inset in figure 5.15 shows that the laser linewidth is quite broad. However, one can easily replace the dichroic mirror with a bulk grating to achieve a well established laser wavelength.

Figure 5.15 also shows the laser power characteristics. Here, the maximum output power was 3.1 W with 34% slope efficiency with respect to the launched pump power. The threshold was 9.2 W of launched pump power. The result does not agree with the predictions of the numerical simulation. However, as is mentioned above, the induced loss at 980 nm can explain this relatively poor result. The laser simulation with a 2.8 dB/m bending loss at 980 nm is similar to the obtained experimental result. Therefore, it is postulated that such a high threshold pump power and low slope efficiency is mostly due to the 980 nm bending loss inevitably induced during suppression of the unwanted 1030 nm lasing. However, if the fibre length could have been shortened and a better suppression of the 1030 nm radiation in the dichroic mirror feedback adopted, a higher slope efficiency would have been achieved.

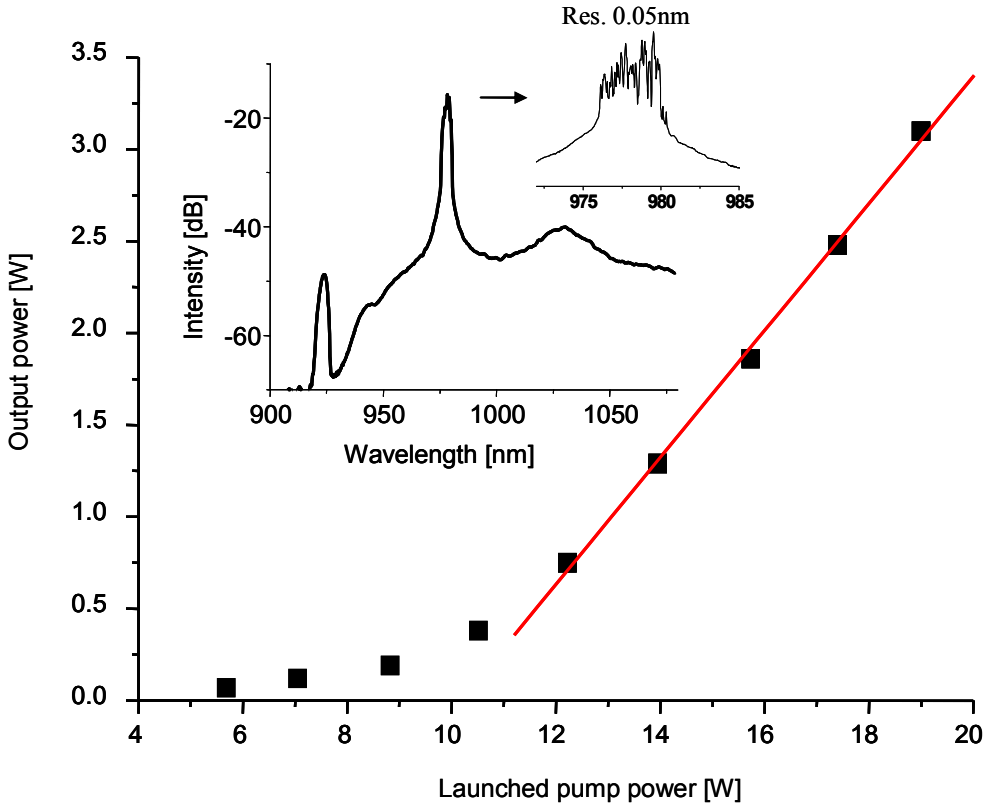

Figure 5.15. The 0.98 μm laser power characteristics. Inset shows a typical spectrum of the laser (broadband graph resolution 1 nm, narrow band graph resolution 0.05 nm).

The laser output beam was ring-shaped as is predicted by the theory in the previous section. However, when the fibre end was collapsed through heating with an electrical arc (i.e., the air hole is collapsed so that the refractive index profile becomes that of a W-type fibre), the measured beam had an M^2-value of 1.09, which represents a diffraction limited single-mode beam. The output power difference between the uncollapsed ring-shaped beam and the collapsed Gaussian beam was negligible. Therefore, it was experimentally shown that one can obtain a very good beam quality from a depressed-clad hollow optical fibre by collapsing the end of the fibre.

In summary, a Yb^{3+}-doped depressed-clad hollow fibre laser operating at 0.98 μm has been demonstrated experimentally. The experimental result did not agree with the predicted numerical simulation. The primary reason for this is the bending loss at the 0.98 μm wavelength, which was inevitably induced during the suppression of the unwanted 1.03 μm lasing. It is noted that such an experimental result was obtained because the fabricated fibre dimensions were different from the designed fibre dimensions. With better control of the fabrication process, significant bending loss at

the signal wavelength may be avoided, as is predicted from the numerical simulation results.

5.4. Summary

A depressed-clad hollow fibre was investigated, focussed on the realisation of an Yb^{3+}-doped fibre laser operating at 0.98 μm. The theory and numerical simulation predicted that efficient operation of Yb^{3+}-doped fibre laser at 0.98 μm would be achieved by efficiently suppressing the competing longer-wavelength emission (~1030 nm). The advantage of the depressed-clad hollow fibre over the W-type fibre in chapter 4 is sharper fundamental mode cut-off characteristics and a large core area.

An experimental result of a Yb^{3+}-doped depressed-clad hollow fibre laser operating at 0.98 μm was also presented. The experimental result is in contrast to the theoretical predictions. The desired design was not matched due to the fabrication uncertainties, which led to an unwanted bending loss at 0.98 μm. Consequently, the slope efficiency was relatively low (34%) and the threshold pump power was large (9.2 W), both with respect to the launched pump power. Nevertheless, the depressed-clad hollow fibre allows larger pump power with low brightness due to the large cladding size, which is an advantage over other approaches such as the previously reported JAC fibre structure [35].

Chapter 6. Modified W-type fibres for long-pass filters

In this chapter, a fibre waveguide design which enhances the gain at longer wavelengths while suppressing the emission at the shorter wavelength is presented. Photonic crystal fibres with a depressed core index was devised already for long wavelength guiding [7]. However, photonic crystal fibres have intrinsic loss, which may degrade the fibre laser performance. Furthermore, crucially, cladding-pumping such micro-structured fibres is difficult. Therefore, I present an alternative idea for long wavelength guiding waveguide structures in solid silica fibres (i.e., not microstructured fibres), by modifying the refractive index of the core structure. Chapter 2 described that, in a multilayered refractive index profile, the mode field shape depends on the difference between the refractive index of each layer and the effective refractive index of that mode. The mode is considered as 'confined in a certain layer', if the refractive index of that layer is larger than the effective refractive index of the mode. Using this property, one can design a long pass filter either in active or passive devices. In this chapter, a waveguide design for long-pass filters is described. Following this I present a numerical simulation of Nd^{3+}-doped fibre amplifier and laser operating at 1.3 μm.

6.1. Fibre design for long-pass filters

In simple step index fibres, the effective refractive index at a shorter wavelength is always higher than that at a longer wavelength for a particular mode. Therefore, the mode fields of shorter wavelengths tend to be more strongly confined in a higher refractive index layer than those of longer wavelengths. The key idea of the long-pass filters I investigate here is to confine the fields of the shorter wavelength, in a certain layer of a multi-layered refractive index structure, while those of the longer

wavelength extend into other, desired, layers. This is possible by inserting an extra layer into a desired position for the longer wavelength, with refractive index lower than the effective refractive index of the shorter wavelength, but higher than that of the longer wavelength.

For effective wavelength control in RE-doped fibres, the shorter wavelength and the longer wavelength do not have to be completely separated, and an undesired wavelength does not have to be completely rejected by the waveguiding structure. It may be enough to keep the net gain of an undesired wavelength sufficiently low. The overlap between the doped region and the signal fields plays an important role in this case. For instance, in a step index fibre, the field of a longer wavelength penetrates further into the cladding region than the (corresponding) field of a shorter wavelength. By utilising ring-doping, one can obtain a larger overlap factor for the longer wavelength than for the shorter wavelength. Using this technique, the competing amplified spontaneous emission at shorter wavelengths, if any, may be significantly suppressed so that the amplification of the desired longer wavelength may work efficiently. Bjarklev *et al.* theoretically demonstrated that 9 dB higher (small signal)

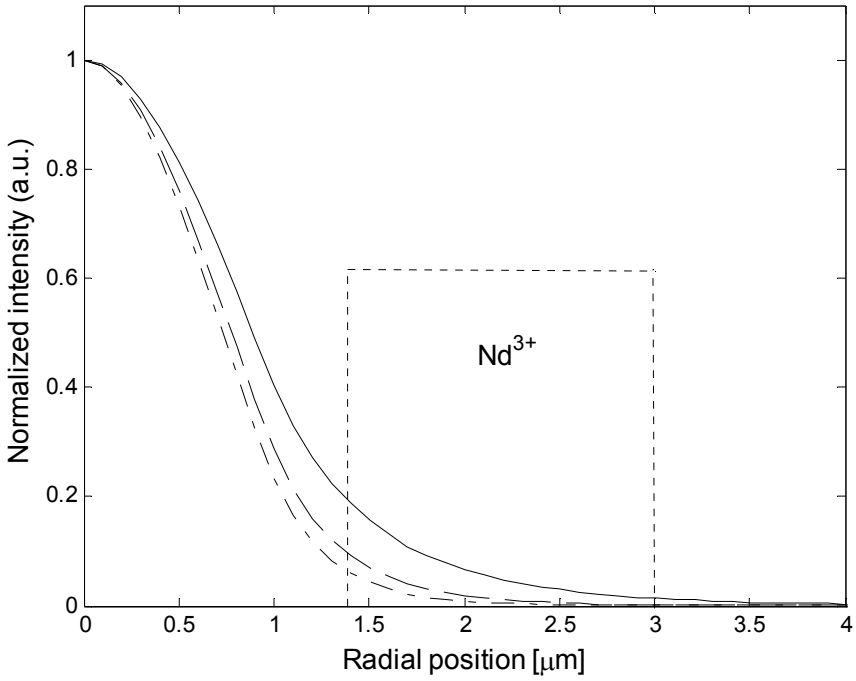

Figure 6.1. The mode fields of a step index fibre at 0.92 (dash-dotted), 1.05 (dashed), and 1.34 μm (solid line). The dotted line represents the doped region.

gain is obtainable at 1.3 μm from a step-index Nd^{3+}-doped ZBLAN fibre using the ring doping technique, compared to the conventional core-doped fibres [8]. In this case ring-doping reduces the doped region confinement factor (i.e., overlap) of competing unwanted 1.05 μm emission relative to the overlap at 1.3 μm.

6.1.1. Long-pass filters involving active ions

The results in [8] are based on a step index fibre with a 0.3 NA core index and a 2 μm core diameter. When the fibre was ring doped with the inner and the outer radius of 1.4 μm and 3 μm respectively, the amplified spontaneous emission at 1.05 μm could be efficiently suppressed. The signal at 1.34 μm was amplified with a net gain of 13.3 dB. By contrast, a core-doped fibre with the same dimension showed only 6 dB gain due to the strong amplified spontaneous emission at 1.05 μm, which saturated the amplifier. The fibre was core-pumped. In this theoretical work, the pump at 0.795 μm was assumed to have excited only the higher-order LP_{11} mode in order to maximise the overlap between the pump and the doped region. Figure 6.1 shows the LP_{01} mode field intensities for different Nd emission wavelengths. Regarding the pump modes at 0.795 μm, pumping in the LP_{01} mode enhanced the signal gain at 1.34 μm by 7 dB while LP_{11} mode pumping enhanced it by 9 dB, both compared to conventional central core-doping. The useable outer diameter of the doped ring was limited by the relatively strong confinement of the pump. Even with LP_{11} mode pumping, Nd^{3+}-doping beyond a radius of 3 μm radius does not enhance the signal gain significantly. The additional enhancement in gain is only 3% when the entire cladding is doped. (Note here that Nd is a four-level system, without reabsorption, at 1.05 μm or 1.34 μm.) While the relative differences in the modal intensity increases with distance from the core, a pump beam guided by the core is only able to excite ions close to the core. Effectively, the pump distribution imposes a constraint on the fibre design. However, when cladding-pumping, one can consider a uniform pump power distribution (e.g. when using a D-shaped cladding [67]). Note that the (doped) core confinement factor of a mode is defined as

$$\Gamma_\lambda = \frac{\int_0^{2\pi}\int_0^{\infty} i_\lambda(r,\phi)\,\bar{N}(r,\phi)\,r\,dr\,d\phi}{\int_0^{2\pi}\int_0^{\infty} i_\lambda(r,\phi)\,r\,dr\,d\phi}, \tag{6.1}$$

where i_λ represents the signal intensity distribution at wavelength λ, r,ϕ the radial position and angle in the transverse plane, and $\bar{N}$ the normalised dopant distribution such that $\bar{N}=0$ in the undoped region and $\bar{N}=1$ in the most highly doped region. Using equation (6.1), the core confinement factors $\Gamma_{0.92\,\mu m}$, $\Gamma_{1.05\,\mu m}$, and $\Gamma_{1.34\,\mu m}$ of the LP_{01} mode from the fibre design in reference [8] are 8.2%, 13.5%, and 27.3%, respectively.

For a W-type refractive index structure, the difference in overlap factors between different wavelengths can be much larger. One of the advantages of the W-type structure is that the depressed region significantly enhances the confinement of the shorter wavelength to the centre of the core (i.e., the raised-index part). Conversely, it makes the confinement factor (to the doped region) of short-wavelength modes much smaller when the fibre is ring-doped. In addition, by placing an extra layer outside the centre core with a carefully chosen refractive index, it is possible to enhance $\Gamma_{1.34\,\mu m}$ while $\Gamma_{1.05\,\mu m}$ stays unchanged. The refractive index of the extra ring layer should lie between the effective refractive indices of the modes at 1.05 μm and 1.34 μm so that the mode at 1.34 μm may well overlap this extra ring layer while that at 1.05 μm does not overlap. The mode field at a certain layer i with a refractive index of n_i is expressed as

$$E_{lp}(r,\theta)=\left\{A_i Z_l\left(u_i^{lp} r\right)+B_i \bar{Z}_l\left(u_i^{lp} r\right)\right\}\cos(l\theta), \tag{6.2}$$

where l, p represent the modal index for mode LP_{lp}, when the linearly polarised mode approximation is used, and $u_i^{lp}=k\sqrt{\left|n_i^2-\left(n_{eff}^{lp}\right)^2\right|}$ where n_{eff}^{lp} represents the effective refractive index of the mode. In equation (6.2), Z_l and $\bar{Z}_l$ are Bessel functions. These have a different form depending on n_{eff}^{lp}, such as

$$\left[Z_l\left(u_i^{lp} r\right)\quad \bar{Z}_l\left(u_i^{lp} r\right)\right]=\begin{cases}\left[J_l\left(u_i^{lp} r\right)\quad Y_l\left(u_i^{lp} r\right)\right], & for\ \ n_i > n_{eff}^{lp},\\ \left[I_l\left(u_i^{lp} r\right)\quad K_l\left(u_i^{lp} r\right)\right], & for\ \ n_i \le n_{eff}^{lp}.\end{cases} \tag{6.3}$$

From equation (6.2) and (6.3), it is apparent that the fields are 'confined' (Bessel J and Y functions, oscillatory) in layer i if $n_i > n_{eff}^{lp}$ and 'die away' (Bessel I and K functions, exponential-like decay), otherwise. The degree of confinement or decay is a

strong function of u_i^{lp} such that a larger u_i^{lp} indicates a stronger confinement or faster decay. Therefore, for a strong confinement or fast decay one needs a large difference between the refractive index n_i of layer i and the effective index of the mode (n_{eff}^{lp}). The depressed-index region of a W-type fibre makes the mode fields decay rapidly due to the large difference $n_{eff}^{lp} - n_i$ where $n_{eff}^{lp} > n_{cl} > n_i$. By contrast, the smaller difference $n_{eff}^{lp} - n_{cl}$ in a conventional step index fibre leads to a smaller decay. (Here, n_{cl} represents the cladding refractive index.)

As is explained in chapter 4, the rapid decrease of the effective refractive index with increasing signal wavelength is possible when the difference between the maximum and the minimum of n_i is large. Therefore, in order to have a strong confinement for signals at short wavelengths in the undoped centre, it is desirable to use the highest and the lowest value of refractive index, which the fabrication technique permits, for the undoped core and the depressed region, respectively. When designing the W-type refractive index profile, one should also be careful so that only a single mode is supported for all 0.92, 1.05, and 1.34 μm signals. Otherwise, the higher mode at 0.92 and/or 1.05 μm may overlap the ring doped region more strongly (for example, LP_{02} or LP_{11} mode) than the LP_{01} mode of 1.34 μm. (Note that the gain at 0.92 μm may suffer from ground-state absorption. Therefore, if the fibre length is sufficiently long, a stronger obstacle to the gain at 1.3 μm may become amplified

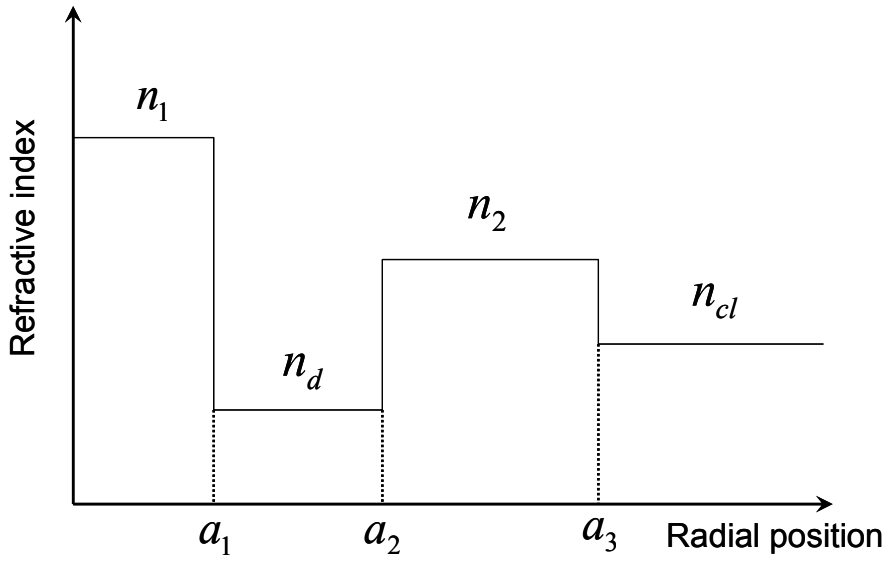

Figure 6.2. Refractive index profile for a W-type fibre with a raised ring.

spontaneous emission at 1.05 μm rather than at 0.92 μm.) As it comes to the LP_{01}-modes, the difference of the effective refractive indices between 1.05 and 1.34 μm should be large enough so that the confinement of 1.34 μm mode fields in an extra high index layer may be maximised.

Bearing all these points in mind, I suggest a design procedure of W-type refractive index profile with an outer raised ring as follows. The refractive index diagram with design parameters is shown in figure 6.2. First, n_1 and n_2 are fixed with equivalent NAs of 0.3 and -0.2, which probably matches the highest and the lowest refractive index which ORC MCVD fabrication technique can provide.

In this analysis, the material dispersion is not considered since the analysis for the designed waveguide is based on the weakly guiding assumption where the refractive indices along all the layers are very similar. For instance, the Sellmeier equation for a fused silica fibre has the refractive index difference of 0.3% in absolute value between 0.9 μm and 1.4 μm [79]. In this case, the material dispersion effect on the NA_{eff} of the mode (defined by $\mathrm{NA}_{\mathrm{eff}} = \mathrm{sgn}\left(n_{eff} - n_i\right) \cdot \sqrt{\left|n_{eff}^2 - n_i^2\right|}$ in a certain layer of refractive index n_i) should be expected to be negligible. In fact, when the Sellmeier equation in [79] is used, the NA_{eff} of the fibre designs in this chapter differs by well below 0.1% from the case of a wavelength-independent refractive index. This negligible difference does not have a serious impact on the confinement nor on the laser performance. The important factors are NA and NA_{eff} rather than the absolute value of refractive indices. The NA and NA_{eff} do not strongly depend on the material dispersion and really decide the modal shape.

Without a raised ring layer ($n_2 = n_{cl}$), the values of a_1 and a_2 ensuring single mode operations for both 0.92 and 1.05 μm are a_1 = 1 μm and a_2 = 2 μm. In this case, the effective refractive index of the LP_{01} mode at 1.05 μm is 1.4625 (when the cladding refractive index is 1.457). The fundamental mode at 1.34 μm is not guided in this case. However, by inserting an extra layer of refractive index n_2 = 1.4625 and varying a_3, one can make the fibre able to support the LP_{01} mode at 1.34 μm. Since the modes at 0.92 and 1.05 μm are now reasonably well confined in the n_1 layer, inserting an extra layer of n_2 =1.4625 does not change the effective refractive indices of 0.92 and 1.05μm greatly. One should be careful in deciding a_3 since if a_3 becomes too large, the LP_{11} and/or LP_{02} at 0.92 and/or 1.05 μm may be guided. The maximum

value of $a_3 - a_2$, avoiding those higher modes at the shorter wavelengths, is 3.4 μm. Thus, all fibre design parameters are now fixed. In this case, the effective refractive indices of the LP_{01} mode at 0.92, 1.05, and 1.34 μm are 1.4664, 1.4626, and 1.4577. (Note that the extra layer does not change much the effective refractive index of the LP_{01}-mode at 1.05 μm).

As seen from equations (6.2) and (6.3), the mode fields of shorter wavelength are 'confined' only in the centre core since the effective refractive indices of those modes are above other layers while the mode fields of 1.34 μm are 'confined' in both the centre core and the outer ring. The mode intensities for the different wavelengths are shown in figure 6.3. Now one has to decide the position of the doped ring. Although the position of the doped region coincides with the high index layer in the conventional rare-earth doped fibres, it is still possible to dope the other regions. Let me denote the inner radius of the doped ring as d_1, and the outer radius as d_2. d_2 can be arbitrarily large up to the cladding radius in theory. However, in practice, the

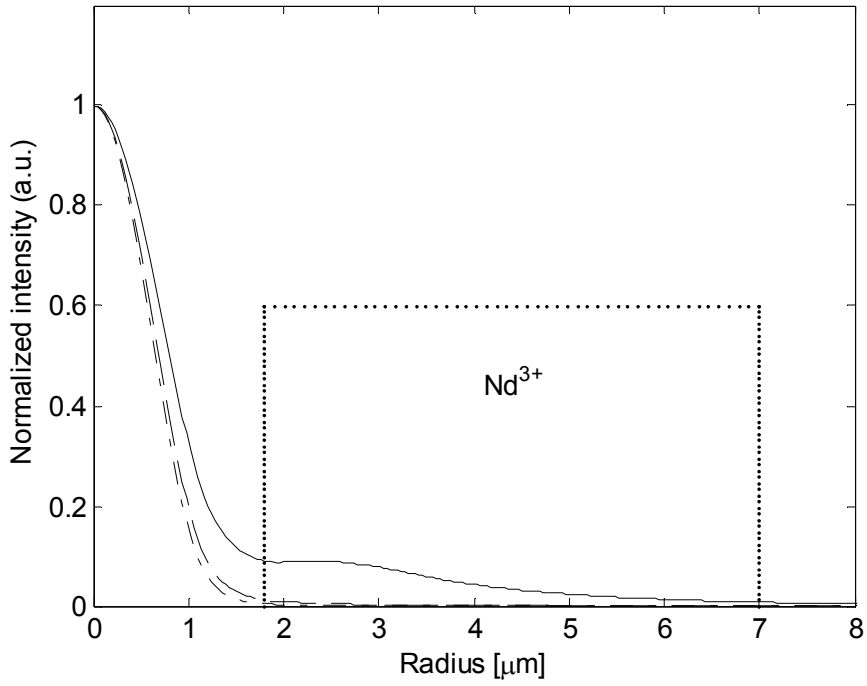

Figure 6.3. Mode intensities of the W-type fibre with a raised–index outer ring. Dashed-dot line for LP_{01} mode at 0.92 μm, dashed line for LP_{01} mode at 1.05 μm, and solid line for LP_{01} mode at 1.34 μm. The dotted line represents the doped area.

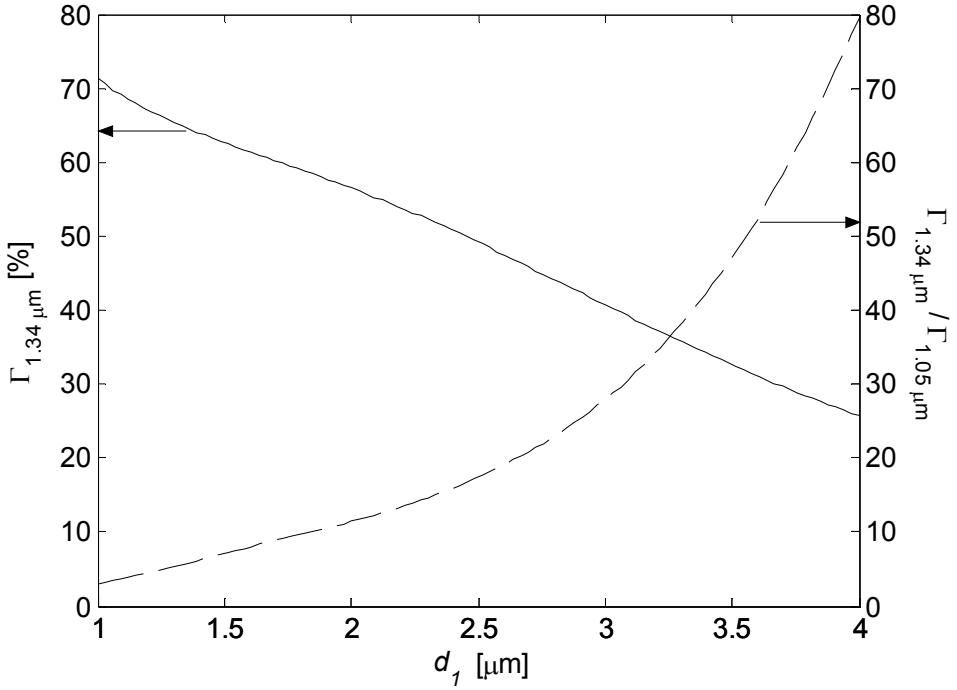

Figure 6.4. The overlap factor $\Gamma_{1.34\,\mu m}$ (solid line) as a function of d_1. The dashed line represents $\Gamma_{1.34\,\mu m} / \Gamma_{1.05\,\mu m}$.

fabrication capability limits d_2. When we limit d_2 as 8 μm (in fact, the difference in overlap factor between $d_2 = 7$ μm and $d_2 = R_{cl}$ where R_{cl} is the cladding radius is negligible, with ~4% difference in most cases), one can calculate the overlap factors as a function of d_1, as shown in figure 6.4. For instance, if d_1 =1.8 μm, the confinement factors $\Gamma_{1.05\,\mu m}$ and $\Gamma_{1.34\,\mu m}$ in the doped region are 6%, and 60%, respectively. Thus, $\Gamma_{1.34\,\mu m}$ is (nearly) 10 times larger than $\Gamma_{1.05\,\mu m}$. At the same time, $\Gamma_{1.34\,\mu m}$ becomes reasonably large. From the graph in figure 6.4, one can choose d_1 to match the desired ratio between the overlap factors.

One should be always careful about the bending loss of the designed mode field. If the bending loss is too high even with a large bending radius, the designed fibre may not work efficiently, losing signal power through radiation, due to inevitable bending. (One must always bend the fibre in practice with fibres of normal length, and micro-bending is an issue, too.) According to [77], the bending loss of a fibre with an arbitrary index profile is expressed as

$$\alpha_B = \frac{\sqrt{\pi}}{2s}\frac{A_e^2}{P}\frac{a\exp\left(\frac{-4\Delta w^3}{3av^2}R\right)}{w\left(\frac{wR}{a}+\frac{v^2}{2\Delta w}\right)^{1/2}}, \tag{6.4}$$

where s=2 for l=0 and s=1 for other modes where l represents the azimuthal modal number, a is the core radius (the radial position of the last refractive index layer, just before the cladding starts), and Δ is the refractive index difference between the maximum refractive index n_m among layers and n_{cl}. In addition, $w = ak\sqrt{\left(n_{eff}^{lp}\right)^2 - n_{cl}^2}$ where k is the wave number, $v = ak\sqrt{n_m^2 - n_{cl}^2}$ is the normalised frequency, and R is the bending radius. The fraction A_e^2 / P represents the normalised fraction of power in the cladding to the total signal power. It can be evaluated as

$$\frac{A_e^2}{P} = \frac{P_{clad}}{P}\frac{1}{a^2\left\{K_{l-1}(w)K_{l+1}(w) - K_l(w)^2\right\}}, \tag{6.5}$$

where P_{clad} and P represent the power in the cladding and the total power,

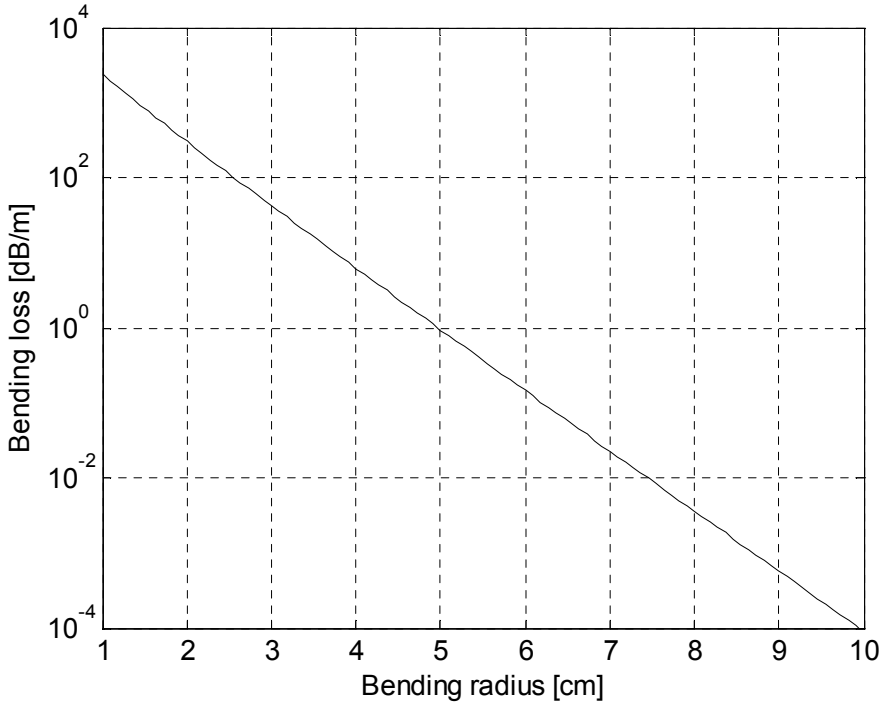

Figure 6.5. The bending loss of LP_{01} mode at 1.34 μm of the designed W-type fibre with a raised ring.

respectively. By calculating equations (6.4) and (6.5), one can predict the bending loss.

Figure 6.5 shows the bending loss of the LP_{01} mode at 1.34 μm as a function of bending radius. The bend-loss coefficient decays almost exponentially with increasing bending radius. At 5 cm bending radius, the bending loss is 1 dB/m and the curve passes the bending loss of 1 dB/km at a bending radius of 8.6 cm. Thus, this fibre is relatively sensitive to bending at 1.34 μm, primarily because the effective index is quite close to the cladding index. Nevertheless, for a sufficiently large bending radius (> 6 cm), bending loss is moderate.

Another important feature one must consider before fabricating such a designed fibre is the output beam quality, i.e. the expected M^2 value of a free-space output beam. (Splice loss to more conventional fibre, e.g., step-index, is another important parameter.) It can be calculated as a Fresnel diffraction integration as in appendix B. The calculated M^2 value is 1.06, which may well be regarded as diffraction limited beam quality.

6.1.2. Long-pass filter in passive fibres

In the previous section, a fibre design which amplifies long wavelength more efficiently than short wavelength was presented. However, this design works only with an amplification process since it relies on differences in gain induced by the differences in the overlap factor between the doped region and the signal fields. In this section, I will introduce another modified W-type fibre design, which has a lower

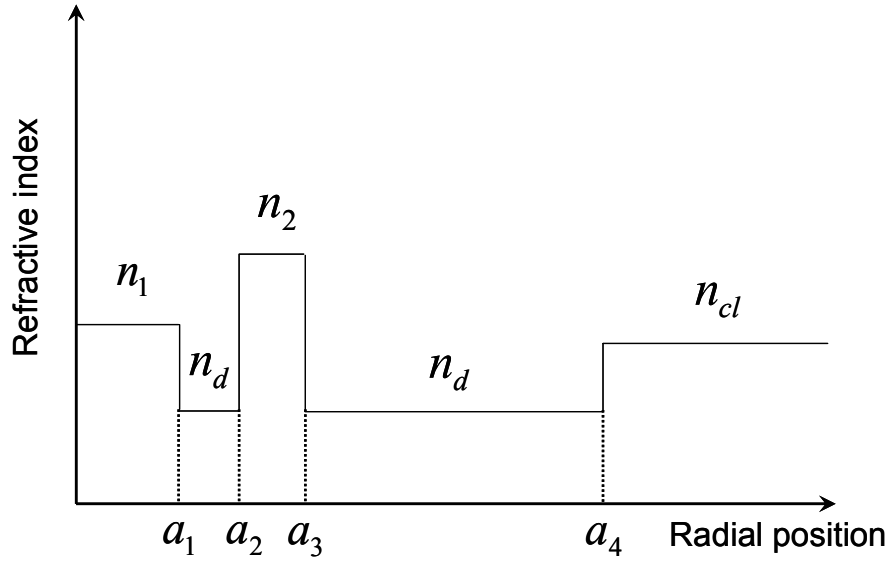

Figure 6.6. Refractive index profile for a passive long-pass filter.

indexed centre core and a higher indexed ring. The key idea now is to confine the shorter wavelength in the outer ring layer where the refractive index is the highest, while maintaining the longer wavelength in the centre core layer, which has a carefully chosen refractive index. This kind of device is useful in that it can be used as a passive filter. One can splice a conventional step-index fibre to this filter and preferentially extract the longer wavelength. Of course, one can also dope the fibre only in the centre core layer for realisation of active devices.

The design procedure is more complicated than for the previous Nd ring-doped fibre. Figure 6.6 shows the refractive index profile. For design simplicity and demonstration purpose, the highest index n_2, depressed index n_d, and the cladding index n_{cl} are fixed to the same values as in the previous design (1.4879, 1.434, and 1.457, respectively).

Although the positions a_2 and a_3 are important, those are fixed for simplicity as a_2=3 μm and a_3=4 μm. The outer depressed index region is intended to confine the fields inside (see equation (6.2) and (6.3)). By inserting this outer depressed region, the fields are better confined to the core region. The position a_4 is fixed to 9 μm for a good confinement. Similarly to the previous section, the refractive index of the centre layer (n_1) is set slightly smaller than or equal to the effective index of the LP_{01} mode (n_{eff}^{01}) at 1.05 μm, in order to avoid confining 1.05 μm in the centre. Although varying n_1 affects n_{eff}^{01} at 1.05 μm a little, the change turns out to be negligible. The value of n_{eff}^{01} at 1.05 μm is 1.4614 when $n_1 = n_{cl}$. Therefore, n_1 is fixed as 1.4614. The radius a_1 should be as large as possible to effectively confine the 1.34 μm signal in the n_1 layer. However, for too large a_1, the LP_{02} modes of shorter wavelengths become guided, and these are very well confined in the n_1 layer. The maximum value of a_1 is determined to be 2.3 μm, which just cuts off the LP_{02} modes of the shorter wavelengths i.e., down to 0.92 μm. Shorter wavelengths than that will have guided LP_{02}-modes. From this design, the modes at 0.92, 1.05, and 1.34 μm are solved with a mode solver for arbitrary refractive index profiles [73].

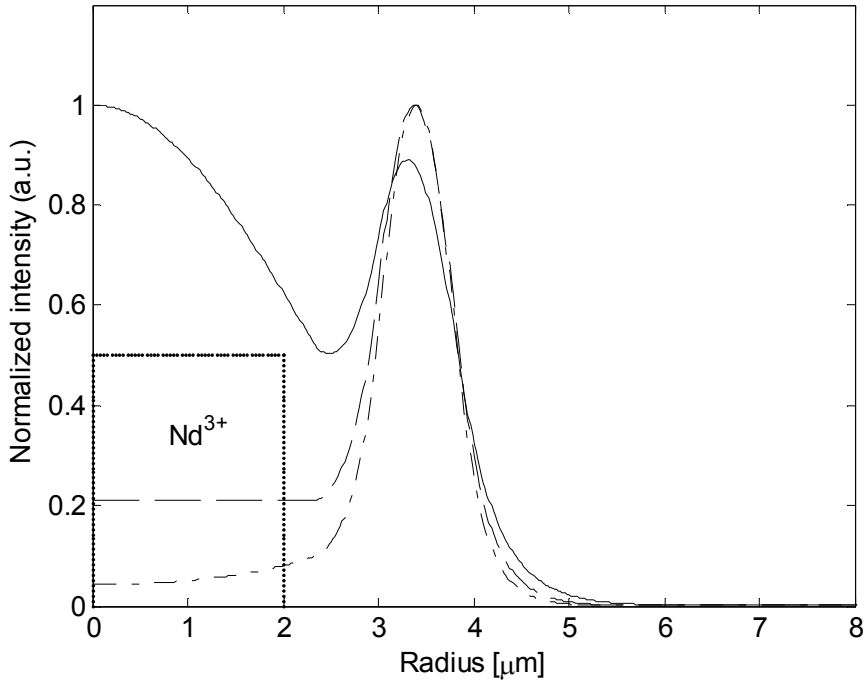

Figure 6.7. The mode intensities of the designed fibre. The LP_{01} modes for 1.34 μm (solid line), 1.05 μm (dashed line), and 0.92 μm (dash-dotted line) are shown. Also shown is the region that would be doped in case of an amplifier (dotted line).

Figure 6.7 shows the mode intensities for each wavelength. The fibre supported both LP_{01} and LP_{11} modes for 0.92 μm and 1.06 μm whereas only the LP_{01} mode is supported for 1.34 μm. However, the confinement of the LP_{11} mode is significantly less than of the LP_{01} mode, and hence, those LP_{11} modes are ignored. Interestingly, the LP_{01} mode of 1.34 μm stays in the centre region while those of shorter wavelengths mostly stay in the outer higher-index layer. Note that the intensity pattern of the LP_{01} mode at 1.05 μm is flat in the centre region since $n_{eff}^{01} - n_1$ is nearly zero. By positioning the dopant ions only into the centre region, as is depicted in figure 6.7, this fibre device can have larger $\Gamma_{1.34\,\mu m}$ than $\Gamma_{1.05\,\mu m}$ as with the previous design.

Figure 6.8 shows the doped region confinement factors as a function of the doping radius d_2. One weak point of this design is that firstly, the ratio $\Gamma_{1.34\,\mu m} / \Gamma_{1.05\,\mu m}$ cannot be large. The maximum value is only 3.3, compared to the (theoretically) unlimited maximum value of the previous design. In addition, the value $\Gamma_{1.34\,\mu m}$ barely reaches

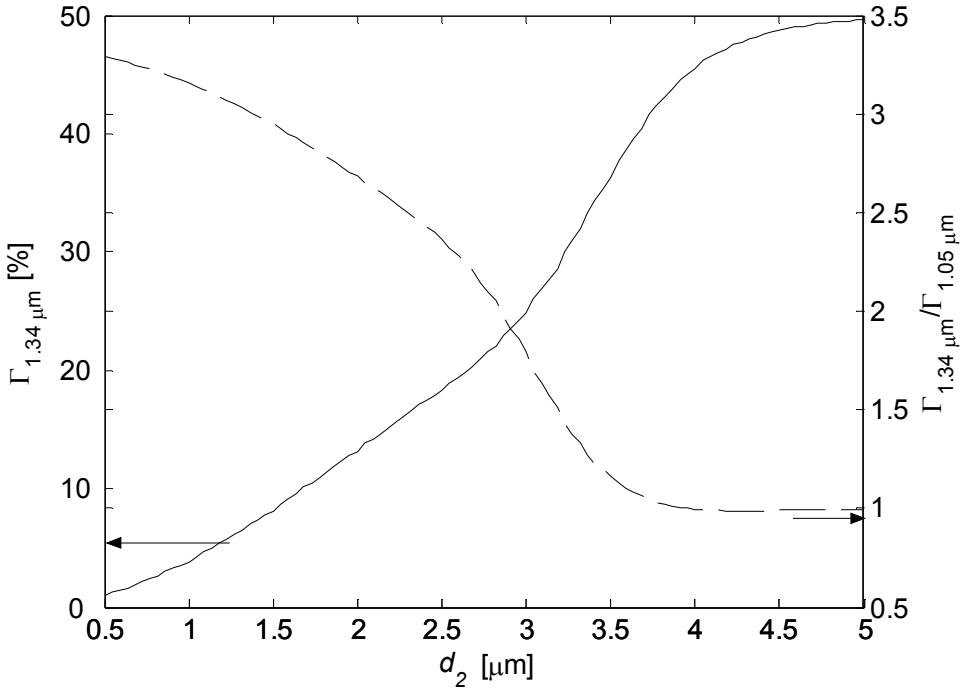

Figure 6.8. The doped region confinement factor $\Gamma_{1.34\ \mu m}$ along with the diameter of the doped region d_2 (solid line). The dashed line represents the ratio $\Gamma_{1.34\ \mu m} / \Gamma_{1.05\ \mu m}$.

50%, compared to 70% with the previous design. However, an overlap of 50% is fully adequate in most cases. If d_2 is 3.5 μm, the ratio $\Gamma_{1.34\,\mu m} / \Gamma_{1.05\,\mu m}$ nearly reaches 1, which means that the advantage of overlap factor vanishes. The attraction is that this design provides a centrally confined long-wavelength mode while the shorter wavelength modes are forced to stay in the outer ring.

Another favourable advantage of this design is the insensitivity to bending. Because the mode is essentially confined to the core region (including the outer raised ring), this design shows relatively strong bending insensitivity even for longer wavelengths, compared to the previous design. Figure 6.9 shows the results of bending loss calculations for the LP_{01} mode at 1.34 μm. The 1 dB/m crossing occurs at bending radius of only 2.4 cm. For larger radii, the bending loss decreases rapidly. The calculated M^2 value of the LP_{01} mode at 1.34 μm is 1.12, which is slightly larger than for the previous design (See appendix B). Nevertheless, this beam could still be considered diffraction-limited for most practical applications.

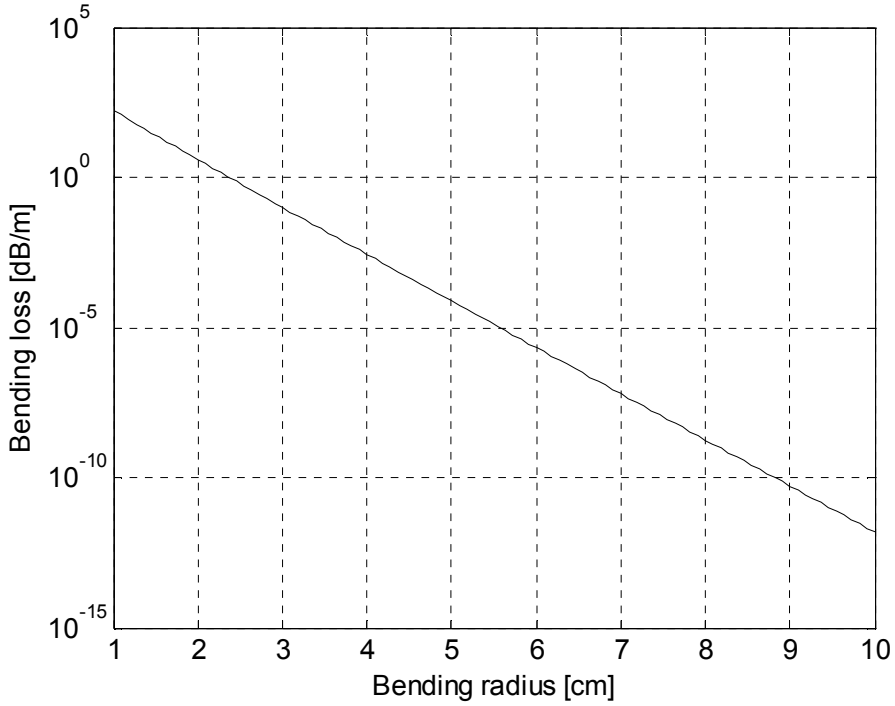

Figure 6.9. The bending loss of LP_{01} mode at 1.34 μm from designed fibre.

In summary, two different long-pass filter designs are introduced. The first one involves active ions discriminating the overlap factors between the long and the short wavelengths. In this design, the dopant ions are located carefully in an outside ring. Through this design one can obtain arbitrarily large ratios of the overlap factors between the short and the long wavelengths. The second one is rather for the passive fibre so that one can use this design as a passive wavelength filter. The disadvantage of this design is that the difference of overlap factors between the short and the long wavelength is much smaller than for the first one.

Nevertheless, the latter design shows a strong insensitivity against bending. The beam quality factor of the latter design ($M^2 = 1.12$) is slightly poorer than of the first one (1.06). Still, both may be still considered to be 'diffraction limited'.

6.2. Numerical simulation of 1.3 μm Nd^{3+}-doped fibre amplifier and laser

In this section, I will present results of numerical simulations of 1.3 μm amplifiers based on the new fibre designs. Nd^{3+}-doped fibre amplifiers at 1.3 μm are difficult to

realise due to a number of practical problems, as briefly reviewed in Chapter 1. There are three main issues to overcome to realise an efficient amplifier or laser. Firstly, the 1.3 μm signal suffers from ESA. The ESA is weaker at longer wavelengths (~1380 nm) than at shorter ones (~1320 nm). Secondly, if one wants to operate at longer wavelengths in order to avoid the strong ESA at shorter wavelengths, one will face the strong OH^- ion absorption line, which is centred at 1380 nm with a typical linewidth (FWHM) of ~20 nm. Thirdly, the stronger emission (hence, the amplified spontaneous emission) at 1050 nm and possibly also at 920 nm may hinder the efficient amplification at 1.3 μm by saturating the amplifier. A problem in this context is the small cross-sections at longer wavelengths (say, 1380 nm), which implies that a comparatively large number of Nd^{3+}-ions will have to be excited to reach sufficient gain. In the following sections, these three issues are reviewed and numerical simulation results for the amplifier and the laser are demonstrated, respectively.

6.2.1. Fundamental limitations of Nd^{3+}-doped fibre amplifier operating at 1.3 μm

The issue of ESA at 1.3 μm in Nd^{3+}-doped ions is identified as a serious one in many published articles. For example, Alcock *et al*. observed strong ESA at 1.3 μm in a Nd^{3+}-doped fibre [27]. Later, it was found that the amount of ESA strongly depends on the host material in silica fibres. Morkel *et al.* compared the ESA cross-sections of Nd, determined from measurements in aluminosilicate and germanosilicate fibre [80]. The aluminosilicate fibre shows a significantly smaller ESA cross-section than the germanosilicate fibre does (ratio approximately 2/3). Furthermore, the stimulated emission cross-section at 1.31 μm in silica fibres is much smaller than the ESA cross-section, hence, there is no gain at 1.31 μm. However, Morkel *et al*. observed the wavelength-dependence of the ESA cross-section so that the stimulated emission cross-section will exceed the ESA cross-section at ~1.4 μm. It suggests that silica Nd^{3+}-doped fibres can show a positive gain at the wavelength around 1.4 μm. Hakimi *et al.* demonstrated a 1.36 μm laser using a phosphosilicate fibre with 2 mW output power and 1% slope efficiency with respect to the absorbed pump power, when pumped at 752 nm [81]. The result was back-calculated to obtain the ESA cross-section at 1.36 μm. It was calculated to be 0.78 times the stimulated emission cross-section, which indicates that the phosphosilicate fibre has a (relatively) smaller ESA

cross-section than germanosilicate or aluminosilicate doped fibres, at the same wavelength.

Nd^{3+}-doped ZBLAN (fluorozirconate) fibre showed more favourable ESA characteristics in the 1.3 µm band. The peak stimulated emission cross-section around 1.3 µm wavelength region was measured to 0.8×10^{-20} cm^2 while the ESA cross-section peak was only 0.45×10^{-20} cm^2 [82]. It was the main reason why most of the significant efforts to develop 1.3 µm amplifiers were focused on ZBLAN fibres. Zemon *et al.* predicted 18 dB small signal gain at 1.34 µm when the amplified spontaneous emission at 1.05 µm was totally suppressed [82]. As a further illustration of the importance of 1.05 µm amplified spontaneous emission, the gain calculated by Zemon *et al*. dropped to 5 dB smaller when the amplified spontaneous emission at 1.05 µm was not suppressed.

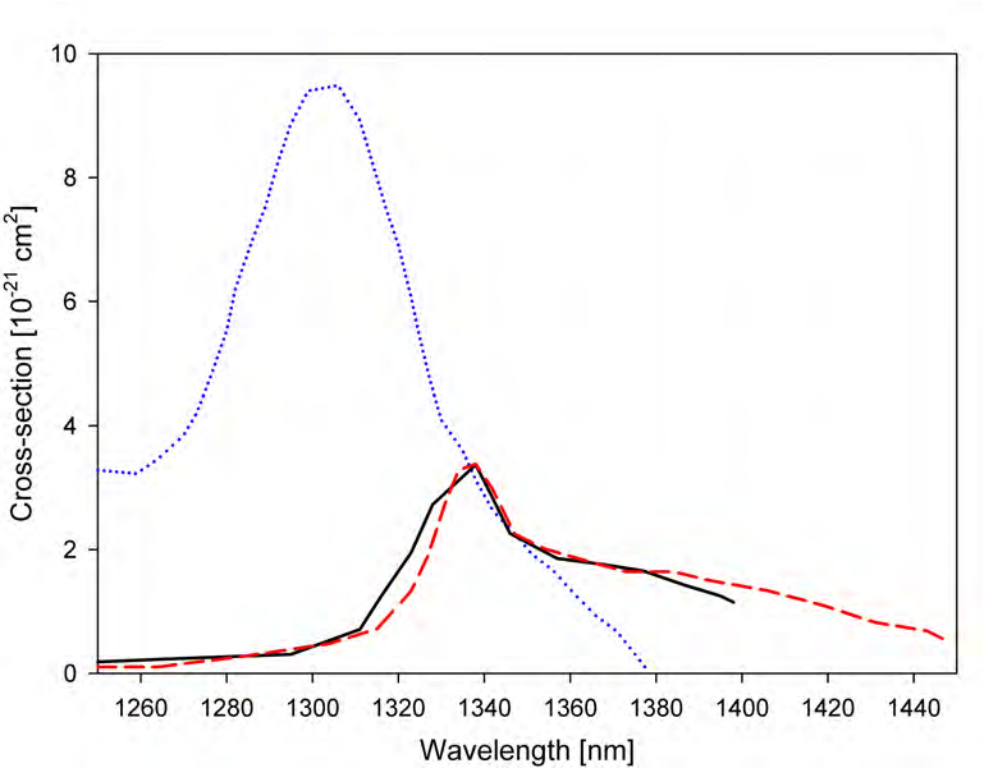

Figure 6.10. Cross-section spectra of Al-Nd doped fibre at 1.3 µm. Emission cross-section from reference [83] (black solid), emission cross-section of F432-LF197 fibre (red dashed), and absorption cross-section of F432-LF197 fibre (blue dotted).

Cross-section spectra for Nd^{3+}-doped aluminosilicate fibres around 1.3 µm wavelength region are shown in figure 6.10. The stimulated emission cross-section spectrum (red dashed line) is calculated from a measurement on a Nd^{3+}-doped aluminosilicate fibre fabricated at ORC (F432-LF197). In addition, the black solid curve represents the emission cross-section and the blue dotted line represents the ESA cross-section, both reconstructed from reference [83]. The ESA cross-section has a peak value at 1.30 µm. Beyond 1.38 µm, there is no ESA. On the other hand, the emission cross-section peaks at 1.34 µm. It is also shown that the two emission cross-section curves are similar. In the figure, the effective emission cross-section σ_e^{eff} ($=\sigma_e^{stim}-\sigma_{ESA}$, where σ_e^{stim}, σ_{ESA} are the stimulated emission cross-section and the ESA cross-section, respectively) can have positive values above 1.346 µm. However, for higher efficiency, it is important that the ESA cross-section is negligible compared to the stimulated emission cross-section.

Figure 6.11 shows the cross-section spectra for the entire band of interest. The

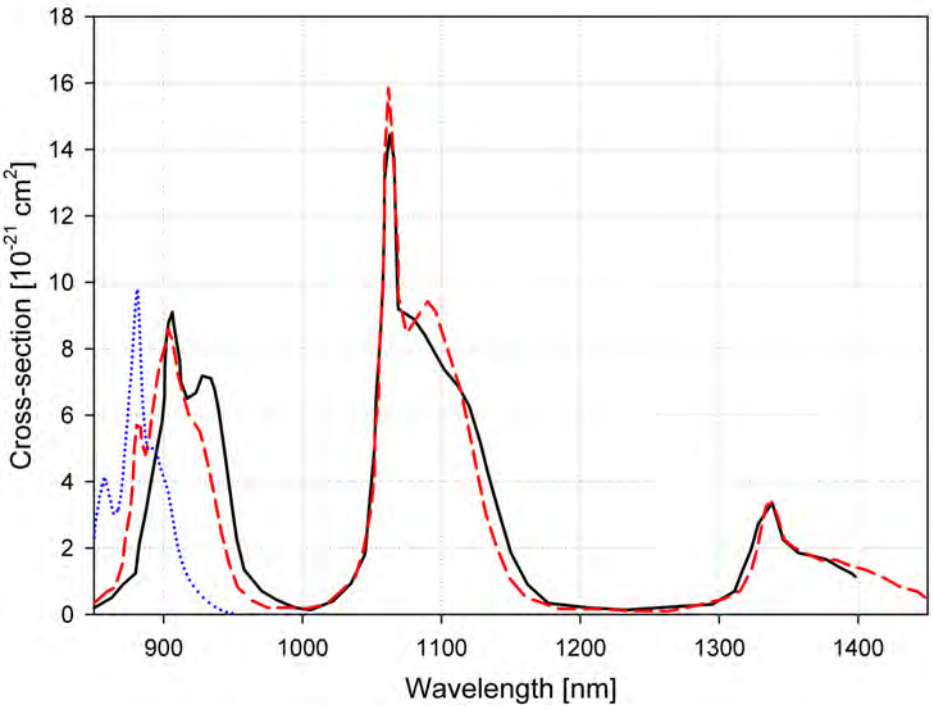

Figure 6.11. Emission and absorption cross-section spectra of Nd-doped aluminosilicate fibres. Emission cross-section from reference [83] (black solid), and emission (red dashed) and absorption cross-section (blue dotted) measured on fibre F432-LF197.

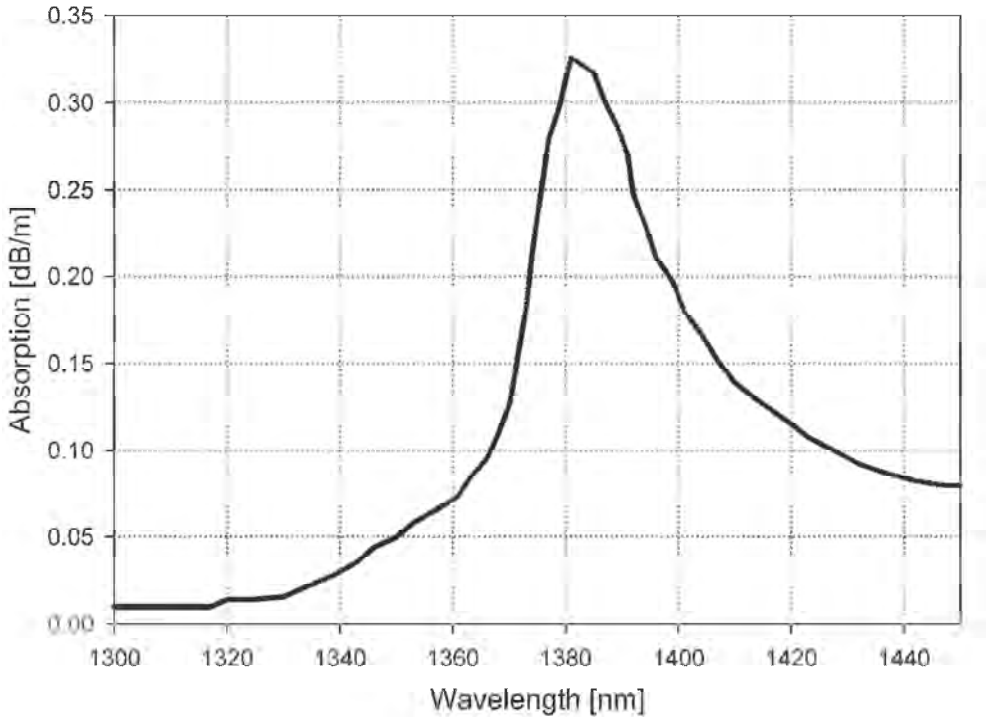

Figure 6.12. OH^--ion absorption spectrum measured in the fibre F432-LF197.

emission spectrum corresponds to transitions to different lower laser levels, including the ground-state in case of the 0.9 μm line. The ground-state absorption in the 0.9 μm band is shown, too. The emission cross-section has a peak at 1.06 μm (which is different from ZBLAN fibres discussed in the previous chapter, which has a peak at 1.05 μm), and is much larger than in the 1.3 μm band. Therefore, in normal step-index core-doped fibre, the amplified spontaneous emission at 1.06 μm may well saturate the amplifier, reducing the gain at 1.3 – 1.4 μm. Due to the absorption in the 0.92 μm band, emission at 0.92 μm is actually challenging to achieve and is not likely to saturate amplifier. Therefore, the main emission that competes against 1.3 μm amplification occurs at 1.06 μm.

The OH^- ion absorption centred at 1.38 μm is another issue. Due to the fabrication process (e.g., MCVD), there may be a degree of hydrogen and thus OH^--ions in the fibre. Although the amount of OH^- can be controlled, provided that proper drying processes (e.g., chlorine drying) are included in the fibre fabrication, the possible effect of OH^--absorption is critical and must be considered. Figure 6.12 shows the OH^--ion absorption spectrum in the core of a fibre, measured with the cut-back

method. The peak absorption occurred at 1.38 μm with a peak value of 0.3 dB/m. If the fibre fabrication incorporates an effective dehydrogenation process, the peak loss may become less than 0.01 dB/m. For instance, the OH^- ion loss in a standard single-mode fibre (Corning SMF28) is less than 0.001 dB/m. In the simulations, the spectrum shown in figure 6.12 is adopted with various peak values.

Finally, as is stated in previous sections, the stronger emission at 1.06 μm is another difficult hurdle to overcome. A number of papers suggest that the amplification at 1.3 μm may be enhanced significantly if the competing amplified spontaneous emission at 1.06 μm is suppressed [8, 81, 82, 84-87].

6.2.2. Numerical simulations for fibre amplifier

For numerical simulations, an Nd^{3+}-doped aluminosilicate fibre is assumed. The Nd^{3+} ion concentration is assumed to be 1.654×10^{19} ions/cm^3, which is similar to the fibre F432-LF197. The fibre design in section 6.1.1 is used with a 2 μm inner radius of the doped ring. The cladding size is assumed to be 125 μm and the fibre length is 15 m. The launched pump power is assumed to be up to 20 W at 808 nm. The emission and absorption cross-sections and wavelength-dependent propagation loss of the F432-LF197 Nd^{3+}-doped aluminosilicate fibre, detailed in the previous section, are used. The details of the numerical simulator are described in appendix A. In order to consider the effect of ESA, a wavelength dependent gain will be used. For the effect of the OH^- ion absorption, a comparison between the cases with and without considering the OH^- ion absorption will be presented. The effect of the amplified spontaneous emission at 1.06 μm is investigated by varying the inner radius of the

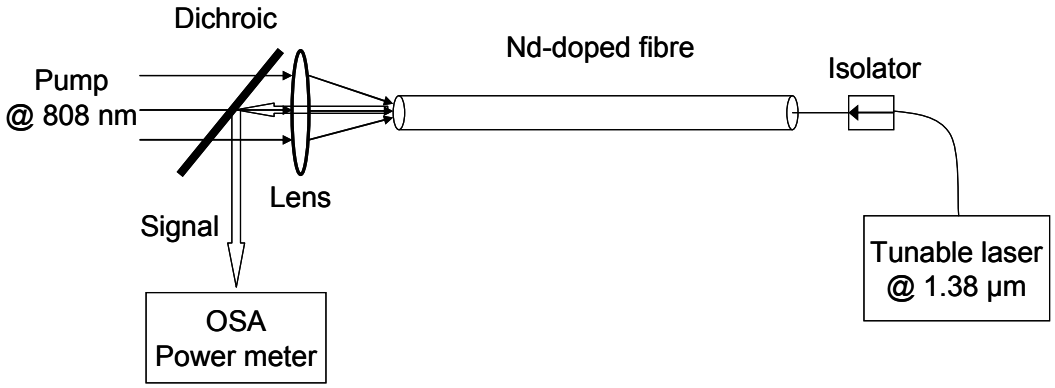

Figure 6.13. Configuration assumed for the numerical simulation of an NDFA operating at 1.38 μm.

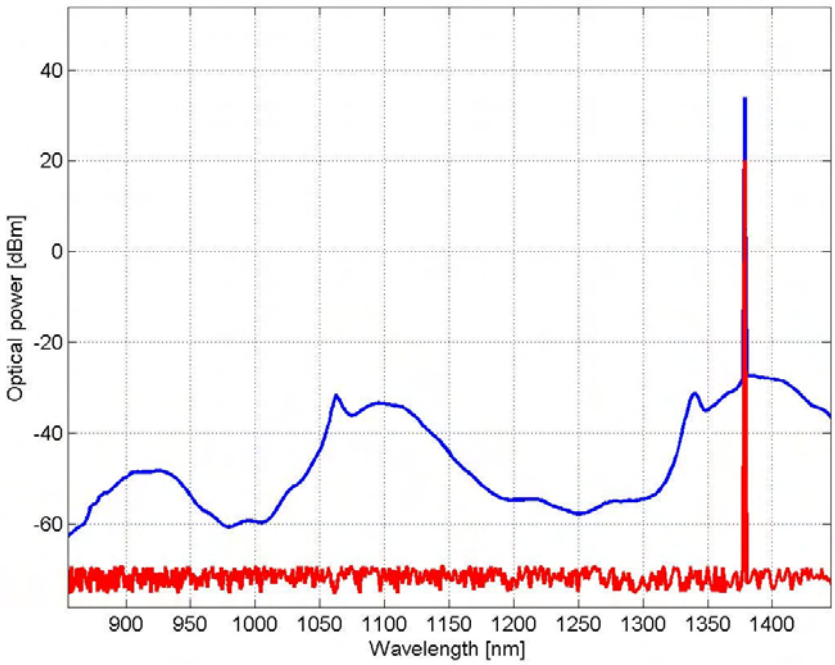

Figure 6.14. A typical spectrum of the output signal (blue solid) from the amplifier. For comparison, the spectrum of the input signal is also shown (red solid). Results of simulations.

Nd^{3+}-doped ring.

The configuration adopted for the simulations is shown in figure 6.13. The Nd^{3+}-doped fibre is cladding-pumped by a diode laser at 808 nm from one end of the fibre. The seed signal is launched from the other end. A dichroic mirror at the pump launch end transmits the pump wavelength and reflects the signal from 850 nm to 1500 nm. A tuneable single-mode laser is assumed for the seed source. The amplified signal is reflected from the dichroic mirror. The fibre end at the pump launching end is assumed to be angle-cleaved in order to prevent back-reflection of the signal.

Figure 6.14 shows a typical spectrum of the output signal from the amplifier. Thanks to the fibre waveguide design, the competing emissions at 0.92 μm and 1.06 μm are well suppressed. For this simulation, a fibre length of 15 m was used, coiled with a sufficiently large coiling diameter so that the wavelength dependent bending loss was negligible (especially compared to the OH^- ion loss). The launched pump power is 10 W of which 6.7 W is absorbed. The seed signal is assumed to be monochromatic at 1380 nm with a power of 100 mW launched into the core. For a realistic simulation, a white noise is inserted to the seed signal with the power level of

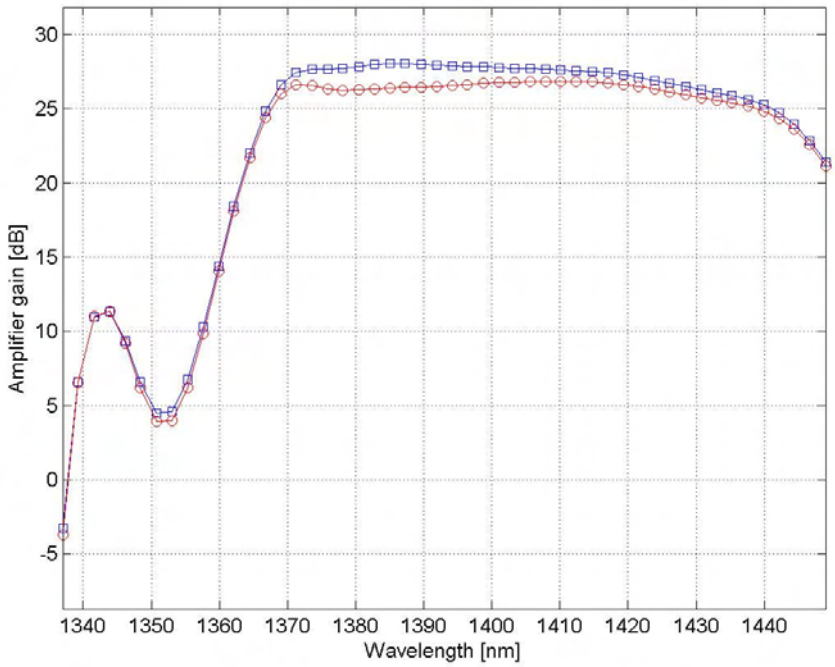

Figure 6.15. The amplifier gain vs. wavelength for a 1.3 – 1.4 μm NDFA. Blue square-marked (red circle-marked) line represents the amplifier gain for 10 mW input signal without (with) OH^- ion absorption, respectively. Results of simulations.

–75 dBm. The output signal power becomes 2.6 W according to the simulations, for a net gain of 14.1 dB. This is difficult to obtain from a step-index conventional neodymium-doped fibre amplifier.

Figure 6.15 shows the amplifier gain for different wavelengths. The circled data points indicate the amplifier gain when a monochromatic seed signal is launched at the specific wavelength. For this simulation, the pump launched power is assumed to be 20 W. The seed signal power is 10 mW for all wavelengths. As is expected from figure 6.10 (the cross-sections), the amplifier shows positive net gain from ~ 1340 nm. In the case of (excess) absorption caused by the presence of OH^--ions, the maximum gain is 26.9 dB at 1410 nm, resulting in the output signal power of 4.86 W. When the OH^--absorption is neglected, the maximum gain is 28.2 dB at 1385 nm, resulting in an output signal power of 6.4 W. The total background loss at 1385 nm is 4.5 dB induced by the OH^- ion absorption. The difference of the amplifier gain at 1385 nm between the case with and without the OH^--absorption is only 2.2 dB, due to the

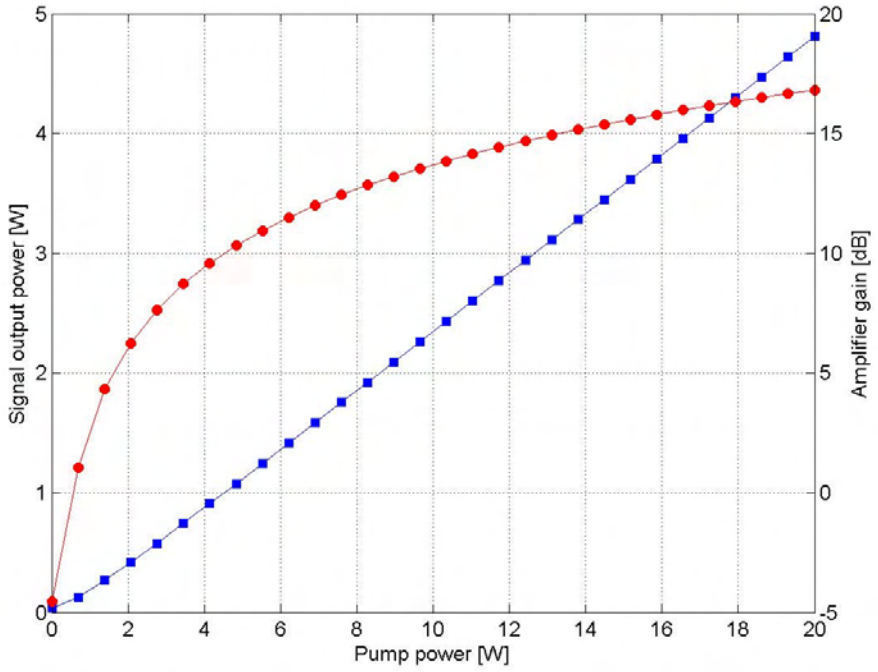

Figure 6.16. Signal output power vs. pump power. The blue line with squares (red line with circles) represents the signal output power (the amplifier gain). The wavelength of the seed signal is 1385 nm with 100 mW input power. Results of simulations.

amplifier gain saturation by the signal power. However, in the small signal regime, the difference approaches 4.5 dB.

Figure 6.16 shows the output power of the signal and amplifier gain with different pump powers. For this calculation, a seed signal with 100 mW power at 1385 nm is assumed. When fully pumped (20 W), the amplifier gain is 16.8 dB. Since there seems to be no sign of roll over in the signal output power, the figure implies that a still higher signal output power may be obtainable if more pump power is launched. The lack of roll-over is indeed what is expected with the used model.

Figure 6.17 shows the effect of the inner radius of the doped ring, i.e., d_1. For this calculation, a 10 mW input signal power was used for 1360 nm and 1385 nm seed signals. The pump power is 20 W. The variation of gain with d_1 depends on the wavelength of the signal. For short wavelengths (~ 1360 nm) where the effective emission cross-section at short wavelengths is small and, hence the gain is small, d_1 plays a significant role. If d_1 becomes small, the overlap factor of the shorter

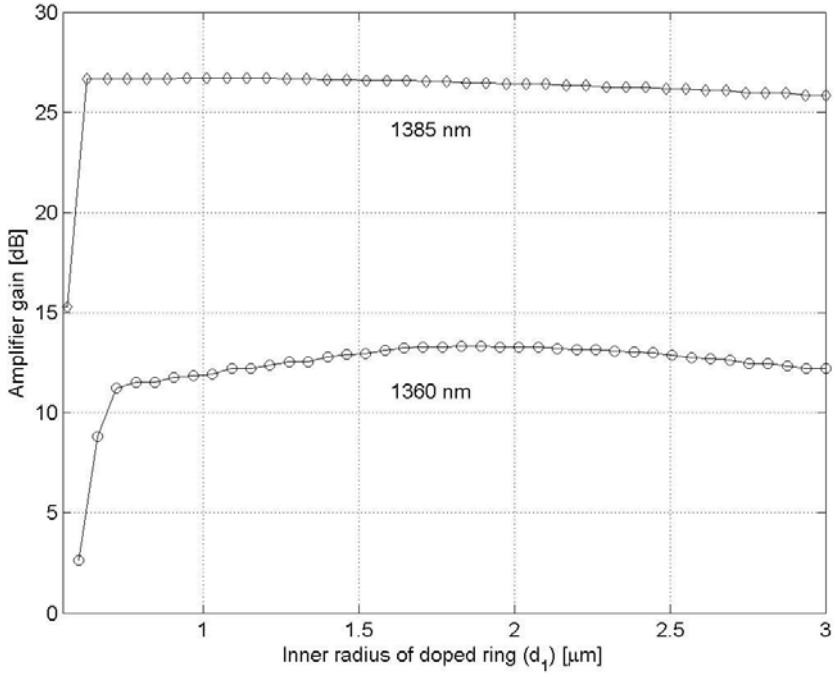

Figure 6.17. The effect of the inner radius of doped ring. The upper and the lower curves represent the gain of a NDFA for the input signal at 1385 nm and 1360 nm, respectively with OH^- ion absorption. Results of simulations.

wavelength increases and, as a consequence, a large amount of amplified spontaneous emission at 1.06 μm may build up. This strong amplified spontaneous emission at 1.06 μm saturates the amplifier so that the gain at longer wavelengths reduces. However, when the signal power at longer wavelength is high due to either large gain of the amplifier or large seed power, the amplified spontaneous emission build-up at 1.06 μm is less efficient since the number of excited Nd^{3+}-ions can be smaller. But, still if d_1 becomes less than 0.7 μm, even strong signal power at longer wavelength does not prevent the build-up of the amplified spontaneous emission at 1.06 μm, and hence, the gain becomes significantly reduced. The maximum gain depends on the signal wavelength (and the seed signal power) as well. For instance, the maximum gain for 1360 nm can be achieved when d_1 is 1.8 μm while that for 1385 nm requires d_1 to be 1.2 μm, both for 10 mW seed signal. It is noteworthy here that going to longer wavelengths with lower cross-sections will clearly degrade performance

requiring higher Nd^{3+} ion excitation. Therefore, for longer wavelength operation, the fibre design becomes more critical.

6.2.3. Numerical simulations for fibre laser

Next, a fibre laser configuration is simulated. The configuration assumed for the numerical simulations is shown in figure 6.18. The pump at 808 nm is launched into the inner cladding of the Nd^{3+}-doped double-clad fibre with a maximum coupled power of 20 W. The forward-propagating signal is collimated through a lens and is reflected from a diffraction grating that provides feedback in one end of the fibre laser cavity. The 4% Fresnel reflection from a perpendicularly cleaved end provides feedback in the other, outcoupling, end of the fibre laser cavity. The output signal from the pump launching end is reflected by the dichroic mirror and runs in free-space. For the numerical simulations, the doping level, cross-section, wavelength-dependent propagating loss, and fibre design and dimensions are the same as for the NDFA in the previous section. The inner radius of the doped region d_1 is 2 μm in this case. The reflectance from the diffraction grating is assumed to be 80% at the tuning wavelength including the loss in the beam pass, such as signal back-launching efficiency, lens loss, etc. The broadband reflectance from the angle-cleave in the grating end of the fibre is assumed to be 0.1%.

A detailed description of the simulation procedure for the 1300 nm fibre laser, with results, is provided in Appendix A. A fibre length of 20 m and the launched pump power of 20 W are used. The absorbed pump power is 16 W. The diffraction

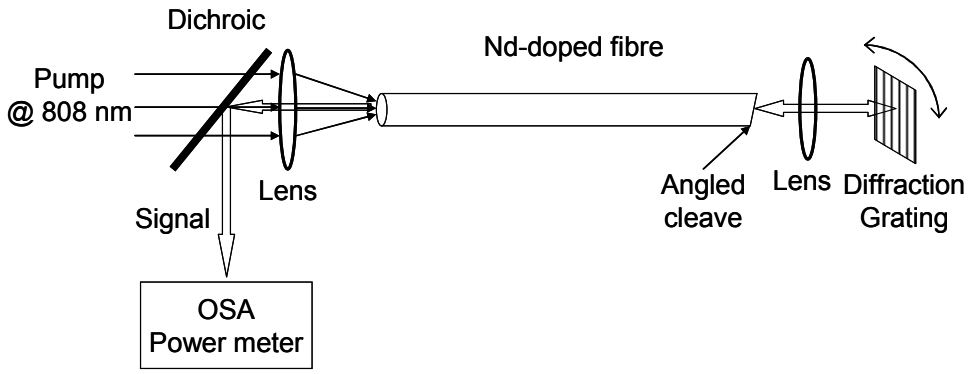

Figure 6.18. Configuration used for simulations of a Nd-doped fibre laser operating at 1.38 μm.

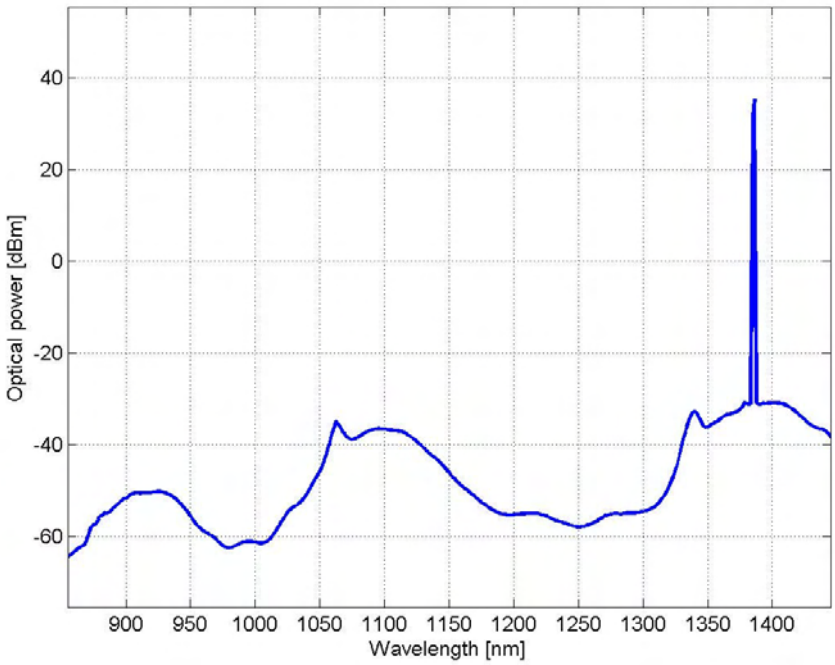

Figure 6.19. The optical output spectrum of a NDFL at 1385 nm. Results of simulations.

grating is tuned to 1.38 μm with a linewidth of 0.5 nm. The optical spectrum in figure 6.19 for the output signal shows an excellent suppression of the competing amplified spontaneous emission at 1.06 μm (and 0.92 μm) thanks to the fibre design. (More detailed simulation results such as the fraction of excited ions along the radial and longitudinal position, and the pump and the signal power evolutions can be found in appendix A.) Even when the cavity was made with broadband 4%-reflecting flat cleaves in both ends, the fibre still emitted at 1.38 μm. Therefore, the gain at 1.38 μm exceeds that of 1.06 μm in the designed fibre.

Figure 6.20 shows the laser output power characteristics with respect to the launched pump power. The signal wavelength is 1.385 μm. The threshold launched pump power is only 0.3 W, which is relatively small since the laser operates on four energy levels without any ground-state absorption. The output signal power grows linearly with the pump power with a slope efficiency of 26% with respect to the launched pump power. The output reaches 5 W when 20 W of pump power is launched.

Next, figure 6.21 shows the tunability of the laser. The signal output power and the slope efficiency are shown in the figure. For this calculation, a launched pump

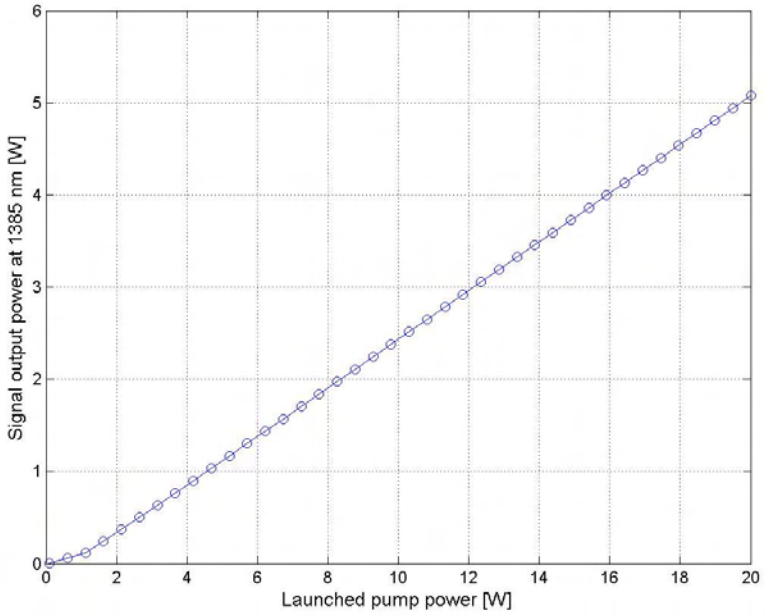

Figure 6.20. NDFL output power at 1385 nm vs. launched pump power. Results of simulations.

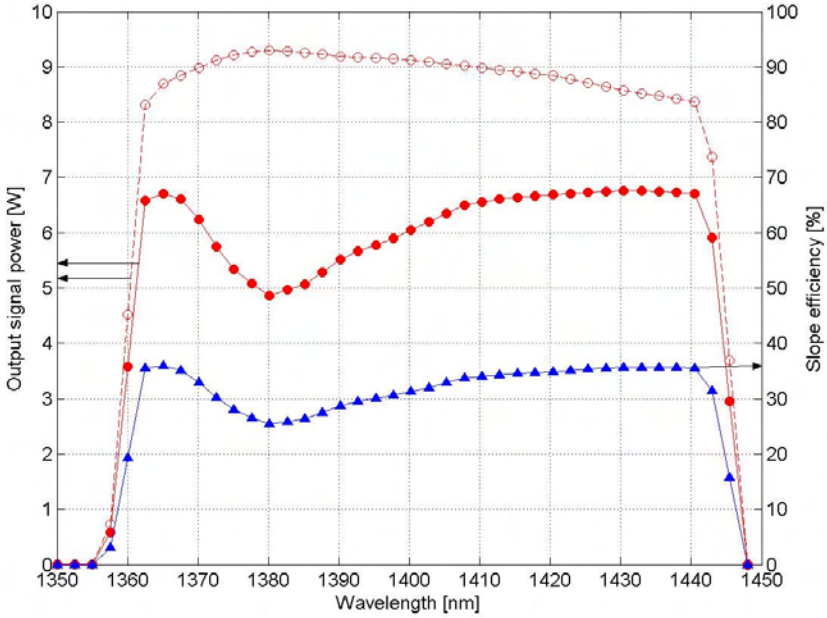

Figure 6.21. Signal output power and slope efficiency vs. operating wavelength. The red circle-marked and the blue triangle-marked curve represent the signal output power and the slope efficiency in the presence of OH^--ion absorption, respectively. The dashed red circle-marked curve represents the signal output power without OH^--absorption. Results of simulations.

power of 20 W is used and the fibre length is 20 m, absorbing 16 W of pump power. Because the threshold pump powers are small for all lasing wavelengths, the slope efficiency curve closely follows the signal output power curve. The laser is tuneable between 1360 nm and 1445 nm, which can be expected from the amplifier gain curve in figure 6.15. The signal output power clearly shows the effect of the OH^--absorption. When the OH^--absorption is neglected, the signal output power at 1380 nm is 9.3 W with a slope efficiency of 57% (45%) with respect to absorbed (launched) pump power. The quantum-defect limited conversion efficiency from 808 nm to 1380 nm is 58.5%, implying that the slope efficiency is close to the quantum limit. However, when OH^--absorption is considered, the output power drops to 4.9 W with a slope efficiency of 31% (26%) with respect to the absorbed (launched) pump power. Therefore, in order to obtain a high efficiency, it is important to reduce the OH^--content through the dehydrogenation processes during fibre fabrication. In a tuneable laser setup, it is also important to reduce the signal back reflection from the angle-cleaved fibre facet. When the end is perpendicularly cleaved, instead of being angle-cleaved, the tuning range reduces down to 1370 - 1435 nm due to the oscillation of stronger emission at 1410 nm.

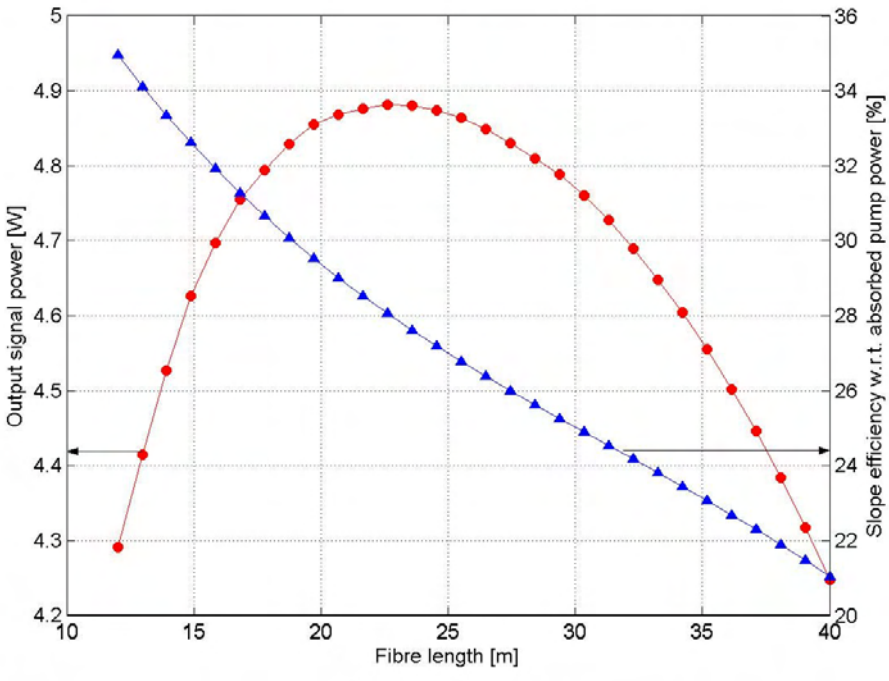

Figure 6.22. Signal output power (red, circles) and slope efficiency w.r.t. the absorbed pump power (blue, triangles) vs. fibre length for NDFL at 1385 nm. Results of simulations.

Figure 6.22 shows how the signal output power and the slope efficiency (with respect to the absorbed pump power) depends on the fibre length. The signal wavelength is 1385 nm and the launched pump power is 20 W. The absorbed pump power changes from 12 W with 12 m fibre to 19.3 W with 40 m fibre. A fibre with OH^--absorption is considered in this case. The maximum output power is obtained with the fibre length of 23 m. Due to the OH^--absorption, the signal output power drops for longer fibres. The slope efficiency with respect to absorbed pump power is more sensitive to the fibre loss than the signal output power is since a longer fibre absorbs more pump power. The slope efficiency changes from 29% with 20 m of fibre to 21% with 40 m of fibre.

6.3. Summary

In chapter 6 I suggested fibre designs for long-wavelength pass filters. Two designs were introduced. A modified W-type refractive index profile with an outer raised ring provided a good overlap factor for long wavelengths relative to that for short wavelengths by confining the short wavelength into the core and by locating the Nd^{3+}-dopants in the outer ring. In addition, a modified W-type refractive index profile with a raised ring with still higher index is also introduced. This design confines short-wavelength LP_{01}-modes into the outer ring while long-wavelength modes remain in the core.

These filters only work with an active dopant. They were further investigated in the context of Nd^{3+}-doped fibres operating at ~ 1.38 μm. There are three main issues to overcome in order to realise an efficient amplifier and laser operating at 1.38 μm, namely, ESA, OH^--ion absorption, and strong amplified spontaneous emission at 1.06 μm. The ESA can be avoided by choosing different hosts which show less ESA in the 1.3 μm band. In preferred silica hosts, the ESA is however significant, but becomes smaller at longer wavelengths. The OH^--absorption can be avoided through a dehydrogenation process during fabrication. The strong amplified spontaneous emission at 1.06 μm can be avoided with a long-pass filter designed into the fibre.

Numerical simulations using a fibre designed with a long-pass filter were presented for an amplifier and a laser operating at 1.38 μm. Excited-state absorption restricts the short-wavelength tuning range, which becomes 1345 nm to 1450 nm for the amplifier and 1355 nm to 1445 nm for the laser. The OH^--ion absorption can

seriously degrade the gain and efficiency at 1.38 μm. If the OH^--absorption is eliminated, the slope efficiency of the fibre laser reached 57% at 1.38 μm, which is near the quantum limit. Such excellent characteristics for the 1.38 μm band are possible with high-purity fibre fabrication and a fibre waveguide structure that efficiently suppresses the (otherwise) strong amplified spontaneous emission at 1.06 μm.

Part III. Modal power decomposition

Chapter 7. Modal power decomposition

Chapters 3-6 presented work on waveguide filters. It was shown that there are a number of waveguide types which can be used for filtering out undesired wavelength ranges. Using these waveguide filters, experimental demonstrations of a Nd^{3+}-doped fibre laser operating at 0.92 μm and a Yb^{3+}-doped fibre laser operating at 0.98 μm were described. From these experimental results the output beam quality was assessed through the conventional M^2-value measurements, which is defined in reference [88]. However, it is well known that such M^2-value measurements do not precisely represent all aspects of the output beam from a fibre laser. For instance, two laser beams with the same M^2 value need not couple into a waveguide with the same coupling efficiency. Therefore, for a more complete determination of the spatial characteristics a laser beam, one needs an alternative method.

The modal power decomposition of the multimode beam from fibre lasers is one candidate. In this method the power of the multimode beam is decomposed to each mode, provided that each modal intensity profile in the fibre is known *a priori*, and that the modes are coherent. Once the power is decomposed into the modes, it is possible to predict precisely the propagation of the multimode beam in free-space. It is also possible to calculate the coupling efficiency into a waveguide. Furthermore because modes are orthogonal (in ideal cases), the power in each mode is conserved during propagation. Therefore the modal power decomposition is truly one of the complete characterization methods for a free-space beam in a strict sense.

For such modal power decomposition, two different kinds of methods have been suggested. One method is based on image processing and the other one is based on wavelength sweeping. The first one utilises the Wigner function associated with the Radon inverse transform. A number of multimode beam images are taken at different distances using two cylindrical lenses. Later the modal power decomposition is

acquired through the mutual intensity profile of the beam images. This is obtained through the Wigner function from the inverse Radon transform of the beam images. The second method utilises a saw-tooth shaped wavelength-sweeping signal. Due to the different phase velocities of the different modes, the interference patterns can be measured with fixed locked-in interferometric frequencies. Using a simple transform method from the many different interferometric images, one can obtain the modal power decomposition. The first method uses a monochromatic signal with many images taken from different distances from the source. The second method uses a wavelength sweeping source with a few images taken from a fixed distance away from the source. One may obtain the modal power decomposition of a laser source only if it is monochromatic, using the first method whereas the second method requires an external source.

This chapter provides a more in-depth look at modal power decomposition with these two methods. For each method, realistic simulation results are also included.

7.1. Introduction to modal power decomposition

Modal decomposition of light beams in multimode optical fibres is an important problem in various areas such as optical fibre communications and optical fibre lasers. For instance, knowledge of the power distribution among modes is necessary in applications such as higher-order mode-dispersion compensation, mode-beating devices and free-space optical communications employing fibre lasers and amplifiers. Furthermore novel multimode fibre devices such as cladding-pumped fibre lasers [22, 89, 90] require a thorough knowledge and analysis of the modal behaviour of launched beams. For example the optical pumping scheme can be optimised to be more efficient.

Approximate methods for multimode fibres that assumed that the modal space is continuous or the modal fields are azimuthally symmetric were developed in the 1980s [37, 38, 91-93]. However before the work presented in this chapter there has not been an exact analytical treatment of modal decomposition of beams in optical fibres based on intensity profile measurements. Recently, a Hermite-Gaussian modal decomposition was demonstrated by Gori *et al.* [39, 94], who successfully decomposed a multimode Hermite-Gaussian beam into eigenmodes and determined the modal power weights. One advantageous property of Hermite-Gaussian beams is

the orthogonality properties of the Fourier-transformed modal intensity functionals [39]. Unfortunately, the linearly polarised (LP) mode intensity profiles of an optical fibre are more difficult to treat because of the complicated nature of the Bessel solutions of the Helmholtz equation with a cylindrical boundary. While one can easily extract modal weights from the complex field profiles, thanks to the orthogonality of the Helmholtz solutions, this requires knowledge of the phase profile of the beam as well as the amplitude. In practice, interferometric measurements have been used to determine the shape of the wavefronts [95, 96]. Alternatively one can use optimizing iterative methods with least-squares fitting based on an *a priori* knowledge of each mode and the measured intensity profile [40]. However, both of these methods are problematic. For instance, the temporal coherence of light sources may be insufficient for interferometric measurements, while iterative methods are often cumbersome.

7.2. Modal power decomposition using tomography

In this section a concise method for determining the modal power weights of a beam in a multimode fibre from intensity measurements is presented. It was published in [97]. The method allows the modal power weights to be calculated from these simple intensity measurements without loss of accuracy. The following subsections present the related theoretical derivation and the numerical simulation for the evaluation of the developed theory.

7.2.1. Theory

For the theory, a conventional refractive index guiding structure supporting several modes is considered. The refractive index profile can be arbitrary. For mathematical convenience, a monochromatic beam is considered. Due to the nature of the governing Helmholtz equation such as linearity and orthogonality, the eigensolutions of the Helmholtz equations are linearly independent. Therefore the complete set of eigensolutions (or simply ‘modes’) forms a basis for the functional space of all the guided multi-mode beams (which are mathematically treated as ‘functionals’). It means that any guided beam can be linearly decomposed into a weighted sum of individual modes. Thus, it is possible to find the modal power distribution in a conventional refractive index guiding structure.

Once the modes are known and the full information of the multimode beam including the spatial intensity profile and the phase is known, it is straightforward to

calculate the modal power distribution by taking an inner product. Since modes are orthogonal, the result of the inner product readily produces the modal weight. However, the real challenge is to find out the modal power distribution from non-interferometric intensity measurements. As is explained in the previous section, the method employing only the intensity measurement is much less sensitive to the measurement environment and thus, may give more accurate results in reality. The following theory reveals how to obtain the modal power distribution without any phase information of the multimode beam.

The outline of the method is as follows: First of all the 'mutual intensity profile', which gives the cross product information and is alternatively called the 'two point correlation function' will be obtained. This is done through successive image processes combining the Wigner transform and the Radon transform. The method relies on multiple intensity measurements taken at different observing distances. Next the modal power distribution will be obtained from the *a priori* knowledge of the modes and the acquired mutual intensity profile.

Modal properties in multimode fibres

The method depends only on the orthogonality of the eigensolutions. Therefore the only requirement is the linear independence of the modes, which is generally true for the refractive index guiding waveguide whether it is planar or circular. Therefore without losing generality, a step-index fibre can be considered with the assumption of weak guiding for simplicity. The electrical field of the monochromatic beam inside the core can be assumed to be of the form:

$$\vec{E}(x,y,z) = \vec{e}(x,y)\exp(i\beta z), \tag{7.1}$$

where x, y, z denote the Cartesian coordinates of a point and β is the propagation constant in the direction of the z axis. The representation in equation (7.1) is for an eigenmode of the fibre with an eigenvalue β, while the general field can be expressed as a superposition of weighted eigenmodes. $\vec{e}$ in equation (7.1) represents the eigensolution of the Helmholtz equation:

$$\left[\nabla_t^2 + k^2 n(r)^2 - \beta^2\right]\vec{e}(x,y) = 0, \tag{7.2}$$

where ∇_t^2 denotes the transverse Laplacian ($=\partial^2/\partial x^2+\partial^2/\partial y^2$), $k=2\pi/\lambda$, λ is the free-space wavelength of the beam and $n(r)$ is the index profile of the fibre. Now assuming the core boundary is located at radius a_{co} and normalizing the radial variable r as $R=r/a_{co}$, the refractive index profile can be represented as

$$n(R)=\begin{cases} n_{co}, & 0\le R\le 1 \\ n_{cl}, & 1<R \end{cases} \tag{7.3}$$

where n_{co} and n_{cl} denote the core and the cladding refractive index, respectively, with $n_{co}>n_{cl}$.

It is well known that the solutions of the Helmholtz equation (7.2) take the approximated form of LP modes [9],

$$\vec{e}^{\,lpij}(x,y)=F_{lp}(R)\left\{\sin\left(l\phi+\frac{\pi}{2}i\right)\hat{x}+\sin\left(l\phi+\frac{\pi}{2}j\right)\hat{y}\right\}, \tag{7.4}$$

where i and j can take any value between 1 and 0, and $\hat{x}$, $\hat{y}$ denote the unit vectors in the direction of the x axis and the y axis, respectively. Here, F_{lp} is a solution of the Bessel equation:

$$\left[\frac{d^2}{dR^2}+\frac{1}{R}\frac{d}{dR}+k^2n(R)^2-\frac{l^2}{R^2}-\beta^2\right]F_{lp}(R)=0\,. \tag{7.5}$$

Note that there are two polarization states in each LP mode, namely the x- and y-polarised states. These two sets of polarizations are mutually perpendicular in space. Hence, one can consider only one polarization at a time without loss of generality. In other words the solution set $\vec{e}^{\,lpij}=e^{lpi}\hat{x}+e^{lpj}\hat{y}$ and $e^{lpi}(x,y)=F_{lp}(x,y)\sin(l\phi+i\pi/2)$ can be considered. Furthermore, e^{lpi} and e^{lpj} are denoted as the sine and the cosine mode, respectively. Each modal solution has sine and cosine modes at the same time unless $l=0$. We still refer to the modal solutions of $l=0$ as cosine modes.

The solutions of the Bessel equation (7.5) are given by

$$F_{lp}(R)=\begin{cases} J_l(U_{lp}R)/J_l(U_{lp}), & 0\le R<1 \\ K_l(W_{lp}R)/K_l(W_{lp}), & \text{otherwise} \end{cases} \tag{7.6}$$

where $U_{lp}\overset{\Delta}{=}a_{co}\sqrt{k^2n_{co}^2-\beta_{lp}^2}$, $W_{lp}\overset{\Delta}{=}a_{co}\sqrt{\beta_{lp}^2-k^2n_{cl}^2}$. For a given l ($l=0, 1, 2, \cdots$), the U_{lp}'s and W_{lp}'s ($p=1,\ 2,\ 3, \cdots$) are the possible solutions satisfying the boundary condition given by equation (7.7).

$$U_{lp}\frac{J_{l+1}(U_{lp})}{J_l(U_{lp})}=W_{lp}\frac{K_{l+1}(W_{lp})}{K_l(W_{lp})}. \tag{7.7}$$

It follows that the propagation constants β_{lp} are different for different modes. Of course, there are degenerate modes with very close (or rather practically indistinguishable) propagation constants. These degenerate modes are treated as the same mode in this context. In equation (7.7), it is well known that the number of possible U_{lp}'s and W_{lp}'s are finite for given finite physical dimensions of a fibre. Hence, for a given fibre with certain physical dimensions, we have maximum numbers of both l and p such that $0\le l\le l_0$, $1\le p\le p_0(l)$ where the maximum number p_0 is a function of l. This can be seen from equation (7.7), which in turn means that the number of modes for a given fibre is finite.

Next the mode set Ω is defined as a set of e^{lpi} functionals such that each U_{lp}, W_{lp} associated with F_{lp} satisfy the boundary condition in equation (7.7). Any linear combination of members of Ω is also a solution of equation (7.2). Hence the solution functional space is a span of Ω. In fact it is a subset of the space of squarely integrable functions in L_2. With a properly defined inner product, Ω forms the basis of a Hilbert space. For this the inner product is defined as $\langle e_i, e_j\rangle\overset{\Delta}{=}\int_{-\infty}^{\infty}\int_{-\infty}^{\infty}e_i(x,y)e_j^{*}(x,y)dxdy$, where e_i, e_j are members of the solution functional space and the star (*) denotes the complex conjugate. It is also possible to define the induced norm of the functional space by $\|e^{lpi}\|=\sqrt{\langle e^{lpi}, e^{lpi}\rangle}$.

The basis of the solution functional space can be chosen as a set of orthogonal solutions of the Helmholtz equation. The modes are a good candidate for the maximal orthogonal set, i.e., the basis for the solution functional space. It is easy to prove that

all the modes are orthogonal and furthermore that the set Ω is the maximal orthogonal set. The proof is as follows: Consider the inner product of two arbitrary modes,

$$\left\langle e_t^{lpi}, e_t^{mqj} \right\rangle = \int_0^{2\pi} \int_0^{\infty} F_{lp}(R) F_{mq}(R) \sin\left(l\phi + \frac{\pi}{2} i \right) \sin\left(m\phi + \frac{\pi}{2} j \right) R dR d\phi , \tag{7.8}$$

where the integral coordinate is changed from Cartesian to polar. It is easy to see that only if $l = m$ and $i = j$, the inner product in equation (7.8) can have a nonzero value because of the sinusoidal term in the integrand.

Now, consider

$$\left\langle e_t^{lpi}, e_t^{lqi} \right\rangle = \int_0^{2\pi} \int_0^{\infty} F_{lp}(R) F_{lq}(R) \sin^2\left(l\phi + \frac{\pi}{2} i \right) R dR d\phi = \begin{cases} 2\pi \int_0^{\infty} F_{lp}(R) F_{lq}(R) R dR, & \text{if } l = 0, \\ \pi \int_0^{\infty} F_{lp}(R) F_{lq}(R) R dR, & \text{otherwise} \end{cases} .$$

(7.9)

Note that there is no sine mode for $l = 0$, i.e. $i = 1$ when $l = 0$. Hence, equation (7.9) is valid for any l. The orthogonality of the F_{lp}'s is proven by classical way by considering the Bessel differential equation (7.5). Consider

$$\left\{ \frac{d^2}{dR^2} + \frac{1}{R} \frac{d}{dR} - \frac{l^2}{R^2} + U_p^2 - V^2 f_n(R) \right\} F_{lp}(R) = 0 , \tag{7.10}$$

$$\left\{ \frac{d^2}{dR^2} + \frac{1}{R} \frac{d}{dR} - \frac{l^2}{R^2} + U_q^2 - V^2 f_n(R) \right\} F_{lq}(R) = 0 , \tag{7.11}$$

where $f_n(R) = \begin{cases} 0, \text{if } 0 \le R < 1 \\ 1, \text{otherwise} \end{cases}$, $V = \sqrt{U_{p,q}^2 + W_{p,q}^2} = a_{co} k \sqrt{n_{co}^2 - n_{cl}^2}$. Now by multiplying equation (7.10) with $F_{lq}(R)$ and equation (7.11) with $F_{lp}(R)$ and subtracting one from the other, one obtains

$$\left\{ F_{lq}(R) R \frac{dF_{lp}(R)}{dR} \right\}_0^{\infty} - \left\{ F_{lp}(R) R \frac{dF_{lq}(R)}{dR} \right\}_0^{\infty} = \left(U_q^2 - U_p^2 \right) \int_0^{\infty} F_{lp}(R) F_{lq}(R) R dR .$$

(7.12)

From equation (7.6), the left-hand side of equation (7.12) is zero. Hence the inner product is zero if p is different from q and otherwise non-zero. On the other hand the maximality is trivial when we recall that all F_{lp}'s are possible solutions of the boundary condition in equation (7.7). Hence the orthogonality and maximality are completely proven.

Now it is possible to construct the orthonormal basis with $\overline{\Omega} = \left\{ \overline{e}^{lpi} \middle| \overline{e}^{lpi} = e^{lpi} / \left\| e^{lpi} \right\| \right\}$. For convenience we reorder the (l, p, i) modes into modes with one index n ($n = 1, 2, 3, \cdots, N$; N is the number of eigenmodes). This is possible since there is a one-to-one, onto mapping from a finite l_3 space to a finite l_1 space. In other words, $\overline{\Omega} = \left\{ \overline{e}^{n} \middle| \overline{e}^{n} = e^{n} / \left\| e^{n} \right\| \right\}$. Then by Hilbert space theory and by the completeness of the L_2 space any solution of the Helmholtz equation (7.2) can be expressed as a linear combination of members in $\overline{\Omega}$ on a complex scalar field:

$$e = \sum_{i=1}^{N} c_i \overline{e}^{i} \,. \tag{7.13}$$

Here if a partially coherent beam is considered, the c_i's are ensemble averaged values of a set of partially coherent beams, i.e., $c_i = \langle c_i \rangle$. It is noteworthy that the c_i's are also complex values because each mode might have a different phase. The power is given by $P = \left\| e \right\|^2 / \eta$, where η denotes the impedance in the fibre. Then by orthogonality, it easily follows that

$$P = \frac{1}{\eta} \sum_{i=1}^{N} \left| c_i \right|^2 , \tag{7.14}$$

because each eigenmode power is given by $\left\| \overline{e}^{i} \right\|^2 / \eta = 1/\eta$. Hence from equation (7.14) one knows that the total power is a linear sum of each modal weight $\left| c_i \right|^2$ divided by the impedance.

Acquisition of modal power distribution

If one knows the amplitude and phase of the electrical field e for the multimode of concern, it is straightforward to evaluate the c_i's by simple inner product

$$c_i = \left\langle e, \bar{e}^i \right\rangle = \int_{-\infty}^{\infty}\int_{-\infty}^{\infty} e(x,y)\bar{e}^{i*}(x,y)dxdy\,. \tag{7.15}$$

The electrical field, e, with phase, is difficult to determine, while the intensity profile $|e|^2$ can be easily obtained with a camera. I propose to calculate the modal power weights $|c_i|^2$ from the mutual intensity profile or two-point correlation function defined as [98, 99]

$$\Gamma(x_1,y_1;x_2,y_2) \overset{\Delta}{=} e(x_1,y_1)e^*(x_2,y_2). \tag{7.16}$$

The mutual intensity profile can be evaluated from measurements of intensity profiles with a camera. Then assuming that the mutual intensity profile at some point in the fibre and all the modes are known, $|c_i|^2$ are calculated as follows. Note that

$$\int_{-\infty}^{\infty}\int_{-\infty}^{\infty} \Gamma(x_1,y_1;x_2,y_2)\bar{e}^i(x_2,y_2)dx_2dy_2 = c_i e(x_1,y_1)\,. \tag{7.17}$$

The above equation is an integral equation and generally not solvable. However if one takes the complex conjugate of (7.17) and multiply this again to (7.17) and integrate with respect to x_1, y_1, one obtains

$$|c_i|^2 \int_{-\infty}^{\infty}\int_{-\infty}^{\infty} e(x,y)e^*(x,y)dxdy = \int_{-\infty}^{\infty}\int_{-\infty}^{\infty}\left|\int_{-\infty}^{\infty}\int_{-\infty}^{\infty}\Gamma(x_1,y_1;x_2,y_2)\bar{e}^i(x_2,y_2)dx_2dy_2\right|^2 dx_1dy_1\,. \tag{7.18}$$

Now according to Parseval's theorem for a Hilbert functional space with orthonormal basis, one has

$$\int_{-\infty}^{\infty}\int_{-\infty}^{\infty}|e(x,y)|^2 dxdy = \sum_{n=1}^{N}|c_n|^2\,. \tag{7.19}$$

Therefore summing both left and right hands in equation (7.18) with respect to index i and employing equation (7.19) gives

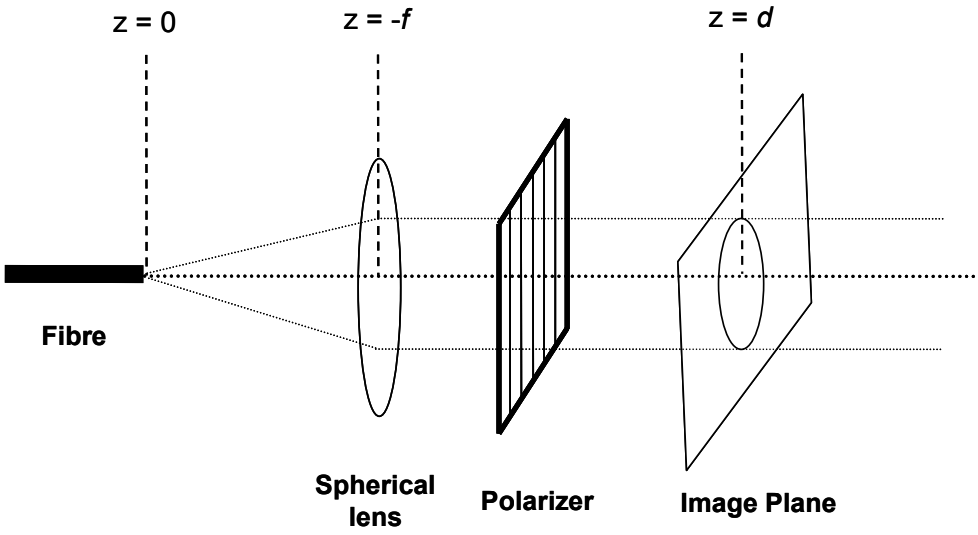

Figure 7.1. Measurement setup for determination of the mutual intensity profile.

$$\left|c_i\right|^2 = \Lambda_i \Big/ \sqrt{\sum_{n=1}^{N} \Lambda_n} \,, \tag{7.20}$$

where

$$\Lambda_i = \int_{-\infty}^{\infty}\int_{-\infty}^{\infty}\left|\int_{-\infty}^{\infty}\int_{-\infty}^{\infty}\Gamma(x_1,y_1;x_2,y_2)\overline{e}^{\,i}(x_2,y_2)dx_2dy_2\right|^2 dx_1dy_1 \,. \tag{7.21}$$

Thus once the mutual intensity profile is known, the modal power weights can be calculated. A necessary condition is that all the mode profiles must be known. On the other hand, there is no assumption about the shape of the waveguide or the modes.

The method requires that the mutual intensity profile of the beam is determined. It is difficult to evaluate the beam properties inside the fibre. Here an alternative method is suggested to evaluate the $\left|c_i\right|$'s at the exit of the fibre with the setup shown in Fig. 7.1. The beam from the fibre end is first collimated using a spherical lens with appropriate focal length f. Then the $\left|c_i\right|$'s can be calculated by considering the orthogonal functionals in free-space as follows.

It follows from the weakly guiding approximation that a paraxial treatment can be adopted [9]. Hence using Fourier optics and with reference to figure 7.1, the electrical field $e(x_1, y_1; z = -f)$ at the $z = -f$ plane and the electrical field $e(x_2, y_2; z = d)$ at

the $z = d(>0)$ plane are related to each other by a Fourier transform multiplied by a phase term [98],

$$e(x_1, y_1; z = -f) = \frac{1}{-j\lambda f} \exp\left[-j\frac{k}{2f}\left(x_1^2 + y_1^2\right)\left(1 - \frac{d}{f}\right)\right] \cdot \int_{-\infty}^{\infty}\int_{-\infty}^{\infty} e(x_1', y_1'; z = d) \exp\left[-j\frac{k}{f}\left(x_1 x_1' + y_1 y_1'\right)\right] dx_1' dy_1' \quad (7.22)$$

where f is the focal length of the spherical lens. It is noted that the inverse mapping from $e(x_1, y_1; z = d)$ to $e(x_1, y_1; z = -f)$ depends on the distance d because of the phase term in the right hand side of (7.22), i.e., $-jk\left(x_1^2 + y_1^2\right)(1 - d/f)/2f$. Physically it means that the wavefronts of the free-space beam change according to the distance from the lens. However with an appropriate focal length the phase term becomes negligible over the distance range of interest, which is much larger than the focal length. Therefore, f is chosen such that $k\left(x_1^2 + y_1^2\right)(1 - d/f)/2f \cong k\left(x_1^2 + y_1^2\right)d/2f^2 << 1$, that is

$$a_{co}\sqrt{kd_M} << f << d_m, \quad (7.23)$$

where a_{co} is the fibre core radius and it is assumed that the distance of interest is in the range $d_m < d < d_M$. Then the phase term in (7.22) can be ignored so that the approximation holds as follows.

$$e(x_1, y_1; z = -f) \cong \frac{1}{-j\lambda f}\int_{-\infty}^{\infty}\int_{-\infty}^{\infty} e(x_1', y_1'; z = d) \exp\left[-j\frac{k}{f}\left(x_1 x_1' + y_1 y_1'\right)\right] dx_1' dy_1'. \quad (7.24)$$

Since the inverse mapping from $e(x_1, y_1; z = d)$ to $e(x_1, y_1; z = -f)$ does not depend on d any more, it holds that

$$\tilde{e}(x, y)\left(\stackrel{\Delta}{=} e(x, y; z = f)\right) \cong e(x, y; z = d), \quad \forall d, \ f < d < f^2/\rho^2 k, \quad (7.25)$$

provided the beam propagates in an isotropic medium such as air.

Next step is to consider the orthogonal functional basis set in free-space. It can be shown that the LP mode fields Fourier transformed as in equation (7.24) also form an orthogonal basis for the free-space beam, by using Parseval's theorem as follows. The transformed LP mode $\bar{e}_F^i$ is defined as

$$\bar{e}_F^i(x,y)=\frac{1}{-j\lambda f}\int_{-\infty}^{\infty}\int_{-\infty}^{\infty}\bar{e}^i(x',y';z=-f)\exp\left[j\frac{k}{f}(xx'+yy')\right]dx'dy'. \qquad (7.26)$$

Note that this is the inverse transform of equation (7.24). Now the general Parseval's theorem shows that

$$\begin{aligned}\left\langle \bar{e}_F^i,\bar{e}_F^j\right\rangle &= \int_{-\infty}^{\infty}\int_{-\infty}^{\infty}\bar{e}_F^i(x,y)\bar{e}_F^{j*}(x,y)dxdy\\ &= \frac{1}{\lambda^2 f^2}\int_{-\infty}^{\infty}\int_{-\infty}^{\infty}\int_{-\infty}^{\infty}\int_{-\infty}^{\infty}\int_{-\infty}^{\infty}\int_{-\infty}^{\infty}\bar{e}^i(x',y')\bar{e}^{j*}(x'',y'')\cdot\\ &\qquad \exp\left[j\frac{k}{f}(x(x'-x'')+y(y'-y''))\right]dx'dy'dx''dy''dxdy\\ &= \frac{1}{\lambda^2 f^2}\int_{-\infty}^{\infty}\int_{-\infty}^{\infty}\int_{-\infty}^{\infty}\int_{-\infty}^{\infty}\bar{e}^i(x',y')\bar{e}^{j*}(x'',y'')\delta(x'-x'')\delta(y'-y'')\lambda^2 f^2 dx'dy'dx''dy''\\ &= \int_{-\infty}^{\infty}\int_{-\infty}^{\infty}\bar{e}^i(x'',y'')\bar{e}^{j*}(x'',y'')dx''dy''\\ &= \left\langle \bar{e}^i,\bar{e}^j\right\rangle.\end{aligned} \qquad (7.27)$$

Hence it is shown that the $\bar{e}_F^i$'s are also an orthonormal set. Then Fourier-transforming in equation (7.13) gives together with equation (7.26) that

$$\tilde{e}(x,y)=\sum_{i=1}^{N}c_i\bar{e}_F^i. \qquad (7.28)$$

with the same expansion coefficients, i.e., modal weight c_i 's. Since $\bar{e}_F^i$'s are also orthonormal, the derivation of equations (7.16) - (7.21) can be similarly applied giving a series of equations

$$\Gamma_F(x_1,y_1;x_2,y_2)\overset{\Delta}{=}\tilde{e}(x_1,y_1)\tilde{e}^*(x_2,y_2), \qquad (7.29)$$

$$\int_{-\infty}^{\infty}\int_{-\infty}^{\infty}\Gamma_F(x_1,y_1;x_2,y_2)\bar{e}_F^i(x_2,y_2)dx_2dy_2=c_i\tilde{e}(x_1,y_1), \qquad (7.30)$$

and hence,

$$\left|c_i\right|^2 = \Lambda_F^i \Big/ \sqrt{\sum_{n=1}^{N} \Lambda_F^n} \,, \tag{7.31}$$

where

$$\Lambda_F^i = \int_{-\infty}^{\infty}\int_{-\infty}^{\infty} \left| \int_{-\infty}^{\infty}\int_{-\infty}^{\infty} \Gamma_F(x_1, y_1; x_2, y_2) \overline{e}_F^i(x_2, y_2) dx_2 dy_2 \right|^2 dx_1 dy_1 \,. \tag{7.32}$$

Thus, one can calculate the original modal weights $\left|c^i\right|^2$ by employing the new orthonormal basis e_F^i's in free-space. If one can get the e^i's by solving equation (7.7) it is easy to get the e_F^i's *via* a Fourier transform in equation (7.26). Now it still remains to get the mutual intensity profile of the free-space beam.

Obtaining the mutual intensity profile

Methods for obtaining the mutual intensity profile of a beam by measuring only the intensity patterns have been studied. For instance, it is possible to retrieve the mutual intensity profile using the Wigner function combined with the Radon transform [99-101] or by using the AF function combined with the Radon transform [102]. One can choose either method. In our case the Wigner function method in reference [101] is adopted for the purpose of numerical simulations. The Wigner function method is based on using two cylindrical lenses and spatially resolved intensity measurements, e.g., with a CCD camera. One thing to note with mutual intensity retrieval techniques is that it is assumed that the phase front of the beam should be reasonably flat against the propagation axis [101], which in our case is guaranteed by choosing an appropriate focal length of the spherical lens as in equation (7.23). The task to get the mutual intensity profile of the paraxial free-space beam is described in reference [101], and is repeated below. The practicability and usefulness of this method is also experimentally proven with real CCD images [100]. While the method was proposed to retrieve an image, we adopt only a part of the proposed method – the retrieval of the mutual intensity profile. From now on, the description in [101] is closely followed.

The Wigner function is defined as follows [103]:

$$W\left(x,k_x,y,k_y\right)=\frac{1}{\pi^2}\int_{-\infty}^{\infty}\int_{-\infty}^{\infty}\exp\left[-2i\left(k_x\Delta x+k_y\Delta y\right)\right]\tilde{\Gamma}\left(x,y;\Delta x,\Delta y\right)d\Delta x d\Delta y, \tag{7.33}$$

where $\widetilde{\Gamma}$ is deduced from the mutual intensity profile Γ as

$$\widetilde{\Gamma}\left(x,y,\Delta x,\Delta y\right)=\Gamma\left(x+\Delta x,y+\Delta y;x-\Delta x,y-\Delta y\right). \tag{7.34}$$

Here each x,y,k_x,k_y is scaled with a common length x_0 and are therefore dimensionless as in reference [101]. Next it is shown that after two mutually perpendicular cylindrical lenses located at $z=d_1$ and $z=d_2$, respectively, this Wigner function is angularly transformed as follows [102]:

$$W'\left(x_\theta,k_\theta;y_\theta,k_\theta\right)=W\left(x,k_x;y,k_y\right), \tag{7.35}$$

where

$$\begin{bmatrix}x_\theta\\k_\theta\end{bmatrix}=\begin{bmatrix}\cos\theta & \sin\theta\\-\sin\theta & \cos\theta\end{bmatrix}\begin{bmatrix}x\\k_x\end{bmatrix},\quad\begin{bmatrix}y_\phi\\k_\phi\end{bmatrix}=\begin{bmatrix}\cos\phi & \sin\phi\\-\sin\phi & \cos\phi\end{bmatrix}\begin{bmatrix}y\\k_y\end{bmatrix}. \tag{7.36}$$

It is also noted that equations (7.36) are based on the Fresnel integration from the $z=0$ plane to the $z=D$ plane after two cylindrical lenses, which relates the electric field distributions between those two planes according to [101]

$$e\left(x,y;z=D\right)=\int_{-\infty}^{\infty}\int_{-\infty}^{\infty}C\exp\left[i\widetilde{\beta}\left(\frac{xx'}{L_1}+\frac{yy'}{L_2}-\frac{\left(x'\right)^2}{2R_1}-\frac{\left(y'\right)^2}{2R_2}\right)\right]\widetilde{e}\left(x,y\right)dx'dy', \tag{7.37}$$

where C is an unimportant constant, $\widetilde{\beta}$ is the scaled, free-space propagation constant ($\widetilde{\beta}=kx_0$) [98, 101],

$$\begin{aligned}&R_i=R_{i0}+d_i,\\&L_i=\left(D-d_i\right)\left(1+d_i/R_{i0}\right),\\&\frac{1}{R_{i0}}=\frac{1}{D-d_i}-\frac{1}{f_i}\quad(i=1,2).\end{aligned} \tag{7.38}$$

After two orthogonal cylindrical lenses with curvature R_{10}, R_{20} and focal lengths f_1, f_2 respectively, the intensity profiles are detected with a CCD camera. The accuracy of the retrieval depends on the resolution and linearity of the CCD camera.

Now a line projection $P_{\theta\phi}$ is introduced as follows:

$$P_{\theta\phi}(x_\theta, y_\phi) = \int_{-\infty}^{\infty}\int_{-\infty}^{\infty} W'(x_\theta, k_\theta; y_\phi, k_\phi)\,dk_\theta dk_\phi . \tag{7.39}$$

The intensity profile at $z = D$, i.e., $|e(x, y; z = D)|^2$, can be expressed as follows

$$|e(x, y; z = D)|^2 = P_{\theta\phi}\left(\left(\tilde{\beta}\sin\theta / L_1\right)x, \left(\tilde{\beta}\sin\phi / L_2\right)y\right), \tag{7.40}$$

where the angles θ, ϕ are related as

$$\theta = -\tan^{-1}\left(R_1 / \tilde{\beta}\right), \quad \phi = -\tan^{-1}\left(R_2 / \tilde{\beta}\right), \tag{7.41}$$

The inverse process to get $W(x, k_x; y, k_y)$ from $P_{\theta\phi}(x_\theta, y_\phi)$ is called the inverse Radon transform. It is noted that for a successful inverse transformation, the angles θ, ϕ should be equally distributed in the interval $(0, \pi)$ [101]. The number of necessary angles for satisfactory exactness of the retrieval depends on the complexity of the Wigner function. The more angles that are used, the more exact results one obtains.

The inverse Radon transform to obtain the Wigner function from intensity images consists of two distinct procedures, first, say, the inverse Radon transform of the x, k_x pairs, then the y, k_y pairs. Because these procedures are mutually independent one can consider only one of the two pairs at a time without loss of generality.

Now consider an arbitrary function $\psi(x_1, x_2)$ in the L_2 functional space. The Radon transform is defined by

$$\Re[\psi](x, \theta) = \int_{-\infty}^{\infty} \psi(x\cos\theta - u\sin\theta, x\sin\theta + u\cos\theta)\,du . \tag{7.42}$$

The Radon transform is equivalently a line projection for a given angle θ, the line of which is parallel to a line through the origin with an angle θ from the reference axis,

say the x axis. Here, x is the distance between two lines. The inverse Radon transform is carried out with Fourier transform as follows:

$$\begin{aligned} M_F(\varpi,\theta) &= F\{\Re[\psi](x,\theta)\}_x \\ &= \int_{-\infty}^{\infty} \Re[\psi](x,\theta)\exp(-i\varpi x)dx \\ &= \int_{-\infty}^{\infty}\int_{-\infty}^{\infty} \psi(x\cos\theta - u\sin\theta, x\sin\theta + u\cos\theta)\exp(-i\varpi x)dudx. \end{aligned} \tag{7.43}$$

Introducing a new variable as

$$\begin{bmatrix} x_1 \\ x_2 \end{bmatrix} = \begin{bmatrix} \cos\theta & -\sin\theta \\ \sin\theta & \cos\theta \end{bmatrix}\begin{bmatrix} x \\ u \end{bmatrix}, \quad \begin{bmatrix} \zeta \\ \xi \end{bmatrix} = \begin{bmatrix} \varpi\cos\theta \\ \varpi\sin\theta \end{bmatrix} \tag{7.44}$$

gives

$$M_F(\zeta,\xi) = \int_{-\infty}^{\infty}\int_{-\infty}^{\infty} \psi(x_1,x_2)\exp(-i\zeta x_1 - i\xi x_2)dx_1dx_2 = F_2[\psi(x_1,x_2)]_{x_1,x_2}. \tag{7.45}$$

Hence, to get $\psi(x_1,x_2)$ one needs to solve the inverse two-dimensional Fourier transform as follows:

$$\begin{aligned} \psi(x_1,x_2) &= F_2^{-1}[M_F(\zeta,\xi)]_{\zeta,\xi} \\ &= \frac{1}{4\pi^2}\int_{-\infty}^{\infty}\int_{-\infty}^{\infty} M_F(\zeta,\xi)\exp(i\zeta x_1 + i\xi x_2)d\zeta d\xi \\ &= \frac{1}{4\pi^2}\int_0^{2\pi}\int_0^{\infty} M_F(\nu,\varphi)\exp(i\nu(x_1\sin\varphi + x_2\cos\varphi)|\nu|d\nu d\varphi, \end{aligned} \tag{7.46}$$

where the integral variables are changed. In practice the integration for the angle ν is carried out as a summation of a number of data sets.

To sum up the modal decomposition is acquired by first getting the mutual intensity profile of the collimated beam after the spherical lens. Then by Fourier transforming each modal solution $\bar{e}^i$ by equation (7.26) and finally calculating each modal coefficient with equations (7.31) and (7.32).

7.2.2. Numerical simulations

To show the feasibility of the proposed algorithm, I next describe simulations with realistic fibre parameters. A step-index fibre with core NA of 0.2 and core radius of 4 μm is considered. The wavelength of the monochromatic beam is 977 nm. These

parameters result in a normalised frequency $V = 5.14$. By using the boundary condition in equation (7.7), the modal numbers l, p and the effective refractive index n_{eff} of each mode was calculated. These are the five LP modes listed in Table 7.1. Note that some modes are split into cosine and sine modes as in equation (7.4) depending on the value of i. Figure 7.2 shows the mode intensity profile of each pair of mode representations $\bar{e}^i(x, y)$ and $\bar{e}_F^i(x, y)$, calculated using equation (7.26).

To evaluate the algorithm, three cases are simulated. In the first case, the exact mutual intensity profile at $z = f$ was assumed to be known (simulation A). To show the practicability of the theory, more simulations were carried out that included retrieval of the mutual intensity profiles by use of the method described in the previous section (simulation B and C). Simulation B assumes the ideal CCD camera response, but the retrieval can be affected by the finite number of pixel points in the CCD array (the number of picture elements). Simulation C included the nonideal response of the CCD camera as well as the finite-grid effect. In simulation C, it was assumed that the image intensity was controlled to be well below the saturation level of the CCD camera by proper attenuation as in [100]. In this case, the non-ideality in CCD camera response is predominantly the intrinsic noise, such as dark current, blooming, shot noise, amplifier noise and quantization noise in the analogue-to-digital converter [104]. The signal-to-noise ratio in a conventional modern CCD cameras is

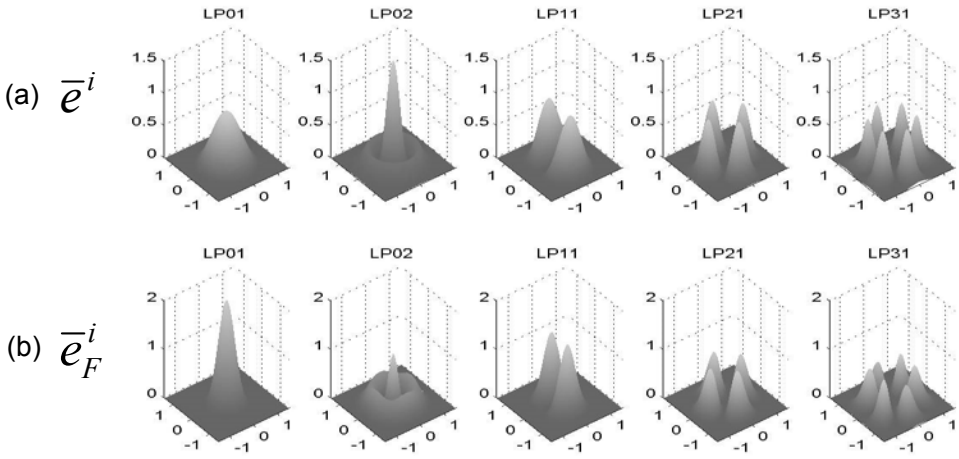

Figure 7.2. The calculated intensity distribution of each mode: (a) the modal solutions inside fibre, (b) the modal solutions after the spherical lens

more than 30 dB. For example, for one CCD camera (COHU 1100) the signal-to-noise ratio is specified at more than 50 dB. On the other hand, reference [104] explains that the overall noise sum is proportional to the averaged mean intensity of an image (which was taken as the sum of all the intensities at each pixel divided by the total number of pixels) and shows that the experimental value for the variance of noise is approximately 1% of the averaged mean intensity. Therefore simulation C includes a normally distributed random noise with variance of 1% of the averaged mean intensity for each image. In addition the linearity (or the photon-electron charge transfer efficiency) of conventional CCD cameras reaches 0.99999 [104]. Therefore the nonlinearity in the response curve was omitted in the simulation.

In the simulations an arbitrary set of test modal power weights $|c_i|^2$ as in table 7.1 were assigned to evaluate the accuracy of the algorithm. For this, a step index fibre with core NA of 0.2 and the core radius of 4 μm is used and the wavelength considered is 977 nm. This results in V number of 5.14. Figure 7.3 shows the intensity of the test multimode beam of concern. Assuming that the collimated free-space beam propagates in free-space according to the Fresnel integration in equations (7.22) and (7.37), one could obtain the calculated CCD images taken at the $z = D$ plane for various values of θ, ϕ.

Modes	Effective Index	Test Modal Weight $\|c_i\|^2$	Calculated Results: Modal Weights $\|c_i\|^2$ (Error (%))		
			Simulation A	Simulation B	Simulation C
LP_{01} cos	1.4686	64	64.03 (0.05)	60.39 (5.64)	60.01 (6.23)
LP_{02} cos	1.4604	25	24.90 (0.40)	27.45 (9.80)	27.53 (10.1)
LP_{11} cos	1.4655	4	3.988 (0.30)	4.391 (9.78)	4.434 (10.9)
LP_{11} sin	1.4655	9	9.045 (0.50)	9.829 (9.21)	9.868 (9.64)
LP_{21} cos	1.4615	1	1.003 (0.30)	1.100 (10.0)	1.093 (9.30)
LP_{21} sin	1.4615	9	9.027 (0.30)	8.630 (4.11)	8.690 (3.44)
LP_{31} cos	1.4570	4	3.981 (0.48)	4.241 (6.01)	4.350 (8.75)
LP_{31} sin	1.4570	1	1.002 (0.20)	0.910 (9.00)	0.894 (10.6)

Table 1. The table lists the modes of the step-index fibre (0.2 NA and 4 μm core radius) considered in the simulations and their effective indices at 977 nm wavelength.

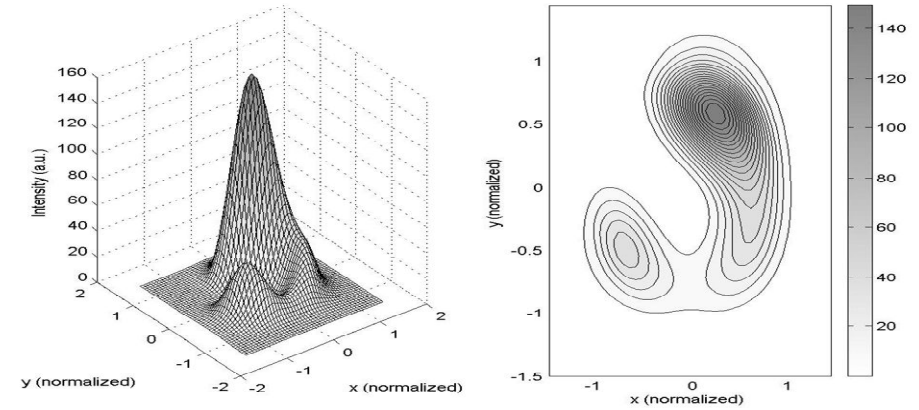

(a) $e(x, y; z = -f)$

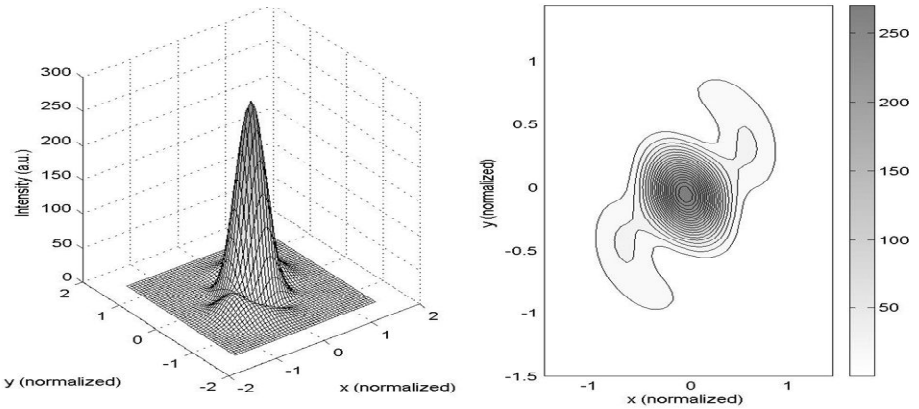

(b) $e(x, y; z = f)$

Figure 7.3. A test multimode beam with arbitrary assigned initial modal power: (a) the beam intensity inside fibre, (b) the free-space beam intensity at $z = f$.

For the numerical verification of our method, each mode was excited with a power represented by the test modal weight. This was then retrieved with three different simulation procedures, A (without retrieval of mutual intensity), B (with retrieval of mutual intensity, but without CCD noise), and C (with retrieval of mutual intensity including CCD noise), with the results shown in the table.

To realise the inverse Radon transform for calculation of the modal power weights, 30 different uniformly distributed angles in the interval $[-\pi/2, \pi/2]$ were used for each combination θ, ϕ. Assuming that the focal lengths of the cylindrical lenses were 20 cm, d_i was varied from 0.87 m to 1.24 m ($i = 1,2$) and D was varied from 1.2 m to 2.0 m to provide full coverage of the required angles θ, ϕ. This is similar to the procedure in reference [100]. Hence the distances d_m and d_M in the relation (7.23)

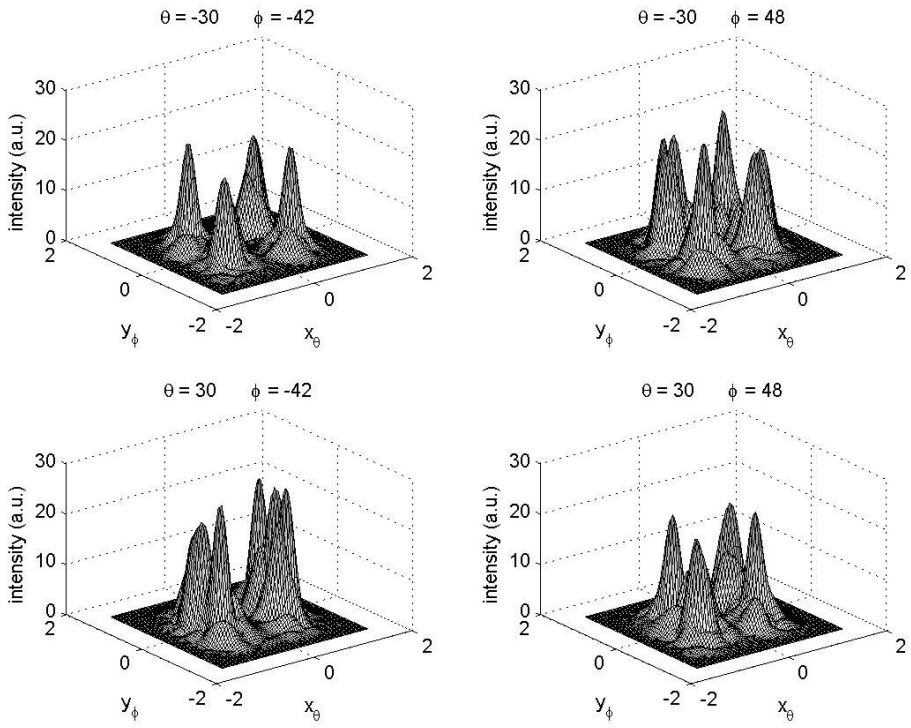

Figure 7.4. Selected CCD images for different θ, ϕ, i.e., with different positions of the lenses and the CCD array.

were 0.87 m and 2 m, respectively, which gave the condition on the focal length f of the spherical lens as 1.4 cm << f << 87 cm. From this the focal length f of the spherical lens was chosen as 11 cm.

In simulation A the modal power weights $|c_i|^2$ were calculated by using the relations (7.29) – (7.32) and by assuming that the exact mutual intensity at $z = f$ was known. In simulation B the values of the $|c_i|^2$ s were calculated by retrieving a mutual intensity profile Γ_F from the intensity patterns after the two cylindrical lenses. Examples of the intensity patterns are shown in figure 7.4 for some values of θ, ϕ. From these intensity patterns the Wigner function at the $z = 0$ plane with the inverse Radon transformation was calculated. From this Wigner function, the mutual intensity profile Γ_F was obtained through a two-dimensional inverse Fourier transform. Now by applying equations (7.29) – (7.32), the modal power weights were calculated as shown in Table 7.1. For simulation C, the same process was used except that a noise was added to the intensity patterns. Figure 7.5 shows the modal power distribution as

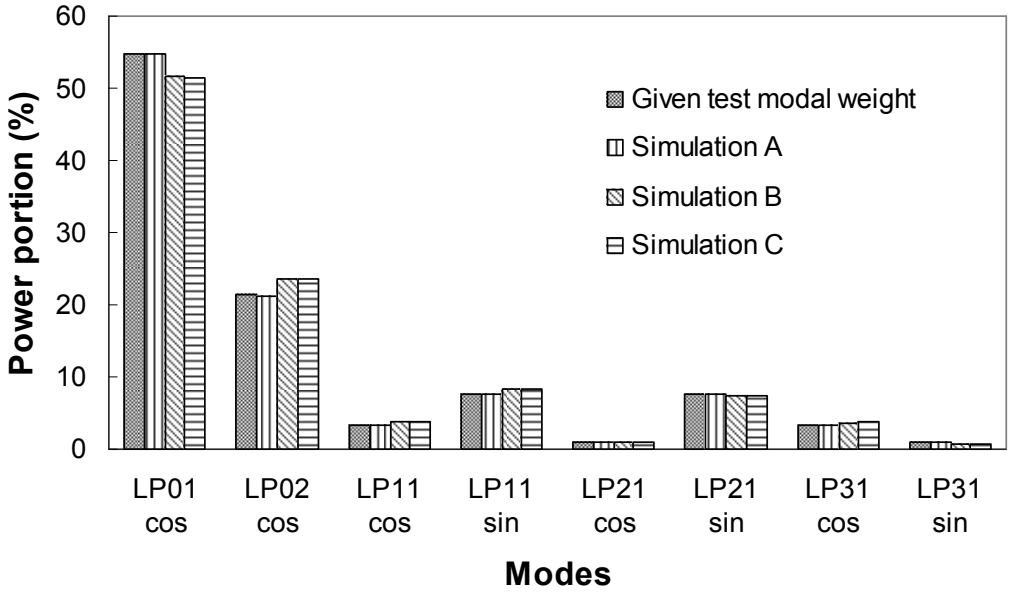

Figure 7.5. The modal power distribution among modes. The test modal power distribution and the results with simulations A, B and C are shown.

a percentage of the total power of the multimode beam. The test modal power distribution and the calculated results from simulations A, B and C are also shown.

Figure 7.6 shows a comparison between the intensity profiles of the test multimode beam inside the fibre and the calculated reconstructed beam. Note that it is impossible to reconstruct the multimode image by using the calculated $|c_i|^2$. For a full reconstruction, the phases must also be known. (Note that the retrieved modal power distribution is independent of the randomly assigned phases.) However, purely for demonstration purposes it was assumed that all the test modal weights are positive numbers with zero phase. The reconstruction through simulation A is almost exact, while simulations B and C resulted in some discrepancy. In the simulations, 50 grid points along each of the x and y axes were used, i.e., 2500 points for one image. The errors between the initially assigned modal weights and the calculated ones were within 0.5% for simulation A and within 10% and 11% for simulation B and C, respectively. This implies that the proposed method of calculating modal distribution is quite accurate provided the mutual intensity profile is known sufficiently well.

Since the difference in errors between simulation B (without noise) and simulation C (with noise) was approximately within 1%, it was concluded that the main cause of the simulation errors in simulation B and C was the limited number of position pixels

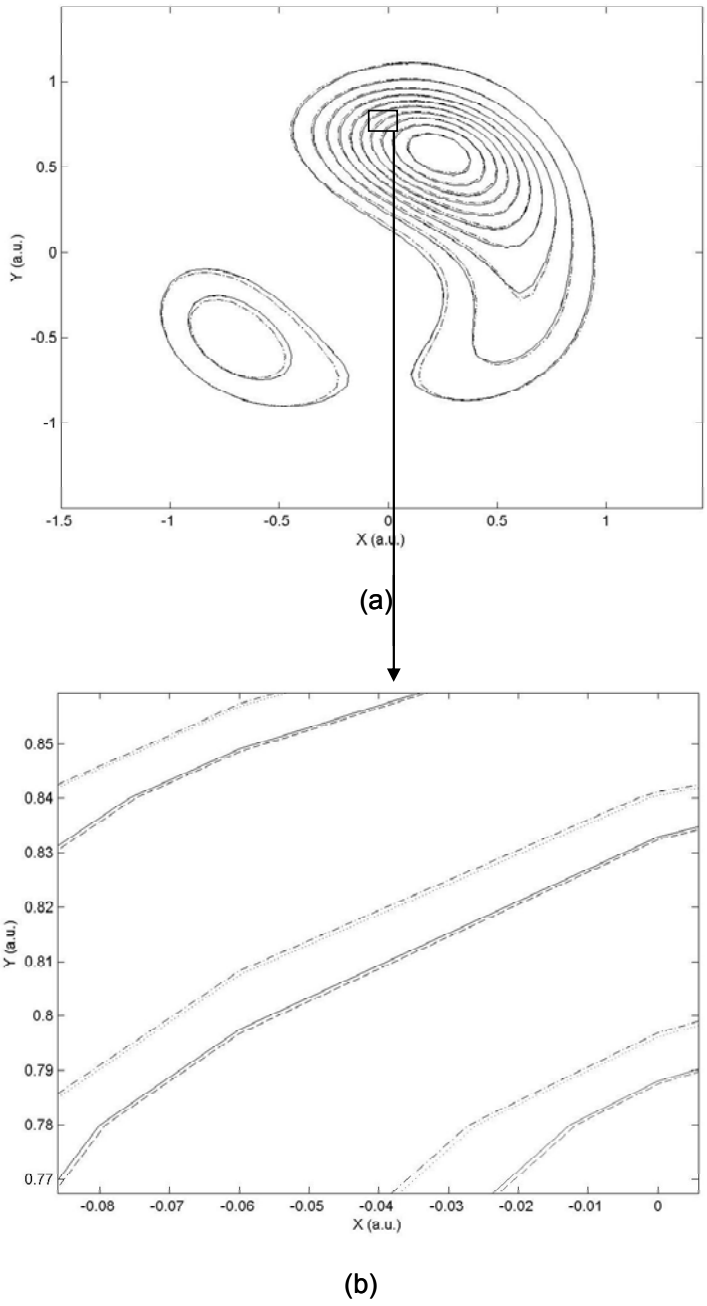

Figure 7.6. Comparison between the test multimode beam and reconstructed beam from calculated results. The figure shows the intensity pattern of the test multimode beam inside the fibre (solid line), the reconstructed image from simulation A (dashed line), the reconstructed image from simulation B (dotted line), and the reconstructed image from simulation C (dash-dotted line). Figure 7.6(b) is a magnified portion of figure 7.6(a) to clarify the small differences between results.

and angles rather than the noise. Therefore the finer the grids and the more pixel points one uses, the more accurate the results one obtains, even in the presence of noise. For instance, the retrieval of the Wigner function from the CCD camera through the Radon transform depended on the number of angles, while the retrieval of mutual intensity profiles from the Wigner function by Fourier transform depended on the number of image pixels. Considering that CCD images normally provide more than 256×256 pixel data points, the accuracy might be quite satisfactory provided that limitations such as a nonlinear response are controlled. In addition, a larger number of angles can be used for more accurate results.

7.3. Modal power decomposition using wavelength sweeping method

The previous section described the modal power decomposition method using image processing. Although the theoretical prediction showed an excellent result, the required experimental procedures are demanding since the number of images required for a sufficient modal power decomposition is large. In the previous section, 900 images are used for full modal decomposition. But, a video camera with a zoom lens acquires 25 images per second, so it seems quite realistic to acquire a very large number of images with different lens positions. One possible practical problem is that one may not easily achieve the required lens positions using commercially available video camera with a zoom lens. Therefore, in collaboration with Dr. Valery Philippov at the ORC, an alternative method using less images and easier measurement procedures was invented. The resulting method is so-called ‘wavelength sweeping modal power decomposition’, which will be explained shortly.

In this section a theory for wavelength sweeping modal power decomposition is presented. A numerical simulation evaluates the developed theory.

7.3.1. Theory

The basic principle used in the method is that each mode has a different propagation constant and so a different delay in the fibre. Therefore if one sweeps the wavelength of the optical source of concern in a saw-tooth shape, the resulting image at the fibre end will contain beat patterns. By analyzing those beat patterns, one can obtain the modal power decomposition.

For the theoretical development, several assumptions were made. First of all, a weakly guiding multimode waveguide is considered so that only linearly polarised (LP) modes are treated. In addition, the sine and cosine modes of a certain mode superpose together to form an elliptical mode, which is treated a single mode in this method. The others are

(1) There is no mode coupling during the propagation of the multimode beam inside the fibre.

(2) Despite the changing wavelength, the change of the effective refractive index associated with each mode along the different wavelength is negligible.

(3) When there are N excited modes with corresponding effective refractive index n_{eff}^{i} ($i = 1,..,N$), all the pairs $\left|n_{eff}^{i} - n_{eff}^{j}\right|$ are distinct values from each other and do not coincide.

The assumption (1) is justified when one considers relatively short fibre lengths. Besides when mode coupling is included, the theoretical derivation may become too complicated to solve. The assumption (2) is justified when the wavelength sweeping range is within a few GHz while the carrier optical frequency exceeds several tens of THz. The assumption (3) is vital in the theoretical development. If some of those differences of the refractive indices coincide it is not possible to decompose the modal powers using this method, which will become clear later. Furthermore it will be shown that this method cannot decompose a beam consisting of only two excited modes. However one of the biggest advantages of this method against the former image processing method is that one does not require an *a priori* knowledge of the individual modal intensity. Instead these are obtained through the experimental procedure. Thus, one can also consider the method to be a way to measure the modal intensity profiles of a multimode fibre.

Figure 7.7 shows the conceptual setup for the proposed method. A wavelength-modulated continuous-wave (i.e., constant instantaneous power) source is launched into a multimode fibre. This source is assumed to be a monochromatic tuneable source. Furthermore, the source should have the same output power over the wavelength range of tuning. The wavelength of the optical source is modulated as a saw-tooth type with the following instantaneous optical frequency:

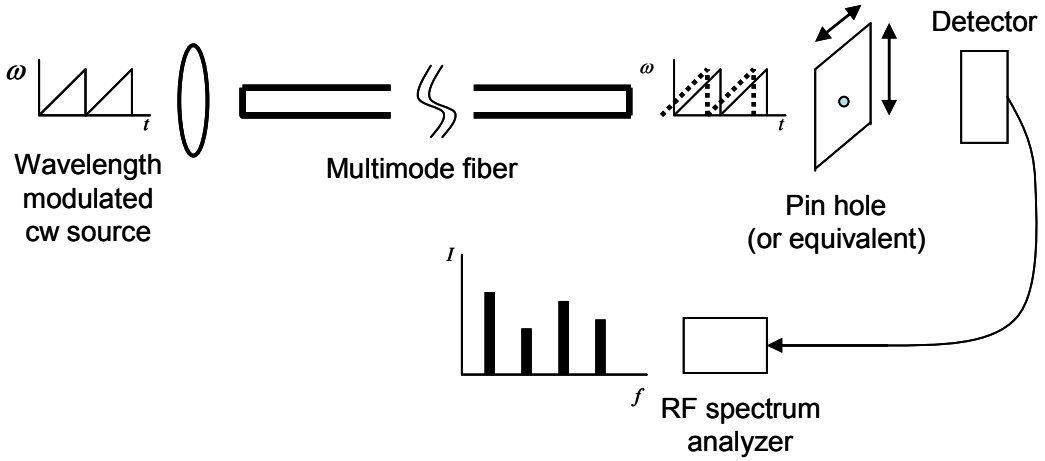

Figure 7.7. Schematic of the setup for the modal power decomposition with the wavelength sweeping method.

$$\omega(t) = (F_\omega / T_0)\,\mathrm{mod}(t, T_0) + \omega_0, \tag{7.47}$$

where $\mathrm{mod}(t, T_0) = t - nT_0$ and n is the greatest integer which makes $t - nT_0$ a non-negative number. Then the launched beam may excite a number of guided modes inside the fibre. Since the propagation constants of excited modes are different each mode will experience a different delay (in phase) in reaching the fibre end. When the multimode beam reaches the end of the fibre the differently delayed modes will interfere with each other forming a certain (time-varying) intensity distribution. One may then use a pin-hole (or equivalent) to obtain the (time-varying) spatial distribution of the image. Finally an RF (radio-frequency) spectrum analyzer detects the (time-varying) optical signal, i.e., the beat signal, at each spatial point.

Now assume there are N excited modes inside the multimode fibre. The task is to find the modal power distribution, which does not change during the propagation inside the fibre due to the assumption (1). If the launching end is denoted as $z = 0$ (z axis is parallel to the propagation axis), the multimode beam at $z = 0$ is described as a weighted superposition of each guided mode such as

$$\psi(x, y; z = 0) = \sum_{m=1}^{N} c_m e_m(x, y) \exp\left[-i\omega(t)t\right], \tag{7.48}$$

where c_m is the complex modal weight and e_m is the normalised modal field of the solution to the Helmholtz equation (7.2). Then the target is to find all the $|c_m|$'s and e_m's. After a propagation distance of L, the field can be described as

$$\psi(x,y;z=L)=\sum_{m=1}^{N} c_m e_m(x,y)\exp\left[-i\left\{\omega\left(t-\Delta t_m\right)\right\}\left(t-\Delta t_m\right)\right], \qquad (7.49)$$

where Δt_m is the propagation (phase) delay of each mode and is described as

$$\Delta t_m=\int_0^L \frac{dl}{v_p^m(l)}, \qquad (7.50)$$

where $v_p^m(l)$ is the phase velocity of mode m at $z=l$. The phase velocity of each mode is again given by $v_p^m(l)=c/n_{eff}^m$ where n_{eff}^m is the effective refractive index of mode m. Rigorously, n_{eff}^m is a function of wavelength and therefore a function of time (since wavelength changes with time). However due to the assumption (2), one can assume that n_{eff}^m is a constant and consequently the phase velocity v_p^m is also a constant. Then the time delay Δt_m is simply given by $\Delta t_m = Ln_{eff}^m/c$. One might question why the phase velocity is used instead of the group velocity in the equation (7.50). The optical source is frequency-modulated, i.e., the phase is modulated and, hence, the phase delay should be considered. In this case the different phase velocity causes the phase delay.

On the other hand, the discontinuity as the wavelength sweep resets complicates the theory. The discontinuity will disrupt the otherwise well establishing beat pattern at the measuring screen. The most straightforward way to handle this in practice is to simply time-gate the measurement and reject data while the sweep resets. However this may not even be necessary, as the discontinuity can be expected to produce a relatively broad and indistinct background to the frequency spectrum of the modal beats. It is quite possible that such a background will not cause any problems. Hence, the discontinuity is not considered in this theoretical treatment.

Then the intensity pattern at $z=L$ becomes

$$
\begin{aligned}
I(x,y;z=L) &= \psi(x,y;z=L)\psi^{*}(x,y;z=L) \\
&= \sum_{m=1}^{N}\left|c_m e_m(x,y)\right|^2 + \sum_{l=1}^{N-1}\sum_{p=l+1}^{N}\left\{c_l c_p^{*} e_l(x,y) e_p^{*}(x,y)\exp\left[i\phi_{lp}(t)\right] + c.c.\right\} \\
&= \sum_{m=1}^{N}\left|c_m e_m(x,y)\right|^2 + \sum_{l=1}^{N-1}\sum_{p=l+1}^{N}\left\{2\left|c_l\right|\left|c_p\right|\left|e_l(x,y)\right|\left|e_p(x,y)\right|\cos\left[\phi_{lp}(t)+\phi_0\right]\right\},
\end{aligned}
\tag{7.51}
$$

where the asterisk (*) represents the complex conjugate and 'c.c.' represents the complex conjugate of the previous term. The phase term $\phi_{lp}(t)$ in equation (7.51) is given as

$$
\phi_{lp}(t) = \left[\frac{F_\omega}{T_0}\bmod\left(t-\frac{L}{c}n_{eff}^{l},T_0\right)+\omega_0\right]\left[t-\frac{L}{c}n_{eff}^{l}\right] - \left[\frac{F_\omega}{T_0}\bmod\left(t-\frac{L}{c}n_{eff}^{p},T_0\right)+\omega_0\right]\left[t-\frac{L}{c}n_{eff}^{p}\right]
\tag{7.52}
$$

and ϕ_0 is a constant. Now consider the instantaneous frequency of the interference pattern $I(x,y;z=L)$ in equation (7.51). The instantaneous frequency of the intensity pattern is given by the time derivative of the phase term such that $\omega_{inst}^{lp}(x,y;z=L) = \partial\phi_{lp}(t)/\partial t$, which yields

$$
\omega_{inst}^{lp}(x,y;z=L) = \frac{2F_\omega L}{T_0 c}\left|n_{eff}^{l} - n_{eff}^{p}\right|.
\tag{7.53}
$$

Therefore there should be ${}_N\mathrm{C}_2\left(=N(N-1)/2\right)$ number of different instantaneous frequency components ω_{inst}^{lp}'s as is assumed in assumption (3). Then the RF spectrum analyzer detects such $N(N-1)/2$ number of distinct frequency components providing the associated amplitude as well. This associated amplitude Γ_{lp} at point (x,y) with instantaneous frequency ω_{inst}^{lp} is given as

$$
\Gamma_{lp}\left(x,y;\omega_{inst}^{lp} = D\left|n_{eff}^{l} - n_{eff}^{p}\right|\right) = 2\left|c_l\right|\left|c_p\right|\left|e_l(x,y)\right|\left|e_p(x,y)\right|,
\tag{7.54}
$$

where $D \triangleq 2F_\omega L/T_0 c$. The amplitude Γ_{lp} could be named as 'modal field cross-correlations'. Therefore it is proved that one can obtain $N(N-1)/2$ number of modal

field cross-correlations through the experimental procedure. For further convenience the modal field cross-correlations Γ_{lp} are decomposed as

$$\Gamma_{lp}\left(x,y;\omega_{inst}^{lp}\right)=2\Phi_{l}\left(x,y\right)\Phi_{p}\left(x,y\right), \tag{7.55}$$

where $\Phi_{i}\left(x,y\right)=\left|c_{i}\right|\left|e_{i}\left(x,y\right)\right|$.

It is possible to choose the parameters F_{ω} and T_0 so that the instantaneous frequencies $\omega_{inst}^{lp}=D\left|n_{eff}^{l}-n_{eff}^{p}\right|$ fall into the observable range of typical RF spectrum analyzers (see equation (7.53)). Therefore using this method, one can obtain the modal field cross-correlations successfully. In fact it is possible to obtain the intensity pattern set $\left\{\Theta_{1}\left(x,y\right),\ \Theta_{2}\left(x,y\right),\ ...,\ \Theta_{N(N-1)/2}\left(x,y\right)\right\}$ (with total $N\left(N-1\right)/2$ elements) and the associated instantaneous frequencies $\left\{\omega_{1},\ \omega_{2},...,\ \omega_{N(N-1)/2}\right\}$ through this measurement. If one has the *a priori* information of the modal intensity pattern $e_{i}\left(x,y\right)$ it is straightforward to find the corresponding modal field cross-correlations from the measured intensity patterns. However a problem arises when one does not have such *a priori* knowledge of the modal intensity patterns. For this, one needs a mathematical trick as follows.

The key idea is to use the measured instantaneous frequency information $\left\{\omega_{1},\ \omega_{2},...,\ \omega_{N(N-1)/2}\right\}$. Using this information all $\left\{\left|\Phi_{1}\right|,\left|\Phi_{1}\right|,...,\left|\Phi_{N}\right|\right\}$ are found first. Once these are found it is straightforward to find the modal power distribution $\left|c_{i}\right|^{2}$'s and the associated unknown $\left|e_{i}\left(x,y\right)\right|^{2}$'s, which will be explained later. For simplicity, it is assumed that the notation of ω_{i}'s is in the ascending fashion so that $\omega_{i}<\omega_{j}$ if $i<j$. Then the largest instantaneous frequency $\omega_{N(N-1)/2}$ must correspond to the case for $\omega_{N(N-1)/2}=D\left|n_{eff}^{\max}-n_{eff}^{\min}\right|$ where $n_{eff}^{\max}$ and $n_{eff}^{\min}$ denote the largest and the smallest effective refractive indices of the excited modes, respectively. Hence one knows that the associated measured intensity pattern $\Theta_{N(N-1)/2}$ is in fact $\Theta_{N(N-1)/2}=\Gamma_{\max,\min}=2\Phi_{\max}\Phi_{\min}$. Now one should be able to find $N-2$ number of the instantaneous frequency pairs $\left(\omega_{i},\omega_{j}\right)$ such that

$$\Omega = \left\{ \left(\omega_i, \omega_j \right) \middle| \, \omega_i + \omega_j = \omega_{N(N-1)/2}, \, \omega_i \le \omega_j \right\}. \tag{7.56}$$

since $\omega_i + \omega_j = \omega_{N(N-1)/2}$ implies $D\left|n_{eff}^{\max} - n_{eff}^{k}\right| + D\left|n_{eff}^{k} - n_{eff}^{\min}\right| = D\left|n_{eff}^{\max} - n_{eff}^{\min}\right|$ and the number of such n_{eff}^{k} is $N-2$ between $n_{eff}^{\min}$ and $n_{eff}^{\max}$. Now one of the pairs $\left(\omega_i, \omega_j\right)$ in the set Ω is chosen. Then one has two sets of algebraic equations

$$\begin{cases} 2\Phi_{\max}\, \Phi_k \;\; = \Theta_i, \\ 2\Phi_k \;\; \Phi_{\min} = \Theta_j, \\ 2\Phi_{\max}\, \Phi_{\min} = \Theta_{N(N-1)/2}, \end{cases} \tag{7.57a}$$

or

$$\begin{cases} 2\Phi_{\max}\, \Phi_k \;\; = \Theta_j, \\ 2\Phi_k \;\; \Phi_{\min} = \Theta_i, \\ 2\Phi_{\max}\, \Phi_{\min} = \Theta_{N(N-1)/2}, \end{cases} \tag{7.57b}$$

since it is not known whether Θ_i is $2\Phi_{\max}\Phi_k$ or $2\Phi_k\Phi_{\min}$. Fortunately both cases give the same solution

$$\left|\Phi_k\left(x,y\right)\right| = \frac{1}{2}\sqrt{\frac{\Theta_i\left(x,y\right)\Theta_j\left(x,y\right)}{\Theta_{N(N-1)/2}\left(x,y\right)}}. \tag{7.58}$$

Please note that the right hand side of equation (7.58) is the measured data. Therefore one has just identified $\left|\Phi_k\right|$. The identified $\left|\Phi_k\right|$ is named as $\left|\Phi_1\right|$ for convenience. Now by picking another pair of $\left(\omega_i, \omega_j\right)$ in the set Ω and finding another $\left|\Phi_k\right|$ using the equation (7.58) it can be named as $\left|\Phi_2\right|$. If one repeats this procedure $N-2$ times, one can find $N-2$ number of $\left|\Phi_k\right|$'s. Now the so far unknown two $\left|\Phi_{N-1}\right|$ and $\left|\Phi_N\right|$ can be found as follows. First of all pick any known $\left|\Phi_k\right|$ ($1 \le k \le N-2$). Then by equations (7.57) and (7.58), the following can be calculated.

$$\left|\Phi_{N-1}(x,y)\right| = \sqrt{\frac{\Theta_i(x,y)\Theta_{N(N-1)/2}(x,y)}{\Theta_j(x,y)}},$$
$$\left|\Phi_N(x,y)\right| = \sqrt{\frac{\Theta_j(x,y)\Theta_{N(N-1)/2}(x,y)}{\Theta_i(x,y)}}. \tag{7.59}$$

Please note that one does not know whether $|\Phi_N|$ is $|\Phi_{\max}|$ or $|\Phi_{\min}|$, which in fact does not affect the final outcome. Therefore all the $\{|\Phi_1|,|\Phi_1|,...,|\Phi_N|\}$ values have now been found. The modal power distribution $|c_i|^2$'s and the associated (normalised) modal intensity can be found as follows:

$$|c_i|^2 = \int_{A_\infty} |\Phi_i|^2 \, dA, \qquad |e_i(x,y)|^2 = \frac{|\Phi_i|^2}{|c_i|^2}. \tag{7.60}$$

7.3.2. Numerical simulation

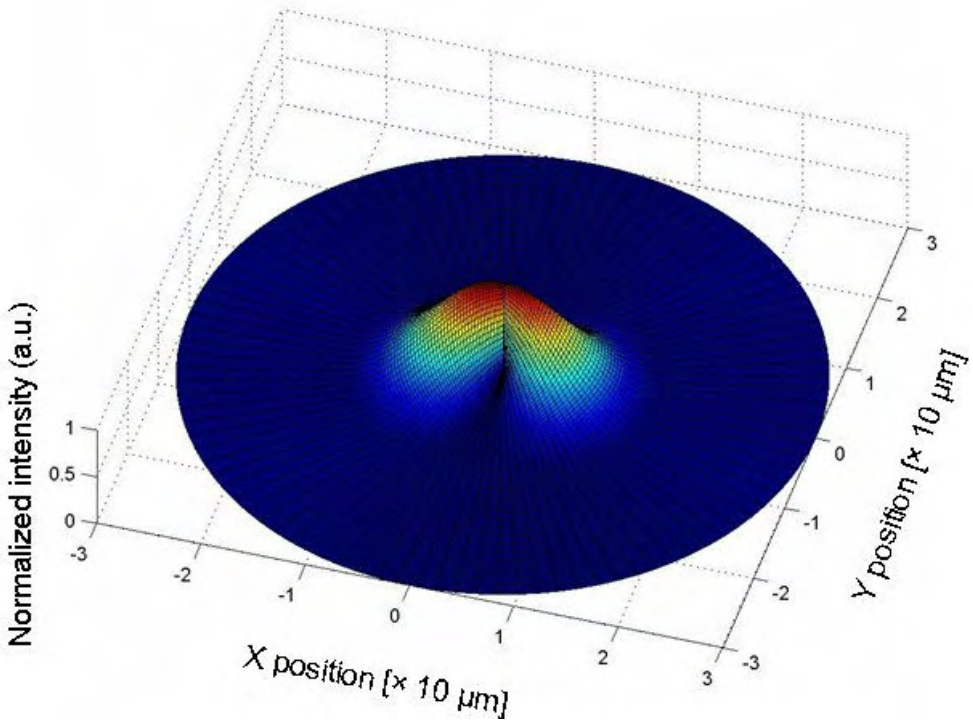

Figure 7.8. The intensity distribution of the test multimode beam inside the fibre. The beam is a combination of LP_{01} (4 W), LP_{11} (2 W), LP_{02} (3 W), and LP_{12} (1 W) modes.

In this section, a numerical simulation is presented evaluating the developed theory. For this a multimode fibre with core radius 15 μm and 0.15 NA is considered, with a signal wavelength of 1.06 μm. I assumed that four modes, namely, LP_{01}, LP_{11}, LP_{02}, and LP_{12} are excited. For evaluation the initially assigned modal powers are 4, 3, 2, and 1 W, respectively. Figure 7.8 shows the multimode beam of concern. In the multimode beam, the phases of each mode are all in phase. However, the proposed method does not depend on the phase of each mode so that it is applicable also to the randomly distributed mode phases.

Once the multimode beam propagates through the fibre with length L, the RF spectrum analyzer will detect six ($=_4C_2$) distinct frequencies in total. Figure 7.9 shows an RF spectrum for one spatial point of the $x-y$ plane. One can scale the frequencies appearing in the RF spectrum analyzer by varying F_ω, T_0 for a given fibre length L, and figure 7.9 shows a normalised frequency instead of the real frequency. As is expected there appear six distinct frequency components in the RF spectrum. Note that the RF spectrum reveals only the amplitude and the associated frequency. By scanning the $x-y$ plane of concern to obtain each RF spectrum as shown in figure 7.9 (for one point in the $x-y$), one can obtain 6 images as shown in figure

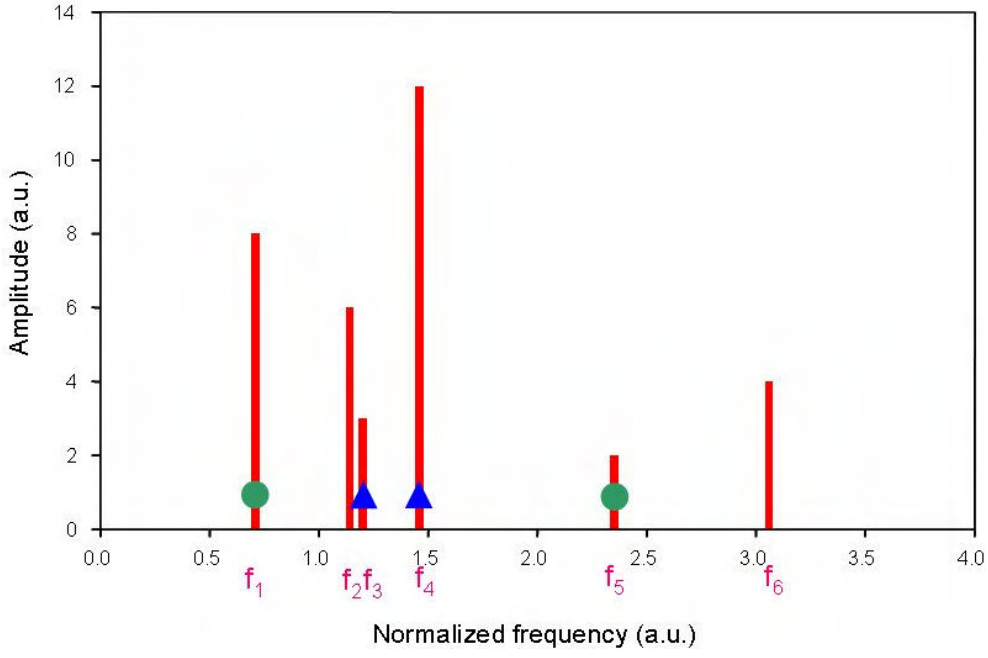

Figure 7.9. An example of the RF spectrum of the experimental procedure. There appear six distinct frequency components.

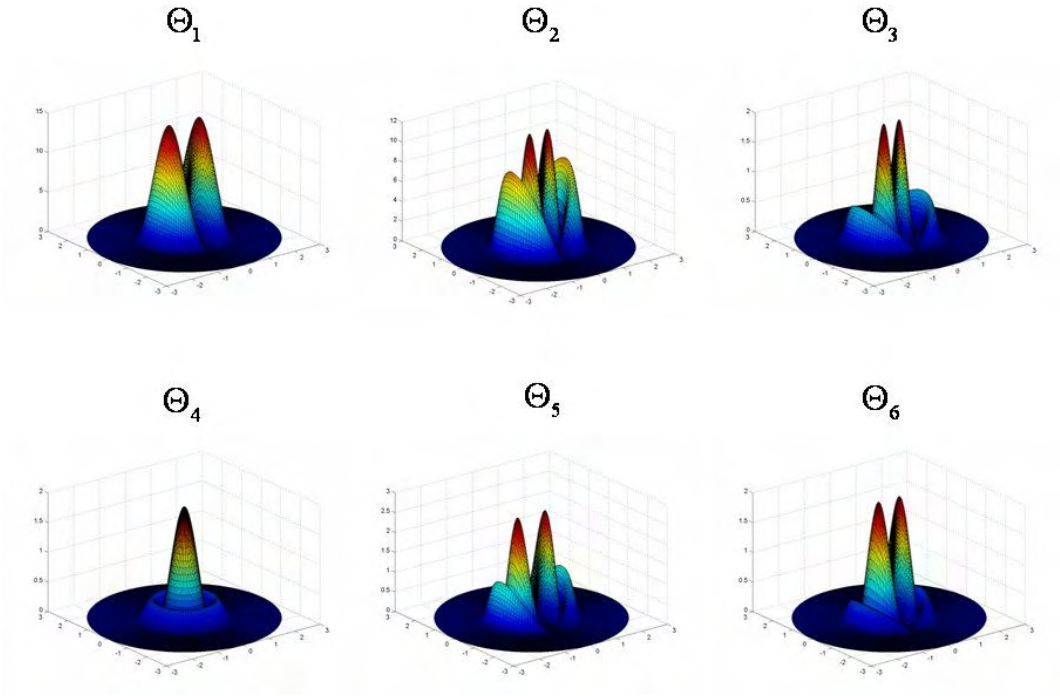

Figure 7.10. The associated intensity patterns for each frequency.

7.10. Each image $\Theta_1, \Theta_2, \cdots, \Theta_6$ is associated with each distinct frequency component $f_1, f_2, \cdots, f_6$, respectively.

Apparently the frequency f_6 (which is the largest) and the associated image represent the modal field cross-correlation of the LP_{01} mode (the largest effective refractive index) and the LP_{12} mode (the smallest effective refractive index). Then as explained in the previous theory section, one can find two pairs of frequencies, the sum of which are equal to f_6. These pairs are (f_1, f_5) and (f_3, f_4). Then from Θ_1, Θ_5, and Θ_6 and using the equations (7.58), (7.59) and (7.60) , the first obtained mode weight and the associated modal intensity can be found. One simply names this first mode as Mode 1. Again from Θ_3, Θ_4, and Θ_6 one obtains the second mode, Mode 2 with a similar method. The last two modes are found from the already obtained Mode 1 and Θ_3, Θ_4, and Θ_6 using the equation (7.59). Figure 7.11 shows the results of the modal power decomposition. The figure shows the obtained normalised intensity patterns of the Mode 1, Mode 2, Mode 3, and Mode 4 with associated modal power weight.

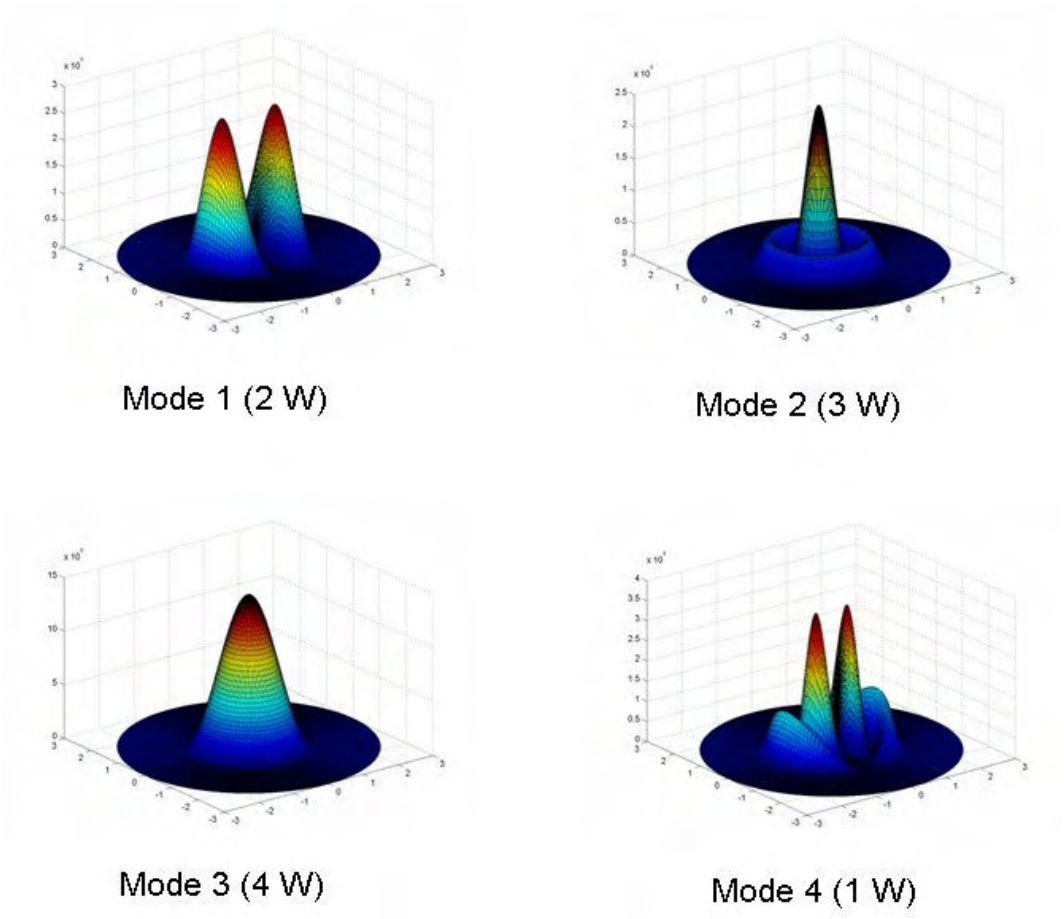

Figure 7.11. The result of the modal power decomposition. Both the obtained normalised mode intensity patterns and the associated modal weights are presented. In each graph, the unit of X- and Y-axis is [×10 μm].

One of the disadvantages of this method is that the information of the effective refractive index for each specific mode is not obtained. Only the normalised modal intensity patterns and the associated modal power weight are found. However, even if the effective refractive index is not known, there is no serious problem to obtain the beam propagation characteristics. For instance once the normalised mode intensity pattern is known, one can easily predict the M^2 value of this specific mode using the method in appendix B. Therefore the more critical information for characterizing the beam quality is the normalised mode intensity patterns with associated modal power distribution rather than the effective refractive indices of each mode. Saying this, the proposed method perfectly characterises the multimode beam and can be used to predict the free-space running beam from this multimode beam.

7.4. Summary

In this chapter, modal power decomposition methods were presented. Proposed modal power decomposition methods are based on intensity measurement so that robust result against environmental uncertainty may be obtained. The first method uses the image processing method of Wigner function followed by inverse Radon transform whereas the second one adopts a wavelength sweeping source to obtain interferometric frequencies between modes. The feasibilities of both methods are verified through numerical simulation results.

Chapter 8. Conclusions and future prospects

This thesis presented work I carried out on wavelength-selective waveguide structures. It was shown theoretically and experimentally that these proposed wavelength-selective waveguides can suppress emission at unwanted wavelengths. The wavelength-selective waveguides enable cladding-pumped high-power fibre lasers operating at specific desired wavelengths that would otherwise be suppressed by unwanted emission from other, stronger, spectral bands. In fibre lasers, amplified spontaneous emission at wavelengths other than the desired signal wavelength may build up to significant power levels. It can degrade significantly the gain and efficiency at the desired signal wavelength. It is then important to suppress emission at unwanted wavelengths. Among many wavelength-suppression methods, waveguide filters offer several advantages over other alternatives. First of all the filtering takes place in the fibre itself rather than in an external filter, with implications for loss, power handling, and component count. Secondly, when the gain fibre itself acts as a distributed spectral filter, it can ensure everywhere that there is no net gain for the unwanted wavelengths. Then, there is no build-up of amplified spontaneous emission. Therefore fibre lasers adopting waveguide filters are compact and efficient compared to other alternatives.

Helical fibres (Chapter 3), W-type fibres (Chapter 4) and depressed-clad hollow fibres (Chapter 5) were proposed for filtering out longer wavelengths. A modified W-type fibre (Chapter 6) was proposed for filtering out shorter wavelengths. Since rare-earth doped fibres have several emission bands, one can use either short-wavelength pass waveguides or long-wavelength pass waveguides to suppress unwanted emission at competing wavelengths. In order to design efficient fibres, I carried out numerical simulations. This was done with a numerical fibre laser simulator which was developed. The simulator was spectrally, longitudinally, and transversally resolved.

Important features such as bending loss properties and output beam quality of the fibre designs were also investigated.

8.1. Summary of the contribution

Below are the contributions made towards the advancement of high-power cladding-pumped fibre lasers operating at a desired wavelength on a weak transition through the use of wavelength-selective waveguides. Included is a summary of each fibre design and its application to cladding pumped fibre lasers.

- **Helical-core fibres**: Chapter 3 described the feasibility of a high power Nd^{3+}-doped fibre laser operating at 0.9 μm while suppressing the competing 1.06 μm emission by adopting a helical core. The principle is to use wavelength-dependent bending loss. Since bending loss at longer wavelengths is larger than that at shorter wavelengths, a helical fibre can act as a long-wavelength rejection filter. The theoretical results show that there exists a helical fibre design, which enables efficient operation of the fibre laser at 0.9 μm. However it was shown that the fibre design is not robust against a small deviation from the intended design. The bending loss property of such helical fibres is very sensitive to small deviations of fibre parameters. Therefore in order to realise a helical fibre laser operating at shorter wavelengths, the fabrication process would have to be much more advanced than the current status to enable more accurate fabrication.
- **W-type fibres**: The W-type fibre employed a negative volume refractive index. Therefore the fibre had a fundamental-mode cut-off wavelength above which no wavelengths were guided in the core. Using this type of fibre a cladding-pumped tuneable Nd^{3+}-doped fibre laser operating at 0.9 μm was experimentally demonstrated. However although the W-type refractive index core successfully suppressed the unwanted longer-wavelength emission, the signal suffered from a relatively large bending loss. In addition, it is difficult to realise a large core area, as needed to improve the pump absorption as well as for pulsed fibre sources with high pulse energies and peak powers. Nevertheless, a 4 W 0.9 μm Nd^{3+}-doped fibre laser was realised. It had a slope efficiency of 40% and a threshold pump power of 1 W, both with respect to

launched pump power. It had a diffraction limited output. This experimental result was the first demonstration of a cladding-pumped Nd^{3+}-doped fibre laser tuneable at ~0.9 μm and operating at room temperature.

- **Depressed-clad hollow fibres**: Following on from the W-type fibre, a depressed-clad hollow fibre was investigated. This fibre had a hole in the centre, which acted as a huge negative volume refractive index. This allowed more freedom in the fibre design, which allowed me to fine-tune the mode characteristics, including the bending loss properties. It was theoretically demonstrated that using a carefully designed depressed-clad hollow fibre, one can realise an efficient Yb^{3+}-doped fibre laser operating at 0.98 μm. The advantages of such depressed-clad hollow fibres over the already demonstrated JAC Yb^{3+}-doped fibre [34, 35] are as follows. First of all, the larger cladding area enables the use of a more powerful diode pump source to scale up the output power. Although pump brightness is crucial for 0.98 μm Yb^{3+}-doped fibre lasers, it is also possible to reduce the pump brightness somewhat. Secondly a larger core area is possible which increases the extractable pulse energy. A 3 W 0.98 μm Yb^{3+}-doped fibre laser was demonstrated with 34% slope efficiency and a 9.2 W threshold pump power, both with respect to the launched pump power. The relatively low efficiency and the large threshold pump power are ascribed to the bending loss. Since the operating wavelength (0.98 μm) is close to the competing wavelength (1.03 μm), the bending loss at the signal wavelength may be large enough to degrade the performance. Theoretically it was shown that a careful design of the fibre may overcome the bending loss at 0.98 μm while suppressing the 1.03 μm emission.
- **Modified W-type fibres**: In addition to the short wavelength pass filters, modified W-type fibres were presented in chapter 6, which were aimed to achieve a high gain at long wavelengths while suppressing emissions at short wavelengths. Two designs were introduced. A modified W-type refractive index profile with an outer raised ring provided a good overlap factor for long wavelengths relative to that for short wavelengths by confining the short wavelength into the undoped core and by locating the Nd^{3+}-dopants in the outer ring. In addition, a modified W-type refractive index profile with a

raised ring with still higher index is also introduced. This design confines short-wavelength LP_{01}-modes into the outer ring while long-wavelength modes remain in the core. They were further investigated in the context of Nd^{3+}-doped fibres operating at ~ 1.38 μm. There are three main issues to overcome in order to realise an efficient amplifier and laser operating at 1.38 μm, namely, ESA, OH^--ion absorption, and strong amplified spontaneous emission at 1.06 μm. Whereas the effect of ESA can be minimised by selecting hosts with less ESA and OH^--ion absorption may be reduced by high purity fabrication technique, the strong amplified spontaneous emission at 1.06 μm can be avoided with a long-pass filter designed into the fibre. Numerical simulations adopting the designed long-pass filter were presented for an amplifier and a laser operating at 1.38 μm assuming silica fibres with a typical amount of OH^- ions. ESA restricts the short-wavelength tuning range, which becomes 1345 nm to 1450 nm for the amplifier and 1355 nm to 1445 nm for the laser. The OH^--ion absorption can seriously degrade the gain and efficiency at 1.38 μm. If the OH^--absorption is eliminated, the slope efficiency of the fibre laser reached 57% at 1.38 μm, which is near the quantum limit. Such excellent characteristics for the 1.38 μm band are possible with high-purity fibre fabrication and a fibre waveguide structure that efficiently suppresses the (otherwise) strong amplified spontaneous emission at 1.06 μm.

- **Modal power decomposition**: Chapter 7 described modal power decomposition to better characterise the transverse properties of the output beam from a fibre. Two methods were proposed for modal power decomposition. These require no phase information so rely only on intensity measurements. Intensity measurements are superior to interferometric measurements in terms of reliability of measured data. The first method utilises an image processing technique, adopting an inverse Radon transformation and a Wigner function approach. Using this method, it was theoretically demonstrated (using realistic simulations) that a multimode fibre laser beam can be successfully decomposed into fibre modes by taking many images at different distances from the fibre source. Due to the large number of images required for the first method, an alternative second method was proposed using a wavelength sweeping technique. The principle is based on the different phase velocities of the different modes propagating through a

multimode optical fibre. With a wavelength-swept source, after a certain length of propagation, each mode will interfere with other modes so that beat signals result at different discrete frequencies. By analyzing the image associated with each frequency, one can obtain the modal power decomposition.

The advantage of the second method compared to the first one is that one does not require any *a priori* knowledge of the modes (i.e., the modal intensity patterns of each mode). During the process, both the unknown mode profiles for each mode and the power distribution among modes are obtained. by contrast, the first method does require an *a priori* knowledge of the mode intensity pattern of each mode. In addition, the second method requires only ${}_N C_2 \left(= N\left(N-1\right)/2\right)$ images (N is the number of modes of concern) whereas the first method used 900 images (with different distances of the CCD camera from the optical source). Nevertheless, the first method characterises the beam out of the fibre source (it is applicable to a black box fibre sources regardless of the configuration inside since it uses only the output beam from the source) while the second method requires a precise wavelength-swept source at the launching end of the multimode fibre. If significant mode coupling occurs inside the fibre, the second method cannot be used.

8.2. Future prospects

There are several issues requiring further scientific investigations. These are summarised below.

- **Pulsed source development**: This thesis is focused on continuous wave fibre sources. A natural next move is the development of the pulsed sources using the proposed waveguide structures. Since more pulse energy may be extracted from a larger core area, the depressed-clad hollow fibre can make a good candidate for a high energy pulsed fibre source. Although my colleagues and I demonstrated the blue (489 nm) frequency doubled source from the (continuous wave) JAC Yb^{3+}-doped fibre master-oscillator power amplifier configuration [43], the frequency doubling efficiency was only 1%. It is expected that the frequency doubling efficiency will be significantly enhanced

with a pulsed fibre laser pump source, since these have much higher peak powers than continuous wave sources. On the other hand, when picosecond or femtosecond pulses are of interest, one should look more into the waveguide dispersion characteristics. Since waveguides have dispersion and especially the proposed waveguides may have stronger waveguide dispersion characteristics than conventional step index fibres, a carefully designed waveguide may contribute towards high power picosecond and femtosecond pulsed fibre sources. For example, one can use parabolic pulse amplification in normal dispersion amplifier fibres [105-107].

- **Better control of fabrication process**: As was shown in chapter 3 (helical fibre), 4 (W-type fibre), 5 (depressed-clad hollow fibre), and 6 (modified W-type fibre), it is very important to fabricate a fibre with the desired waveguide structure. Especially the helical fibres are very sensitive to small deviations of the fibre parameters. In addition the fabricated depressed-clad Yb^{3+}-doped fibre in chapter 6 showed too large bending loss at 0.98 μm, which eventually degraded the efficiency of the fibre laser. Therefore future research may involve the improvement of the preform and fibre fabrication process to meet tight fibre specifications.
- **Experimental demonstration of the proposed modal power decomposition methods**: Although it was shown theoretically that the proposed two modal power decomposition methods based only on intensity measurements were feasible, there was no experimental demonstration. There are requirements in the proposed methods such that the first method requires the fibre source to be monochromatic and the second method that the multimode fibre is free from mode-coupling. It is difficult to say how much these assumptions and other limitations will affect the accuracy of the proposed modal power decomposition methods. Furthermore during experimental procedures, one may identify other important parameters and factors, which should be overcome for successful modal power decomposition. Therefore experimental demonstrations of such proposed algorithms are required.

Appendix A. Numerical simulation of fibre amplifiers and lasers

A numerical simulation technique for fibre amplifiers and lasers is introduced in this appendix. All of the numerical simulation results in the main chapters are based on this method. The simulator is spatially and spectrally resolved. Therefore, one can observe the spatial variation of the excited number of ions and the signal spectrum at each propagation distance (longitudinal coordinate). The numerical simulator does not depend on the rare-earth dopants, and here a Nd^{3+}-doped fibre amplifier operating at 1.3 μm is used as an example. Figure A.1 illustrates the energy level diagram. The simulator considers pump absorption, spontaneous emissions, stimulated emissions, stimulated absorptions, and signal ESA. The solid arrows represent radiative transitions whereas the white arrows represent rapid non-radiative transitions (e.g. rapid multi-phonon relaxation). For ESA, ions excited to energy level 6 are assumed to instantly lose energy to the metastable level 4, as in reference [85]. In fact, small portions of ions excited to energy level 6 may lose energy by radiative decay ending up at level 4, 3, 2, and 1, all of which are assumed to be negligible compared to the dominant near-instant non-radiative decay to level 4. In this case, the ESA only absorbs the signal photons, not affecting the number of excited ions in level 4. Therefore, no ESA term appears in the rate equation. Instead, the ESA effect appears in the propagation equation as a signal-absorbing term.

The $N_i(i=1,\cdots,6)$ represents the number of ions residing in the i'th energy level. R_{15} represents the pumping rate and W_{ij} represents the transition rate from the i'th level to the j'th level. Furthermore, level 2 and 3 are assumed to be empty with ions losing energy through rapid multi-phonon relaxation. Then the only populated levels are level 1 and level 4 and the rate equation is as follows.

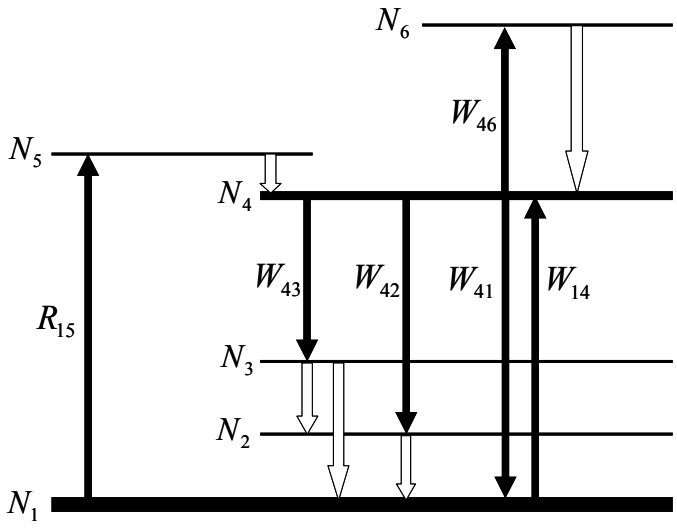

Figure A.1. An energy level illustration for Nd-doped fibre amplifier numerical simulator

$$\frac{\partial N_4(r,\phi,z)}{\partial t}\left(=-\frac{\partial N_1(r,\phi,z)}{\partial t}\right)=R_{15}N_1-\left(W_{4e}+\frac{1}{\tau_4}\right)N_4+W_{14}N_1, \qquad \text{(A.1)}$$

where τ_4 represents the lifetime of energy level 4 and

$$\begin{cases} R_{15}=\int_\nu \dfrac{\sigma_a(\nu)}{h\nu} i_p(r,\phi)\left\{S_p^+(z;\nu)+S_p^-(z;\nu)\right\}d\nu, \\ W_{4e}=\int_\nu \dfrac{\sigma_e(\nu)}{h\nu} i_s(r,\phi;\nu)\left\{S_s^+(z;\nu)+S_s^-(z;\nu)\right\}d\nu, \\ W_{14}=\int_\nu \dfrac{\sigma_a(\nu)}{h\nu} i_s(r,\phi;\nu)\left\{S_s^+(z;\nu)+S_s^-(z;\nu)\right\}d\nu. \end{cases} \qquad \text{(A.2)}$$

Here, W_{4e} includes the ion (radiative) decays to all levels below. In equation (A.2.), σ_a and σ_e represent the cross-sections for absorption from level 1 and emission from level 4, respectively. r,ϕ are the coordinates in the plane transverse to the propagation axis z, and ν represents the optical frequency. The normalised modal intensity i_s depends on the optical frequency ν. The modes are found by an arbitrary mode solver [73] and normalised such that $\int_0^{2\pi}\int_0^{\infty} i_s(r,\phi;\nu)rdrd\phi=1$. The pump intensity distribution i_p may depend on r,ϕ. However, for cladding pumping, it was

assumed to be a constant throughout the inner cladding. The pump and signal spectral power density $S_k^{\pm}$ ($k = s$ for signal and $k = p$ for pump and +,− represent propagation in the positive and negative z-direction, respectively) are in the unit of W/Hz so that the total power $P_k^{\pm}$ in the spectral range $[\nu_1, \nu_2]$ is calculated as $P_k^{\pm}(z;[\nu_1,\nu_2]) = \int_{\nu_1}^{\nu_2} S_k^{\pm}(z;\nu)d\nu$. In steady state, the fraction of excited ions can be expressed by equation (A.1) as

$$\frac{N_4(r,\phi,z)}{N_0} = \frac{R_{15} + W_{14}}{R_{15} + W_{14} + W_{4e} + 1/\tau_4}, \tag{A.3}$$

where N_0 represents the number of doped ions per unit volume.

The propagation equations for the signal and pump beams are considered next. The expressions include stimulated emission, stimulated absorption, ESA (as explained above), spontaneous emission, and the spectrally (i.e., wavelength) dependent fibre intrinsic loss [108, 109].

$$\begin{aligned} \pm\frac{dS_k^{\pm}(z;\nu)}{dz} = &\int_0^{2\pi}\int_0^{\infty} i_k(r,\phi)\left[\{\sigma_e - \sigma_{ESA}\}N_4 - \sigma_a N_1\right] r dr d\phi \times S_k^{\pm}(z;\nu) \\ &+ \int_0^{2\pi}\int_0^{\infty} i_k(r,\phi)\sigma_e N_4 r dr d\phi \times 2h\nu - \alpha(\nu)S_k^{\pm}(z;\nu), \end{aligned} \tag{A.4}$$

where α represents the spectrally dependent intrinsic fibre loss in unit of Np/m.

Therefore, the simulation variables are S_s^+, S_s^-, S_p^+, and S_p^-. In fact, there is no need to discriminate $S_s^{\pm}$ from $S_p^{\pm}$ since all light can be described by a single spectrum, and $i_s(r,\phi;\nu)$ can represent the field distribution of the pump as well as of the signal and amplified spontaneous emission. In the special case of cladding pumping, a constant i_p may be used for all (r,ϕ), if it is assumed that the pump intensity is evenly distributed over the inner cladding. This assumption is reasonable for fibres in which the pump modes are mixed at a high rate and for modes that are relatively evenly distributed across the inner cladding (e.g., with a D-shaped inner cladding [67]). In case of amplifier simulations, the boundary conditions are the optical spectrum of the seed signal at one end and the pump optical spectrum either at both ends or at one end, depending how the fibre is pumped. In the case of a laser, the

boundary conditions are the spectrally dependent reflectivity of mirrors (e.g., fibre Bragg gratings, bulk gratings, dichroic mirrors, Fresnel reflection etc.) at each end and the pump optical spectrum at one end or both ends.

The simulator is based on the Matlab® software with optimised codes for the fastest simulations. A Runge Kutta 4th order differential equation solver is used for equation (A.4). At each small step, the number of excited ions in equation (A.3) is calculated from the data of the previous step, which again feeds the differential equation (A.4) for the current step. Please note that the calculated number of excited ions is spatially distributed. The simulator uses a relaxation method described in reference [110] to meet the boundary conditions and to solve for the forward- and backward-propagating spectra. At the end of each pass, the initial conditions of the undetermined variables are adjusted towards convergence.

Regarding the simulation resolution, for instance, in case of the Nd^{3+}-doped fibre amplifier operating at 1.3 μm described in Chapter 6, the fibre length was divided into 500 pieces (at fixed points) and the number of spectral points was 600 between 850 nm and 1450 nm. The number of spatial points were 200 for the r variable only (not the φ variable), because the fibre design supported only the circularly symmetric LP_{01} mode for all wavelengths of concern. In fact, the laser simulation in chapter 6 was very stiff so it often took too long a time to converge (especially for the amplified spontaneous emission spectra other than the signal spectral components). A huge number of r variable grids encouraged the convergence. The reason seems to be the relatively complicated modal field of the modified W-type fibres. However, typically 20 spatial grids or less are enough for good simulation accuracy. Regarding computer resources, the memory usage was approximately 2 MB and the simulation time for one set of simulation was 10 – 20 seconds when a Pentium 4 (Intel®) 3.0 GHz computer was used. The total number of pass for simulation convergence was six round-trips on average.

Figure A.2 shows the simulation results for a cladding pumped Nd^{3+}-doped laser. The fibre design in section 6.2.1 was used, namely, a raised-ring W-type fibre with Nd ring-doping. The Nd^{3+}-doped ring has an inner diameter of 2 μm and an outer diameter of 8 μm. The Nd^{3+}-concentration is assumed to be 1.645×10^{25} ions/m^3. The fibre length is 20 m and the outer cladding diameter is 125 μm. The launched pump power is 20 W from a single end. The cross-sections and wavelength-dependent fibre

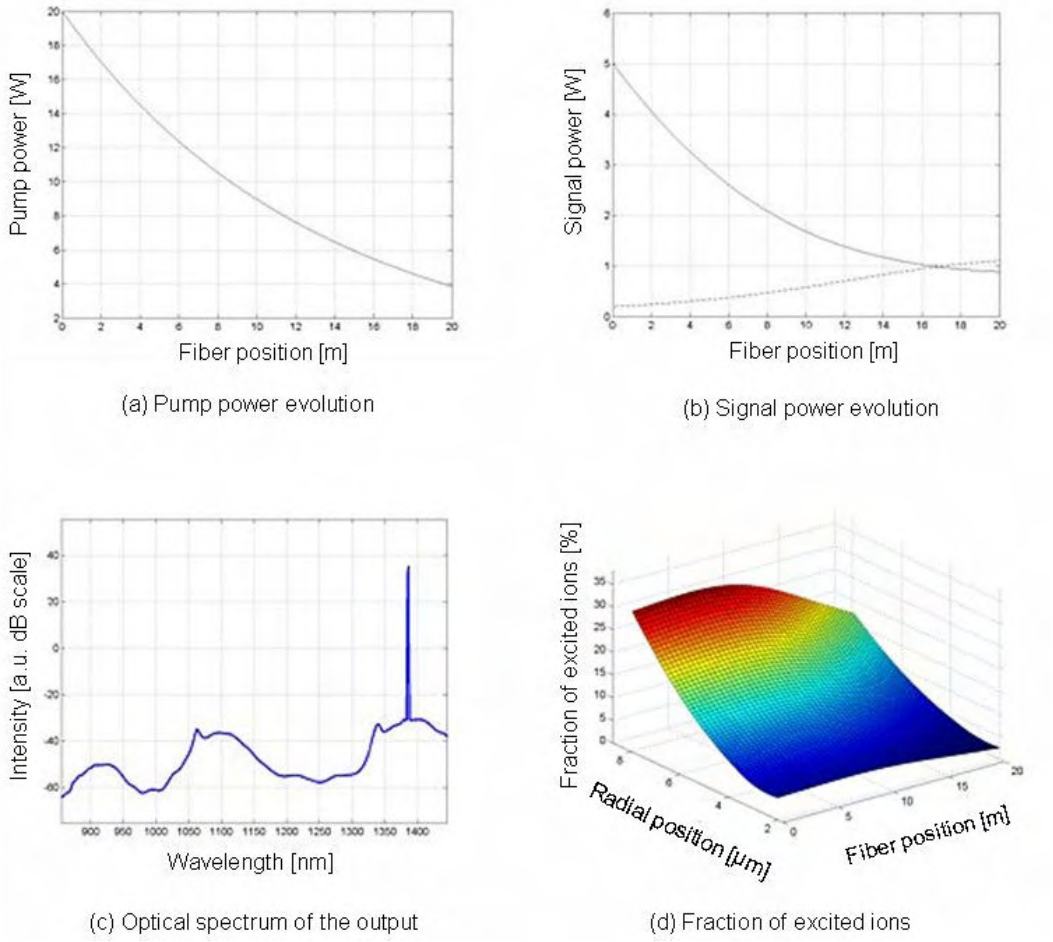

Figure A.2. Numerical simulation results of a Nd^{3+}-doped fibre laser at 1.38 μm. (a) The pump power evolution, (b) the signal power evolution with dashed line (solid line) represents the backward (forward) signal power, respectively, (c) the optical spectrum of the output, and (d) the fraction of excited ions along the radial and longitudinal position in fibre core.

intrinsic propagation loss are given in Chapter 6. The laser cavity consists of a Fresnel-reflecting (~4%) cleaved fibre facet at the pump launching end and a diffraction grating with 80% reflectivity at the signal feed-back end. The grating is tuned for 1.38 μm signal reflection with a linewidth of 1 nm. Figure A.2(a) shows the pump power along the fibre. Figure A.2(b) shows the signal power along the fibre with the solid line for the counter-propagating signal (relative to the pump) and the dashed line for the co-propagating signal. Figure A.2(c) shows the optical spectrum of the output signal. Figure A.2(d) shows the fraction of excited ions *vs*. longitudinal and radial fibre position. The ion excitation is more saturated in the central regions than in the outer regions due to the signal intensity distribution.

Appendix B. M^2 calculation

In this appendix, it will be shown how the beam quality parameter (M^2 value) of the output beam from a fibre mode can be calculated. For this, the mode field inside the fibre is assumed to be known. Figure B.1 depicts the conventional M^2 measurement process. The beam from a mode inside the fibre is collimated through lens 1 which has a focal length f_1. After propagation over a distance d, the beam is focused through lens 2 with focal length f_2. Then, the beam sizes in orthogonal planes are measured as a function of the distance. The measured waists are processed though an M^2 fitting algorithm. A typical value of d is 1 m, however the key is that the optical system used for the measurements does not aberrate the beam. For the simulations, I assumed f_1 = 8 mm and f_2 = 10 cm. If the field distribution of the fibre mode is denoted as U_0, all the fields of the propagating beam can be calculated through the Fresnel integration, including the effects of lenses. For instance, U_1^- denoting the fields just before lens 1 is calculated through [98]

$$U_1^-(x_1, y_1; f) = \frac{\exp(ikf)}{ikf} \int_{-\infty}^{\infty} \int_{-\infty}^{\infty} U_0(x_0, y_0) \exp\left[\frac{ik}{2f} \left\{ (x_1 - x_0)^2 + (y_1 - y_0)^2 \right\} \right] dx_0 dy_0 \text{ , (B.1)}$$

where k is the free-space wave number. In addition, U_1^+ is calculated from U_1^- through

$$U_1^+(x_1, y_1) = U_1^-(x_1, y_1) P(x, y) \exp\left[-\frac{ik}{2f_1} \left(x_1^2 + y_1^2 \right) \right], \qquad \text{(B.2)}$$

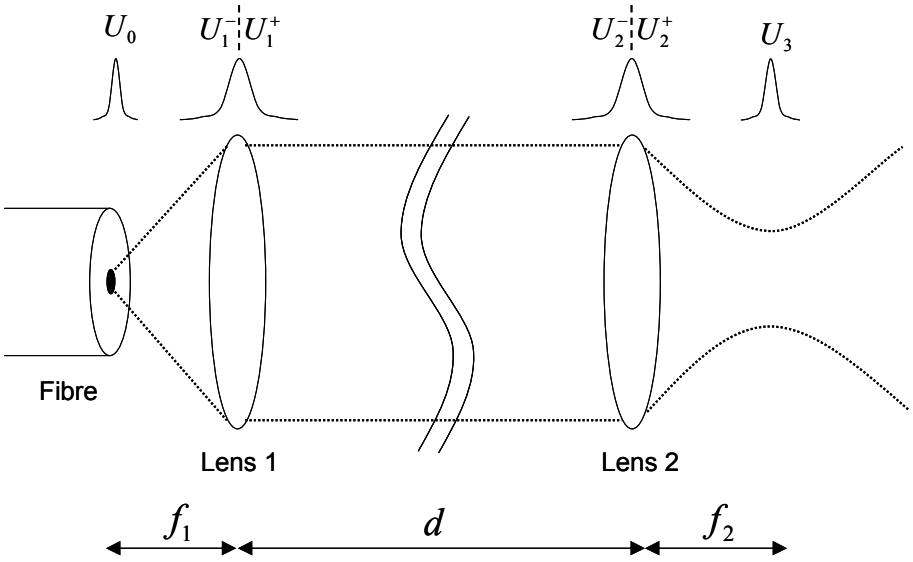

Figure B.1. M^2 measurement diagram

where P denotes the lens aperture function having value 1 if (x_1, y_1) falls within the lens and 0 otherwise. Using equations (B.1) and (B.2) successively, one can obtain the required fields at any z where z denotes the propagation distance from lens 2.

The beam radius is calculated from the second moment method in [88] as

$$w_x = \left[\frac{\int x^2 I(x)dx}{\int I(x)dx} - \left(\frac{\int xI(x)dx}{\int I(x)dx} \right)^2 \right]^{1/2}, \tag{B.3}$$

where w_x denotes the beam radius in x-axis and I the intensity distribution. In a purely Gaussian beam, the radius based on the second moment as in equation (B.3) coincides with the beam radius where the intensity has $1/e^2$ of the maximum value. The w_y can be obtained in a similar manner as in equation (B.3). Then, one can obtain the beam waist radius as a function of z.

The M^2 value is then found from a fitting procedure based on the minimisation of the error between the calculated beam waist data and the data that would be predicted with a certain M^2 value. According to theory, the beam radius should follow

$$w(z) = w_f \left[1 + \left(\frac{M^2 \lambda z}{\pi w_f^2} \right)^2 \right]^{1/2}, \tag{B.4}$$

where w_f denotes the smallest beam radius (waist) at $z = f_2$ and λ the wavelength. By minimising the error

$$e(M^2) = \int \left(w_{Fresnel}(z) - w_{M^2}(z)\right)^2 dz\,, \tag{B.5}$$

one can obtain the fitted M^2 value. Here, $w_M{}^2$ denotes the beam radius distribution for a specific value of M^2 as calculated by equation B.4 and $w_{Fresnel}$ denotes the actual beam waist distribution. In the fitting procedure, one can choose to vary the value of w_f while iterating, since the measured (or calculated) w_f may be slightly different from reality due to reasons such as measurement equipment resolution. For instance, conventional beam profilers have a resolution of 1 – 2 μm. In this case, the measured w_f (typically a few tens of micrometers to a hundred micrometers) may be affected by the beam profiler's resolution. Therefore, by imposing ± 5% deviation range of measured w_f in the fitting process, one may obtain better M^2 fitting.

Bibliography

[1] J. Dawson, R. Beach, A. Drobshoff, Z. Liao, D. Penningto, S. Payne, L. Taylor, W. Hackenberg, and D. Bonaccini, "938 nm Nd-doped high power cladding pumped fiber amplifier," in *Advanced Solid-State Photonics 2003 Technical Digest* (The Optical Society of America, Washington DC, 2003), pp. 118-121.

[2] P. D. Dragic and G. C. Papen, "Efficient amplification using the $^4F_{3/2}$ -> $^4I_{9/2}$ transition in Nd-doped silica fiber," *IEEE Photonics Technology Letters*, vol. 11, pp. 1593-1595, 1999.

[3] D. B. S. Soh, S. W. Yoo, J. K. Sahu, L. J. Cooper, S. Baek, J. Nilsson, and K. Oh, "A cladding pumped neodymium-doped fiber laser tunable from 932 nm to 953 nm," in *Advanced Solid-State Photonics 2004 Technical Digest on CD-ROM* (The Optical Society of America, Washington DC, 2004), Paper MD-10.

[4] T. J. Kane, G. Keaton, M. A. Arbore, D. R. Balsley, J. F. Black, J. L. Brooks, M. Byer, L. A. Eyres, M. Leonardo, J. J. Morehead, C. Rich, D. J. Richard, L. A. Smoliar, and Y. Zhou, "3-Watt blue source based on 914-nm Nd:YVO_4 passively-Q-switched laser amplified in cladding-pumped Nd:fiber," vol. 94, *OSA Trends in Optics and Photonics Series* (The Optical Society of America, Washington DC, 2004), pp. 160.

[5] M. J. Söderlund and S. K. T. Tammela, "A depressed-index cladding filter for suppressing 1.06 μm emission in a Nd-doped silica fiber amplifier," in *Proceedings of Conference on Optical Fiber Communication*, vol. 95 B, *OSA Trends in Optics and Photonics Series* (The Optical Society of America, Washington, DC, 2004), pp. 542.

[6] D. B. S. Soh, S. Yoo, J. Nilsson, J. K. Sahu, K. Oh, S. Baek, Y. Jeong, C. Codemard, P. Dupriez, J. Kim, and V. Philippov, "Neodymium-doped cladding-pumped aluminosilicate fiber laser tunable in the 0.9 μm wavelength range," *IEEE Journal of Quantum Electronics*, vol. 40, pp. 1275-1282, 2004.

[7] B. J. Mangan, J. Arriaga, T. A. Birks, J. C. Knight, and P. S. J. Russell, "Fundamental-mode cutoff in a photonic crystal fiber with a depressed-index core," *Optics Letters*, vol. 26, pp. 1469-1471, 2001.

[8] A. Bjarklev, T. Rasmussen, J. H. Povlsen, O. Lumholt, K. Rottwitt, S. Dahl-Petersen, and C. C. Larsen, "9 dB gain improvement of 1300 nm optical amplifier by amplified spontaneous emission suppressing fibre design," *Electronics Letters*, vol. 27, pp. 1701-1702, 1991.

[9] A. W. Snyder and J. D. Love, *Optical waveguide theory*: Chapman & Hall, 1983.

[10] R. D. Maurer, "Optical waveguide light source," US Patent 3808549, Apr. 30, 1974.

[11] B. Ortega and L. Dong, "Characteristics of mismatched twin-core fiber spectral filters," *IEEE Photonics Technology Letters*, vol. 10, pp. 991-993, 1998.

[12] Z. M. Mao and W. P. Huang, "An ARROW optical wavelength filter: design and analysis," *IEEE Journal of Lightwave Technology*, vol. 11, pp. 1183-1188, 1993.

[13] K. Morishita, "Optical fiber devices using dispersive materials," *IEEE Journal of Lightwave Technology*, vol. 7, pp. 198-201, 1989.

[14] J. Nishimura and K. Morishita, "Control of spectral characteristics of dispersive optical fibers by annealing," *IEEE Journal of Lightwave Technology*, vol. 15, pp. 294-298, 1997.

[15] J. Nishimura and K. Morishita, "Mode-field expansion and reduction in dispersive fibers by local heat treatments," *IEEE Journal of Selected Topics in Quantum Electronics*, vol. 5, pp. 1260-1265, 1999.

[16] S. Kawakami and S. Nishida, "Characteristics of a doubly clad optical fiber with a low-index inner cladding," *IEEE Journal of Quantum Electronics*, vol. QE10, pp. 879-887, 1974.

[17] M. Monerie, "Propagation in doubly clad single-mode fibers," *IEEE Microwave Theory and Techniques*, vol. QE-18, pp. 535-542, 1982.

[18] S. B. Poole, D. N. Payne, and M. E. Fermann, "Fabrication of low-loss optical fibres containing rare-earth ions," *Electronics Letters*, vol. 21, pp. 737-738, 1985.

[19] M. Arbore, Y. Zhou, H. Thiele, J. Bromage, and L. Nelson, "S-band erbium-doped fiber amplifiers for WDM transmission between 1488 and 1508 nm," presented at Optical Fiber Communication Conference and Exhibition 2003, Atlanta, GA, 23-28 March 2003, paper WK2.

[20] E. Snitzer, "Optical maser action of Nd^{3+} in a barium crown glass," *Physics Review Letters*, vol. 7, pp. 444-446, 1961.

[21] R. J. Mears, L. Reekie, S. B. Poole, and D. N. Payne, "Neodymium-doped silica single-mode fibre lasers," *Electronics Letters*, vol. 21, pp. 738-740, 1985.

[22] E. Snitzer, H. Po, F. Hakimi, R. P. Tümminelli, and B. C. McCollum, "Double-clad, offset core Nd fiber laser," in *1988 OSA Technical Digest Series*, vol. 2 (The Optical Society of America, New Orleans, 1988), Paper PD5.

[23] J. D. Minelly, E. R. Taylor, K. P. Jedrzejewski, J. Wang, and D. N. Payne, "Laser-diode-pumped neodymium-doped fibre laser with output power in excess of 1 Watt," presented at Conference on Lasers and Electro-Optics, Anaheim CA, May 1992, Paper CWE6.

[24] H. Po, J. D. Cao, B. M. Laliberte, R. A. Minns, R. F. Robinson, B. H. Rockney, R. R. Tricca, and Y. H. Zhang, "High power neodymium-doped single transverse mode fibre laser," *Electronics Letters*, vol. 29, pp. 1500-1501, 1993.

[25] H. Zellmer, A. Tünnermann, H. Welling, and V. Reichel, "Double-clad fiber laser with 30 W output power," in *Optical Amplifiers and their Applications*, vol. 16, *OSA Trends in Optics and Photonics* (The Optical Society of America, Washington DC, 1997), pp. 137-140.

[26] L. Reekie, R. J. Mears, D. N. Payne, and S. B. Poole, "Tunable single-mode fiber laser," in *Proceedings of IOOC-ECOC '85: 5th International Conference on Integrated Optics and Optical Fibre Communication - 11th European Conference on Optical Communication.*, vol. 3 (Istituto Int delle Comunicazioni, Venice, Italy, 1985), pp. 85-87.

[27] I. P. Alcock, A. I. Ferguson, D. C. Hanna, and A. C. Tropper, "Tunable, continuous-wave neodymium-doped monomode-fiber laser operating at 0.900-0.945 and 1.070-1.135 μm," *Optics Letters*, vol. 11, pp. 709-711, 1986.

[28] H. Po, F. Hakimi, R. J. Mansfield, R. P. Tümminelli, B. C. MacCollum, and E. Snitzer, "Neodymium fiber lasers at 0.905, 1.06, and 1.4 μm," in *Abstracts of the Annual Meeting of the Optical Society of America* (The Optical Society of America, Washington DC, 1986), pp. 103.

[29] W. J. Miniscalco, L. J. Andrews, B. A. Thompson, R. S. Quimby, L. J. B. Vacha, and M. G. Drexhage, "1. 3 μm Fluoride fibre laser," *Electronics Letters*, vol. 24, pp. 28-29, 1988.

[30] L. Reekie, I. M. Jauncey, S. B. Poole, and D. N. Payne, "Diode-laser-pumped Nd^{3+}-doped fibre laser operating at 938 nm," *Electronics Letters*, vol. 23, pp. 884-885, 1987.

[31] A. L. Cook and H. D. Hendricks, "Diode-laser-pumped tunable 896-939.5-nm neodymium-doped fiber laser with 43-mW output power," *Applied Optics*, vol. 37, pp. 3276-3281, 1998.

[32] Y. Jeong, J. K. Sahu, D. N. Payne, and J. Nilsson, "Ytterbium-doped large-core fiber laser with 1 kW of continuous- wave output power," *Electronics Letters*, vol. 40, pp. 470-472, 2004.

[33] Y. Jeong, J. Nilsson, J. K. Sahu, D. B. S. Soh, G. Alegria, P. Dupriez, C. A. Codemard, D. N. Payne, R. Horley, L. M. B. Hickey, L. Wanzcyk, C. E. Chryssou, J. A. Alvarez-Chavez, and P. W. Turner, "Single-frequency, single-mode, plane-polarized ytterbium-doped fiber master oscillator power amplifier source with 264 W of output power," *Optics Letters*, vol. 30, pp. 459-461, 2005.

[34] J. K. Sahu, C. C. Renaud, K. Furusawa, R. Selvas, J. A. Alvarez-Chavez, D. J. Richardson, and J. Nilsson, "Jacketed air-clad cladding pumped ytterbium-doped fibre laser with wide tuning range," *Electronics Letters*, vol. 37, pp. 1116-1117, 2001.

[35] K. H. Ylä-Jarkko, R. Selvas, D. B. S. Soh, J. K. Sahu, C. A. Codemard, J. Nilsson, S. A. Alam, and A. B. Grudinin, "A 3.5 W 977 nm cladding-pumped jacketed air-clad ytterbium-doped fiber laser," in *Advanced Solid-State Photonics 2003 Technical Digest*, vol. 83, *Trends in Optics and Photonics Series* (The Optical Society of America, Washington DC, 2003), pp. 103-107.

[36] L. E. Lago and R. de la Fuente, "Wavefront sensing by diffracted beam interferometry," *Journal of Optics A - Pure and Applied Optics*, vol. 4, pp. 299-302, 2002.

[37] O. G. Leminger and G. K. Grau, "Near-field intensity and modal power distribution in multimode graded-index fibres," *Electronics Letters*, vol. 16, pp. 678-679, 1980.

[38] D. Rittich, "Practicability of determining the modal power distribution by measured near and far fields," *IEEE Journal of Lightwave Technology*, vol. LT-3, pp. 652-661, 1985.

[39] F. Gori, M. Santarsiero, R. Borghi, and G. Guattari, "Intensity-based modal analysis of partially coherent beams with Hermite-Gaussian modes," *Optics Letters*, vol. 23, pp. 989-991, 1998.

[40] G.-Z. Yang, B.-Z. Dong, B.-Y. Gu, J.-Y. Zhuang, and O. K. Ersoy, "Gerchberg-Saxton and Yang-Gu algorithms for phase retrieval in a nonunitary transform system: a comparison," *Applied Optics*, vol. 33, pp. 209-218, 1994.

[41] D. B. S. Soh, C. Codemard, J. K. Sahu, J. Nilsson, V. Philippov, C. Alegria, and Y. Jeong, "A 4.3W 977 nm ytterbium-doped jacketed-air-clad fiber amplifier," *Advanced Solid-State Photonics 2004 Technical Digest on CD-ROM* (The Optical Society of America, Washington DC, 2004), Paper MA3.

[42] D. B. S. Soh, C. Codemard, J. K. Sahu, J. Nilsson, S. Baek, S. Wang, and F. Laurell, "An 18 mW, 488.7 nm cw frequency doubled fiber MOPA source," San Jose, CA, United States, 5335.

[43] D. B. S. Soh, C. Codemard, S. Wang, J. Nilsson, J. K. Sahu, F. Laurell, V. Philippov, Y. Jeong, C. Alegria, and S. Baek, "A 980-nm Yb-doped fiber MOPA source and its frequency doubling," *IEEE Photonics Technology Letters*, vol. 16, pp. 1032-1034, 2004.

[44] D. Marcuse, *Light transmission optics*. New York: Van Nostrand Reinhold Company, 1972.

[45] P.-A. Belanger, *Optical fiber theory*. London: World Scientific Co. Pte. Ltd., 1993.

[46] M. Movassaghi and M. K. Jackson, "Design and compact modeling of saturated erbium-doped fiber amplifiers with nonconfined doping," *Optical Fiber Technology*, vol. 7, pp. 312-323, 2001.

[47] M. J. F. Digonnet, "Closed-form expressions for the gain in 3-Level and 4-Level laser fibers," *IEEE Journal of Quantum Electronics*, vol. 26, pp. 1788-1796, 1990.

[48] H. Coic, "Analytic modelling of high-gain ytterbium-doped fibre amplifiers," *Journal of Optics A - Pure and Applied Optics*, vol. 4, pp. 120-129, 2002.

[49] S. Jarabo, "Analytical theoretical model of erbium-doped fibre amplifiers," *Optics Communications*, vol. 181, pp. 303-311, 2000.

[50] G. C. Valley, "Modeling cladding-pumped Er/Yb fiber amplifiers," *Optical Fiber Technology*, vol. 7, pp. 21-44, 2001.

[51] A. Bertoni and G. C. Reali, "A model for the optimization of double-clad fiber laser operation," *Applied Physics B-Lasers and Optics*, vol. 66, pp. 547-554, 1998.

[52] E. Yahel and A. Hardy, "Modeling high-power Er^{3+}-Yb^{3+} codoped fiber lasers," *IEEE Journal of Lightwave Technology*, vol. 21, pp. 2044-2052, 2003.

[53] E. Desurvire, *Erbium-doped fiber amplifiers*. New York: John Wiley & Sons, Inc., 1994.

[54] D. Gloge, "Dispersion in Weakly Guiding Fibers," *Applied Optics*, vol. 10, pp. 2442-2444, 1971.

[55] D. Gloge, "Weakly Guiding Fibers," *Applied Optics*, vol. 10, pp. 2252-2258, 1971.

[56] D. Marcuse, "Loss Analysis of Single-Mode Fiber Splices," *Bell System Technical Journal*, vol. 56, pp. 703-718, 1977.

[57] R. D. Birch, "Fabrication and characterisation of circularly birefringent helical fibres," *Electronics Letters*, vol. 23, pp. 50-52, 1987.

[58] A. Altintas and J. D. Love, "Effective cut-offs for modes on helical fibres," *Optical and Quantum Electronics*, vol. 22, pp. 213-226, 1990.

[59] A. Altintas and S. G. Tanyer, "Examination of the effect of polarization on the radiation losses of bent optical fibres," *Optical and Quantum Electronics*, vol. 25, pp. 105-112, 1993.

[60] G. Chen and Q. Wang, "Local fields in single-mode helical fibres," *Optical and Quantum Electronics*, vol. 27, pp. 1069-1074, 1995.

[61] G. Chen and Q. Wang, "Mode coupling in single-mode helical fibres under perturbations," *Optical and Quantum Electronics*, vol. 30, pp. 209-216, 1998.

[62] J. D. Love and A. W. Snyder, "Radiation from single-mode helical fibres," *Electronics Letters*, vol. 23, pp. 1109-1110, 1987.

[63] D. B. S. Soh, J. Nilsson, J. K. Sahu, and L. J. Cooper, "Geometrical factor modification of helical-core fiber radiation loss formula," *Optics Communications*, vol. 222, pp. 235-242, 2003.

[64] W. A. Gambling, H. Matsumura, and C. M. Ragdale, "Field deformation in a curved single-mode fibre," *Electronics Letters*, vol. 14, pp. 130-132, 1978.

[65] J. N. Ross, "The rotation of the polarization in low birefringence monomode optical fibres due to geometric effects," *Optical and Quantum Electronics*, vol. 16, pp. 455-461, 1984.

[66] D. Marcuse, "Field deformation and loss caused by curvature of optical fibers," *Journal of the Optical Society of America*, vol. 66, pp. 311-320, 1976.

[67] L. Philippe, V. Doya, R. Philippe, P. Dominique, M. Fabrice, and L. Olivier, "Experimental study of pump power absorption along rare-earth-doped double clad optical fibres," *Optics Communications*, vol. 218, pp. 249-254, 2003.

[68] D. B. S. Soh, S. W. Yoo, C. A. Codemard, S. Baek, J. K. Sahu, J. Nilsson, and K. Oh, "Tunable cladding pumped neodymium-doped three-level fiber laser," in *Advanced Solid-State Photonics 2004 Technical Digest*, vol. 94, *OSA Trends in Optics and Photonics Series* (Optical Society of America, Washington, DC 2004), pp. 113.

[69] D. B. S. Soh, S. W. Yoo, J. Nilsson, J. K. Sahu, S. Baek, Y. Jeong, L. J. Cooper, C. Codemard, P. Dupriez, C. Alegria, V. Philippov, and K. Oh, "Cladding pumped Nd-doped fiber laser tunable from 908 to 938 nm," presented at Conference on Lasers and Electro-Optics, San Francisco, CA, 7-12 May 2004, Paper CMK4.

[70] R. Selvas, *Cladding-pumped neodymium and ytterbium-doped fibre lasers*, PhD thesis, Optoelectronics Research Centre, University of Southampton (Southampton, United Kingdom), 2004.

[71] S. Yoo, D. B. S. Soh, J. Kim, Y. Jung, J. Nilsson, J. K. Sahu, J. W. Lee, and K. Oh, "Analysis of W-type waveguide for Nd-doped fiber laser operating near 940 nm," *Optics Communications*, vol. 247, pp. 153-162, 2005.

[72] J. Kim, P. Dupriez, D. B. S. Soh, J. K. Sahu, J. Nilsson, and D. N. Payne, "Nd:Al-doped depressed clad hollow fiber laser at 930 nm," in *Advanced Solid-State Photonics 2005 Technical Digest on CD-ROM* (The Optical Society of America, Washington DC, 2005), Paper MC5.

[73] K. Morishita, "Numerical analysis of pulse broadening in graded index optical fibers," *IEEE Transactions on Microwave Theory and Techniques*, vol. MTT-29, pp. 348-352, 1981.

[74] J. Nilsson, W. A. Clarkson, R. Selvas, J. K. Sahu, P. W. Turner, S. U. Alam, and A. B. Grudinin, "High-power wavelength-tunable cladding-pumped rare-earth-doped silica fiber lasers," *Optical Fiber Technology*, vol. 10, pp. 5-30, 2004.

[75] H. Ito, K. Sakaki, T. Nakata, W. Jhe, and M. Ohtsu, "Optical potential for atom guidance in a cylindrical-core hollow-fiber," *Optics Communications*, vol. 115, pp. 57-64, 1995.

[76] S. Choi and K. Oh, "A new LP_{02} mode dispersion compensation scheme based on mode converter using hollow optical fiber," *Optics Communications*, vol. 222, pp. 213-219, 2003.

[77] J. Sakai and T. Kimura, "Bending loss of propagation modes in arbitrary-index profile optical fibers," *Applied Optics*, vol. 17, pp. 1499-1506, 1978.

[78] J. Kim, D. B. S. Soh, C. Codemard, S. Yoo, Y. Jeong, J. Nilsson, and J. K. Sahu, "Yb:Al-doped depressed clad hollow optical fiber laser operating at 980 nm," presented at Conference on Lasers and Electro-Optics Pacific Rim, Tokyo, 11-15 Jul 2005, Paper CTuI4-5.

[79] I. H. Malitson, "Interspecimen comparison of the refractive index of fused silica," *Journal of the Optical Society of America*, vol. 55, pp. 1205-1209, 1965.

[80] P. R. Morkel, M. C. Farries, and S. B. Poole, "Spectral variation of excited-state absorption in neodymium doped fiber lasers," *Optics Communications*, vol. 67, pp. 349-352, 1988.

[81] F. Hakimi, H. Po, R. Tümminelli, B. C. McCollum, L. Zenteno, N. M. Cho, and E. Snitzer, "Glass fiber laser at 1.36 μm from SiO_2:Nd," *Optics Letters*, vol. 14, pp. 1060-1061, 1989.

[82] S. Zemon, B. Pedersen, G. Lambert, W. J. Miniscalco, B. T. Hall, R. C. Folweiler, B. A. Thompson, and L. J. Andrews, "Excited-state-absorption cross sections and amplifier modeling in the 1300-nm region for Nd-doped glasses," *IEEE Photonics Technology Letters*, vol. 4, pp. 244-247, 1992.

[83] E. Rochat, A. Woodtli, and R. Dandliker, "Excited-state absorption and gain measurement at 1.3 μm in Nd^{3+}-doped silica fibers with different codopants: Effect of cesium on ESA cross section," *IEEE Journal of Lightwave Technology*, vol. 15, pp. 1573-1577, 1997.

[84] M. Brierley, S. Carter, P. France, and J. E. Pedersen, "Amplification in the 1300 nm telecommunications window in a Nd-doped fluoride fibre," *Electronics Letters*, vol. 26, pp. 329-330, 1990.

[85] M. L. Dakss and W. J. Miniscalco, "Fundamental limits on Nd^{3+}-doped fiber amplifier performance at 1.3 μm," *IEEE Photonics Technology Letters*, vol. 2, pp. 650-652, 1990.

[86] T. Sugawa, Y. Miyajima, and T. Komukai, "10dB gain and high saturation power in a Nd^{3+}-doped fluorozirconate fibre amplifier," *Electronics Letters*, vol. 26, pp. 2042-2044, 1990.

[87] M. Obro, B. Pedersen, A. Bjarklev, J. H. Povlsen, and J. E. Pedersen, "Highly improved fibre amplifier for operation around 1300nm," *Electronics Letters*, vol. 27, pp. 470-472, 1991.

[88] ISO 11146-2, "Lasers and laser-related equipment - Test methods for laser beam widths, divergence angles and beam propagation ratios - Part 2: General astigmatic beams," International Organization for Standardization, 2005.

[89] L. Zenteno, "High-power double-clad fiber lasers," *IEEE Journal of Lightwave Technology*, vol. 11, pp. 1435-1446, 1993.

[90] T. Weber, W. Luthy, H. P. Weber, V. Neuman, H. Berthou, G. Kotrotsios, J. P. Dan, and H. E. Hintermann, "Cladding-pumped fiber laser," *IEEE Journal of Quantum Electronics*, vol. 31, pp. 326-329, 1995.

[91] G. K. Grau and O. G. Leminger, "Relations between near-field and far-field intensities, radiance, and modal power distribution of multimode graded-index fibers," *Applied Optics*, vol. 20, pp. 457-459, 1981.

[92] A. R. Mickelson and M. Eriksrud, "Mode-continuum approximation in optical fibers," *Optics Letters*, vol. 7, pp. 572-574, 1982.

[93] A. R. Mickelson, M. Eriksrud, S. Aamlid, and N. Ryen, "Role of the fusion splice in the concatenation problem," *IEEE Journal of Lightwave Technology*, vol. 2, pp. 126-138, 1984.

[94] F. Gori, M. Santarsiero, R. Simon, G. Piquero, R. Borghi, and G. Guattari, "Coherent-mode decomposition of partially polarized, partially coherent sources," *Journal of the Optical Society of America A*, vol. 20, pp. 78-84, 2003.

[95] C. Elster and I. Weingartner, "Solution to the shearing problem," *Applied Optics*, vol. 38, pp. 5024-5031, 1999.

[96] E. L. Lago and R. de la Fuente, "Wavefront sensing by diffracted beam interferometry," *Journal of Optics A - Pure and Applied Optics*, vol. 4, pp. 299-302, 2002.

[97] D. B. S. Soh, J. Nilsson, S. Baek, C. Codemard, Y. C. Jeong, and V. Philippov, "Modal power decomposition of beam intensity profiles into linearly polarized modes of multimode optical fibers," *Journal of the Optical Society of America A*, vol. 21, pp. 1241-1250, 2004.

[98] J. W. Goodman, *Introduction to Fourier optics*. New York: McGraw-Hill, 1968.

[99] K. A. Nugent, "Wave field determination using 3-dimensional intensity information," *Physical Review Letters*, vol. 68, pp. 2261-2264, 1992.

[100] D. F. Mcalister, M. Beck, L. Clarke, A. Mayer, and M. G. Raymer, "Optical-phase retrieval by phase-space tomography and fractional-order Fourier-transforms," *Optics Letters*, vol. 20, pp. 1181-1183, 1995.

[101] M. G. Raymer, M. Beck, and D. F. Mcalister, "Complex wave-field reconstruction using phase-space tomography," *Physical Review Letters*, vol. 72, pp. 1137-1140, 1994.

[102] J. Tu and S. Tamura, "Wave field determination using tomography of the ambiguity function," *Physical Review E*, vol. 55, pp. 1946-1949, 1997.

[103] J. Bertrand and P. Bertrand, "A tomographic approach to Wigner function," *Foundations of Physics*, vol. 17, pp. 397-405, 1987.

[104] G. E. Healey and R. Kondepudy, "Radiometric CCD camera calibration and noise estimation," *IEEE Transactions on Pattern Analysis and Machine Intelligence*, vol. 16, pp. 267-276, 1994.

[105] M. E. Fermann, V. I. Kruglov, B. C. Thomsen, J. M. Dudley, and J. D. Harvey, "Self-similar propagation and amplification of parabolic pulses in optical fibers," *Physical Review Letters*, vol. 84, pp. 6010-6013, 2000.

[106] D. B. S. Soh, J. Nilsson, and A. B. Grudinin, "Efficient femtosecond pulse generation using a parabolic amplifier combined with a pulse compressor I. stimulated Raman scattering effect," *Journal of Optical Society of America B*, 2005, to appear.

[107] D. B. S. Soh, J. Nilsson, and A. B. Grudinin, "Efficient femtosecond pulse generation using a parabolic amplifier combined with a pulse compressor II. finite gain bandwidth effect," *Journal of Optical Society of America B*, 2005, to appear.

[108] C. R. Giles and E. Desurvire, "Modeling erbium-doped fiber amplifiers," *IEEE Journal of Lightwave Technology*, vol. 9, pp. 271-283, 1991.

[109] B. Pedersen, K. Dybdal, C. D. Hansen, A. Bjarklev, J. H. Povlsen, H. Vendeltorp-Pommer, and C. C. Larsen, "Detailed theoretical and experimental investigation of high-gain erbium-doped fiber amplifier," *IEEE Photonics Technology Letters*, vol. 2, pp. 863-865, 1990.

[110] W. H. Press, S. A. Teukolsky, W. T. Vetterling, and B. P. Flannery, *Numerical recipes in C*. New York: Cambridge University Press, 1992.